Results of the application and demonstration calculations

Authors : Dr. Georgios ALEXANDRIDIS (NTUA), Christoph Bläsius (GRS), Christophe Demaziere (Chalmers), Christophe Destouches (CEA), Abdelhamid Dokhane (PSI), Aiden Durrant (University of Lincoln), Vladimir Fiser (UJV Rez), Gaëtan Girardin (KKG), Joachim Herb (GRS), Georgios Ioannou (ICCS-NTUA), Robert Jacqmin (CEA), Alexander Knospe (TU Dresden), Stefanos Kollias (University of Lincoln), Carsten Lange (TU Dresden), Georgios Leontidis (University of Lincoln), Sandor Lipcsei (MTA EK), Cristina Montalvo (UPM), Antonios Mylonakis (Chalmers), Laurent Pantera (CEA), Yann Perin (GRS), Christoph Pohl (TÜV), Marcus Seidl (PEL), Andreas Stafylopatis (ICCS-NTUA), Petr Stulik (UJV Rez), Luis Alejandro Torres (UPM), Gumersindo Verdu Martin (UPV), Vasudha Verma (PSI), Antoni Vidal-Ferràndiz (UPV), Marco Viebach (TU Dresden), Paolo Vinai (Chalmers)

CORTEX - Contract Number: 754316

Project officer: Foivos MARIAS

Document title	Results of the application and demonstration calculations
Author(s)	Dr. Georgios ALEXANDRIDIS, Christoph Bläsius (GRS), Christophe Demaziere (Chalmers), Christophe Destouches (CEA), Abdelhamid Dokhane (PSI), Aiden Durrant (University of Lincoln), Vladimir Fiser (UJV Rez), Gaëtan Girardin (KKG), Joachim Herb (GRS), Georgios Ioannou (ICCS-NTUA), Robert Jacqmin (CEA), Alexander Knospe (TU Dresden), Stefanos Kollias (University of Lincoln), Carsten Lange (TU Dresden), Georgios Leontidis (University of Lincoln), Sandor Lipcsei (MTA EK), Cristina Montalvo (UPM), Antonios Mylonakis (Chalmers), Laurent Pantera (CEA), Yann Perin (GRS), Christoph Pohl (TÜV), Marcus Seidl (PEL), Andreas Stafylopatis (ICCS-NTUA), Petr Stulik (UJV Rez), Luis Alejandro Torres (UPM), Gumersindo Verdu Martin (UPV), Vasudha Verma (PSI), Antoni Vidal-Ferràndiz (UPV), Marco Viebach (TU Dresden), Paolo Vinai (Chalmers)
Number of pages	192
Document type	Deliverable
Work Package	WP04
Document number	D4.4
Issued by	NTUA
Date of completion	2020-07-31 01:00:13
Dissemination level	Public

Summary

This report describes the results of the application of the newly developed tools for reactor noise analysis, advanced signal processing and machine learning methodologies to actual plant data. More specifically, the modeling tools developed in WP1 are used to simulate and analyze real plant measurements from the pre-Konvoi 3-loop NPP at Gösgen, a German pre-Konvoi 4-loop reactor, a Hungarian VVER-440 reactor and a Czech VVER-1000 reactor. Subsequently, the techniques developed in WP3 are used to identify the root causes of neutron flux fluctuations in the actual plant data for the reactors presented above. The results are compared with the simulation results corresponding to the selected power plants, based on the hypotheses developed for reactor noise analysis.

Approval

Date	By
2020-07-31 01:10:23	Mr. Joachim HERB (GRS)
2020-07-31 13:13:27	Pr. Christophe DEMAZIERE (Chalmers)

Table of Contents

List of Tables

List of Figures

Abbreviations

APSD	Auto-Power Spectral Density
AVS	Absorber of Variable Strength
AWGN	Additive White Gaussian Noise
BOC	Beginning Of Cycle
CB	Core Barrel
CNN	Convolutional Neural Network
CPSD	Cross-Power Spectral Density
CRV	Control Rod Vibration
DA	Domain Adaptation
EFPD	Equivalent Full Power Days
EOC	End Of Cycle
FA	Fuel Assembly
FAV	Fuel Assembly Vibration
FFT	Fast Fourier Transform
FSI	Fluid-Structure Interaction
GAP	Global Average Pooling
HHT	Hilbert Huang Transform
InD	**In** reactor middle **D**etectors
IrD	**I**n I**r**i vicinity **D**etectors
IRI	Incomplete Rod Insertion
JTFS	Joint Time Frequency Spectrum
KWU	Kraftwerk Union
LSTM	Long Short-Term Memory
MAE	Mean Absolute Error
ML	Machine Learning
MOC	Middle of cycle
NRMS	Normalized Root Mean Square
PeD	**Pe**ripheral **D**etectors
PSD	Power Spectral Density
RPV	Reactor Pressure Vessel
S3K	SIMULATE-3K
SDOF	Single Degree of Freedom
SNR	Signal to Noise Ratio
SSA	Singular Spectrum Analysis
SPND	Self-Powered Neutron Detector

SVD	Single Value Decomposition
SVM	Support Vector Machines
SSA	Singular Spectrum Analysis
TH	Thermal-Hydraulic
TP	Travelling Perturbation

Summary

This report describes the results of the application of the newly developed tools for reactor noise analysis, advanced signal processing and machine learning methodologies to actual plant data. More specifically, the modeling tools developed in WP1 are used to simulate and analyze real plant measurements from the pre-Konvoi 3-loop NPP at Gösgen, a German pre-Konvoi 4-loop reactor, a Hungarian VVER-440 reactor and a Czech VVER-1000 reactor. Subsequently, the techniques developed in WP3 are used to identify the root causes of neutron flux fluctuations in the actual plant data for the reactors presented above. The results are compared with the simulation results corresponding to the selected power plants, based on the hypotheses developed for reactor noise analysis.

1   Introduction

The Horizon 2020 EU project CORTEX aims at developing techniques that can be used to detect and characterize operational problems in nuclear reactor cores, before those problems have any inadvertent effect on plant safety and availability. This is primarily achieved by recording the inherent fluctuations in neutron flux, using in-core and ex-core instrumentation. Based on the aforementioned recorded signals, the main objective is to be able to differentiate the anomalies, depending on their type, location and characteristics, thereby obtaining a deepened understanding of the physical processes involved.

In this deliverable, actual plant measurements, originating from four different reactors, are going to be used, in order to demonstrate the applicability, as well as the usefulness of the developed tools at the previous stages of the project, especially those based on the inversion of the reactor transfer function complemented by advanced signal processing techniques. Emphasis will be placed on the detection of abnormal fluctuations, on the understanding of their origin, and on the classification of the anomalies according to their safety impact.

In Section 2 of the current deliverable, the various modeling software (CORE SIM+, SIMULATE-3K, FEMFFUSION), either developed within the CORTEX project or not, are briefly introduced. Then the four reactors are described (German pre-Konvoi 4-loop reactor, Swiss pre-Konvoi 3-loop reactor, Hungarian VVER-440 reactor, Czech VVER-1000 reactor), together with the corresponding scenarios of anomalies that were investigated.

In Section 3, fluid-structure interactions simulations are analyzed, starting with the simulations with the GRS mechanical model, under generic excitation scenarios. Then, noise simulations with an upgraded version of the system code DYN3D, which includes the ROM for mechanical vibrations of reactor core internals, for full core analysis of the same pre-Konvoi 4-loop reactor are presented.

In Section 4, the actual plant measurements are being processed, using standard and advanced signal processing techniques. These range from the Fourier analysis and the computation of the Auto Power Spectral Densities, to the Hilbert-Huang Transform and the Joint Time Frequency and Singular Spectra Analysis.

In Section 5, the machine learning-based classification and localization techniques are outlined. These include the voxel-wise, semantic segmentation for simulated data classification and localization of multiple, simultaneously occurring perturbations, along with convolutional, recurrent neural network architectures for perturbation classification and localization. Finally, this report concludes in Section 6, where some general observations and remarks are being made

2   Neutron noise simulations

In this Section, the simulations of the neutron noise induced by postulated noise sources in the reactors considered in Task 4.2 are presented. First, the various modelling software, some of them developed within the CORTEX project, are briefly introduced. Thereafter, the various reactors are described, together with the corresponding scenarios of anomalies that were investigated.

2.1   Modelling tools

2.1.1   CORE SIM+

CORE SIM+ is a frequency-domain modelling tool developed at CHALMERS as part of the CORTEX project (Mylonakis et al., 2020). This tool estimates the effect of macroscopic cross-section stationary perturbations onto the neutron flux using the two-group diffusion approximation and linear theory. One group of delayed neutrons is considered. The spatial discretization of the balance equations is based on finite differences, assuming Cartesian geometry. Depending on the problem of interest, different numerical methods and non-uniform computational meshes can be selected for effective numerical performances and accuracy. The simulator can generate neutron noise databases for nuclear power reactors via the Green's function method in a fully automated manner. These databases can be useful to study the neutron noise behavior in a reactor and to train machine learning algorithms for core monitoring and diagnostics.

2.1.2   SIMULATE-3K

SIMULATE-3K (S3K) is a time-domain commercial core simulator developed by Studsvik Scandpower (Grandi, 2011). The calculations are performed considering the interdependence between the neutronics and the thermal-hydraulics. On the neutronic side, the modelling is based on the time-dependent two-group diffusion approximation and using six groups of delayed neutrons. The spatial discretization of the balance equations is based on nodal methods. On the thermal-hydraulic side, the modelling is based on a macroscopic modelling of the mass conservation equation, momentum conservation equation, and energy conservation equation. For mass and energy, phasic balance equations are considered, whereas for momentum, a mixture balance equation is considered. The discretization of the balance equations is based on finite volumes. The tool does not rely on linear theory, i.e. the non-linear terms are explicitly modelled. Perturbations are defined in terms of perturbations of variables such as coolant inlet temperature, core flow rate or water gap thickness (for fuel assembly vibrations and core barrel vibrations) via dedicated scripts developed by PSI.

2.1.3   FEMFFUSION

FEMFFUSION is a time- and frequency-domain modelling tool developed at UPV as part of the CORTEX project (Vidal-Ferràndiz et al., 2020a, 2020b). This tool estimates the effect of macroscopic cross-section stationary perturbations onto the neutron flux using the two-group diffusion approximation. In the time-domain, non-linear terms are explicitly modelled, whereas in the frequency-domain, linear theory is used. Six group of delayed neutrons are considered. The spatial discretization of the balance equations is based on finite elements, using a high order continuous Galerkin method. Any kind of structured or unstructured mesh is allowed, as long as the elements are composed of quadrilaterals in 2-D or hexahedras in 3-D. In the case of reactors with hexagonal fuel assemblies, each hexagon is discretized into three quadrilateral cells, as represented in Figure 1. A simple extrusion of this geometry is performed to take the axial variation into account.
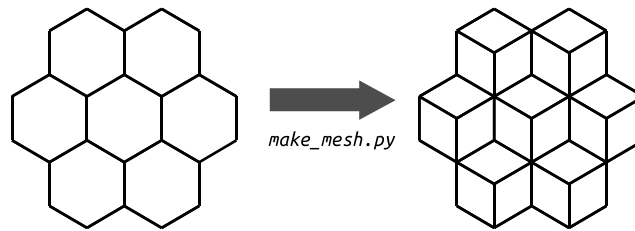
Figure 1: Spatial discretization of hexagonal fuel assemblies into quadrilaterals.

2.1.4 DYN3D

DYN3D is a three-dimensional, time domain reactor code, developed by HZDR (Helmholtz-Zentrum Dresden-Rossendorf), for thermal reactor cores (Rohde, 2016). It utilizes a three-dimensional nodal model to solve the two-group or multi-group diffusion equation for neutrons in both Cartesian and hexagonal-z geometry. The modelling of the thermal hydraulics inside the core is based on a four-equation model representing the conservation of mass, momentum, energy of the mixture and the mass balance of the vapour (in the case of a boiling water reactor). These are solved numerically by the method of characteristics (for the energy conservation) and a so-called MIRONOV scheme (for the solution of the coupled mass and momentum balance). The coupled neutronic and thermal hydraulic models are solved via an internal iteration loop until a convergence of the feedback parameters is reached.

2.2 Description of the considered reactors and of the corresponding scenarios

2.2.1 German pre-Konvoi 4-loop reactor

The reactor considered hereafter is a 4-loop reactor of pre-Konvoi design. The core layout with the position of the various neutron detectors (both in-core and ex-core detectors) is given in Figure 2 and in Figure 3. The modelling parameters used in the simulations are representative of the core conditions corresponding to the noise measurements performed on February 28th, 2012, during the fuel cycle 30, with a soluble boron concentration of 78 ppm, a thermal output of 3730 MWth and an average coolant temperature of 304.2 °C. A more complete description of the reactor, of the measuring equipment and of the core conditions can be found in the deliverables D4.2 and D4.3 (Kuentzel et al., 2018; Lipcsei et al., 2018).
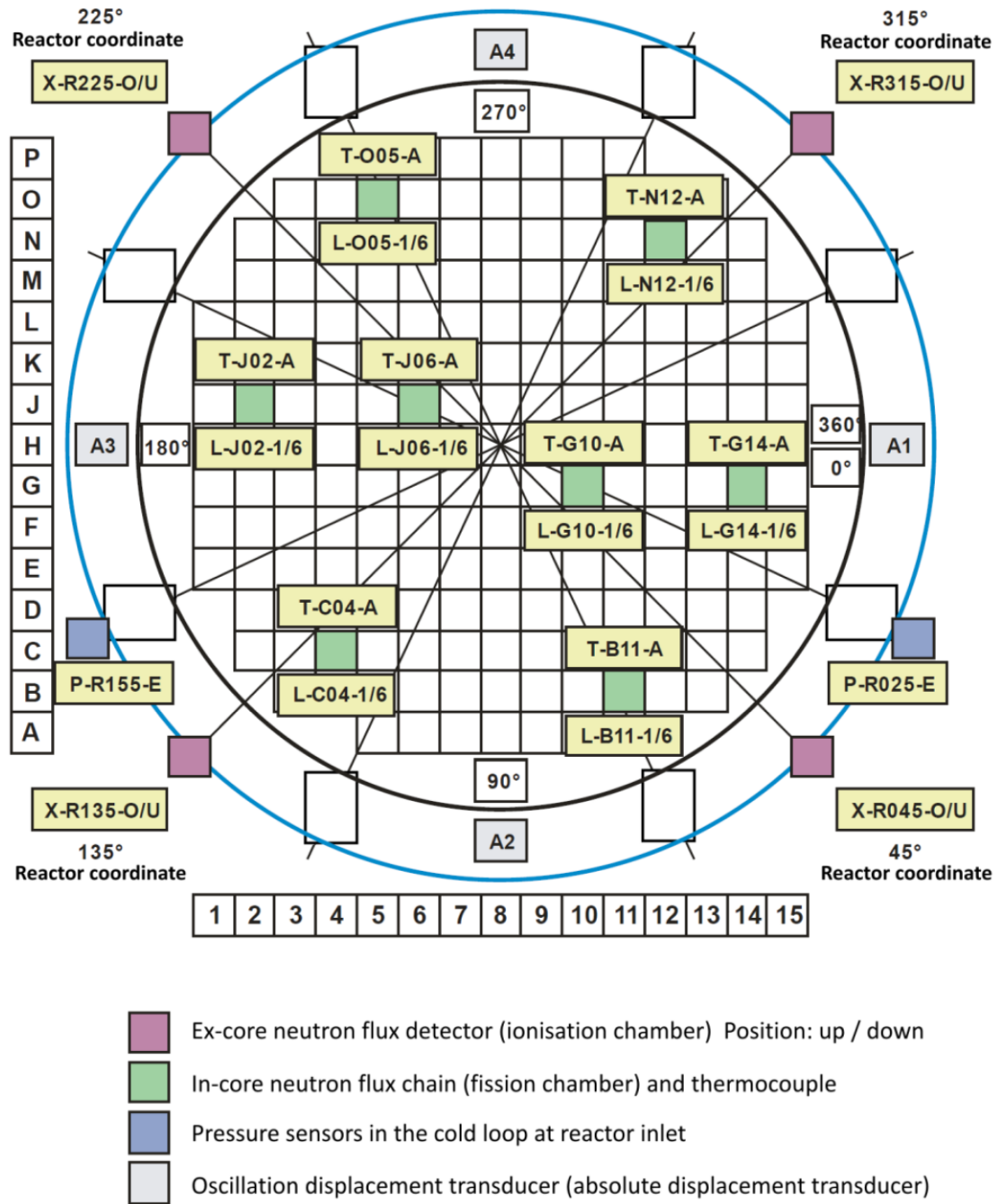
Figure 2: Radial detector position in the German pre-Konvoi 4-loop reactor [reproduced from (Lipcsei et al., 2018)].
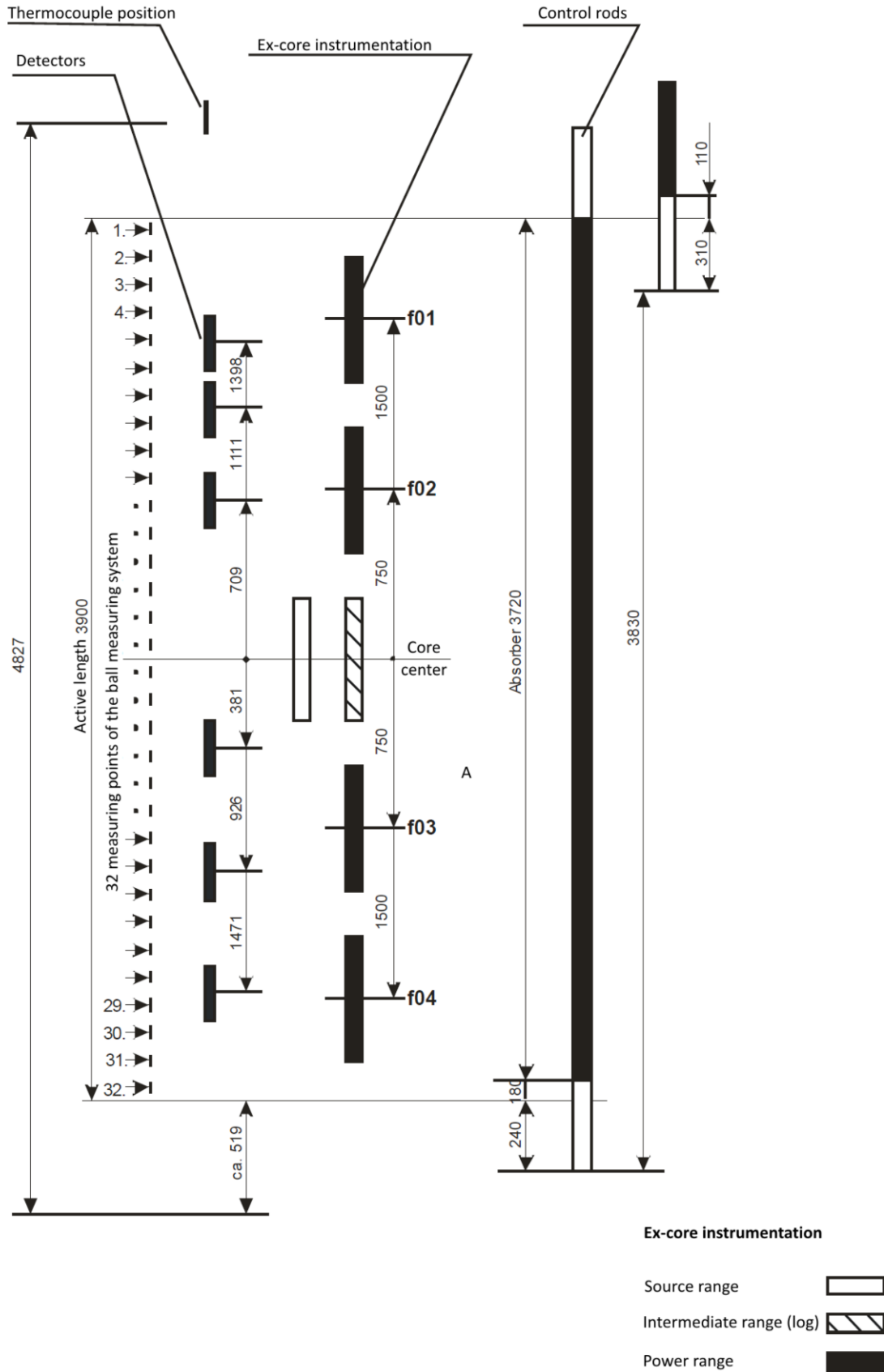
Figure 3: Axial detector position in the German pre-Konvoi 4-loop reactor [reproduced from (Lipcsei et al., 2018)].

The modelling of the effect of various noise sources was performed in the frequency-domain using the CORE SIM+ tool, following the strategy presented in the deliverables D3.1 and D3.2 (Demazière and Dokhane, 2019; Dokhane and Mylonakis, 2019). The static macroscopic cross-sections used for both performing the static CORE SIM+ calculations and on which the noise sources are defined for carrying out the dynamic calculations were provided by another core simulator, in the present case SIMULATE-3 (thanks to PSI).The CORE SIM+ tool estimates at the angular frequency ω the neutron noise $\delta\phi_1(\mathbf{r}, \omega)$ and $\delta\phi_2(\mathbf{r}, \omega)$ in the fast and thermal energy groups, respectively, solution of the following balance equations:

$$\{\boldsymbol{\nabla} \cdot [\mathbf{D}(\mathbf{r})\boldsymbol{\nabla}] + \Sigma_{dyn}(\mathbf{r}, \omega)\} \times \begin{bmatrix} \delta\phi_1(\mathbf{r}, \omega) \\ \delta\phi_2(\mathbf{r}, \omega) \end{bmatrix}$$
$$= \boldsymbol{\phi}_r(\mathbf{r})\delta\Sigma_r(\mathbf{r}, \omega) + \boldsymbol{\phi}_a(\mathbf{r}) \begin{bmatrix} \delta\Sigma_{a,1}(\mathbf{r}, \omega) \\ \delta\Sigma_{a,2}(\mathbf{r}, \omega) \end{bmatrix} + \boldsymbol{\phi}_f(\mathbf{r}) \begin{bmatrix} \delta\upsilon\Sigma_{f,1}(\mathbf{r}, \omega) \\ \delta\upsilon\Sigma_{f,2}(\mathbf{r}, \omega) \end{bmatrix} = \begin{bmatrix} S_1(\mathbf{r}, \omega) \\ S_2(\mathbf{r}, \omega) \end{bmatrix} \tag{1}$$

The definition of the different quantities can be found in Mylonakis et al. (2020). Different postulated scenarios were then investigated, and the simulations performed accordingly:

- *Generic "absorber of variable strength"*. In this scenario, a Dirac-like perturbation in point $\mathbf{r}'$ is considered. In such a case, the right-hand side of Eq. (1) is replaced by $\delta(\mathbf{r} - \mathbf{r}')$ being introduced either in the fast group or in the thermal group. The corresponding solution to Eq. (1) is given by the Green's function $G_{g' \to g}(\mathbf{r}, \mathbf{r}', \omega)$, thus giving the neutron noise induced in the spatial point $\mathbf{r}$ and energy group g due to a Dirac-like perturbation in the spatial point $\mathbf{r}'$ and energy group g'. Calculations are performed in the frequency range 0.1 to 25 Hz.

- *Axially travelling perturbations at the velocity of the coolant flow*. In this scenario, a perturbation of the coolant is assumed. Although it is more likely that this perturbation is created outside of the core, we will consider, for the sake of generality, that the perturbation can also be created inside the core. The perturbation is assumed to travel upwards with the coolant along the z-axis at a velocity v. For simplicity, it is further assumed that the velocity is axially independent. Furthermore, the effect of the coolant perturbation is supposed to only modify the removal macroscopic cross-section, expressed in the frequency-domain as:

$$\delta\Sigma_r(\mathbf{r} \equiv (x, y, z), \omega) = \begin{cases} 0, \text{if}(x, y) \neq (x_0, y_0) \\ 0, \text{if}(x, y) = (x_0, y_0) \text{ and } z < z_0 \\ \delta\Sigma_r(x_0, y_0, z_0, \omega)\exp\left[-\frac{i\omega(z-z_0)}{v}\right], \text{if}(x, y) = (x_0, y_0) \text{ and } z \geq z_0 \end{cases} \tag{2}$$

where (x_0, y_0, z_0) represents the location in the core in which the perturbation is applied, and z corresponds to the axial elevation within the core. The perturbation introduced at (x_0, y_0, z_0) is further assumed to be white, which in the frequency domain has thus no frequency dependence. The corresponding noise source is then given by:

$$\begin{bmatrix} S_1(\mathbf{r}, \omega) \\ S_2(\mathbf{r}, \omega) \end{bmatrix} = \boldsymbol{\phi}_r(\mathbf{r})\delta\Sigma_r(\mathbf{r}, \omega) \tag{3}$$

Calculations are performed in the frequency range 0.1 to 25 Hz.

- *Fuel assembly vibrations*. In this scenario, a fuel assembly is assumed to vibrate in the x- and/or y-direction. Concerning the vibration mode in the axial direction, several possibilities exist: the cantilevered beam mode, the simply supported on both sides mode (with its two first harmonics), and the cantilevered beam and simply supported mode (with its two first harmonics), as described in the CORTEX deliverable D3.1. Each vibration mode has a given axial shape and a corresponding eigenfrequency, as summarized in Figure 4. Because of the homogenization of the material data at the nodal level, the modelling of fuel assembly vibrations corresponds to the introduction in the (x, y) plane of Dirac-like perturbations at the

boundary of each homogeneous region, each perturbation being given by the difference of static macroscopic cross-sections between the moving region and its neighboring region. Using the notations introduced in Figure 4, denoting by h the displacement in the (x, y) plane and ε_x and ε_y its projection on the x- and y-directions, respectively, the perturbations of the macroscopic cross-sections of type α are then given as:

$$\delta\Sigma_{\alpha,g}^{x}(x, z, \omega) = h(z, \omega)\delta(x - a_0)[\Sigma_{\alpha,g,I} - \Sigma_{\alpha,g,II}] + h(z, \omega)\delta(x - b_0)[\Sigma_{\alpha,g,II} - \Sigma_{\alpha,g,III}] \quad (4)$$

$$\delta\Sigma_{\alpha,g}^{y}(y, z, \omega) = h(z, \omega)\delta(y - c_0)[\Sigma_{\alpha,g,IV} - \Sigma_{\alpha,g,II}] + h(z, \omega)\delta(y - d_0)[\Sigma_{\alpha,g,II} - \Sigma_{\alpha,g,V}] \quad (5)$$

The noise source is then given by the following expression:

$$\begin{bmatrix} S_1(\mathbf{r}, \omega) \\ S_2(\mathbf{r}, \omega) \end{bmatrix} = \boldsymbol{\phi}_r(\mathbf{r})\delta\Sigma_r(\mathbf{r}, \omega) + \boldsymbol{\phi}_a(\mathbf{r}) \begin{bmatrix} \delta\Sigma_{a,1}(\mathbf{r}, \omega) \\ \delta\Sigma_{a,2}(\mathbf{r}, \omega) \end{bmatrix} + \boldsymbol{\phi}_f(\mathbf{r}, \omega) \begin{bmatrix} \delta\nu\Sigma_{f,1}(\mathbf{r}, \omega) \\ \delta\nu\Sigma_{f,2}(\mathbf{r}, \omega) \end{bmatrix} \quad (6)$$
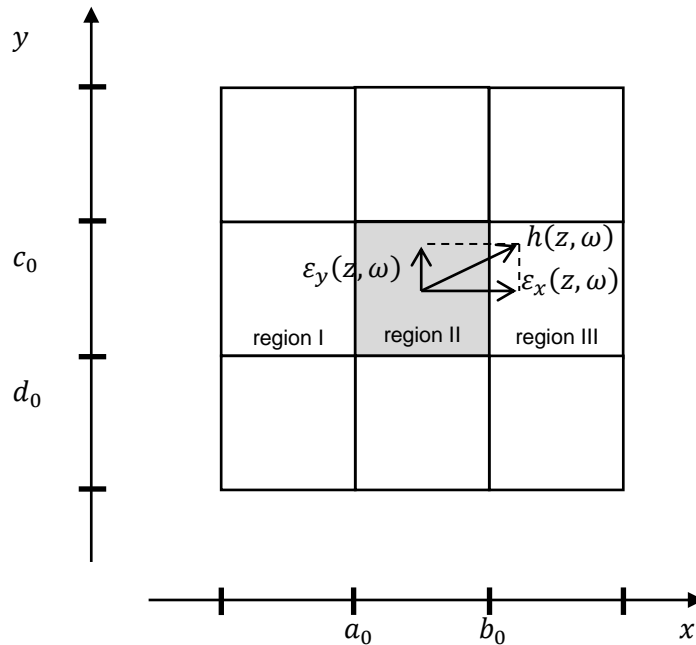
Figure 4: Notations used for describing the vibrations of a homogeneous region (labelled II) in relation to four neighbouring homogeneous regions (labelled I, III, IV and V).

The frequencies at which the calculations are performed are given as follows:
- o For the cantilevered beam mode: 0.6-1.2 Hz.
- o For simply supported on both sides: first mode 0.8-4 Hz, and second mode 5-10 Hz.
- o For cantilevered beam and simply supported: first mode 0.8-4 Hz, and second mode for 5-10 Hz.
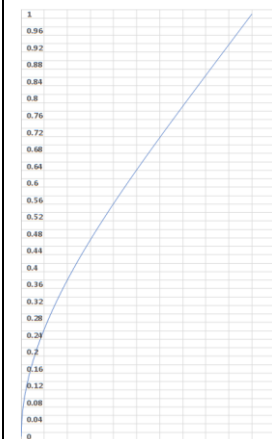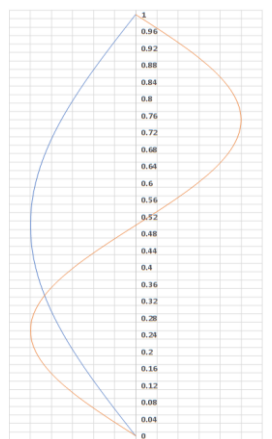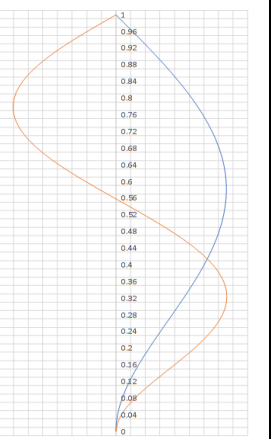
- *Control rod vibrations.* The vibration of a control rod is assumed to be described by a one-dimensional structure along the z-direction vibrating perpendicularly to the two-dimensional (x, y) plane. Furthermore, the vibrating rod is assumed to always remain parallel to itself and to have the most significant effect on the thermal macroscopic absorption cross-section. In those conditions, the vibration of the rod will create a perturbation of the thermal absorption cross-section that is represented as:

$$\delta\Sigma_{a,2}(\mathbf{r}, t) = \gamma\Theta(z - z_0)\left[\delta\left(\mathbf{r}_{xy} - \mathbf{r}_{p,xy} - \boldsymbol{\varepsilon}(t)\right) - \delta\left(\mathbf{r}_{xy} - \mathbf{r}_{p,xy}\right)\right] \quad (7)$$

where γ is the strength of the perturbation, $\mathbf{r}_{p,xy}$ is the equilibrium position of the rod in the (x, y) plane, $\boldsymbol{\varepsilon}(t)$ is a vector representing the displacement of the rod from its equilibrium position in the (x, y) plane, and z_0 represents the axial elevation at which the rod is inserted

(insertion from the top of the core). $\Theta(z - z_0)$ is the Heaviside function. Using a one-term Taylor expansion for Eq. (7) and after some algebra, the corresponding induced neutron noise can be estimated – see CORTEX deliverable D3.1 for the details. Calculations are performed in the frequency range 0.1 to 20 Hz.

Table 1: Description of the considered fuel assembly vibration modes for the frequency-domain simulations.

	Cantilevered beam	Simply supported on both sides	Cantilevered beam and simply supported
Axial shape of the displacement $d(z,t)$ in arbitrary units as a function of the relative core elevation z		first mode in blue, second mode in orange	first mode in blue, second mode in orange
Oscillation frequency	Ca. 0.6 – 1.2 Hz	Ca. 0.8 – 4 Hz for the first mode Ca. 5 – 10 Hz for the second mode	Ca. 0.8 – 4 Hz for the first mode Ca. 5 – 10 Hz for the second mode

- *Core barrel vibrations.* Several modes of vibrations are possible for the core barrel. Only the so-called beam or pendular mode were considered. Two types of beam or pendular motions can occur: the so-called in-phase and out-of-phase modes (Bläsius, 2018; Demazière and Dokhane, 2019). These modes result from the interplay between the oscillations of the reactor pressure vessel with respect to the environment and the oscillations of the core barrel with respect to the reactor pressure vessel, to which the core barrel is attached. In the in-phase mode, the two oscillators move in the same directions, whereas in the out-of-phase mode, the two oscillators move in opposite directions. For both modes of pendular or beam motions of the core barrel, the axial shape of the displacement of the active core with respect to the environment can be described in the same manner as a linear variation from the bearing points of the reactor pressure vessel downwards. From a neutronic viewpoint, the modelling of the pendular mode can be performed much alike the modelling of fuel assembly vibrations earlier described. Core barrel vibrations can be considered as the relative motion of the active fuel core region with respect to the reflector. Core barrel vibrations can thus be seen as a collective movement of all fuel assemblies with respect to the reflector. The perturbations introduced by core barrel vibrations can be considered as localized perturbations taking place at the boundary between the active core region and the reflector region. Calculations are performed in the frequency range 7 to 13 Hz.

For all the scenarios described above and for all relevant frequencies (as described in the CORTEX deliverables D3.1 and D3.2), the Cross-Power Spectral Densities (CPSD) of the relative induced neutron noise between detector pairs were estimated, i.e. quantities of the form

$$CPSD_{\delta\phi/\phi_0}(\mathbf{r}_1, \mathbf{r}_2, \omega) \propto \frac{\delta\phi(\mathbf{r}_1,\omega)\delta\phi^*(\mathbf{r}_2,\omega)}{\phi_0(\mathbf{r}_1)\phi_0(\mathbf{r}_2)} \tag{8}$$

were calculated, using the methodology presented in detail in the CORTEX deliverable D3.2. It should nevertheless be emphasized that contrary to the method described in this deliverable where the neutron noise $\delta\phi(\mathbf{r},\omega)$ was used in the CPSD estimates, it is the *relative* neutron noise $\delta\phi(\mathbf{r},\omega)/\phi_0(\mathbf{r})$ that was estimated in the present case, so that the simulated data are directly compatible with the measured data.

The data are provided in the format described in D3.2. Contrary to the method described in D3.2 where the data regarding only the 1/8th of the core were provided, it is the complete dataset that is provided in the present case. Therefore, the user must skip the process described in the paragraph 3.2.3 of D3.2.

The dataset is used similarly to the one described in D3.2. The use of the dataset is performed in two fully automated steps. In the first step, the complex quantities $\delta\phi_1(\mathbf{r},\omega)$ and $\delta\phi_2(\mathbf{r},\omega)$ are generated for each scenario and for all relevant frequencies. This step is performed with the provided script "GREEN_POSTPROCESSING" (MATLAB/Python versions available). In the second step, the CPSDs are computed (see Eq. (8)). Instead of the MATLAB function described in D3.2, the MATLAB function "DETECTOR_PSD" is used in the current case. This function generates the CPSD of each detector pair for a selected perturbation.

The simulated data along with the postprocessing scripts were delivered to the concerned CORTEX partners in February 2020.

2.2.2 Swiss pre-Konvoi 3-loop reactor

The reactor considered hereafter is the Gösgen (KKG) reactor, which is a 3-loop reactor of pre-Konvoi design. The core layout with the position of the various neutron detectors (both in-core and ex-core detectors) is given in Figure 5 and in Figure 6. The modelling parameters used in the simulations are representative of the core conditions corresponding to the noise measurements performed on February 7th, 2018, during the fuel cycle 39, with a soluble boron concentration of 303 ppm, a thermal output of 3002 MWth and an average coolant temperature of 308.5 °C. A more complete description of the reactor, of the measuring equipment and of the core conditions can be found in the deliverables D4.1, D4.2 and D4.3 (Pohlus et al., 2018; Kuentzel et al., 2018; Lipcsei et al., 2018).
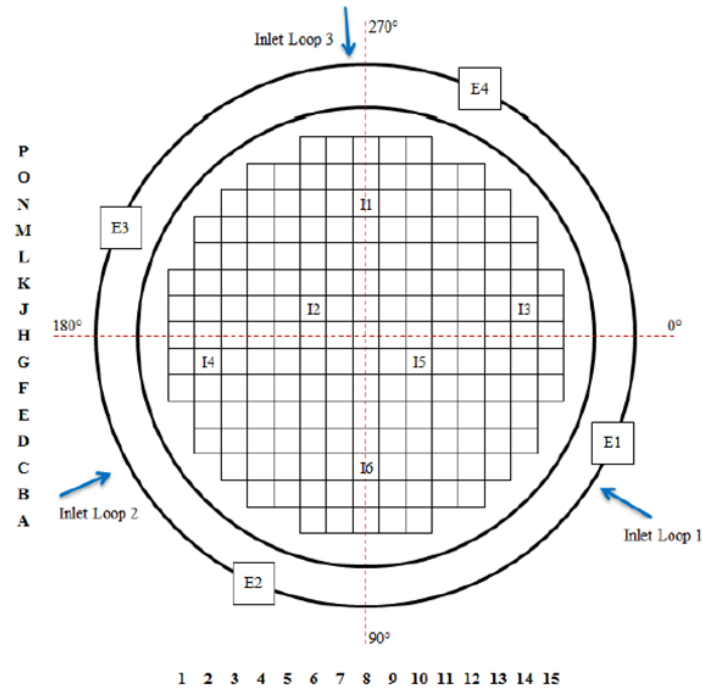
Figure 5: Radial detector position in the Swiss pre-Konvoi 3-loop reactor.

The simulations for this reactor were carried out both in the frequency-domain and in the time-domain.

Frequency-domain simulations

The modelling of the effect of various noise sources was performed in the frequency-domain using the CORE SIM+ tool, following the strategy presented in the deliverables D3.1 and D3.2 (Demazière and Dokhane, 2019; Dokhane and Mylonakis, 2019). This strategy was briefly summarized in Section 2.2.1 of this report.

The simulated data along with the postprocessing scripts were delivered to the concerned CORTEX partners in April/May 2020.
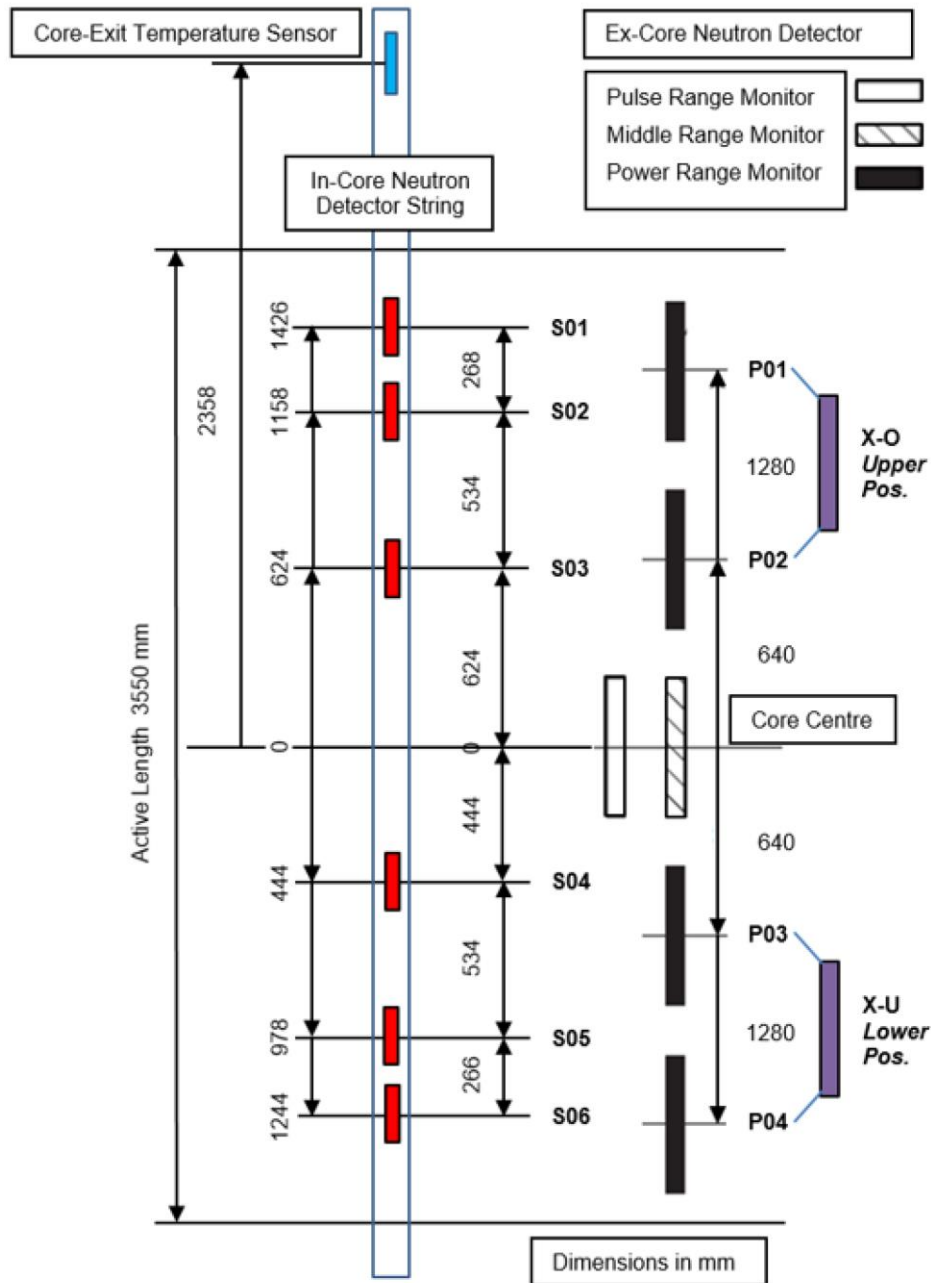
Figure 6: Axial detector position in the Swiss pre-Konvoi 3-loop reactor [reproduced from (Lipcsei et al., 2018)].

Time-domain simulations

The following are the steps performed in order to generate the desired simulated data:

1. First, a CASMO-5 model is prepared corresponding to the selected core design for preparation of the cross-section nuclear library that will be read later by SIMULATE-3K. The model includes the delta gap model (additional branch calculation in terms of water gap between fuel assemblies), which generates perturbed two-group macroscopic cross sections for water-gap variation representative of only static fuel assembly displacement. This allows S3K to simulate modified water gap width between the fuel assemblies in a time-dependent manner, in case one or more fuel assemblies are vibrating. The modelling scheme contains a module that enables the user to impose pre-defined functions representative of the vibration modes of the fuel assemblies by assigning factored coefficients between zero and one to each axial node.

2. Second, after choosing the desired scenario, corresponding SIMULATE-3K input is prepared, using a MATLAB program, by providing all necessary information about the desired scenario, e.g. time step and duration of simulation, amplitude fuel assembly vibration, location of vibrating fuel assemblies, etc. Once the input is ready, the SIMULATE-3K is run in order to solve the 3D time-dependent neutron diffusion equation.

3. Finally, a MATLAB program is used to extract the time series of the neutron flux of all the in-core and ex-core neutron detectors. This is done by extracting the data from S3K "cms" output file and save them in a ".mat" format file, comprising seven matrices.

The S3K based simulation results are stored in a MATLAB format "ScenarioX.mat" (where ScenarioX is scenario's title), located in the central FTP repository available to the CORTEX partners in the path:

/home/PSI/WP3/T3.1.3/2020.02.Dataset8_PSI_CORTEX_Data_Export

Those data were delivered on February 13th, 2020. In total, 366 different scenarios have been simulated, as given in Table 2. It should be mentioned that although emphasis is put in this section on the noise measurements performed on February 7th, 2018, during the fuel cycle 39, middle of cycle (MOC), the data set delivered by PSI contains the simulations corresponding to noise measurements at beginning of cycle (BOC) conditions for fuel cycle 40, MOC conditions for fuel cycle 40 and EOC conditions for fuel cycle 40. The various cycle conditions together with the dates of the noise measurements are summarized in Table 2.

Table 2: Definition of the scenarios modelled with S3K.

Case ID	Scenario no.	Core condition	Type	Frequency	Amplitude	Comments
2020-02-Dataset8-C1a	1 - 177	BOC 40	Vibration of one FA in cantilevered mode	1.2 Hz	1.0 mm	X-direction
2020-02-Dataset8-C1b	1 - 177	BOC 40	Vibration of one FA in C-shape mode	1.2 Hz	1.0 mm	X-direction
2020-02-Dataset8-C2	1	BOC 40	Random fluctuation in inlet temperature; synchronized loops	-	±1°C	Mean value = 556.70 °C
	2	MOC 40	Random fluctuation in inlet temperature; synchronized loops	-	±1°C	Mean value = 557.89 °C
	3	EOC 40	Random fluctuation in inlet temperature; synchronized loops	-	±1°C	Mean value = 549.11 °C
2020-02-Dataset8-C3	1	BOC 40	Random fluctuation in	-	2%	Mean value = 100%

			inlet flow; synchronized loops			
	2	MOC 40	Random fluctuation in inlet flow; synchronized loops	-	2%	Mean value = 100%
	3	EOC 40	Random fluctuation in inlet flow; synchronized loops	-	2%	Mean value = 100%
2020-02-Dataset8-C4	1	BOC 40	Simplistic lateral vibration of central 5x5 FA cluster + random TH fluctuations	1.2 Hz	1.0 mm + ±1 °C + 2%	X-direction, Mean value = 556.70 °C, Mean value = 100%
	2	MOC 40	Simplistic lateral vibration of central 5x5 FA cluster + random TH fluctuations	1.2 Hz	1.0 mm + ±1 °C + 2%	X-direction, Mean value = 557.89 °C, Mean value = 100%
	3	EOC 40	Simplistic lateral vibration of central 5x5 FA cluster + random TH fluctuations	1.2 Hz	1.0 mm + ±1 °C + 2%	X-direction, Mean value = 549.11 °C, Mean value = 100%
2020-02-Dataset8-C5	1	BOC 40	Cantilevered mode vibration of central 5x5 FA cluster + random TH fluctuations	1.2 Hz	1.0 mm + ±1 °C + 2%	X-direction, Mean value = 556.70 °C, Mean value = 100%
	2	MOC 40	Cantilevered mode vibration of central 5x5 FA cluster + random TH fluctuations	1.2 Hz	1.0 mm + ±1 °C + 2%	X-direction, Mean value = 557.89 °C, Mean value = 100%
	3	EOC 40	Cantilevered mode vibration of central 5x5 FA cluster + random TH fluctuations	1.2 Hz	1.0 mm + ±1 °C + 2%	X-direction, Mean value = 549.11 °C, Mean value = 100%

Table 3: Core conditions for the measurement campaigns.

Date of the noise measurements	2018-02-07	2018-05-15	2018-07-10	2018-12-11	2019-05-X
Cycle	MOC 39	EOC 39	BOC 40	MOC 40	EOC 40
EFPD [days]	223	320	16	171	325
Boron concentration [ppm]	303	34	911	442	4
Core burnup during the measurement [MWd/kgHM]	40	44	32	38.3	44.4

These scenarios are organized in six cases as follows:

1. **2020-01-Dataset8-C1a: Vibration of each fuel assembly individually, in cantilevered mode at BOC 40,** only in the **x-direction**, **sine wave function** with nominal frequency of **1.2 Hz,** with displacement amplitude of **1.0 mm**. This case comprises 177 scenarios corresponding to each fuel assembly vibration.

2. **2020-01-Dataset8-C1b: Vibration of each fuel assembly individually, in C-shaped mode at BOC 40,** only in the **x-direction**, **sine wave function** with nominal frequency of **1.2 Hz,** with displacement amplitude of **1.0 mm**. This case comprises 177 scenarios corresponding to each fuel assembly vibration.

3. **2020-01-Dataset8-C2: Random fluctuations of inlet coolant temperature** in all the three synchronized loops with amplitude of **±1 °C** around the mean value of **556.70 °C, 557.89 °C and 549.11 °C** at **BOC 40, MOC40 and EOC 40,** respectively.

4. **2020-01-Dataset8-C3: Random fluctuations of inlet coolant flow** in all the three synchronized loops with amplitude of **±2%** around the relative value of **100% flow** at **BOC 40, MOC40 and EOC 40,** respectively.

5. **2020-01-Dataset8-C4:** Combination of **simplistic vibration of 5x5 central cluster of FAs** in the **x-direction**, following a **sine wave function** with nominal frequency of **1.2 Hz**, with displacement amplitude of **1.0 mm**. and **synchronized fluctuations of inlet coolant temperature** in all the three loops and **synchronized fluctuations of inlet coolant flow** in all the three loops. Note that, the inlet coolant temperature is randomly fluctuating with amplitude of **±1 °C** around the mean value of **556.70 °C, 557.89 °C and 549.11 °C** at **BOC 40, MOC40 and EOC 40,** respectively. Also, the inlet coolant flow is randomly fluctuating with an amplitude of **2%** over the relative flow of **100%.**

6. **2020-01-Dataset8-C5:** Combination of **cantilevered mode vibration of 5x5 central cluster of FAs** in the **x-direction**, following a **sine wave function** with nominal frequency of **1.2 Hz,** with displacement amplitude of **1.0 mm** and **synchronized fluctuations of inlet coolant temperature** in all the three loops and **synchronized fluctuations of inlet coolant flow** in all the three loops. Note that, the inlet coolant temperature is randomly fluctuating with amplitude of **±1 °C** around the mean value of **556.70 °C, 557.89 °C and 549.11 °C** at **BOC 40, MOC40 and EOC 40,** respectively. Also, the inlet coolant flow is randomly fluctuating with an amplitude of **2%** over the relative flow of **100%.**

The random fluctuations mentioned above are stochastic fluctuations of the inlet coolant temperature and coolant flow. The fluctuations are introduced in a synchronous manner in the three coolant loops, i.e. the fluctuations are identical.

The coolant properties ($f_{i,j}$) are modified at every time step t using a normally distributed random number generator, based on the following expression:

$$f_{i,j}(t) = f_{i,j}(0) + A_{i,j} \cdot rand$$

where $f_{i,j}(0)$ are the initial coolant properties, and $A_{i,j}$ describe the user defined amplitude of fluctuation of the ith coolant property at the jth coolant loop.

The fuel assemblies are labelled according to Figure 5. In the cases '2020-02-Dataset8-C1a' and '2020-02-Dataset8-C1b', the scenario number 'n' = 1 to 177 correspond to the fuel assembly labels 'P6', 'P7', 'P8', 'P9', 'P10', 'P11', 'O3', so on and so forth until 'A10', and are meant to be read row wise.

For cases '2020-02-Dataset8-C1a', '2020-02-Dataset8-C1b', '2020-02-Dataset8-C4' and '2020-02-Dataset8-C5', the modes of vibrations are illustrated in Figure 7.

For cases '2020-02-Dataset8-C2', '2020-02-Dataset8-C3', '2020-02-Dataset8-C4' and '2020-02-Dataset8-C5', the synchronized fluctuation of either the inlet coolant temperature and/or flow means that all core locations are equally affected by the perturbation of these thermal-hydraulic parameters.

0.6 - 1.2 Hz   0.6 - 1.2 Hz   0.8 - 4.0 Hz
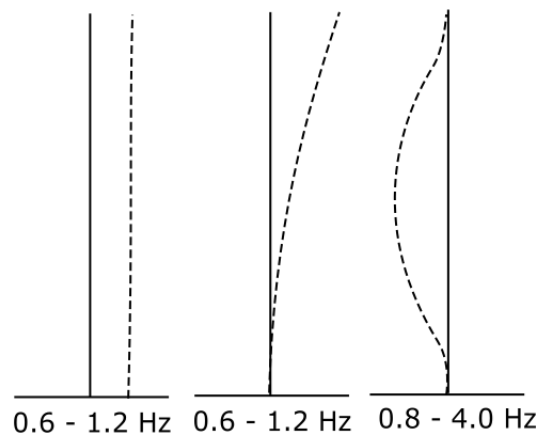
Figure 7: Fuel assembly vibrations in simplistic lateral vibration mode, cantilevered mode and C-shaped mode, respectively.

The results of the 366 simulation scenarios of Dataset8 are provided in MATLAB matrices, in the same format as introduced above. Every simulation scenario has a duration of 100 s and a time step of 0.01 s and includes the in/ex-core neutron responses of 36 in-core and 8 ex-core neutron detectors, respectively, and the time-dependent reactivity (in absolute values and in dollars).

Seven matrices are stored within every '.mat' file:

- T: Time domain in seconds.
- InDet: Matrix with dimension 10001x36, including the 36 in-core neutron detectors responses in the time domain.
- InDet_labels: Cell array with dimension 1x36, including the labels of the 36 in-core neutron detectors whose responses are stored in InDet.
- ExDet: Matrix with dimension 10001x8, including the 8 ex-core neutron detectors responses in the time domain.
- ExDet_labels: Cell array with dimension 1x8, including the labels of the 8 ex-core neutron detectors whose responses are stored in ExDet.
- rho_abs: Time-dependent reactivity in absolute values (Δk/k, k is keff).
- rho_dollar: Time dependent reactivity in dollars (Δk/k/β, β is the delayed neutron fraction).

The output files, placed in five folders with title format '2020-02-Dataset8-CX', have a name format '2020-02-Dataset8-CX-CycleY-compact_description-n.mat', where 'X' is the case number, 'CycleY'

is the core condition, "compact_description" is the compact name that gives information about the scenario, and "n" is the fuel assembly number defining the perturbed fuel assembly.

For instance, the compact_description 'FA1-CantMode-SIN-1.2Hz-1mm' stands for vibration of 1 fuel assembly sinusoidally in cantilevered mode at 1.2 Hz with amplitude of 1 mm, as described in Table 2. Similarly, the compact description 'FA5x5-SIN-1.2Hz-1mm-ICT-WN-1C-ICF-WN-2P' stands for vibration of 5x5 central fuel assemblies cluster sinusoidally at 1.2 Hz with amplitude of 1 mm, in combination with inlet coolant temperature fluctuations with white noise with an amplitude of 1 °C, and inlet coolant flow fluctuations with white noise and amplitude of 2%.

2.2.3 Hungarian VVER-440 reactor

The reactor considered hereafter is the unit 2 of the Paks reactor, which is a 6-loop reactor of VVER-440/213 design. The core layout with the position of the various neutron detectors (both in-core and ex-core detectors) is given in Figure 8 and in Figure 9. The modelling parameters used in the simulations are representative of the core conditions corresponding to the noise measurements performed on March 1st, 2017, during the fuel cycle 32, at 7 EFPD. A more complete description of the reactor, of the measuring equipment and of the core conditions can be found in the deliverables D4.2 and D4.3 (Kuentzel et al., 2018; Lipcsei et al., 2018).
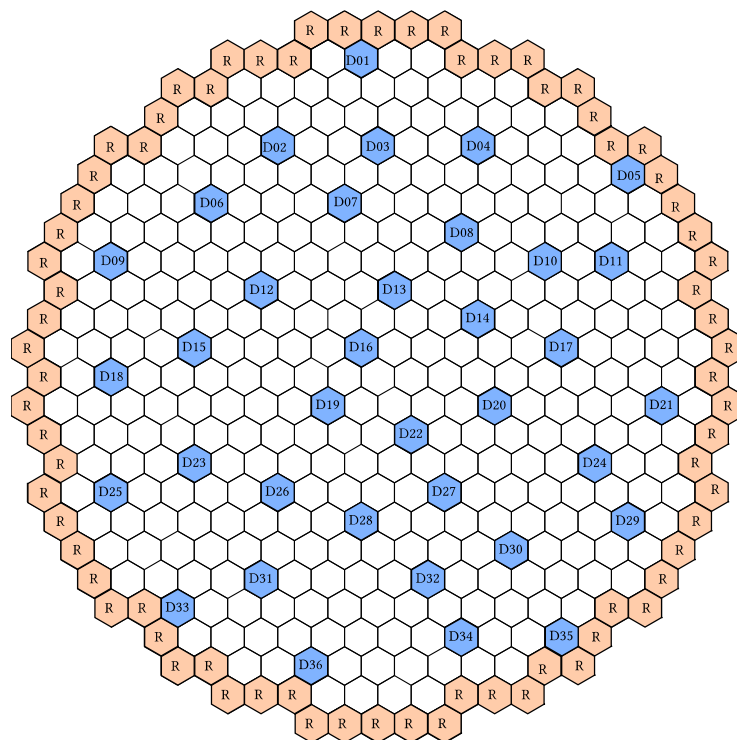
Figure 8: Radial detector position in the Hungarian VVER-440 reactor.
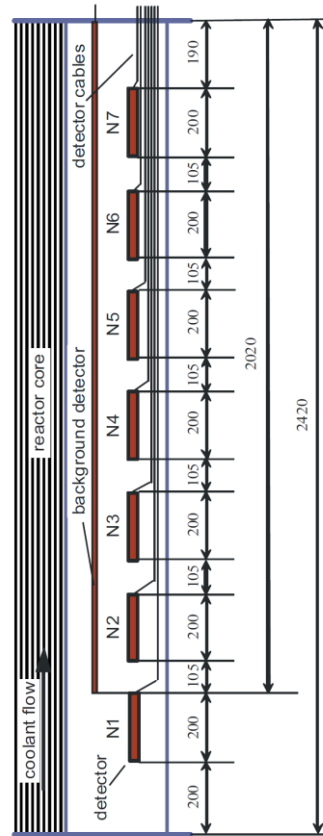
Figure 9: Axial detector position in the Hungarian VVER-440 reactor [reproduced from (Lipcsei et al., 2018)].

The simulation set is composed of a large number of .dtc files, each one corresponding to one neutron noise simulation. They are performed with the frequency domain code FEMFFUSION (Vidal-Ferràndiz et al., 2020a, 2020b). The results of the simulations were delivered in February 2020 using the central FTP repository available to the CORTEX partners and are available in the path:

/home/upv/3D_VVER440_NOISE

A folder is available for each of the simulated scenarios: GenericAbsorber (for a generic absorber of variable strength) and TravellingPerturbation (for an axially travelling perturbation). Inside these folders, there are different subfolders specifying the frequency of the simulated perturbation and of the corresponding neutron noise. Finally, each .dtc file contains an id specifying the spatial location of the perturbation.

For example:

/home/upv/3D_VVER440_NOISE/VibratingAbsorber/10Hz/VVER440_EFPD_007_va_17.dtc

indicates a simulation of a generic vibrating absorber in the VVER-440 reactor at the cell number 17.

In each .dtc file, the noise data at each detector position are given. For example, the /home/upv/3D_VVER440_NOISE/VibratingAbsorber/VVER440_EFPD_007_va_1.dtc starts as:

```
# det_num  det_radial  det_axial  noise_real_part  noise_imag_part
1   1   1   -1.94642e-06    5.03457e-07
2   1   2   -2.06591e-06    5.80197e-07
3   1   3   -1.82722e-06    5.74047e-07
4   1   4   -1.51262e-06    5.37182e-07
```

```
5    1    5    -1.22962e-06    4.89317e-07
6    1    6    -9.87891e-07    4.29849e-07
7    1    7    -7.26159e-07    3.3441e-07
8    2    1    -5.28697e-06    1.26956e-06
```

where:

- The first column indicates the detector number (det_num).
- The second and the third columns are the detector radial identifier (det_radial) and the detector axial identifier (det_radial).
- Finally, the fourth and fifth numbers are the noise real and imaginary part at the detectors position for the thermal group. In order to minimize the size of the transferred files, only the data at the location of detectors and for the thermal group are given. The noise value at the detectors position is averaged over the hexagonal cell containing the detector. The neutron noise given in these files is the *absolute* neutron noise for the thermal group. The *relative* neutron noise can be obtained by dividing the absolute neutron noise by the static flux at the position of the detectors, as:

$$\delta\phi_{2,rel}(\mathbf{r}_i, \omega) = \frac{\delta\phi_2(\mathbf{r}_i, \omega)}{\phi_{2,0}(\mathbf{r}_i)} \tag{9}$$

The static neutron flux for the thermal group can be found in the file:

/home/upv/3D_VVER440_NOISE/VVER440_EFPD_007_static.dtc

With the neutron noise data, the CPSD between detectors and auto-power spectral density (APSD) of a detector can be calculated using the Wiener-Khinchin theorem as:

$$APSD_{\delta\phi}(\mathbf{r}_i, \omega) = \delta\phi(\mathbf{r}_i, \omega) \cdot \delta\phi^*(\mathbf{r}_i, \omega) \tag{10}$$

$$CPSD_{\delta\phi}(\mathbf{r}_i, \mathbf{r}_j, \omega) = \delta\phi(\mathbf{r}_i, \omega) \cdot \delta\phi^*(\mathbf{r}_j, \omega) \tag{11}$$

where $\delta\phi^*$ represents the complex conjugate of the neutron noise. The APSD and the CPSD data can be normalized by any arbitrary number. The same normalization would have thus to be used when analyzing the measurement data.

The reactor was modelled using 421 vertical assemblies discretized in 48 planes, representing a total of 20208 hexagonal cells. The cross sections data used were transferred by MTA-EK. The hexagonal cells are numbered using the same convention as the one used by MTA-EK in the CORTEX deliverable D4.2 (Kuentzel et al., 2019), as represented in Figure 10. Axially, the numbering is carried out incrementally from the bottom to the top of the system.
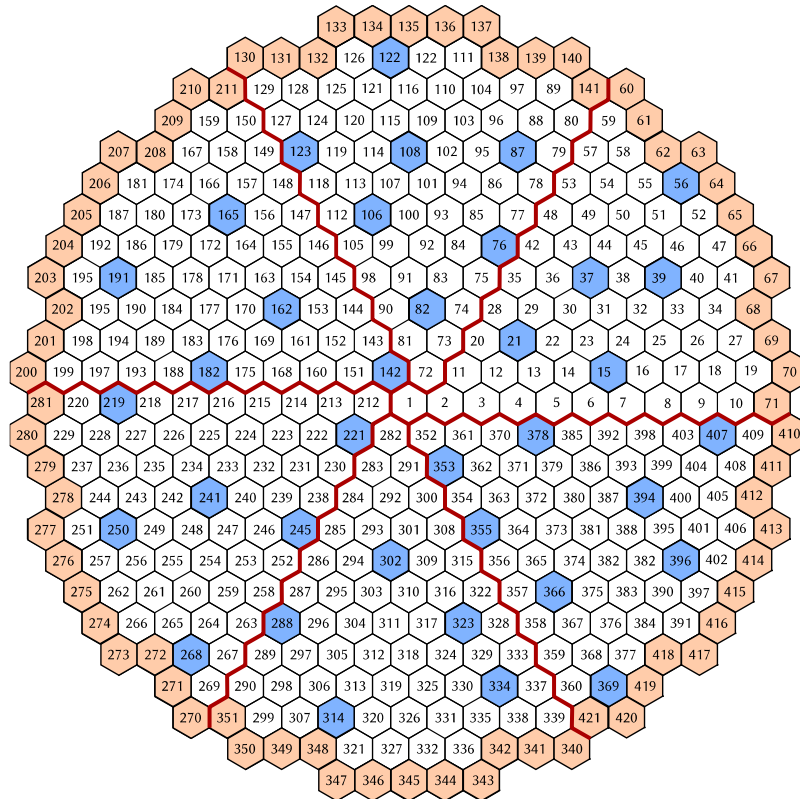
Figure 10: Numbering of the hexagonal cells in the Hungarian VVER-440 reactor.

The modelling of the noise sources follows the same procedure as the one presented in the CORTEX deliverable D3.1 and summarized in Section 2.2.1 of this report for the following two scenarios:

- *Generic absorber of variable strength*. A Dirac-like perturbation at the hexagonal cell i is considered and is directly expressed as a perturbation of the macroscopic cross-sections. This scenario is particularly important since it can be used to localize any kind of perturbation that does not fit any of the other categories. The perturbation inserted at each simulation is set to $\delta\Sigma_{a,1}(c,\omega) = 0.1$ and $\delta\Sigma_{a,2}(c,\omega) = 0.1$, where the hexagonal cell label c is used in the filename. Three frequencies for the perturbation are considered: 0.1 Hz, 1 Hz and 10 Hz, giving a total of 20624 simulations.
- *Travelling perturbation*. This scenario considers a perturbation traveling along a fuel assembly with the coolant flow, from the inlet (bottom of the core) to the outlet (top of the reactor). The water flow velocity is set to $v = 1.0 \, \text{m.s}^{-1}$. The perturbed cross section is thus defined as:

$$\delta\Sigma_{s,1\to2}(c,\omega) = 1.0 \cdot \exp\left(-z\frac{\omega}{v}i\right) \tag{12}$$

Three frequencies for the perturbation are considered: 0.1 Hz, 1 Hz and 10 Hz. This scenario is simulated for each vertical assembly (including reflectors cells) giving a total of 1263 simulations.

It should be mentioned that the FEMFFUSION static calculations were compared with the C-PORCA code run at MTA-EK. Rather large differences were detected: about 100 to 200 pcm difference in the computed effective multiplication factor of the system and about 2% mean error in the relative power distribution. Those differences are attributed to that fact that no discontinuity factors were used in FEMFFUSION.

2.2.4 Czech VVER-1000 reactor

The reactor considered hereafter is the Temelin unit 1 reactor, which is a 4-loop reactor of VVER-1000 design. The core layout with the position of the various neutron detectors (both in-core and ex-core detectors) is given in Figure 11 and in Figure 12. The modelling parameters used in the simulations are representative of the core conditions corresponding to the noise measurements performed from 17th to 28th of December 2016, at the beginning of the fuel cycle 9. A more complete description of the reactor, of the measuring equipment and of the core conditions can be found in the deliverables D4.2 and D4.3 (Kuentzel et al., 2018; Lipcsei et al., 2018).
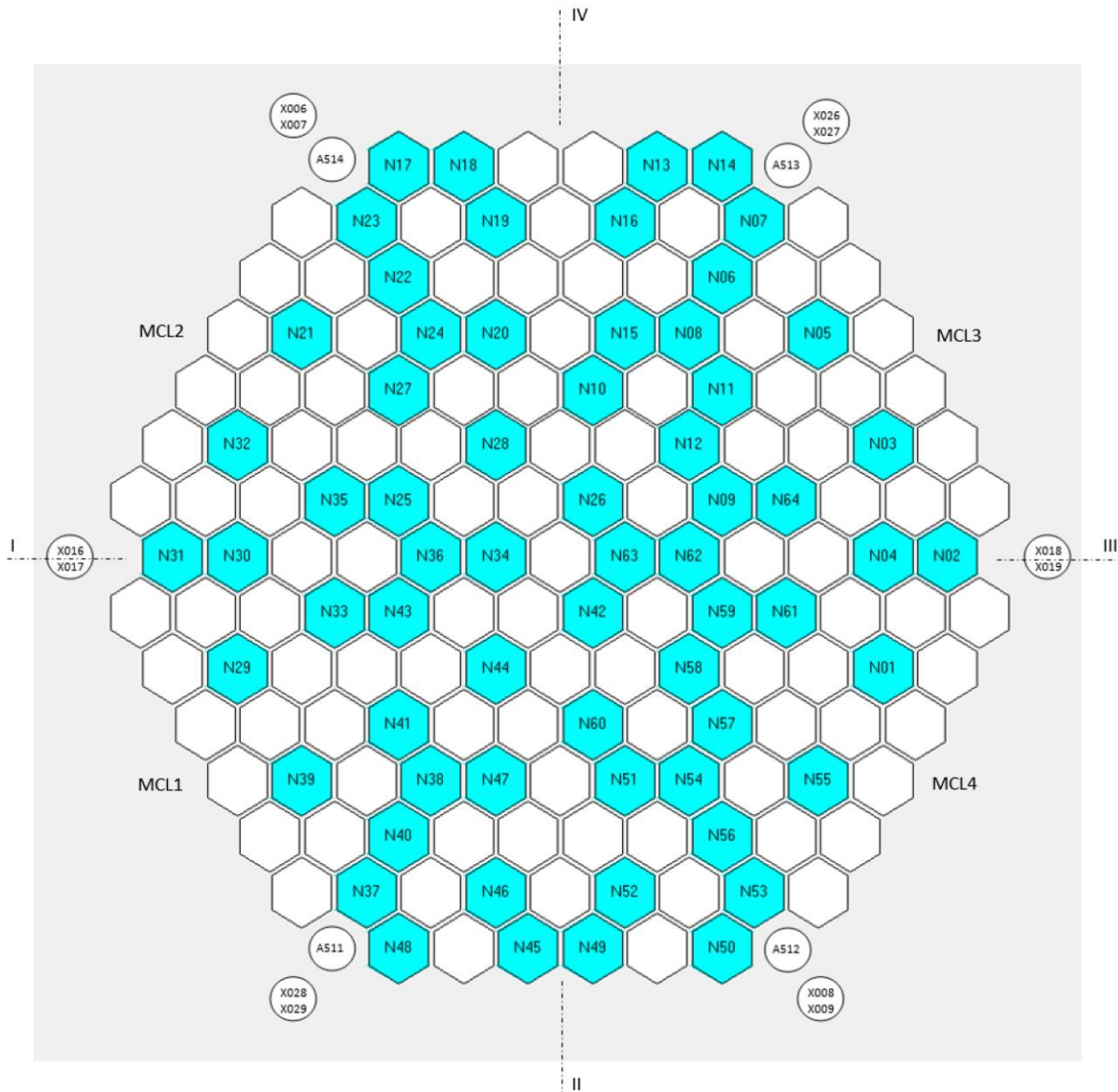
Figure 11: Radial detector position in the Czech VVER-1000 reactor [reproduced from (Lipcsei et al., 2018)]. The in-core detectors are labelled as Ndd, and the ex-core detectors are labelled as Xddd.
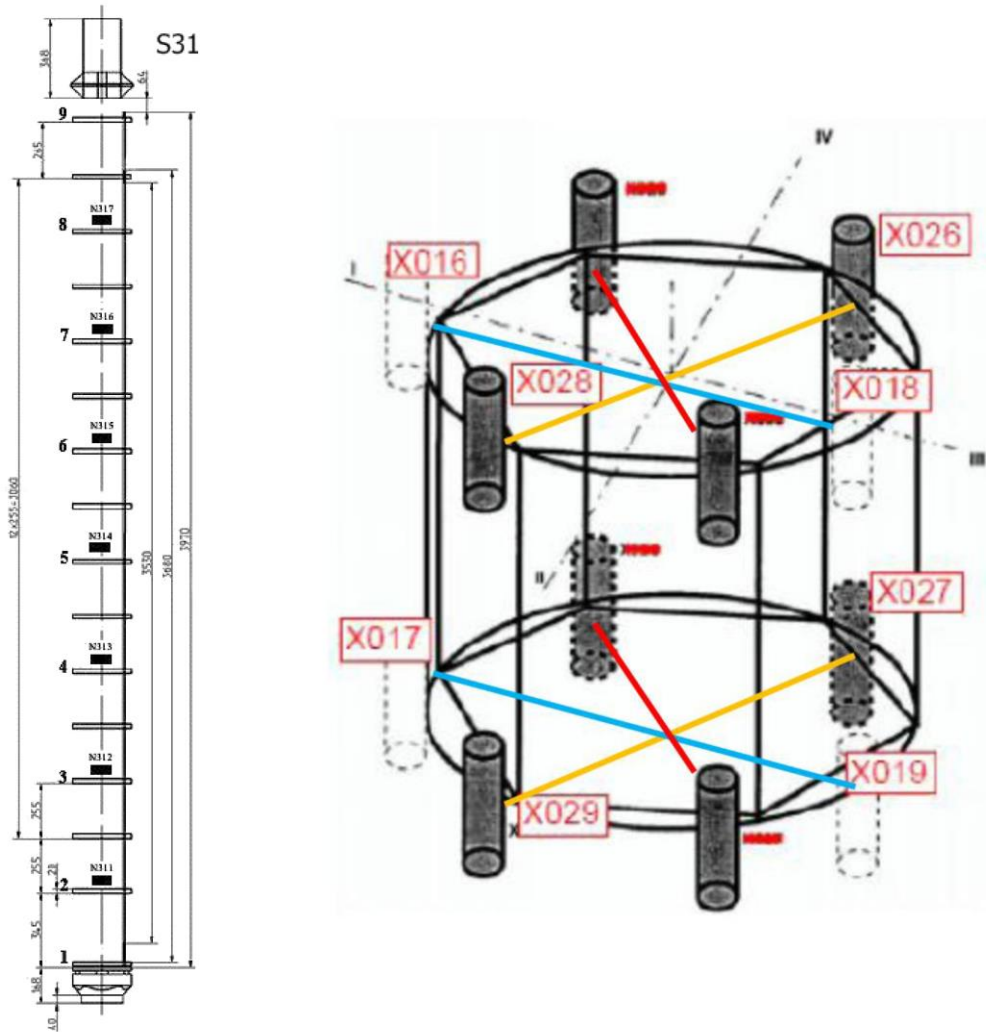
Figure 12: Axial detector position in the Czech VVER-1000 reactor [reproduced from (Lipcsei et al., 2018)]. The in-core detectors are labelled as Ndd, and the ex-core detectors are labelled as Xddd.

The simulation data set is composed of a large number of .dtc files, each one corresponding to one neutron noise simulation. The results of the simulation were delivered in February 2020 using the central FTP repository available to the CORTEX partners and are available in the path:

/home/upv/3D_VVER1000_NOISE

A folder is available for each of simulated scenarios: GenericAbsorber (for a generic absorber of variable strength) and TravellingPerturbation (for an axially travelling perturbation). Inside these folders, there are different subfolders specifying the frequency of the simulated perturbation and of the corresponding neutron noise. Finally, each .dtc file contains an id specifying the spatial location of the perturbation.

The same convention for naming the various files as explained in Section 2.2.3 is used.

It has again to be emphasized that the neutron noise given in these files is the *absolute* neutron noise for the thermal group. The *relative* neutron noise can be obtained by dividing the absolute neutron noise by the static flux at the position of the detectors, as:

$$\delta\phi_{2,rel}(\mathbf{r}_i, \omega) = \frac{\delta\phi_2(\mathbf{r}_i, \omega)}{\phi_{2,0}(\mathbf{r}_i)} \tag{13}$$

The static neutron flux for the thermal group can be found in the file:

/home/upv/3D_VVER1000_NOISE/VVER1000_static.dtc

With the neutron noise data, the CPSD between detectors and APSD of a detector can be calculated using the Wiener-Khinchin theorem as:

$$APSD_{\delta\phi}(\mathbf{r}_i, \omega) = \delta\phi(\mathbf{r}_i, \omega) \cdot \delta\phi^*(\mathbf{r}_i, \omega) \tag{14}$$

$$CPSD_{\delta\phi}(\mathbf{r}_i, \mathbf{r}_j, \omega) = \delta\phi(\mathbf{r}_i, \omega) \cdot \delta\phi^*(\mathbf{r}_j, \omega) \tag{15}$$

where $\delta\phi^*$ represents the complex conjugate of the neutron noise. The APSD and the CPSD data can be normalized by any arbitrary number. The same normalization would have thus to be used when analyzing the measurement data.

The reactor was modelled using 221 vertical assemblies discretized in 50 planes, representing a total of 10550 hexagonal cells. The numbering of the hexagonal cells is illustrated in Figure 13. Axially, the numbering is carried out incrementally from the bottom to the top of the system.
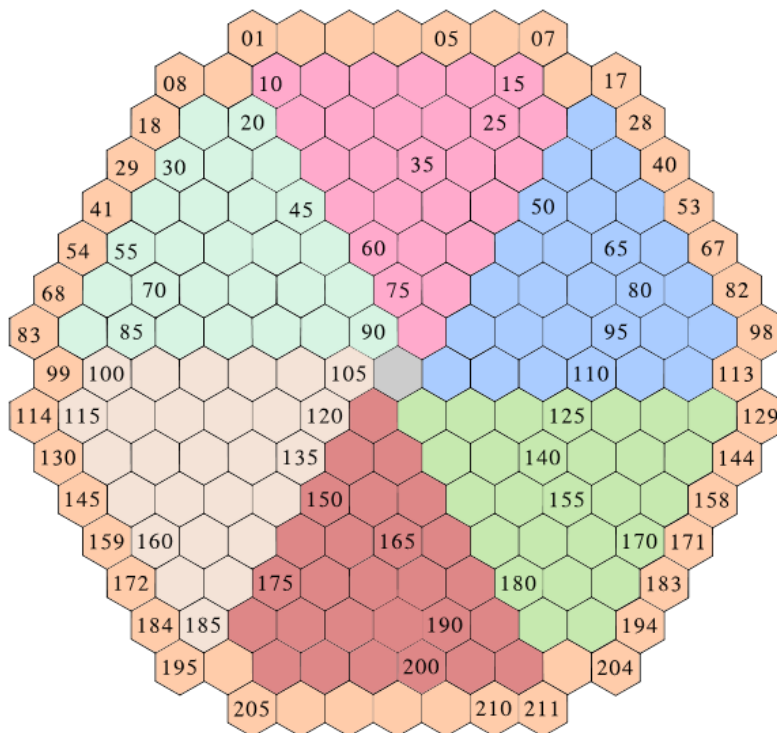
Figure 13: Numbering of the hexagonal cells in the Czech VVER-1000 reactor.

The modelling of the noise sources follows the same procedure as detailed in Section 2.2.3.

3   Fluid-Structure Interactions simulations

3.1 *Simulations with the GRS mechanical model under generic excitation scenarios*

3.1.1   *Model and input parameters*

Geometry noise is the share of neutron noise, which arises from fluid-induced vibrations of the RPV and its internals. For its simulation, a multidisciplinary approach is necessary (Figure 14). In this section, the part of the simulation chain representing the mechanical component motions (central box in Figure 14) is addressed. Simulations with the mechanical model described in CORTEX Deliverable 1.2 for a German 4-loop pre-Konvoi (Figure 15) under generic excitation scenarios are performed. In a first approach, reactive fluidic effects are considered in form of parametric studies on reactive forces from fluidic near-field coupling and fluidic damping.
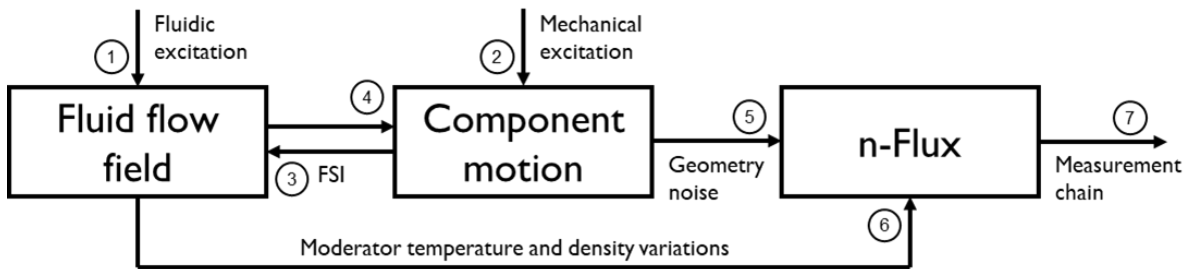
Figure 14: Schematic representation of the relations between the disciplines.
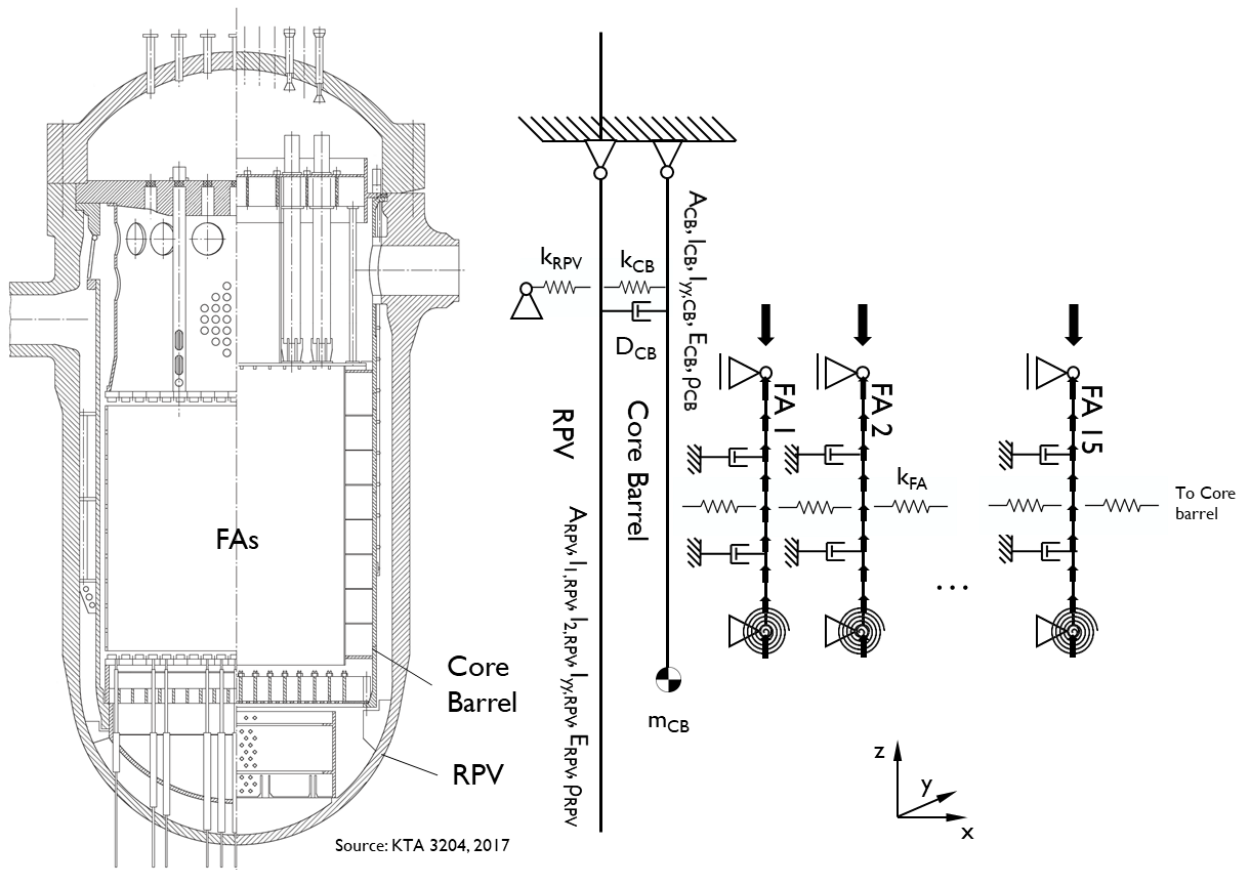
Figure 15: GRS-model of the coupled system of RPV internals.

For a so far unexplained phenomenon observed in PWR built by KWU, which is characterized by an in-phase signal correlation in axial direction, an anti-phase signal correlation between opposite core quadrants, and a $1/\omega^2$-like shape of the APSD with an additional peak around 1 Hz, a mechanical source has been proposed. The phenomenon is associated with a strong neutron-flux signal increase in the time-interval between about 2000 and 2010 (Seidel, Kosowski, Schüler, & Belblidia, 2015), (Herb, Bläsius, Perin, Sievers, & Velkov, 2017), (Pohlus & Paquée, 2018). Simulations of the mechanical oscillation behavior of the components are expected to give further clues about the underlying physics of the phenomenon.

Excitation forces acting on core internals encompass a wide field of known and hypothetical phenomena. These include e.g. turbulent buffeting, pressure oscillations, oscillating mass-flow profiles, lateral flow, vortex-induced vibrations, seismic accelerations or external mechanical excitations. In the special case of self-induced oscillations, the oscillation of the system may arise even from the bidirectional interplay between fluid flow field and the component itself.

In this work, the reactions of the coupled system of RPV internals to generic forced excitation scenarios are investigated. Stochastic, seismic and self-induced excitations are not considered here. The generic excitation scenarios include the following:

- Correlated sinusoidal excitation of all FAs with 20 N at 1 Hz.
- Correlated sinusoidal excitation of all FAs with 200 N at 1 Hz.
- Local sinusoidal excitation of 3 of 15 FAs at the core edge with 200 N at 1 Hz.
- Shifted sinusoidal excitation of all FAs with $200N * sin\big(2\pi * (1Hz * t + n/15)\big)$, n = FA position.
- Sinusoidal excitation of the core barrel (CB) and (in anti-phase) the RPV with 30 kN at 1 Hz.

For each excitation scenario, studies with different parameters are performed:

- Fluidic damping of the individual FAs either neglected or set to D = 0.5.
- Fluidic near-field coupling between FAs/core barrel either neglected or set to k = 20 N/mm.
- Loading pattern either uniform with Type 1 FA (150 N/mm lateral stiffness) or alternately Type 1/ Type 2 BOL/ Type 2 EOL (150 N/mm, 60 N/mm and 30 N/mm lateral stiffness).

Damping acts on the FAs only if they move relative to the fluid. The assumed value was determined based on data from shaker table tests and corresponding calculations, which have been performed in conjunction with seismic analysis (see CORTEX Deliverable 1.2). If the FAs are excited by the fluid itself and the relative movement is smaller, the damping will decrease as well. A weak fluidic near-field coupling exists between the FAs, but its magnitude is unclear and cannot be determined exactly from literature. A parametric study will therefore reveal its potential influence. Lastly, the parametric variation of loading patterns reflects the heterogeneous core loading and the effect of lateral stiffness decrease during the cycle.

3.1.2 Results

Figure 16 shows the calculated oscillatory response of the components to a correlated sinusoid excitation of all FAs in a heterogeneous loading pattern with 200 N amplitude at 1 Hz with damping and fluidic coupling enabled. The plots represent the time history of the amplitude at mid height position of the FAs, assuming that the FA bending shape is predominantly of C-form and pendulum-like for core barrel and RPV. In the upper part of the diagram, the responses of the FAs are depicted. The graphs are shifted by 1.6 mm each, which coarsely corresponds to the gap between FAs in the real reactor. The amplitude is magnified by factor 10 for visualization. In the lower part, the response of the RPV and the core barrel can be seen in an arbitrary distance to each other and to the FAs. The amplitude of RPV and core barrel is magnified by factor 1000.

The FAs perform almost uniform oscillations except for the outermost positions, which are influenced by the coupling to the stiffer core barrel via the fluidic near-field coupling. The oscillation is transferred to the core barrel via upper and lower fixation of the FAs as well. The core barrel reaction shows an almost $\pi/2$ phase-shift and a motion amplitude, which accounts for about 1/2000 of the amplitude of the FAs. For a real reactor situation, this means, that a significant excitation of the core barrel from FA oscillations alone is unlikely and the motions of the core barrel observed in reality probably have mainly other sources, e.g. fluidic forces in the downcomer. The reaction amplitude of the RPV is even lower (about 1/12 compared to the core barrel) due to its rigidity and the fact that it is not directly coupled to the FAs.
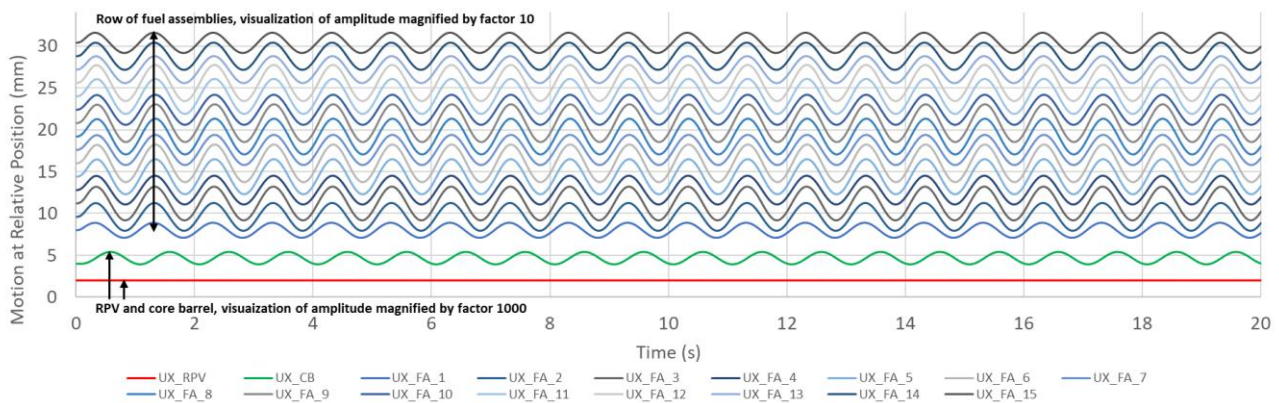
Figure 16: Component oscillation from correlated sinusoidal excitation of all FAs with 200 N amplitude at 1 Hz, damping enabled, fluidic coupling enabled, heterogeneous loading pattern.

The same simulation but with an excitation amplitude of 20 N instead of 200 N (graph not shown here) reveals an amplitude response of exactly 1/10 size, which is not surprising due to the linearity of the system. A cliff-edge effect might be seen when collisions between neighbor FAs and the core barrel/core shroud will be taken into account. Consideration of collisions is one of the objectives in further model development.

When comparing the results shown in Figure 16 to those of the same excitation case, but without fluidic coupling (Figure 17), it can be seen that the coupling homogenizes the response amplitude of all FAs although they differ considerably regarding lateral stiffness. For a real reactor situation, it means that the FA oscillation amplitudes of core-wide oscillations are not determined by the individual lateral stiffness of the FAs, but rather by some regional average. This matches the

observation, that the observed global neutron flux noise increased proportional to the number of FAs with a new design and lower lateral stiffness (Girardin, Meier, Alander, & Jatuff, 2017). The simulations with a homogeneous loading pattern thus differ not considerably from those with a heterogeneous loading pattern and fluidic coupling, except for the general lateral stiffness level.
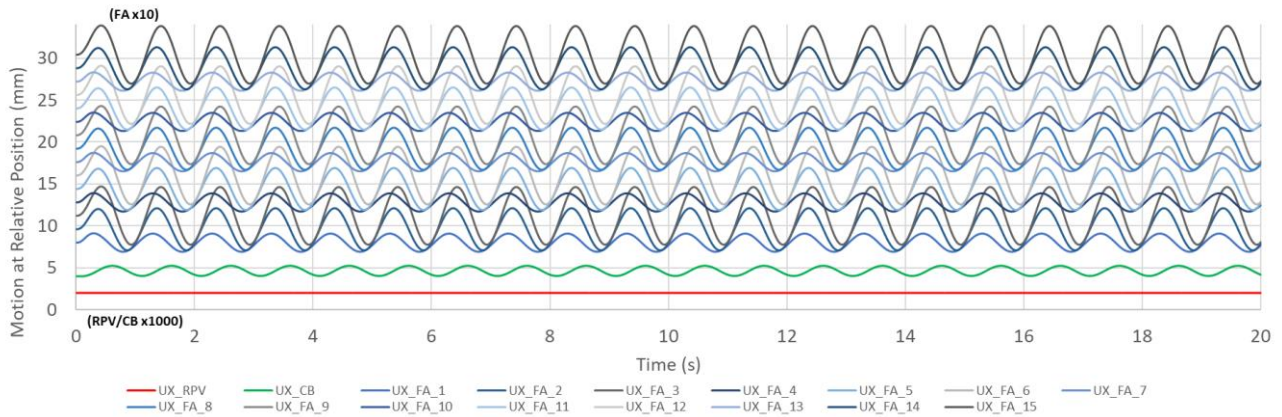
Figure 17: Component oscillation as in Figure 16, but fluidic coupling disabled.

When comparing the results shown in Figure 16 to those of the same excitation case, but without FA damping (Figure 18), it can be seen that the damping suppresses individual motions of the components, that could otherwise lead to non-sinusoidal chaotic coupled motions of the FAs and the core barrel. The chaotic behavior can be explained by the double-pendulum-like configuration between core barrel and FAs. The simulations show that the non-periodic behavior of the signals observed in PWR built by KWU could not only be a result of an already chaotic excitation, but also evoked by the interaction and superposition of oscillators with different frequency or phase.
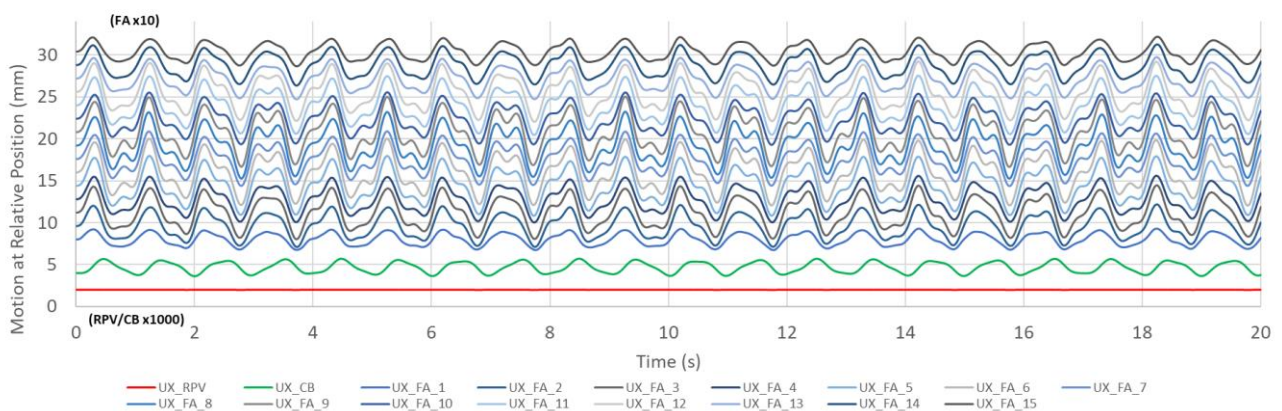
Figure 18: Component oscillation as in Figure 16, but damping disabled.

Nevertheless, the strong fluidic damping observed in experiments performed in conjunction with seismic analysis suggests that a purely mechanic oscillation in an otherwise unaffected axial flow is unlikely. A more likely scenario is that FAs tend to follow a (possibly oscillating) flow field.

When looking at the amplitude response to a local excitation (Figure 19), it could be seen that the oscillation does not spread over the whole core by fluidic near-field coupling alone. The observation

is the same for simulations without damping. The global oscillation observed in PWR built by KWU is thus likely to be an original global phenomenon. It is questionable if collisions between FAs or other not yet considered coupling phenomena might result in a coupling strong enough to spread local phenomena over the whole core.
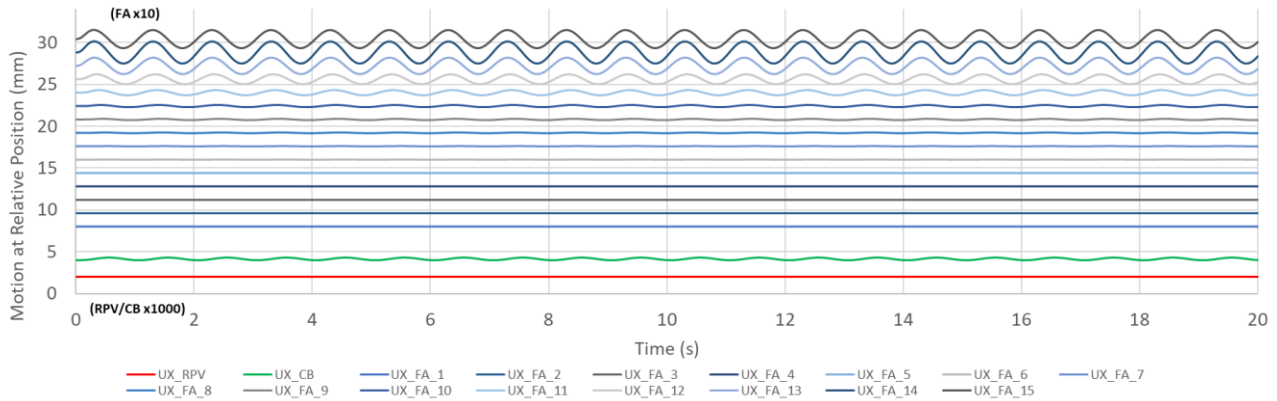
Figure 19: Component oscillation from local sinusoidal excitation of 3/15 neighbor FAs at the core edge with 200 N amplitude at 1 Hz, damping enabled, coupling enabled, heterogeneous loading pattern.

In the amplitude reaction to a shifted sinusoidal excitation (Figure 20), it can be seen that the core barrel is only excited when the forces acting on the FAs do not compensate each other and a non-zero net reaction force arises.
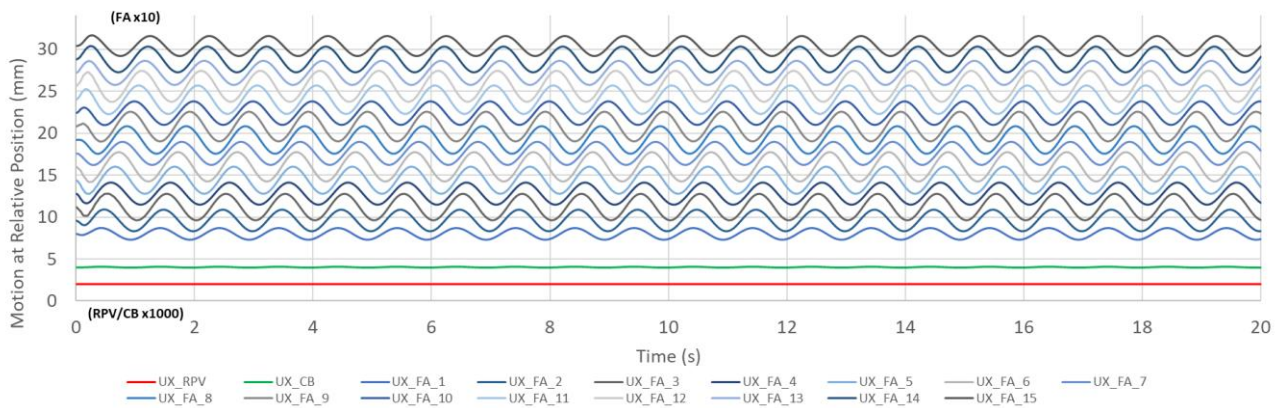
Figure 20: Component oscillation from shifted sinusoidal excitation of all FAs in form 200 N *sin(2π*(1 Hz *t+n/15)), n = number of FA, damping enabled, coupling enabled, heterogeneous loading pattern.

In the case of an excitation of the system of RPV and core barrel instead of FAs (Figure 21), the reaction is similar to the case shown in Figure 16 except for the ratio between core barrel and FA response amplitude (note the different amplification factor of the amplitude in the graph). The excitation is transferred from core barrel to the FAs predominantly via top and bottom mounting. The mid of the FAs, which is plotted here, stays more or less in its position due to its inertia. This indicates that a global excitation of the FAs via core barrel excitation is unlikely, although large forces could arise in the annular shaped downcomer (Runkel, 1987). The observed signal correlation between

core barrel and FA oscillation in PWR built by KWU might come from a concurrent fluidic excitation rather than from a strong mechanical coupling.
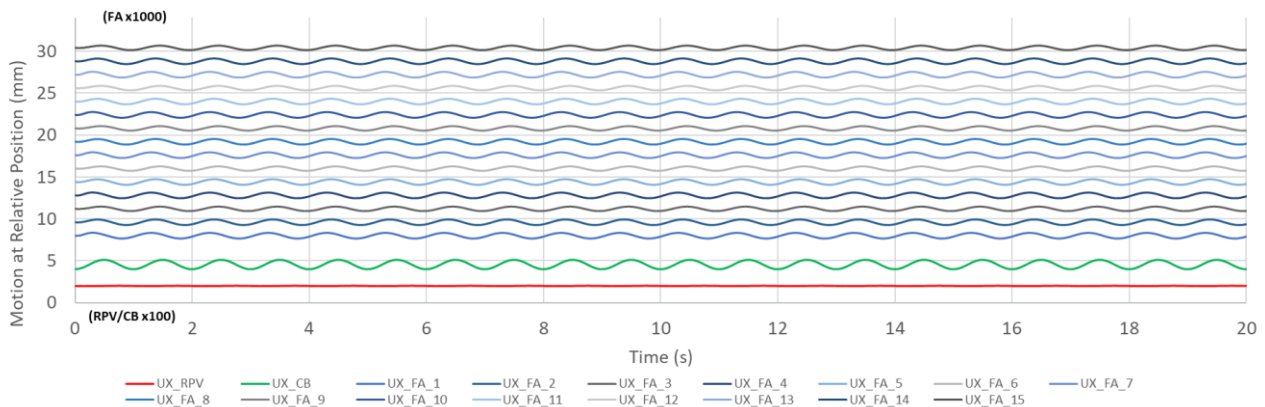
Figure 21: Component oscillation from sinusoidal excitation of the core barrel and (in anti-phase) RPV with 30 kN amplitude at 1 Hz.

3.1.3 Conclusions and outlook

In this section, simulations with the GRS mechanical model of the coupled system of RPV internals (see CORTEX Deliverable 1.2) under generic excitation scenarios considering reactive fluidic effects in form of parametric studies are described. The main findings include:

- The fluidic near-field coupling homogenizes the FA reaction amplitudes, which means that the individual amplitudes of core-wide FA oscillations are determined rather by some local average of the FA stiffness than by the individual stiffness of the affected FAs.
- The fluidic damping evoked by FA motions relative to the fluid suppresses individual motions of the FAs and withdraws energy from the oscillators. A purely mechanic oscillation seems to be unlikely, and the FAs rather tend to follow the (oscillating) flow field.
- A non-periodic motion behavior may be evoked either by a non-periodic excitation or a coupled interaction and superposition of FAs with different frequency and phase.
- A local oscillation is not spread over the whole core by fluidic near-field coupling or via the fixation in the core barrel. A core-wide oscillation is thus unlikely to have a local source.
- Motions of FAs are transferred to the core barrel only weakly and only if there is a non-zero net reaction force. The reaction shows a phase shift. The mechanic transfer in the other direction is weak as well, although much higher forces might act on the core barrel.

In a next step, the mechanical model could be enhanced, e.g. by considering collisions between neighbouring FAs or additional components. Deeper insights might be also revealed by the application of more complex excitation scenarios calculated with hydraulic codes or even a bidirectional coupling, which would allow the investigation of hypothetical self-excited oscillations.

3.2 Noise simulations with an upgraded version of DYN3D

3.2.1 Description of the Approach

Fluid-induced vibrations of the reactor core components affect the neutron flux by changing the local material parameters of the fission chain reaction, the moderation of neutrons as well as the cooling of the fuel assemblies. The reactor code DYN3D (originally) does not model the impact of these effects on the neutron flux in the core. It was therefore necessary to provide a means to couple mechanical vibrations of the reactor core components to the neutron flux. For this reason, an upgraded version of DYN3D, was used for the work presented hereinafter (which is based on previous work described in (Viebach, 2019)). This upgraded version of DYN3D makes it possible to simulate the effect of the mechanical vibrations on the neutron flux by changing the nodal cross sections based on the node by node elongation of the respective fuel assembly and its adjacent fuel assemblies via an average fuel assembly pitch. This procedure admits a coupling of a mechanical model, as described in CORTEX Deliverable 1.2, with the neutron flux and thermal hydraulics simulations in DYN3D.

The mechanical model that was used to represent the vibrations of the reactor core components of a German 4-loop pre-Konvoi reactor is based on a model implemented in Ansys and developed by GRS as part of the CORTEX project. This model incorporates the core barrel, the RPV and up to 4 different classes of fuel assembly types (denoted by types 1-4) with decreasing stiffness. The stiffness of a fuel assembly depends on both its material parameters and on the time the fuel assembly has been subjected to the neutron field. It is thus an important parameter to model geometry noise. Other parameters include the damping and fluidic near-field coupling of the fuel assemblies, as described in the previous section. For the investigations presented in this work, no damping and no fluidic near-field coupling were used. Consequently, it is expected that the APSDs show peaks corresponding to the eigenmodes of the system, which would be expected to be less pronounced in the dampened case. The driving force of the vibrations is assumed to be stochastic in nature. It is modelled by generating a series of normally distributed random numbers with zero expectation value and non-zero standard deviations at a given sampling frequency. In between the samples, the values of the driving forces are interpolated – see Viebach (2020). The driving force is assumed to be acting on the RPV and the core barrel to which the fuel assemblies are fixed. This assumes wide area forces arising, as a result of e.g. the redirection of the coolant flow inside the core.

It was anticipated that a detailed model of the mechanical properties of the reactor core in conjunction with the simulation of the neutron kinetics and thermal hydraulics, would yield long computing time. Therefore, model order reduction techniques were used for the mechanical simulations in order to reduce computing time, while maintaining the necessary features of the dynamics. A detailed description of these methods and the model can be found in CORTEX Deliverable 1.2.

The approach was tested with a set of generic scenarios with different core loading schemes and driving forces. The results of the DYN3D simulations were transformed to the frequency domain for the evaluation.
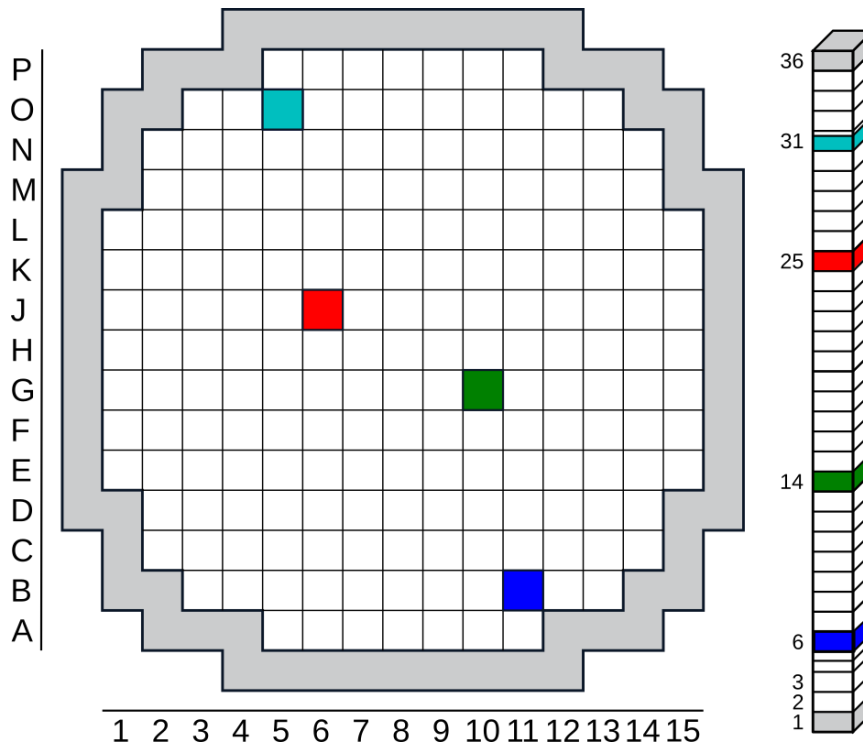
Figure 22: Positions for the radial and axial comparison of the analyses in DYN3D. On the left the positions for the radial comparison and on the right the axial nodalization in DYN3D with the axial positions.

All analyses were performed in the following positions inside the core as depicted in Figure 22:

- For the axial comparison, the DYN3D positions Ch33-6, Ch33-14, Ch33-25, and Ch33-31 were used. These correspond approximately to the in-core detector positions L-B11-6, L-B11-4, L-B11-3 and L-B11-1 (compare Figure 2 and Figure 3).
- For the radial comparison, the in-core detector positions at L-B11, L-G10, L-J06 and L-O05 were used. These correspond to the DYN3D positions Ch33-18, Ch114-18, Ch144-18 and Ch225-18.
- In both cases, the detector position L-B11 (Ch33) was used as reference for the evaluation of the coherence and the phase.

3.2.2 Results

In the first scenario, a random distribution of fuel assembly types inside the core according to Figure 23 was used. This scenario provides a generic baseline "proof of concept" for the approach used. It is expected to show the same qualitative behaviour for the APSD and the phase shift between detectors is expected to be zero.

The axial comparison of the neutron flux signals is shown in Figure 24. The APSD shows a decrease in spectral power for higher frequencies. As expected, the APSDs have pronounced peaks due to the lack of damping of the reactor core components. The coherence of the axial detectors is high and phase with respect to the reference detector is zero over a wide range of frequencies with only narrow jumps to π.
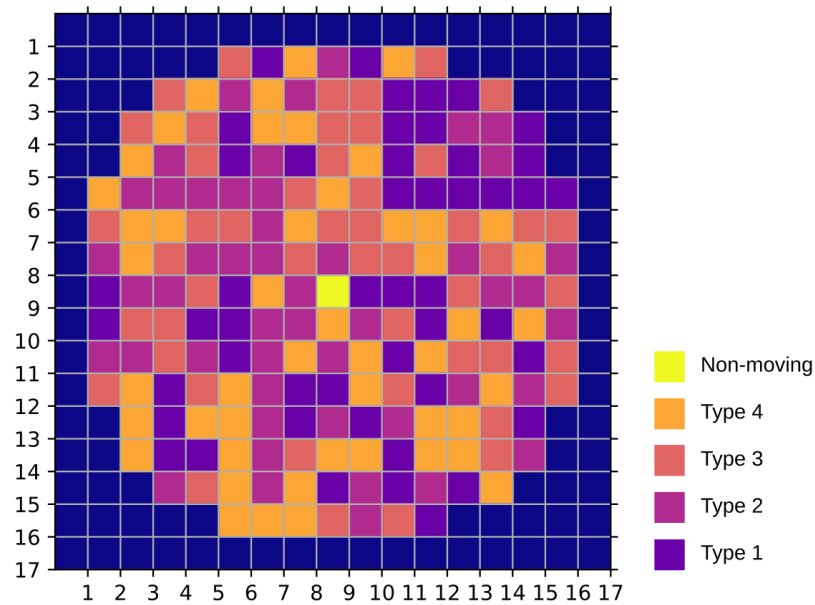
Figure 23: Distribution of fuel assembly types for scenario 1 which is a random distribution. Type 1-4 have decreasing stiffness. The centre fuel assembly is assumed to be fixed in place.

For the radial comparison of neutron flux signals, as shown in Figure 25, the overall shape of the APSD is the same for all detectors. The coherence of the signal is high for low frequencies decreasing only for the detector opposite of the reference (L-O05 or Ch225). The phase is zero over a wide range of frequencies with only small deviations. The results are in agreement with expectations.
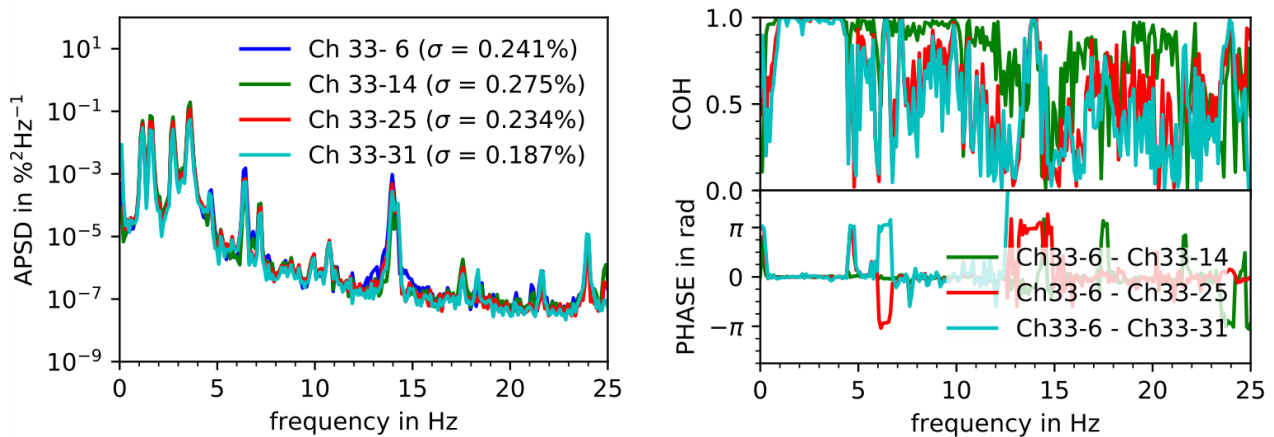
Figure 24: Axial comparison of APSD (left) and coherence and phase (right) for scenario 1. Depicted are the detector positions L-B11-6, L-B11-4, L-B11-3 and L-B11-1 corresponding to the DYN3D positions Ch33-6, Ch33-14, Ch33-25 and Ch33-31.
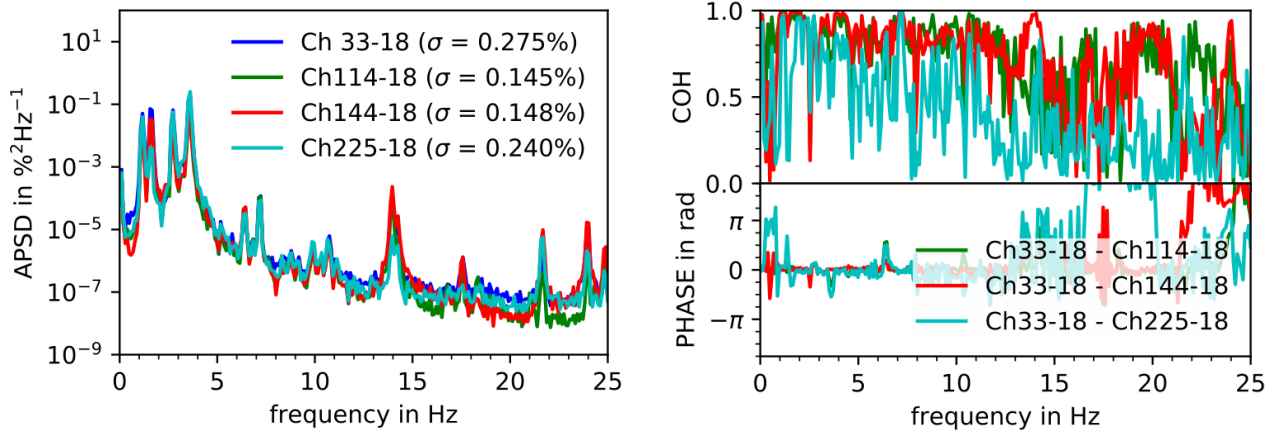
Figure 25: Radial comparison of APSD (left) and coherence and phase (right) for scenario 1. Depicted are the detector positions L-B11, L-G10, L-J06 and L-O05 at mid height corresponding to the DYN3D positions Ch33-18, Ch114-18, Ch144-18 and Ch225-18.

The second test scenario was a generic test, where the fuel assemblies are arranged in four rings in the core according to Figure 26. This scenario was chosen because it was expected to show a phase shift of π for opposite core halves.
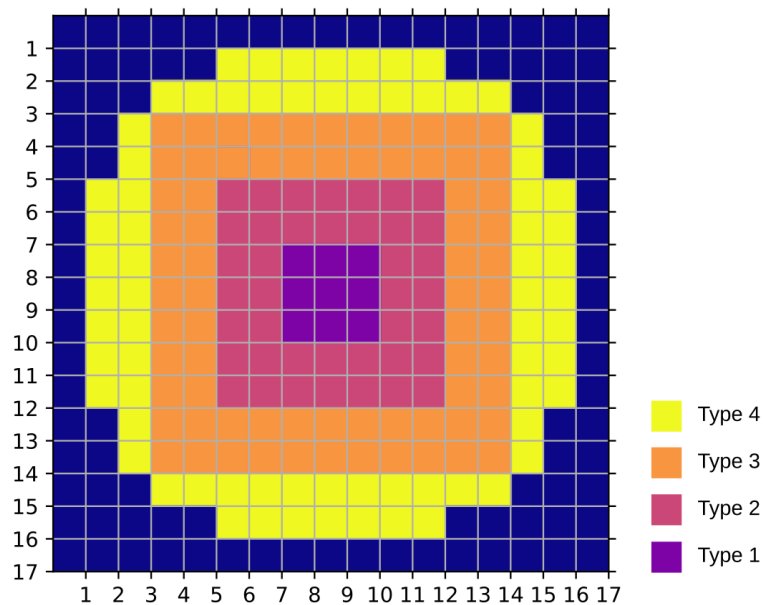
Figure 26: Distribution of fuel assembly types for scenario 2 consisting of 4 rings in the core. Type 1-4 have decreasing stiffness.
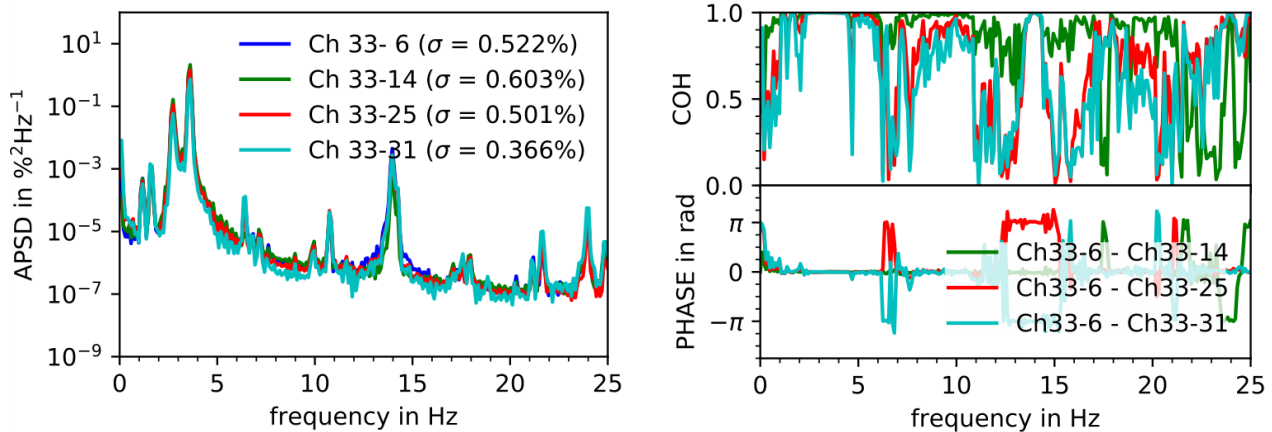
Figure 27: Axial comparison of APSD (left), coherence and phase (right) for scenario 2. Depicted are the detector positions L-B11-6, L-B11-4, L-B11-3 and L-B11-1 corresponding to the DYN3D positions Ch33-6, Ch33-14, Ch33-25 and Ch33-31.
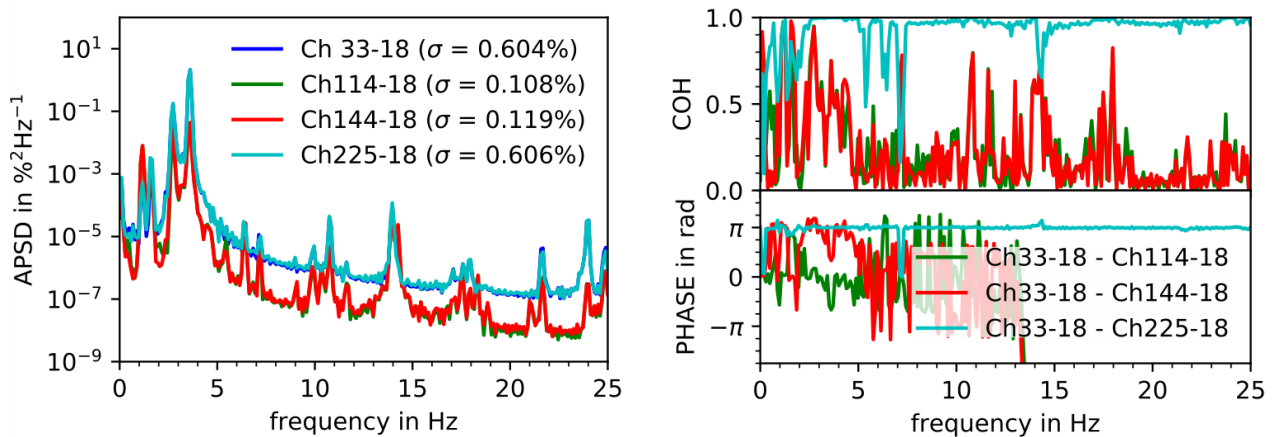
Figure 28: Radial comparison of APSD (left), coherence and phase (right) for scenario 2. Depicted are the detector positions L-B11, L-G10, L-J06 and L-O05 at mid height corresponding to the DYN3D positions Ch33-18, Ch114-18, Ch144-18 and Ch225-18.

The axial APSDs (see Figure 27) show a decrease to higher frequencies with a number of distinct peaks in the signal, as in the previous case. The coherence is again close to one over a wide range of frequencies and the axial phase with respect to the reference is zero except for small areas.

The radial frequency dependency (see Figure 28) differs from the previous scenario in that the inner detector positions (L-J06 and L-G10 corresponding to Ch114 and Ch144) have a lower magnitude of the APSD than the outer detector positions (L-B11 and L-O05 corresponding to Ch33 and Ch225). The coherence of the exact opposite detector position to the reference is near one over the whole frequency range, whereas the other detector positions show high coherence only for low frequencies. The opposite detector position with respect to the reference shows an out of phase behaviour. The other detector positions are in phase with the reference. These results show that, provided the coupling of the fuel assemblies is small (apart from there common fixation onto the core barrel) the symmetry of the loading scheme of the core contribute to the out-of-phase behaviour of neutron detectors in opposite core halves.

For the third test scenario a distribution of fuel assembly types based on the burnup of a realistic core was chosen. The distribution of the fuel assembly types in the core is depicted in Figure 29.

The burnup of the fuel assemblies was categorized into 4 categories, where it was assumed that more burnup would lead to lower stiffness.

Figure 30 shows the axial comparison of the neutron noise signals. The overall characteristics of the APSDs are the same as before. The coherence with respect to the reference detector is near one, especially in regions of low frequency. The phase with respect to the reference is zero nearly everywhere, except for small frequency bands, where it is π.

The radial comparison in Figure 31 reveals an overall similar characteristic of the APSDs with slightly lower magnitude of the inner detector positions (L-J06 and L-G10 corresponding to Ch114 and Ch144) compared to the outer detector positions (L-B11 and L-O05 corresponding to Ch33 and Ch225). This is an effect similar to scenario 2 and could thus be attributed to the symmetry of the core loading. The coherence of the outer detector position L-O05 with respect to the reference is near one, with lower coherence for the inner detectors. The phase with respect to the reference is approximately π for detector positions in the opposite core half and zero for detector positions in the same core half.
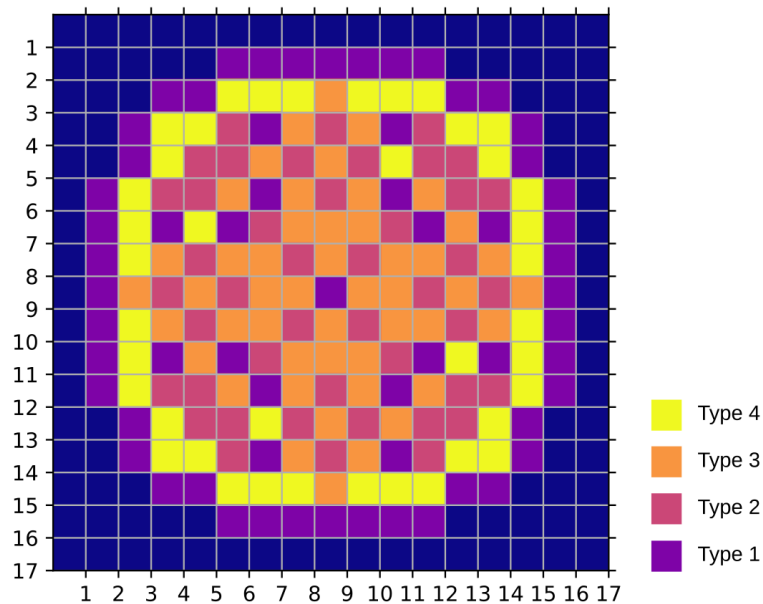
Figure 29: Distribution of fuel assembly types for scenario 3, which is a distribution according to the burnup of fuel assemblies. Type 1-4 have decreasing stiffness.
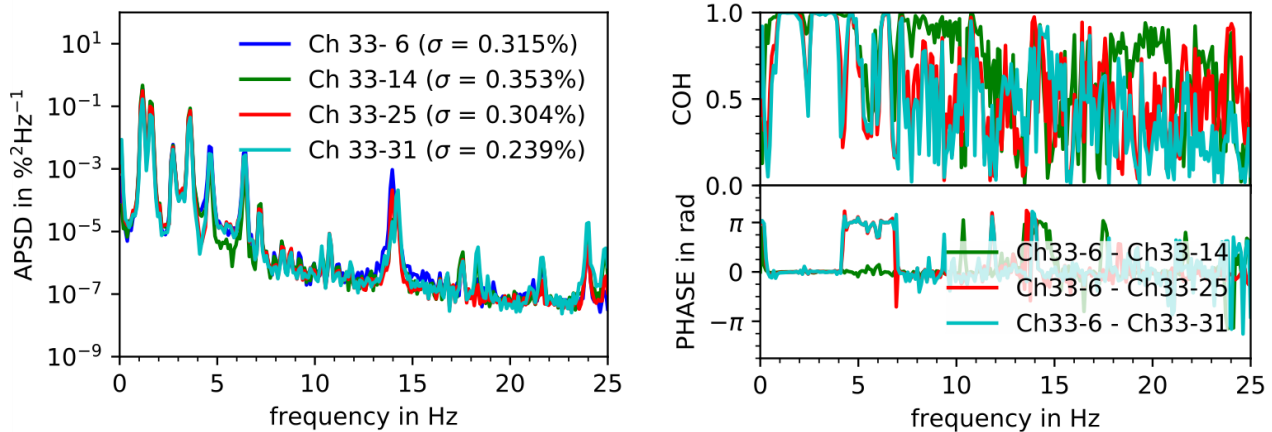
Figure 30: Axial comparison of APSD (left), coherence and phase (right) for scenario 3. Depicted are the detector positions L-B11-6, L-B11-4, L-B11-3 and L-B11-1 corresponding to the DYN3D positions Ch33-6, Ch33-14, Ch33-25 and Ch33-31.
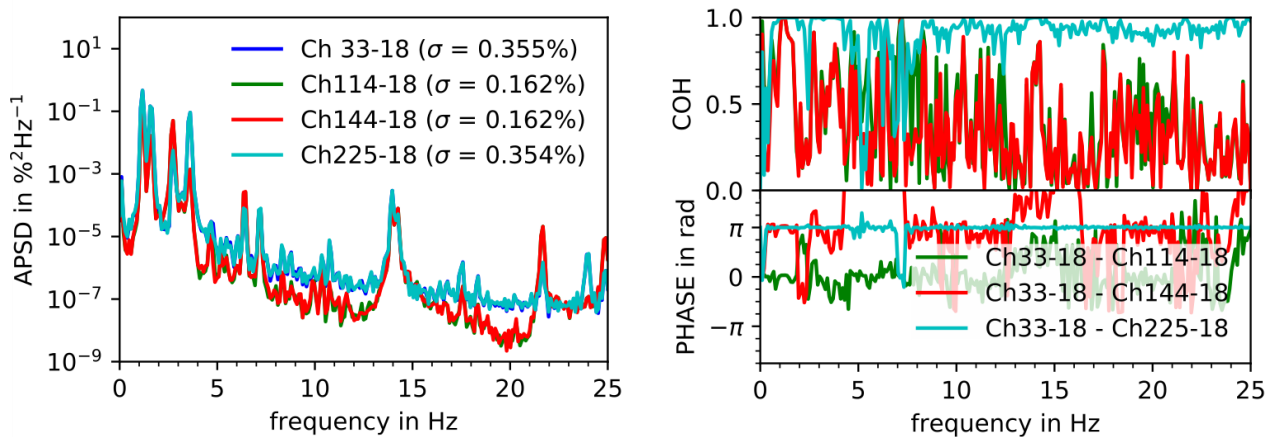
Figure 31: Radial comparison of APSD (left), coherence and phase (right) for scenario 3. Depicted are the detector positions L-B11, L-G10, L-J06 and L-O05 at mid height corresponding to the DYN3D positions Ch33-18, Ch114-18, Ch144-18 and Ch225-18.

3.2.3 Conclusion and outlook

In this section, coupled simulations of a reduced order mechanical model and the reactor core code DYN3D were performed. It was shown that a coupling of both tools is possible and yields plausible results. It could be demonstrated that under the assumption that the fluidic near-field coupling is very weak and that the driving force of the mechanical oscillations is mainly a stochastic force on the core barrel and RPV, an out-of-phase behaviour of neutron noise signals in opposite core halves was observed. This shows that the loading pattern of a core could be a factor in the noise characteristics due to different mechanical properties of the fuel assemblies.

Both the APSDs as well as the coherence and phase of the signals resemble the measurement data only qualitatively. In a next step, simulations with damping should be conducted, where it is expected that peaks in the APSDs will be smoothed. Also, the fluidic near-field coupling of fuel assemblies could be investigated as a reason for the phase observed between different detectors.

4 Processing of the neutron noise measurements

In Deliverable D3.5, Fourier analysis and Hilbert Huang Transform were used to perform an analysis on the measurements registered on 15th May 2018 (EOC 39) in the German pre-Konvoi 4-loop reactor and on the measurements registered on 27th March 2012 in the Swiss pre-Konvoi 3-loop reactor.

The Fourier Analysis results provided a large amount of information. On the one hand, the APSDs (Auto Power Spectral Densities) of all the detectors were presented for both all radial and axial distributions. On the other hand, a large series of coherences and phases between pairs of in-core and ex-core sensors was calculated, the analysis performed were also carried out for the radial and axial distributions. The use of Fourier analysis techniques in an extensive way allowed us to characterize and determine the neutron noise spectral features during normal operation in both reactors.

Hilbert Huang Transform analysis did not provide any further information and presented important limitations mainly due to the stationarity of the signals. Hilbert spectrum (time-frequency-amplitude spectrograms) does not allow to contribute to the differentiation of the scenarios, or in the characterization of the perturbations. The high similarity among all the spectrograms makes the differentiation of scenarios quite unfeasible through data visualization. Besides, the univariate approach with HHT analysis present difficulties to analyze a spatial-multivariate scenario. It does not compile the information in an efficient way – the decomposition process adds more data, but it does not provide more information.

Some remarkable spectral characteristics in both measurements were:
- Linear phase between in-core detectors of the same string. The phase difference relationships between in-core sensors of the same string show a very small slope in the low frequency range. This slope points out the existence of a transport phenomenon with a quite high transit speed.
- High response amplitude at low frequencies, below 1 Hz. The neutron noise below 1 Hz has its highest spectral amplitude around 1 Hz. This characteristic seems to be related to the thermal-hydraulic oscillations that are produced in the core and whose response range is located around 1 Hz.
- Out-of-phase relationship between opposite detectors. This has been observed in the simulated data when fuel assemblies vibrate.
- An exponential response amplitude decreasing above 1Hz.

The mentioned Fourier analyses performed in Deliverable D3.5 were also carried out for the rest of measurements delivered, the analysis demonstrated that in general terms, the spectral characteristics keep almost identical from cycle to cycle. These characteristics were shown and detailed in Deliverable D3.5 for both reactors. Therefore, to add the same analysis in the present report would not add new information. We instead refer to the Deliverable D3.5.

Axial and radial analysis

In the following subsections, we consider two types of sensor configurations that we call axial and radial analysis. In the axial analysis, we consider all the measurements available from the detectors in the same string or radial position. In the radial analysis, we consider all the measurements available from the detectors at the same level or axial position. These configurations were used to analyze the data from both type of reactors, KWU, and VVER.

The methodology based on Singular Value Decomposition

In the current section an approach based on Singular Value Decomposition is presented. This methodology is widely used in Modal Analysis as can be seen in (Greiner, 2008; Rainieri & Fabbrocino, 2015).

To perform the methodology, in the first place, we calculate a PSD matrix which is arranged as follows:

$$G_{yy}(j\omega)_i = \begin{bmatrix} APSD_{11} & CPSD_{12} & \cdots & CPSD_{1n} \\ CPSD_{21} & APSD_{22} & \cdots & CPSD_{2n} \\ \vdots & \vdots & \ddots & \vdots \\ CPSD_{n1} & CPSD_{n2} & \cdots & APSD_{nn} \end{bmatrix}_i \tag{16}$$

where Gyy is the PSD matrix of measured response channels. The dimension of Gyy is nxn, being n the number of the measurement channels considered. When the PSD is calculated in a single signal, it is denominated auto power spectral density (APSD), but in the case of considering two different signals, we call it cross power spectral density (CPSD).

As a reminder, PSD is defined as the Fourier transform of the auto correlation signal. The PSD function can be visualized as how the power of a single signal is distributed within the frequency spectrum. The Integral of the PSD over a certain frequency range denotes the energy contained in the signal at that frequency range. Due to the fact that the direct component from pre-Konvoi 4-loop and VVER-1000 were not available, and to standardize the analysis in the report, the APSDs have been normalized in order to ensure that the area below the curve is equal to the signal's variance.

Thereafter, the singular value decomposition or SVD is performed. In general terms the singular value decomposition of an mxn matrix A is the following factorization:

$$A = U\Sigma V^H \tag{17}$$

Σ is a diagonal matrix that contains the real singular values in descending order. For a Hermitian and positive definite matrix, such as the PSD matrix Gyy, it follows that U and V are identical and contains the respective singular vectors. The decomposition can be rewritten as:

$$G_{yy} = U\Sigma U^H \tag{18}$$

The singular value decomposition is performed for each of the matrices at each frequency.

The number of nonzero elements in the diagonal of the singular matrix corresponds to the rank of each spectral density matrix. The singular vectors correspond to an estimation of the mode shapes and the corresponding singular values are the spectral densities of the SDOF system expressed in Eq. (18).

If only one mode is dominating at a particular frequency, then only one singular value will be dominating at this frequency. In the case of close or repeated modes, there will be as many dominating singular values as there are close or repeated modes.

In case of resonance, only one or a few close modes contribute to the motion. Thus, there is only one term in Eq. (18), which means that there is only one singular value dominating in the SVD and

the corresponding singular vector is an estimate of the mode shape for that resonance frequency. Therefore, the first singular vector is a good approximation of the mode shape vector for that frequency.

In other words, the singular values establish a hierarchy of the dominant phenomenon taking place at a particular frequency range. The bigger the singular value, the more dominant is the phenomenon associated to the singular value at that frequency. It also allows to condense a large amount of information considering as many detectors as required in each type of analysis. The possibility to condense information allow us to observe in detail the global noise spectral characteristics of several signals at the same time. It is important to mention that the modulus and phases observed in the singular vectors have strong analogies with the traditional calculation of the coherence and phase relationships.

Processed data for machine learning analysis

As a part of the current task, to continue deepening in the neutron noise, the data from all the measurements available of three reactors (pre-Konvoi 4-loop, pre-Konvoi 3-loop, and the VVER-1000) were processed and stored in .mat files. The processed data was delivered to be analyzed through machine learning tools.

The format and structure of the files were designed in order to compile the most relevant information and to ease the use in the analysis. Considering all the possible pairs of detectors, each file contains for the in-core and the ex-core detectors:

- Matrixes with PSDs (APSDs and CPSDs).
- Matrixes with coherences, and phases.
- Statistic parameters. Matrixes that contains the NRMS, the skewness and the kurtosis for all the detector signals.
- Labels that describe the order of the detectors considered in the matrixes.
- General information about the type of reactor, cycle, date of the register, and measurement parameters.

The main objective of the current Section 4 is to present a brief summary of the results that helps to explain what we found in the data, to draw general conclusions about the neutron noise spectral characteristics in the reactors as well as to develop better ways to present the data that allow more suitable monitoring and visualization.

Subsections 4.1 and 4.2 present a summary of the results obtained in both KWU reactors, firstly based on the singular values and secondly, on the singular vectors. The axial analysis considers the six detectors of the string J06, the radial analysis the eight detectors at level 2. Subsection 4.3 summarizes the analyses performed on the VVER-440. Subsection 4.4 presents the analysis based on recorded signals in the VVER-1000. In this case, the analyses are based on Fourier, JTFS and SSA analysis techniques.

4.1 German pre-Konvoi 4-loop reactor

In this section, Singular Value Decomposition (SVD) was applied on the measurement registered on 17th April 2014. In total, this measurement considers 45 in-core and 8 ex-core neutron detectors. There are 3 locations, G14-2, C04-1, and G10-3 which are not included in the analysis because they consider pressure measurements.

Two types of approaches are considered in the analysis, axial and radial (eight and six detectors, respectively). In both cases we have considered the radial and axial locations where all the sensors seem to behave normally, that is, detectors in the string J06 and J02 and in the level 4.

Note that we have as many singular values as detectors considered in the analysis. Nevertheless, only the first singular values are important in amplitude. The singular values go in decreasing values and they never cross each other.

In the case of the singular values, the first singular one is the global envelope of the highest amplitudes, whilst the next singular values are below it and show somehow the resulting amplitude due to secondary phenomena. The first singular vector has strong analogies with the calculation of the phase relationship. This analogy is found in both analyses, axial and radial.

4.1.1 Axial Analysis

Figure 32 and Figure 34 upper side show the APSDs of the six detectors of the string J02 and J06 respectively. In the lower side we can see the three first corresponding singular values.

In Figure 33 and Figure 35 we can observe the phase distribution of the first three singular vector corresponding to each string J02 and J06 respectively. J02 is near the periphery and J06 is near the centre.

Some general observations on the singular values are summarized below – see Figure 32 and Figure 34:
- In both radial positions (J02 and J06), the three singular values show a very similar behaviour in the radial analysis.
- The larger differences among the three singular values are located in the low-frequency range, below 2 Hz, in the thermal-hydraulic range. However, the differences in amplitude are very important until approximately 15 Hz.
- Above 15 Hz approximately, the difference in amplitude among the singular values decrease to the minimum.
- Singular values 2 and 3 are separated from singular value 1 and show a remarkable lower amplitude in the low-frequency range (in the thermal-hydraulic peak and the resonance at 7.5 Hz).
- The singular values show different configurations in the frequency range. We can see that in some resonances only one or two singular values are important, in other resonances like the one at 25 or 50 Hz, all the singular values seem to be influenced.

General observations on the singular vectors are drawn below – see Figure 33 and Figure 35:
- In both radial positions (J02 and J06), the corresponding singular vectors show a very similar phase distribution in the radial analysis. As mentioned, there is radial symmetry between strings J02 and J06.
- In the phase distribution, we can distinguish two zones. The first zone, up to 15 Hz and the second zone above 15 Hz. In the first zone, we have a series of linear patterns mainly in the low frequency range that show the existence of a transport phenomenon in the first singular vector. In the second zone, the pattern is chaotic.

- The singular vectors 2 and 3 exhibit patterns different to the singular vector 1. We can also appreciate some clear linear phases with different slopes.
- We can observe that these phase distributions are much more complex than those in the simulations evaluated in Deliverable D3.3.
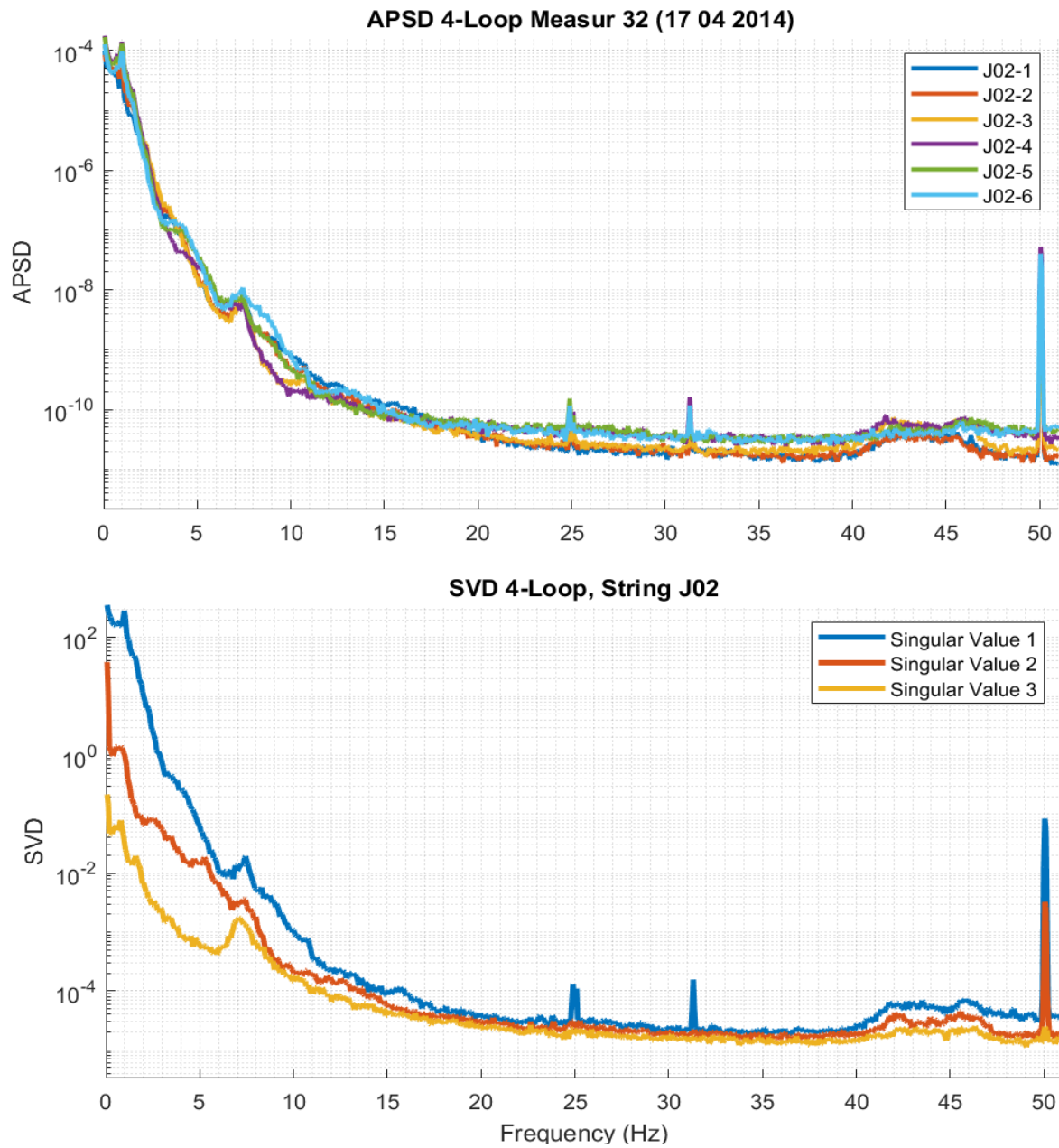
Figure 32: APSDs of the detectors in the string J02 (in the upper side). Singular values 1 to 3 of the axial analysis of the detectors in the string J02 (in the lower side).
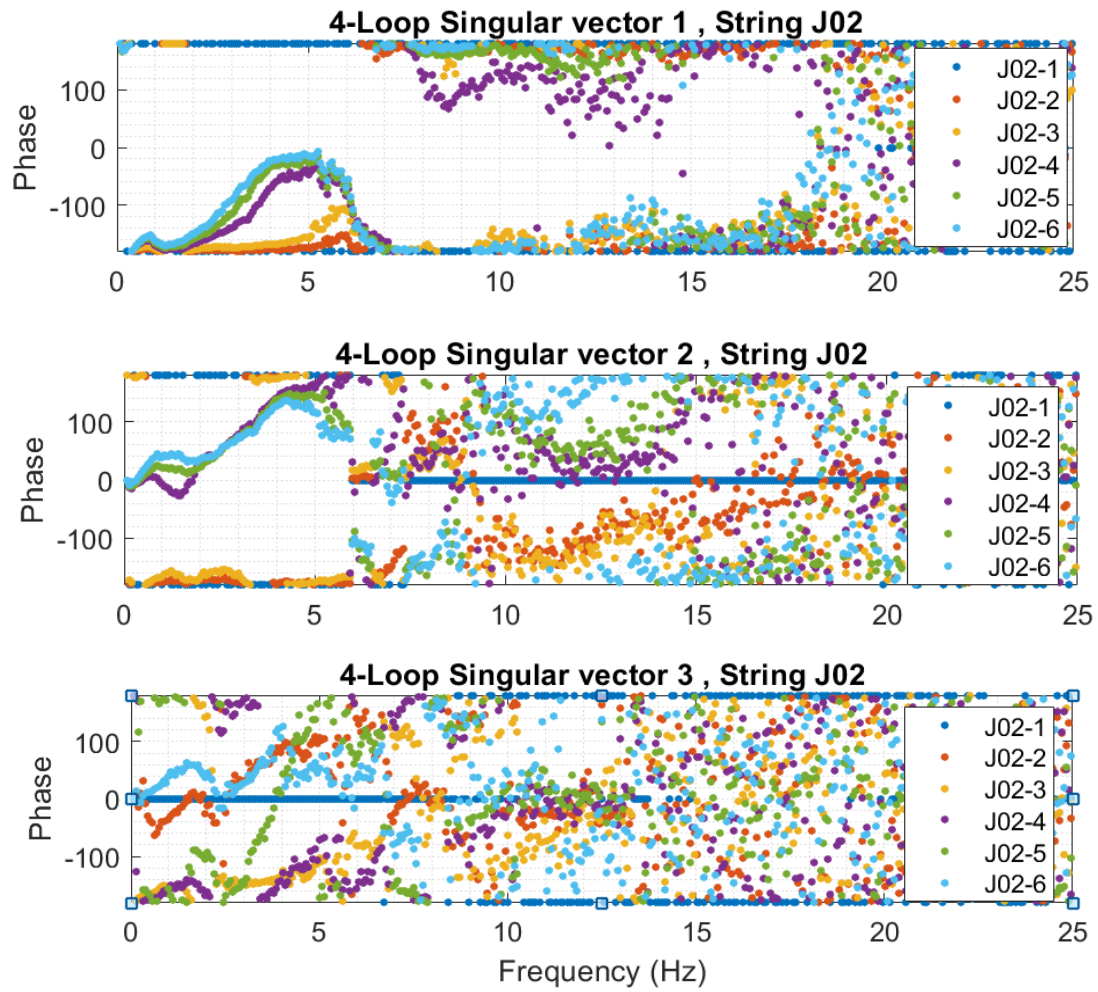
Figure 33: Singular vectors 1 to 3 of the axial analysis of the detectors in the string J02.
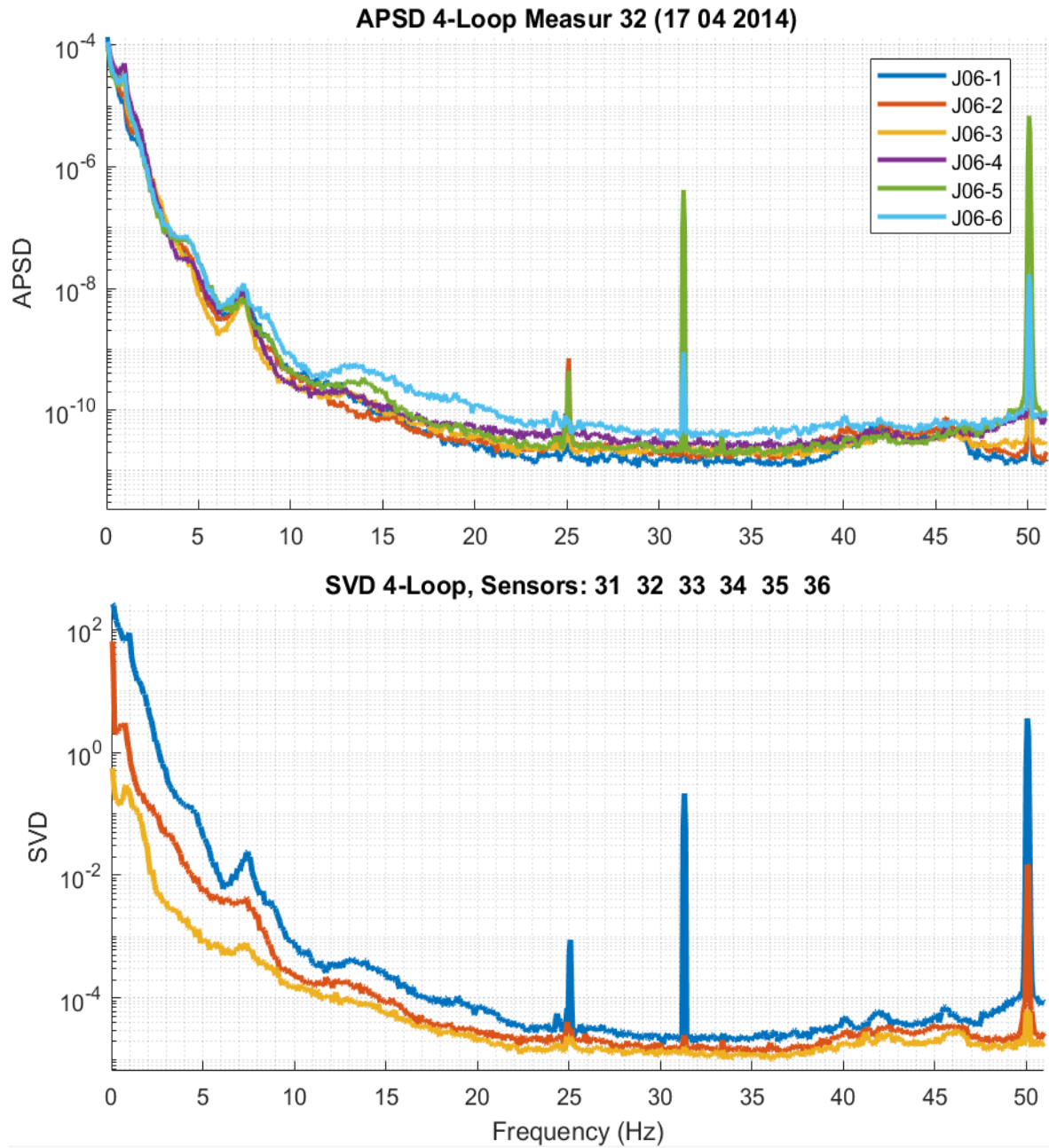
Figure 34: APSDs of the detectors in the string J06 (in the upper side). Singular values 1 to 3 of the axial analysis of the detectors in the string J06 (in the lower side).
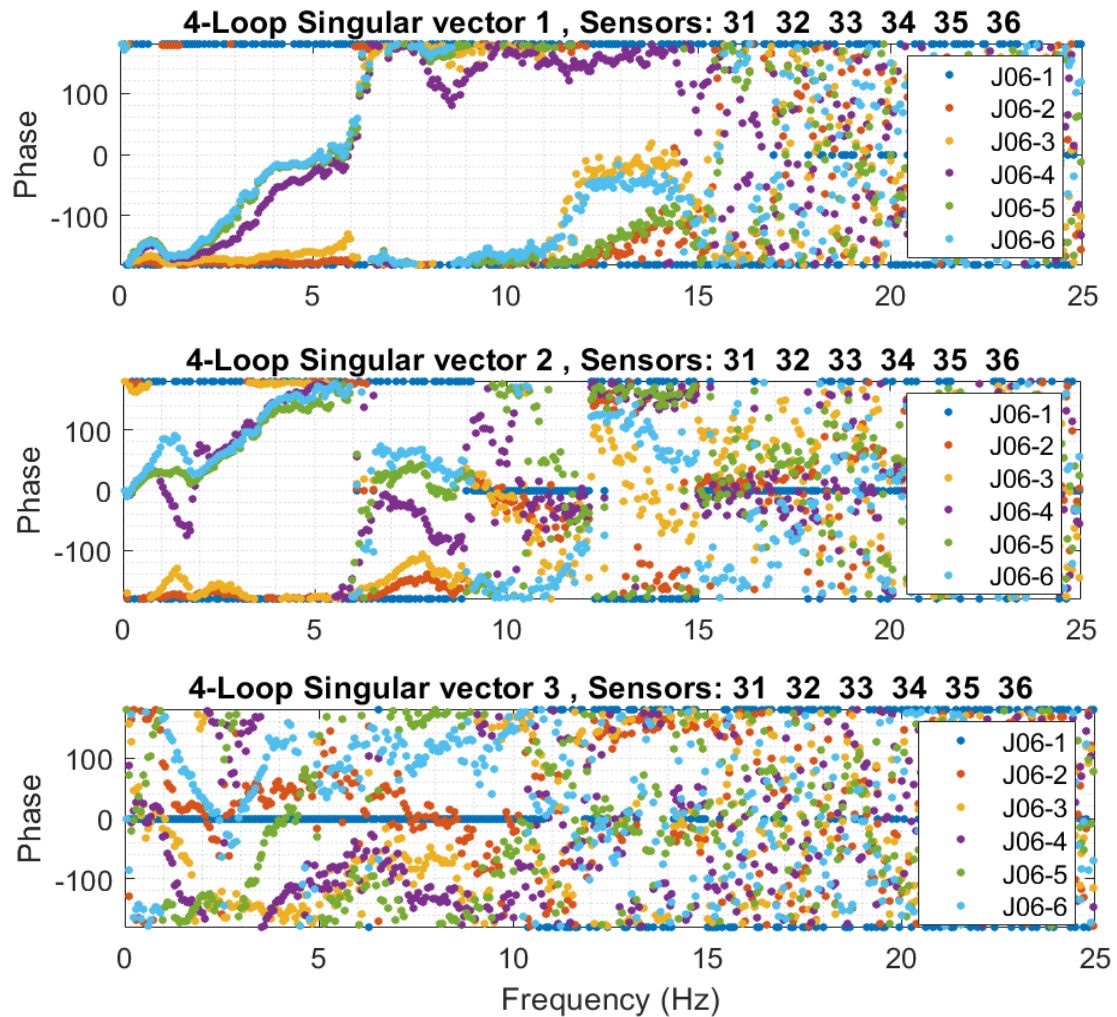
Figure 35: Singular vectors 1 to 3 of the axial analysis of the detectors in the string J06.

4.1.2 Radial Analysis

Figure 36 upper side shows the APSDs of the eight detectors at level 4, respectively. In the lower side, we can see the three first corresponding singular values.

In Figure 37, we can observe the phase distribution of the first three singular vector corresponding to the detectors at level 4.

Some general observations on the singular values are given below - see Figure 36:

- In the radial analysis (Level 4), the three singular values show less differences than in the case of axial analysis. The separation among them is smaller than in the axial analysis.
- In some resonances, only one or two singular values are important, in other resonances like the one at 25 or 50 Hz, all the singular values overlap.

APSD 4-Loop Measur 32 (17 04 2014)

SVD 4-Loop, Sensors: Level 4
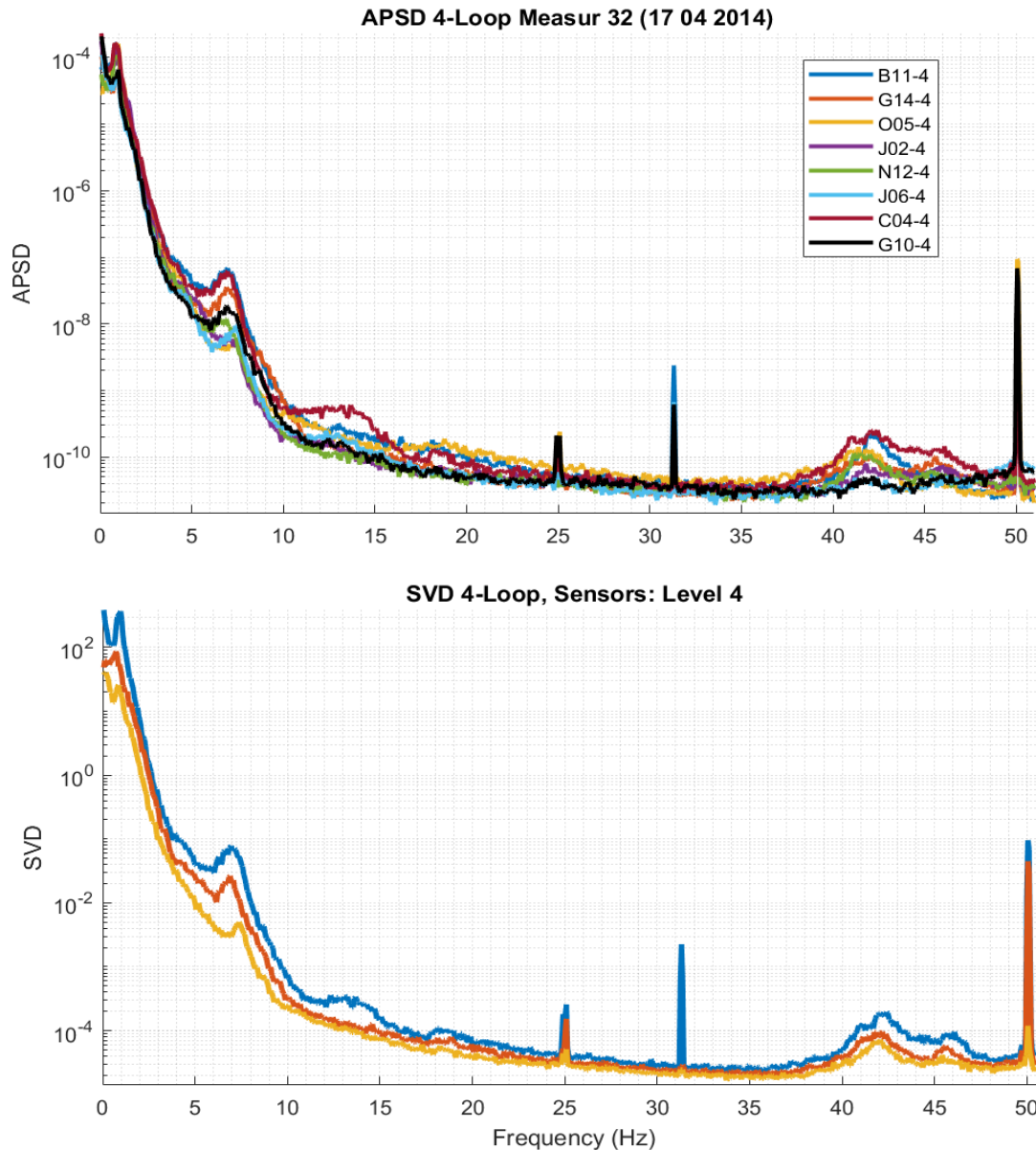
Figure 36: APSDs of the detectors in the level 4 (in the upper side). Singular values 1 to 3 of the radial analysis of the detectors in the level 4 (in the lower side).

Some general observations on the singular vectors are summarized hereafter – see Figure 37:

- In the first singular vector, we can observe that above 15 Hz approximately, the phase distribution is random.
- In the case of singular vector 2 and 3, the phase distribution is random above 10 Hz.
- Singular vectors 2 and 3 exhibit patterns different to the singular vector 1.
- In the radial analysis, we can notice the absence of clear linear phases like in the axial case. This points out to the non-existence of transport phenomena in the axial direction.

As seen in Figure 37, the phase distribution in each singular vector is different. There are strong analogies between the calculation of the phase relationship and the singular vector 1. In order to illustrate this, Figure 38 on the left shows the zones of the reactor which are out of phase for the 3.5-6 Hz range and, Figure 38 on the right hand side, shows the phase-behaviour for the 7-8.5 Hz range.

CORTEX
Core monitoring techniques and
experimental validation and demonstration

D4.4 Results of the application and demonstration calculations
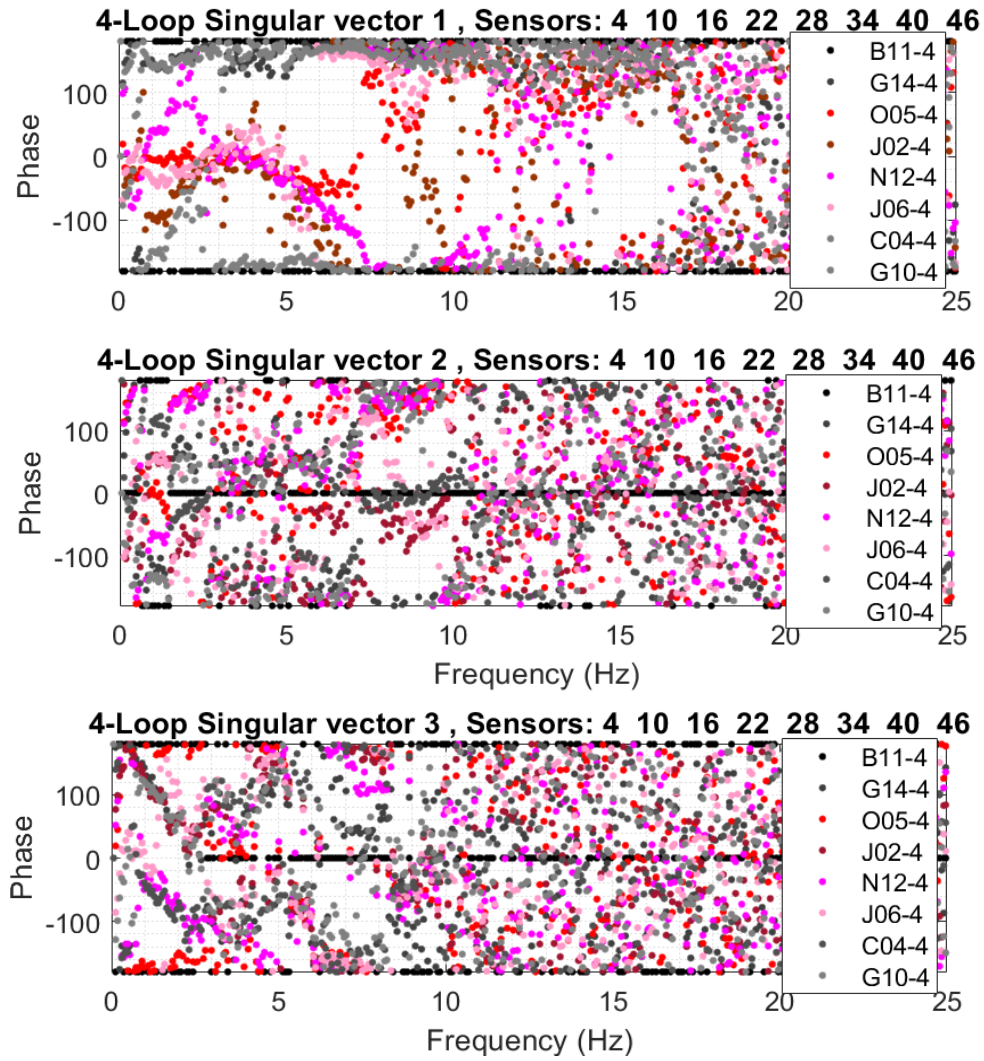
Figure 37: Singular vectors 1 to 3 of the radial analysis of the detectors in the Level 4.
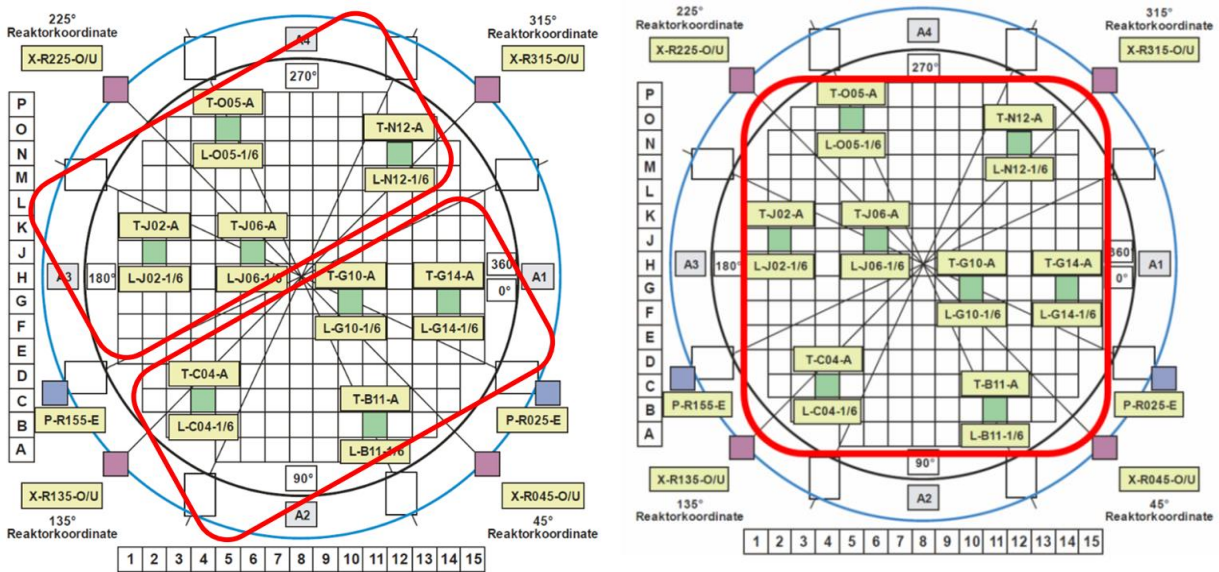
Figure 38: Phase distribution of the Singular vector 1. (3.5 - 6) Hz on the left hand side and (7 – 8.5) Hz on the rigth hand side.

4.2 Swiss pre-Konvoi 3-loop reactor

In this section, the Singular Value Decomposition methodology was applied on the measurement (MOC40) corresponding to cycle 40. In total, the measurement considers 36 in-core and 8 ex-core neutron detectors. There were also 5 defective sensors in the considered measurement: G02-6, C08-4, J06-2, N08-2, N08-4.

Two types of analysis are considered, axial and radial (six detectors in both cases). In both cases, we have considered the radial and axial locations where all the sensors seem to behave normally, that is, detectors in the string J14 and in the level 3.

Note that we have as many singular values as detectors considered in the analysis. Nevertheless, only the first singular values are important in amplitude. The singular values go in decreasing values and they never cross each other.

In the case of the singular values, the first singular one is the global envelope of the highest amplitudes, whilst the next singular values are below it and show somehow the resulting amplitude due to secondary phenomena. The first singular vector has strong analogies with the calculation of the phase relationship. These analogies are found in both analyses, axial and radial.

4.2.1 Axial Analysis

Figure 39 upper side, show the APSDs of the six detectors of the string J14. In the lower side, we can see the three first corresponding singular values.

In Figure 40, we can observe the phase distribution of the first three singular vectors corresponding to the string J14.

Some general observations on the singular values are presented below – see Figure 39:

- The three singular values show a very similar behaviour in the radial analysis.
- The larger differences among the three singular values are located in the low-frequency range, below 2 Hz, in the thermal-hydraulic range. However, the differences in amplitude are very important until approximately 15 Hz.
- Above 15 Hz approximately, the difference in amplitude among the singular values decrease to the minimum.
- The singular values 2 and 3 are separated from singular value 1 and show a remarkable lower amplitude in the low-frequency range (in the thermal-hydraulic peak and the resonance at 7.5 Hz).
- The singular values show different configurations in the frequency range. We can see that in some resonances not all the singular values represent them, only one or two singular values are important, in other resonances like the one at 25 or 50 Hz, all the singular values overlap.
- We can observe that these phase distributions are much more complex than those in the simulations evaluated in Deliverable D3.3.
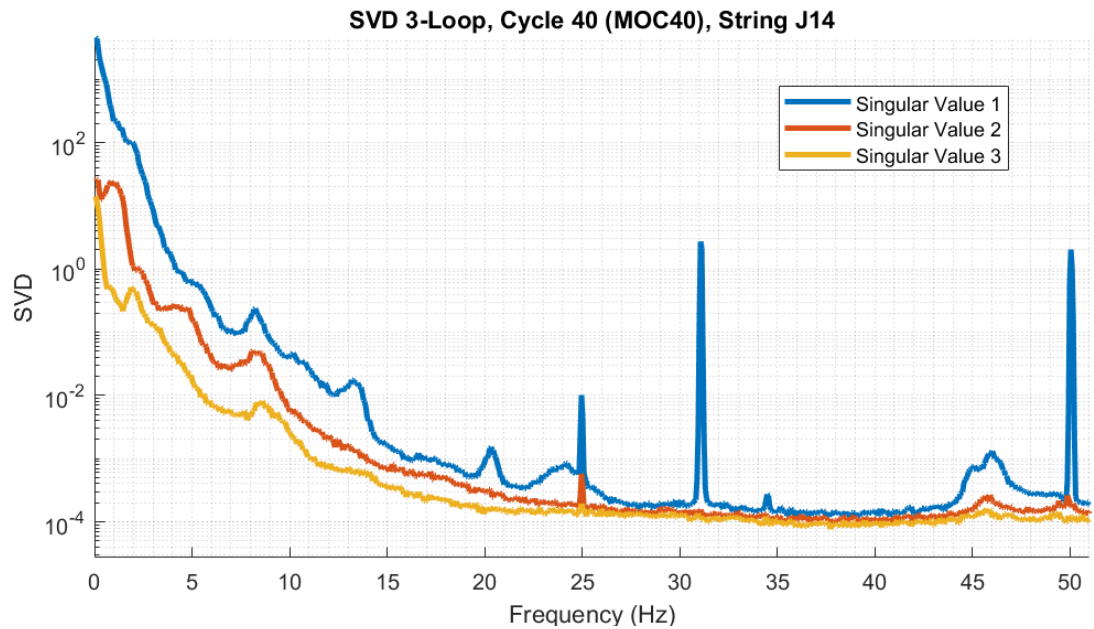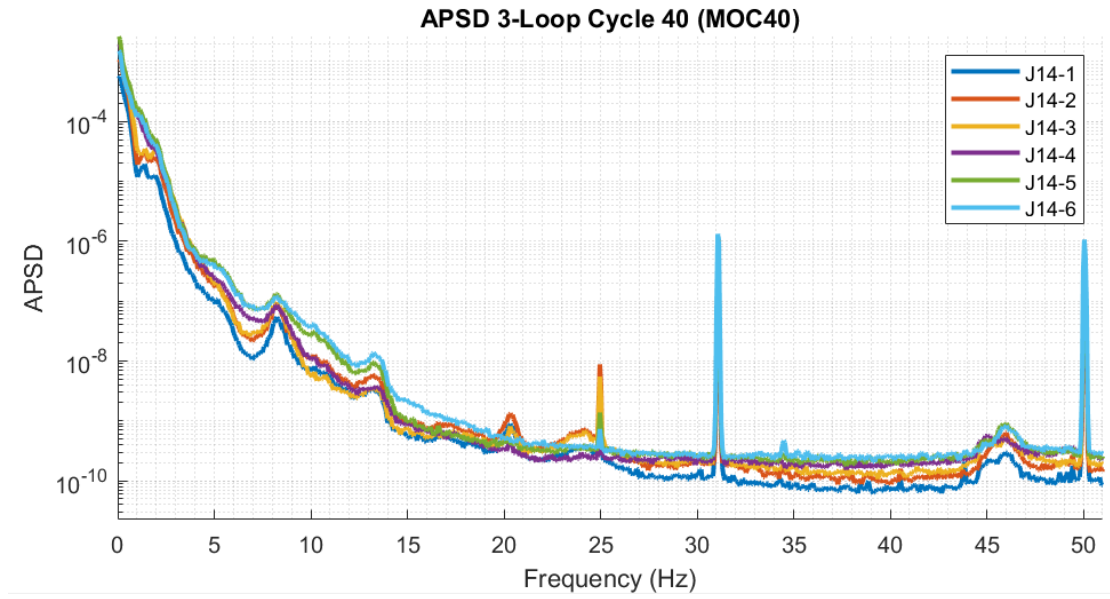
Figure 39: APSDs of the detectors in the string J14 (in the upper side). Singular values 1 to 3 of the axial analysis of the detectors in the string J14 (in the lower side).
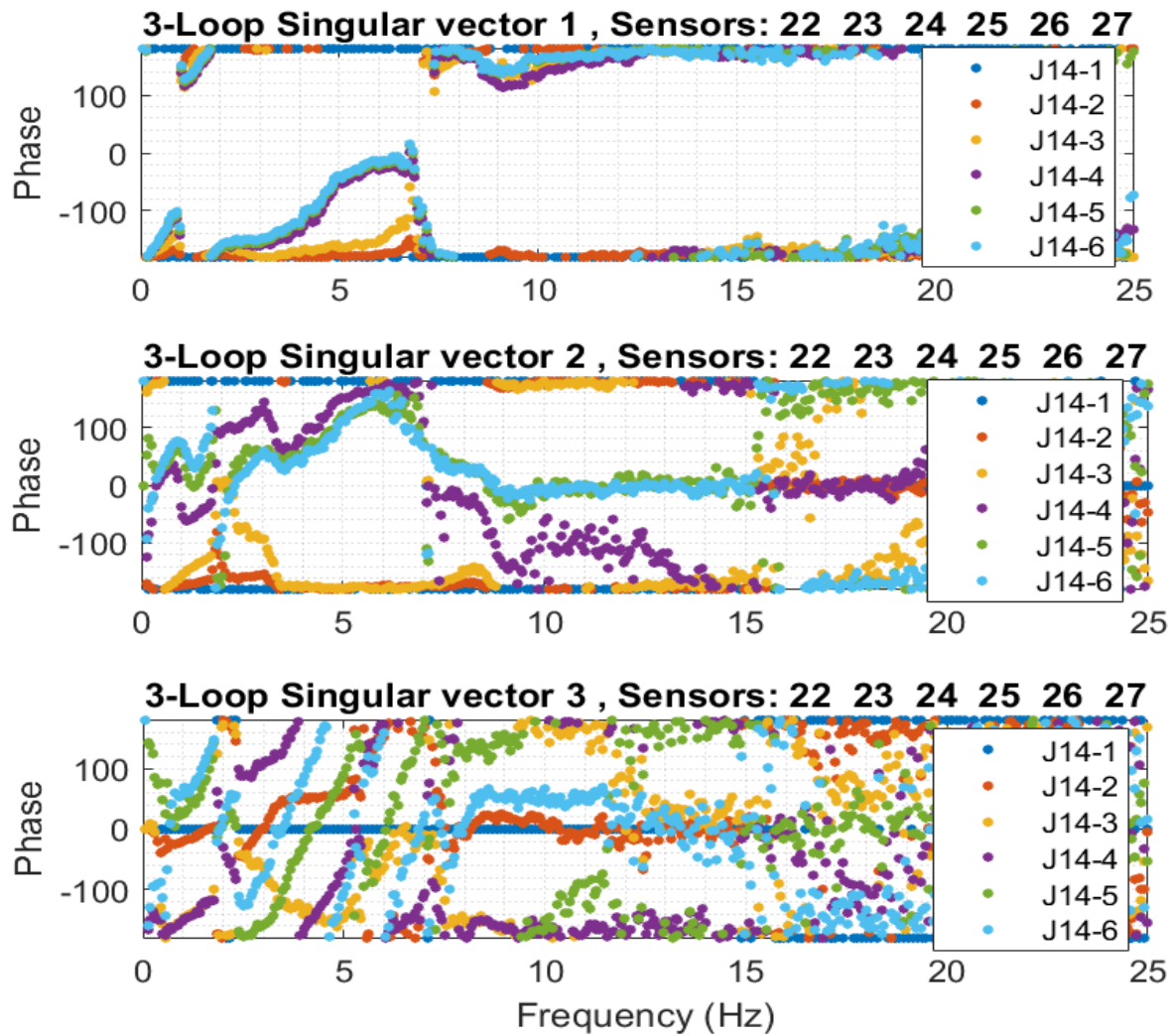
Figure 40: Singular vectors 1 to 3 of the axial analysis of the detectors in the string J14.

Some general observations on the singular vectors are summarized hereafter – see Figure 40:

- In the phase distribution, we can distinguish two zones. The first zone, up to 15 Hz and the second zone above 15 Hz. In the first zone, we have a series of linear patterns mainly in the low frequency range that shows the existence of a transport phenomenon in the first singular vector. In the second zone, the pattern is chaotic.
- The singular vector 2 and 3 exhibit patterns different from the singular vector 1. We can also appreciate some clear linear phases with different slopes.

4.2.2 Radial Analysis

Figure 41 upper side shows the APSDs of the six detectors at level 3, respectively. In the lower side, we can see the three first corresponding singular values.

In Figure 42, we can observe the phase distribution of the first three singular vectors corresponding to the detectors at level 3, respectively.

APSD 3-Loop Cycle 40 (MOC40)

SVD 3-Loop, Cycle 40 (MOC40), Level 3
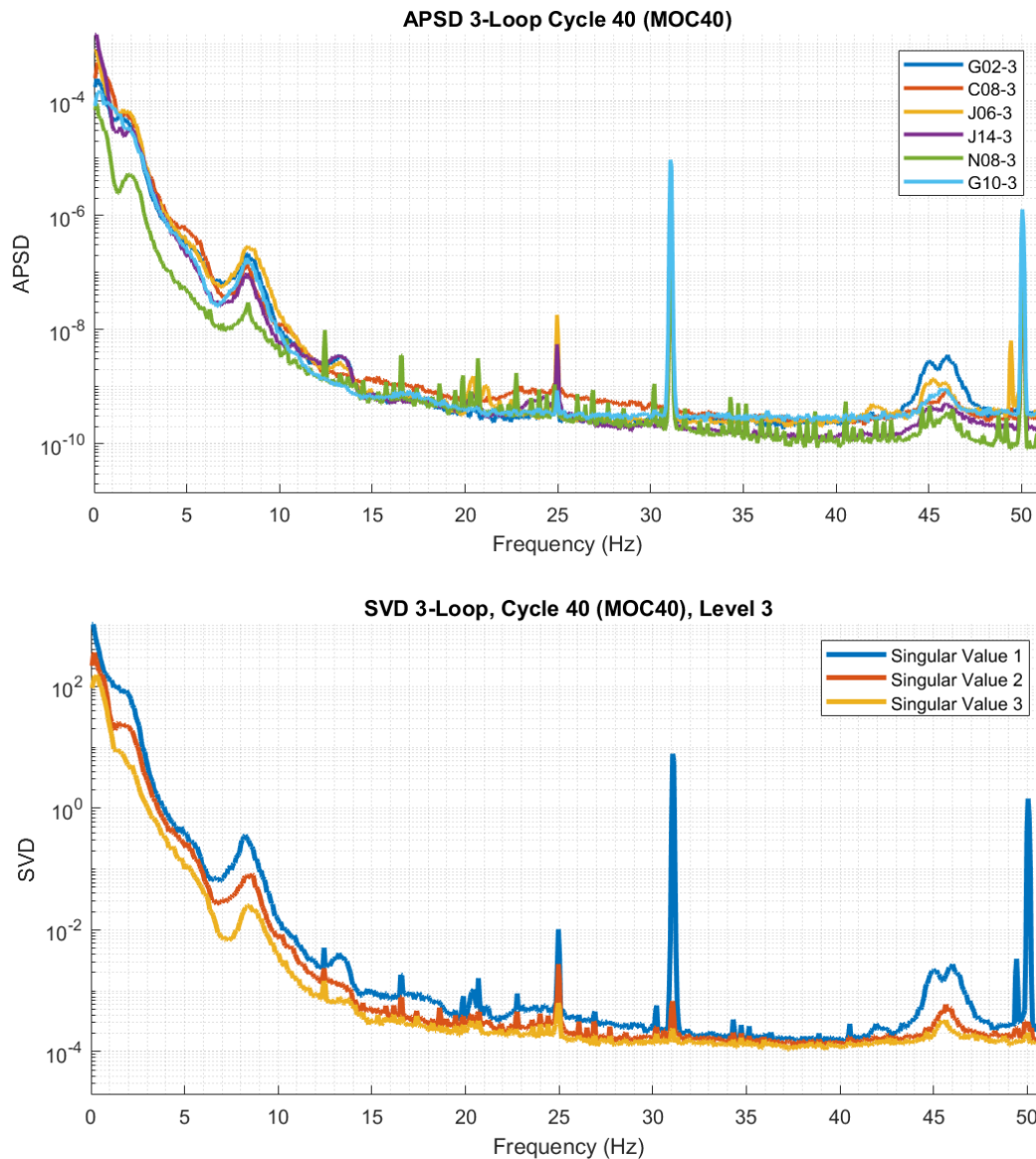
Figure 41: APSDs of the detectors in the level 3 (in the upper side). Singular values 1 to 3 of the radial analysis of the detectors in the level 3 (in the lower side).

Some general observations on the singular values are drawn below – see Figure 41:

- In the radial analysis (level 3), the three singular values show less differences than in the case of axial analysis. The separation among them is smaller than in the axial analysis.
- In some resonances, only one or two singular values are important, in other resonances like the one at 25 or 50 Hz, all the singular values overlap.

Some general observations on the singular vectors are detailed below – see Figure 42:

- In the first singular, vector we can observe that above 20 Hz approximately, the phase distribution is random.
- In the case of the singular vectors 2 and 3, the phase distribution is random above 10 Hz.
- The singular vectors 2 and 3 exhibit patterns different from the singular vector 1.
- In the radial analysis, we can notice the absence of clear linear phases like in the axial case. This points out the non-existence of transport phenomena in the axial direction.

As seen in Figure 42, the phase distribution in each singular vector is different. There are strong analogies between the calculation of the phase relationship and the singular vector 1. In order to

illustrate this, Figure 43 on the left shows the zones of the reactor which are out of phase for the 3.5-6 Hz range and, Figure 43 on the right hand side, shows the phase-behaviour for the 7-8.5 Hz range.
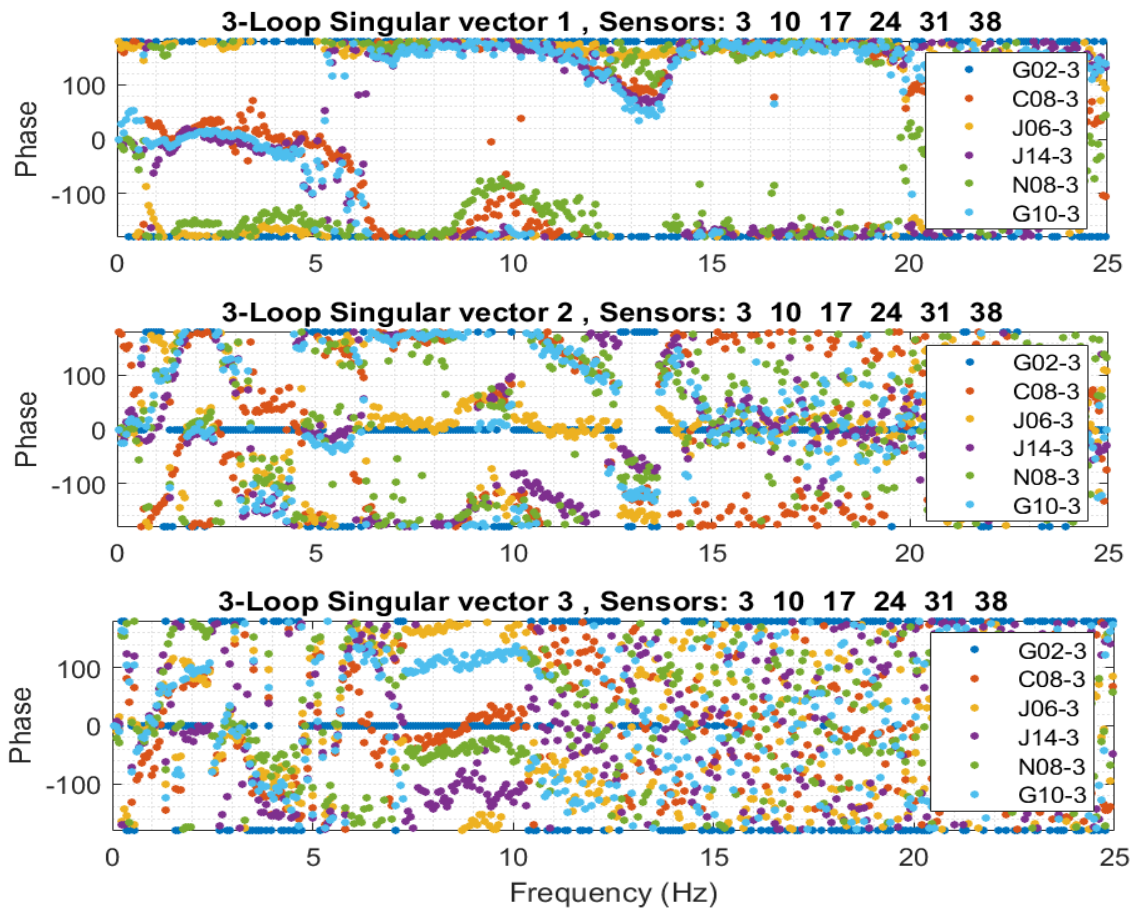
Figure 42: Singular vectors 1 to 3 of the radial analysis of the detectors in the Level 3.
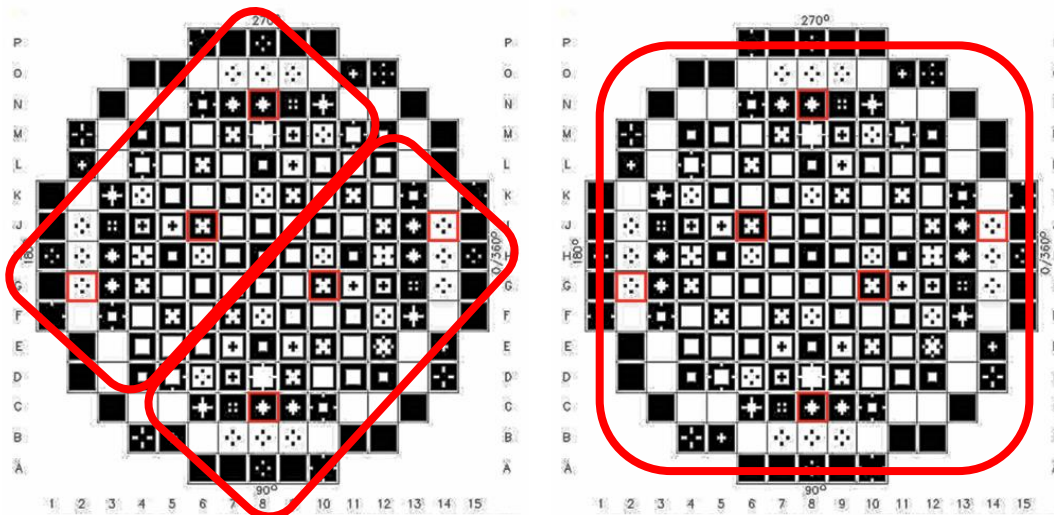
Figure 43: Phase distribution in Singular vector 1 (3.5 - 6) Hz on the left hand side and (7 – 8.5) Hz on the rigth hand side.

4.3 Hungarian VVER-440 reactor

Three measurements of fuel cycle 32 of Unit 2 of the Paks VVER 440/213 reactor were made available for the project: one from the beginning (BOC), one from the middle (MOC) and one from the end of the cycle (EOC), or more exactly measurements at 7, 149 and 335 effective full power days (EFPD) (see Table 4). The measurements are one hour long with 100 Hz sampling frequency.

Table 4: Dates of the available measurements

date	EFPD [days]	relative to cycle
2017-01-03 11.59.58	7.96	BOC
2017-05-26 12.00.03	149.73	MOC
2017-11-29 12.00.12	335.13	EOC

4.3.1 Available signals in the measurement

The VVER 440 measurements contain 288 in-core neutron noise signals and 44 thermocouple noise signals. Here a short summary is given. For more details, we refer to Section 4 of deliverable D4.3 (Lipcsei et al., 2018) where the main features of the VVER 440 reactor, its detectors and the measurement system are described, as well as the measured data collected within subtask 4.1.1 are provided.

The stationary (DC) and fluctuating (AC) parts of the signals are produced with filters and measured separately. The filters applied are as follows:

- DC: low pass 0.4 Hz.
- AC: high pass: 0.03 Hz, low pass 40 Hz, notch: 50 Hz.

The DC parts of the signals are digitally down-sampled and stored at 3.125 Hz.

4.3.1.1 In-core neutron noise signals

The reactor core of the VVER 440/213 reactors are equipped with uncompensated Rh SPND detectors: detector chains are installed in the central tube of 36 fuel assemblies (their positions are shown on the left side of Figure 44). Each chain consists of 7 detectors and a compensation cable (see Figure 44, right), the latter is also measured as the 8th detector of the chain and can serve as a background detector.
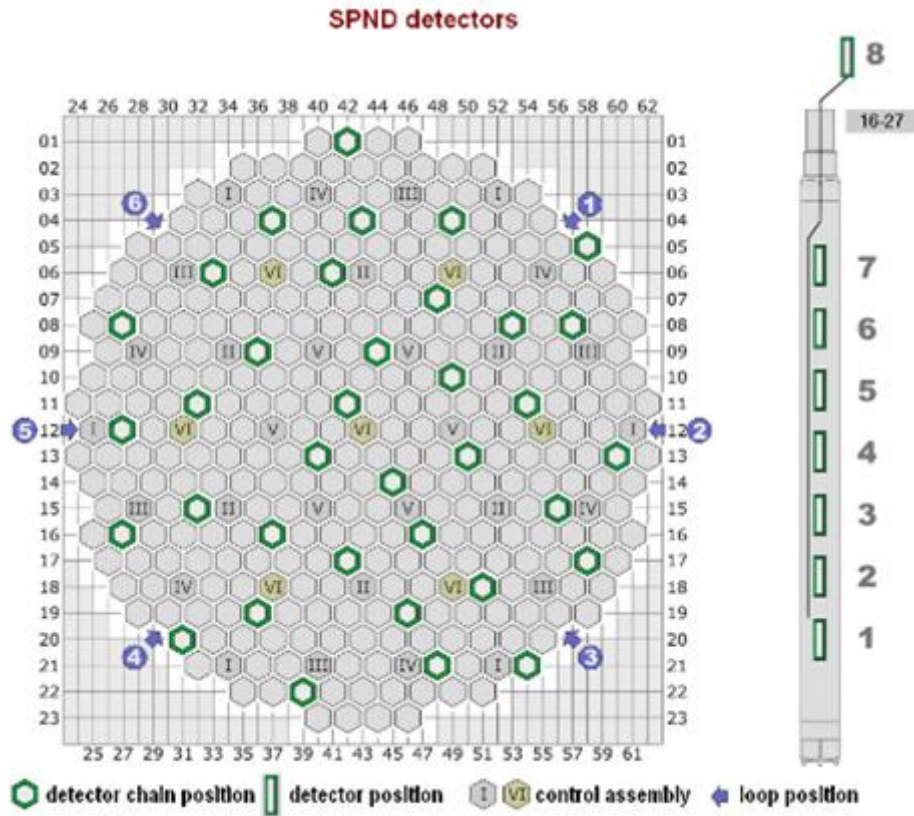
Figure 44: Radial arrangement of the SPND chains (left) and axial positions of the detectors in the chains (right).

4.3.1.2 *Thermocouple signals*

Thermocouples (TCs) are installed and measured at each loop of the hot and cold leg of the reactor vessel as well as at the outlet of several fuel assemblies. In Figure 45, the assemblies equipped with core outlet thermocouples are marked with red hexagons, while the TCs used in the measurements are highlighted with yellow markers.
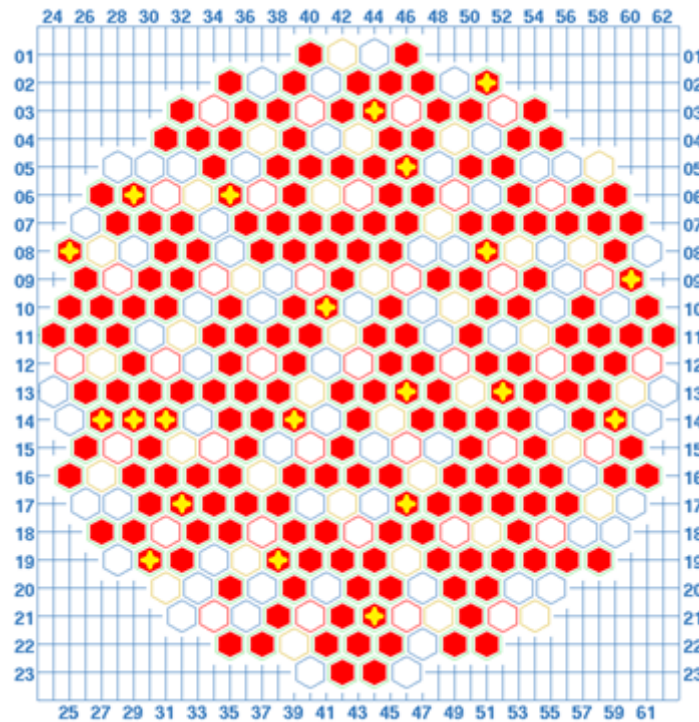
Figure 45: Radial positions of the measured core outlet thermocouples (with yellow markers).

4.3.1.3 Normalization

The signals are normalized with their DC as commonly used for the noise signals of western-type reactors. However, it is important to emphasize that the SPND detectors used here have two important features which reduce the usability of this normalization.

The neutron detectors are Rh SPNDs, having only 6-7% of prompt signal part in steady state depending on the manufacturing technology of the detectors.

Additionally, these SPNDs are uncompensated, thus the measured signals contain a non-neglectable part from the detector cables of different length. Hence, the estimation formula of the neutron noise provided in page 65 of deliverable D4.3 (Lipcsei et al., 2018) is applicable only when the fluctuating signals contain global noise only.

4.3.2 Settings and results of the calculations

The spectra of the measurements were calculated in MATLAB and provided in separate .mat files to the CORTEX partners.

4.3.2.1 Parameter setting of the Fourier Transform

The Fourier Transforms (FTs) are calculated with a window width of 4096, Hanning window and 50% overlapping. This results in 2049-point width spectra, the frequency point of which are from 0 to 50 Hz with increments of 100/4096 Hz.

4.3.2.2 Content and structure of the provided data

All results of the same measurement are stored in a variable structure called 'Data'. The fields of the structure are listed and explained in Table 5.

Table 5: Field structure of the stored results

Field name	Data type	Description
Incore_psd_phase Thermo_psd_phase	{288×288 cell} {44×44 cell}	The upper triangles of these matrices contain data: [2049×2 double], the columns of which are absolute value and phase of the complex CPSD. Coherence can be calculated from the absolute values of the CPSDs.
Incore_Stat Thermo_Stat	[288×4 double] [44×4 double]	DC, NRMS, Skewness and Kurtosis of the signals
Label_Stat_Param	{1×4 cell}	{'DC' 'NRMS' 'Skewness' 'Kurtosis'} meaning of the columns of the *_Stat matrices
frequency	[2049×1 double]	frequency values assigned to the rows of the *_psd_phase matrix elements
Cycle	char array	cycle and EFPD of the measurement
Date	char array	date of the start of the measurement
Reactor	char array	reactor type
label_incore label_thermo	{1×288 cell} {1×44 cell}	names of the signals

In addition to the .mat files, a folder called 'plots' was uploaded on the server used for delivering the data to the CORTEX partners. This folder contains graphs of the auto and cross spectra of the SPND signals for an easier overview of the results. Each graph contains the spectra of the detector signals of the same SPND chain. Two kind of arrangements are provided for each chain:

- APSD*.wmf   8 APSDs of the same SPND chain in one graph (Figure 46).
- CPSD*.wmf   8 APSDs and all phases and coherences in a matrix arrangement (Figure 47).
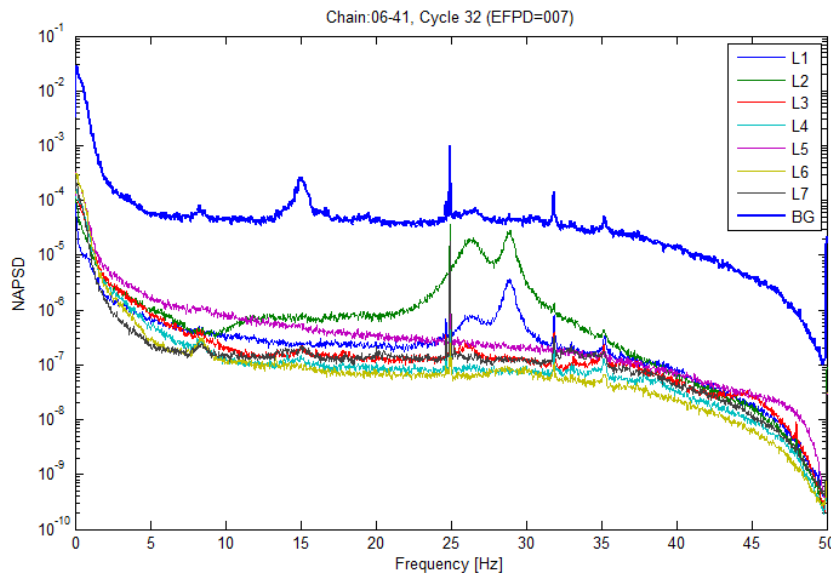
Figure 46: APSDs of chain 06-41.
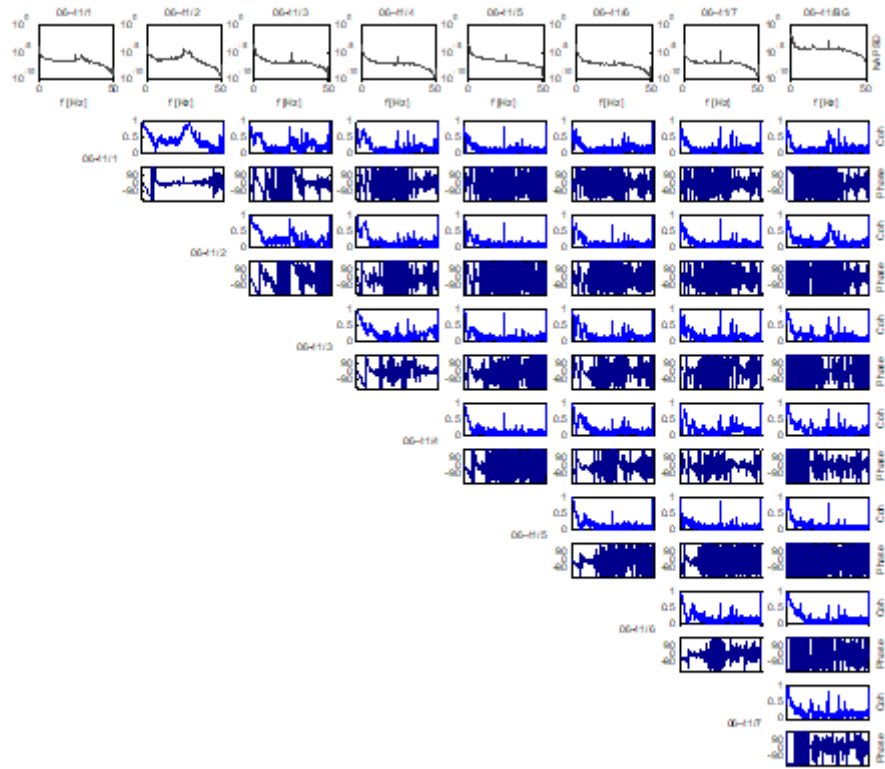
Figure 47: Auto and cross spectra of chain 06-41.

4.4 Czech VVER-1000 reactor

This section presents the Fourier and Singular Spectrum analysis performed on the VVER-1000 reactor signals. The techniques used were the calculation of Auto Power Spectral Density (APSD), the coherence with phase relationships between pairs of sensors, JTFS spectrograms in FFT analysis and non-parametric SSA techniques in time and frequency domain.

4.4.1 Measurement considered and detectors

For the FFT, two types of analysis are considered, axial and radial (16 and 4 detectors, respectively). Figure 48, upper part, shows the 16 positions of the detectors considered in the radial analysis at level 5. Figure 48, lower part, shows the 16 strings considered in the axial analysis, 4 detectors at 4 levels (1, 3, 5, and 7). In the VVER-1000, level 1 is the lowermost and the level 9 is the uppermost.

The measurement considered in the FFT analysis was registered on September 23th, 2013 and correspond to the cycle 12 when the core burn-up and loading conditions are closer to the ones corresponding to the KWU measurements. Each measurement consists of sets of 16 channels in different levels and different strings. The measurements are divided in 4 sets of 16 measurements;

Fa 1, strings; (N20, N22, N24, N27)
Fa 3, strings; (N38, N40, N41, N47)
Fa 4, strings; (N06, N08, N11, N15)
Fa 6, strings; (N51, N54, N56, N57)

The measurements considered in the JTFS analysis cover the selected SPND signal behaviour in the vicinity of the migrating fuel assembly CF06 during the cycles C09 –C12 (Figure 49) before the IRI occurrence at EOC 12 (Figure 50-Figure 51), i.e. strings N31, N15, N38 and N41.

The SSA analysis investigates the sensor structures, as shown in the upper part of Figure 48, for raw data pre-processing, frequency observations and detrending signal studies, for the data coming from the cycle C09.

All data sets are divided into three regions for the solution of IRI problem, core mid and periphery behavior, taking the cycle C09 as reference. All data sets are recorded during the physical tests of neutron instrumentation calibration at the very start of the cycle. The SPND data are also supplemented by date from ionization chambers and reactor cover accelerometers. The data sets corresponding to the noise plant measurements and the detector arrangements are described in more detail in an internal WP4 Progress Report on subtask T4.2.3 (Stulik et al., 2020).

It is necessary to realize the difference between the measurements at the KWU units and the VVER1000 data sets. While the KWU data sets were recorded at various core burnup, the VVER 1000 data were recoded during physical neutron instrumentation tests at BOC in four consecutive cycles, each starting with fresh fuel load.
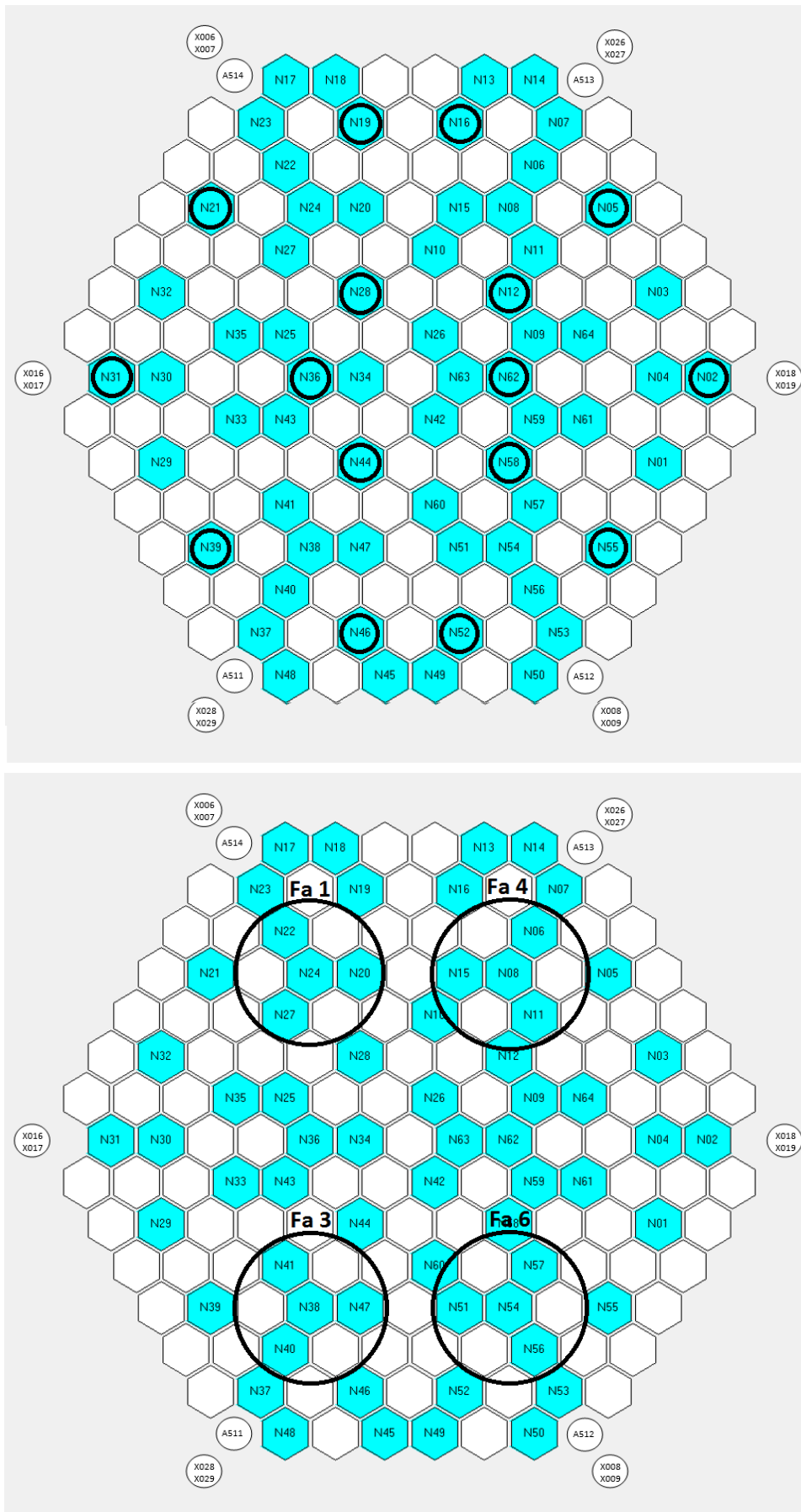
Figure 48: Radial layout of the detectors considered in the analysis.
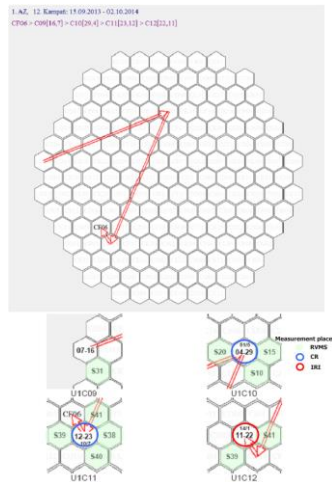
Figure 49: Fuel assembly CF06 migration during the fuel cycles C09 – C12.
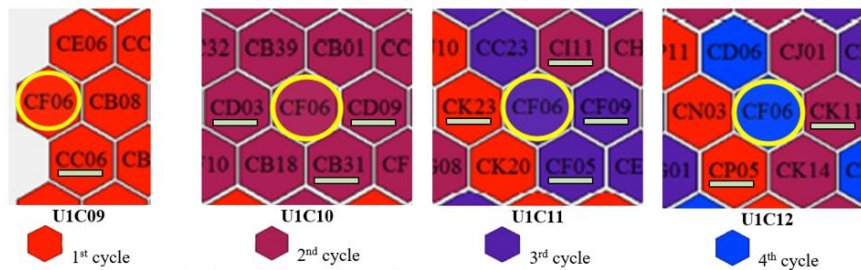
Figure 50: Burn-up condition of the fuel assemblies in the CF06 vicinity in U1C09 – U1C12.
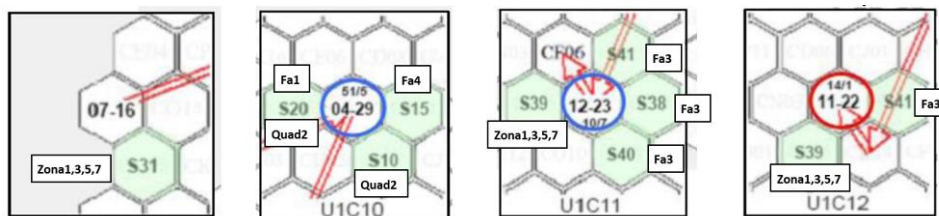
Figure 51: Selection of SPND in the close vicinity of the migrating fuel assembly CF06 in U1C09 – U1C12.

4.4.2 FFT analysis

4.4.2.1 APSDs

This section presents and describes the APSDs calculated. Firstly, we present the APSDs of the four sensors for the sixteen strings considered. In the second place, we present the APSDs corresponding to the sixteen detectors at level 5.

4.4.2.1.1 APSDs in the same string

Figure 52 to Figure 55 present the APSDs for the in-core detectors in the same radial position (four levels per string), the radial positions considered are:

Fa 1, strings; (N20, N22, N24, N27)
Fa 3, strings; (N38, N40, N41, N47)
Fa 4, strings; (N06, N08, N11, N15)
Fa 6, strings; (N51, N54, N56, N57)

Figure 56 presents the RMS values at the axial levels 3, 5 and 7 relative to the lowermost level (axial level 1) for the configuration sets Fa1, 3, 4 and 6 in the 0 – 50 Hz band from the calculated APSDs.

In the analyzed VVER-1000, level 1 is the lowermost level and level 7 is the uppermost level.
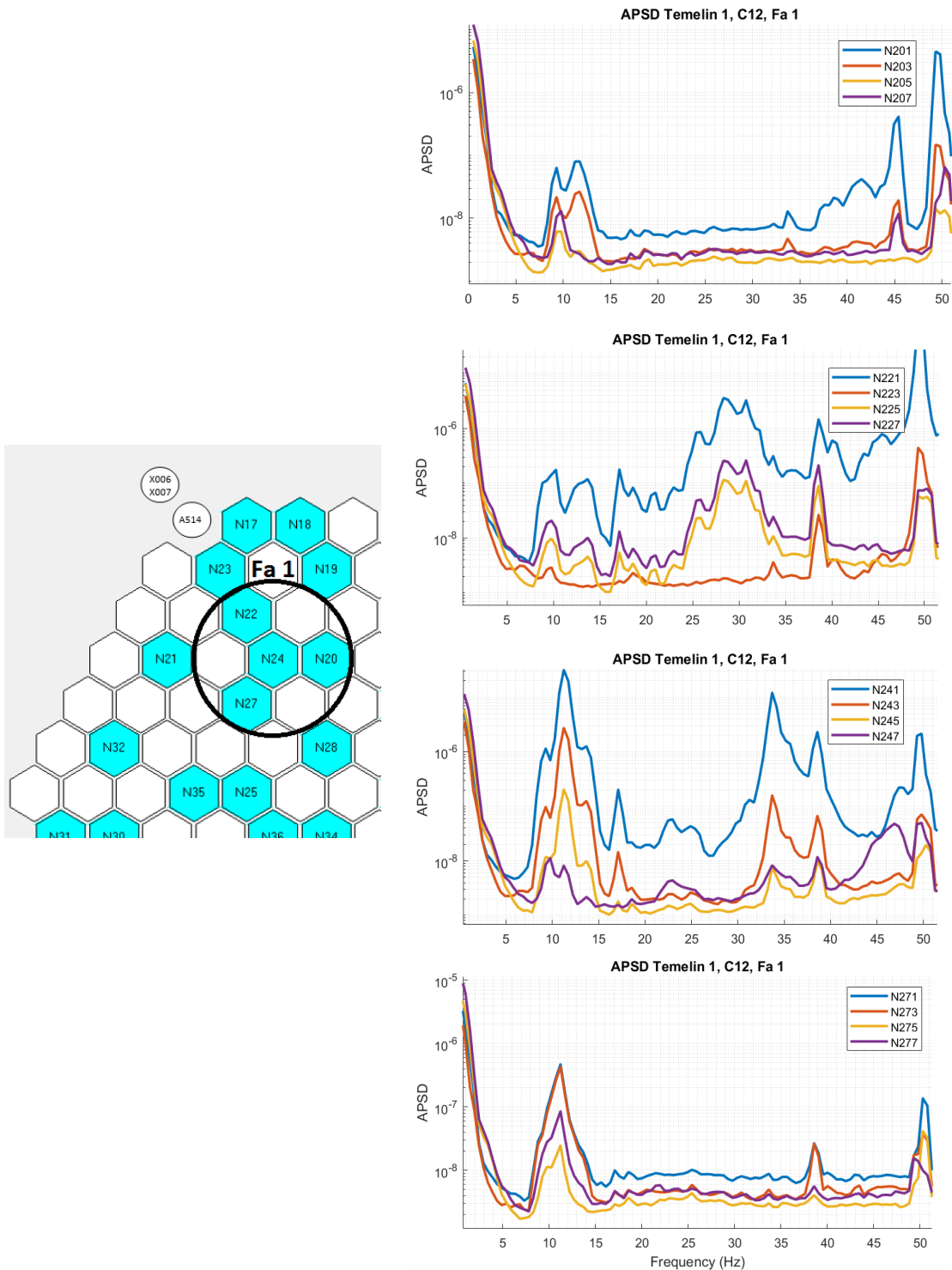
Figure 52: APSDs of the sensors in the strings N20, N22, N24, and N27 – from top to bottom, respectively – and at levels 1, 3, 5, 7.
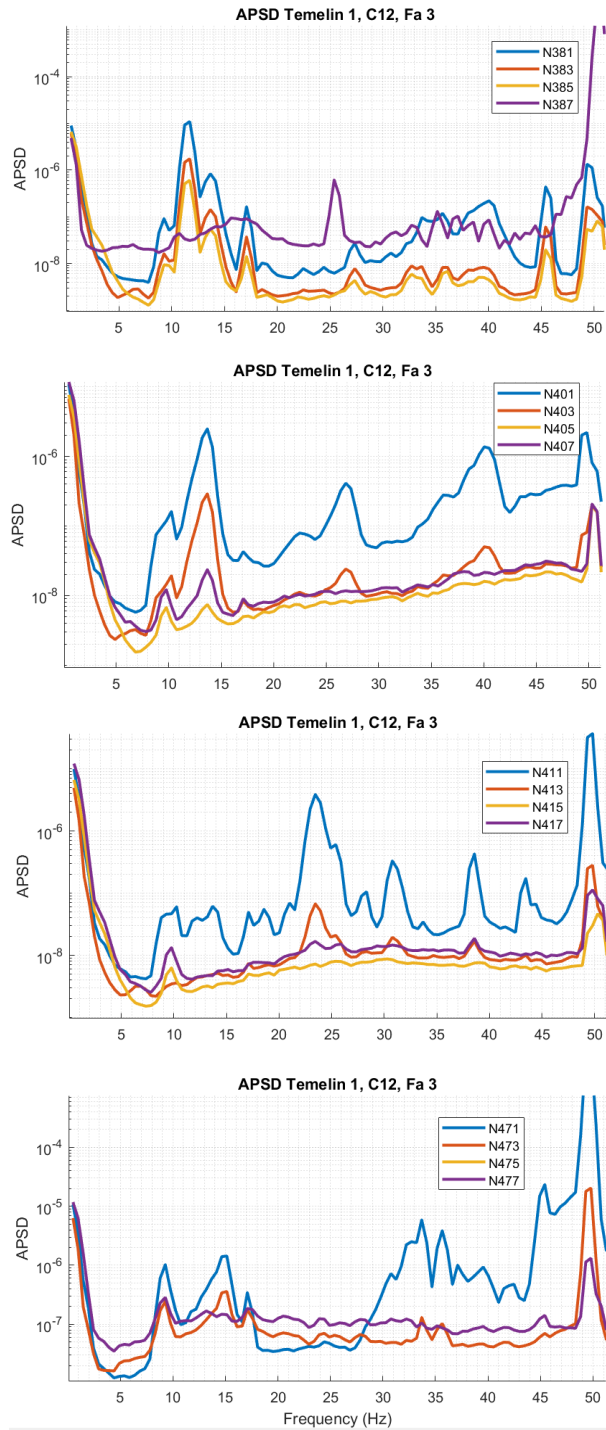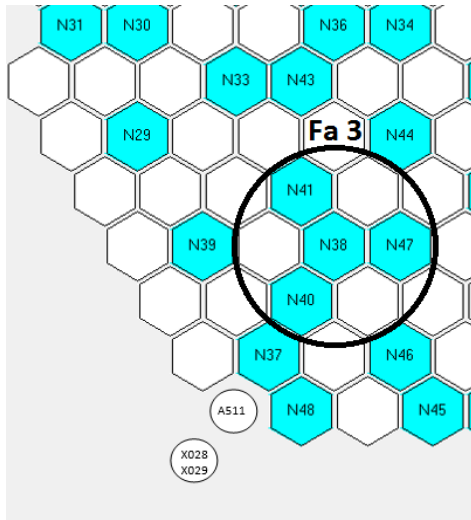
Figure 53: APSDs of the sensors in the strings N38, N40, N41, and N47 – from top to bottom, respectively – and at levels 1, 3, 5, 7.
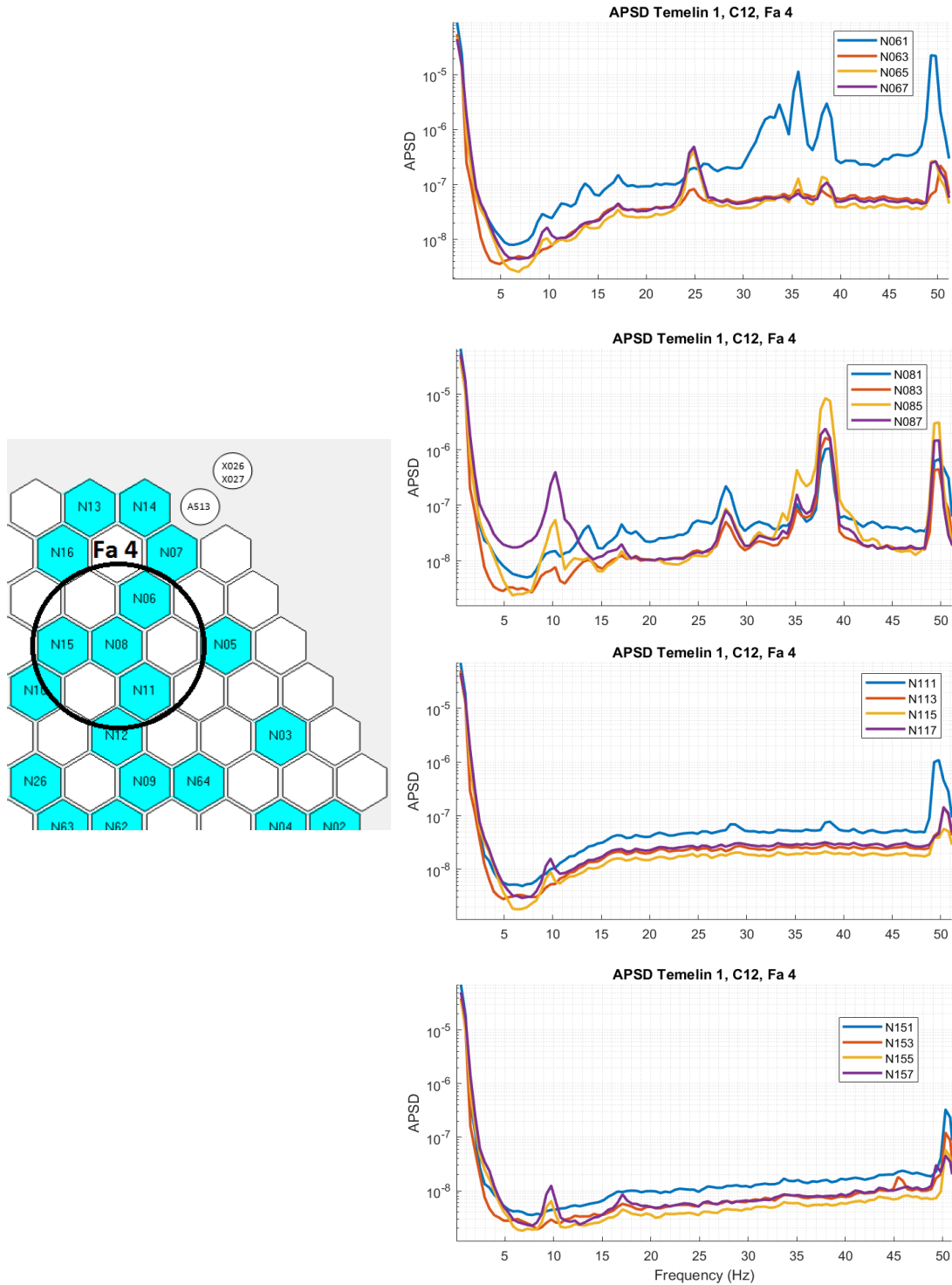
Figure 54: APSDs of the sensors in the strings N06, N08, N11, and N15 – from top to bottom, respectively – and at levels 1, 3, 5, 7.
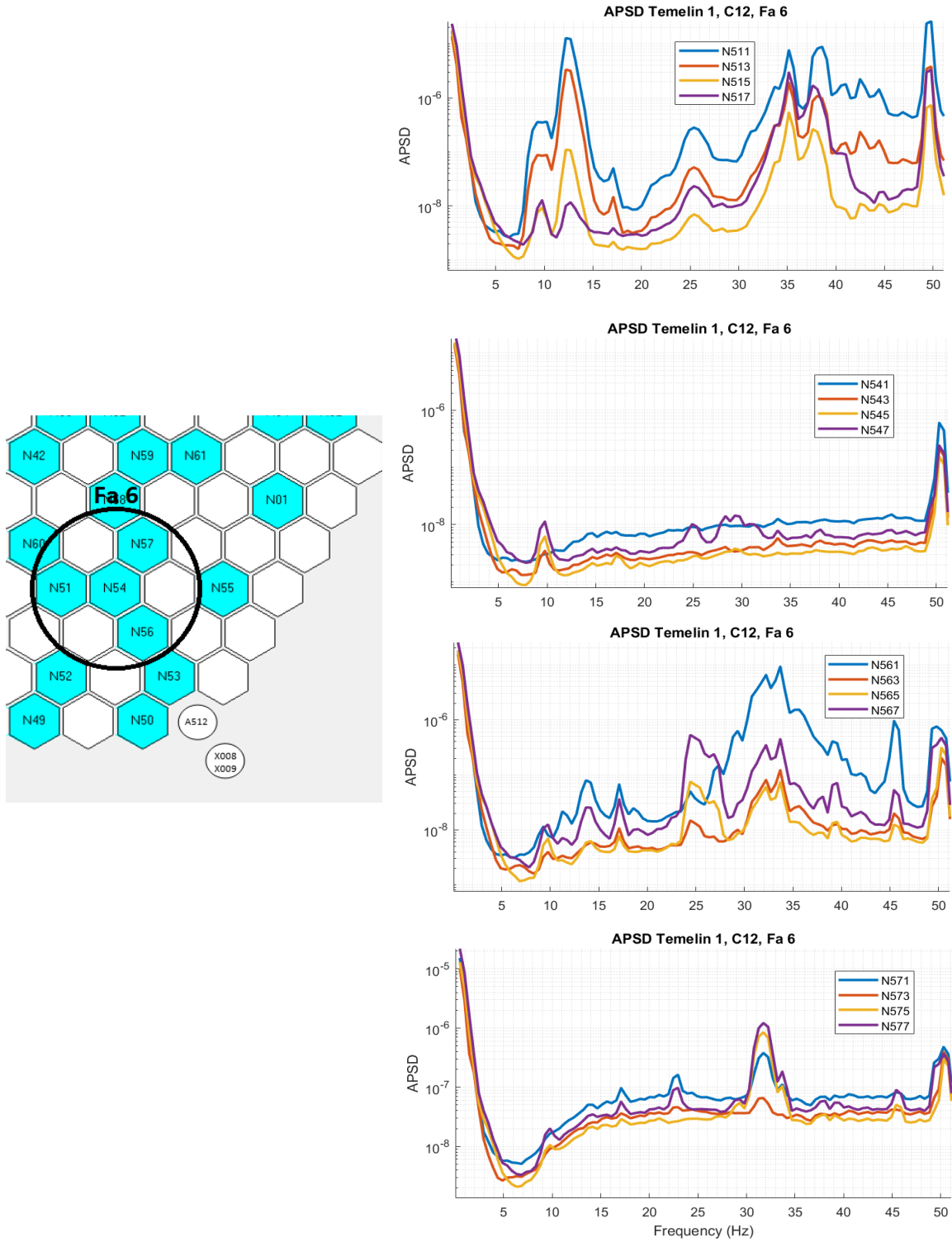
Figure 55: APSDs of the sensors in the strings N51, N54, N56, and N57 – from top to bottom, respectively – and at levels 1, 3, 5, and 7.
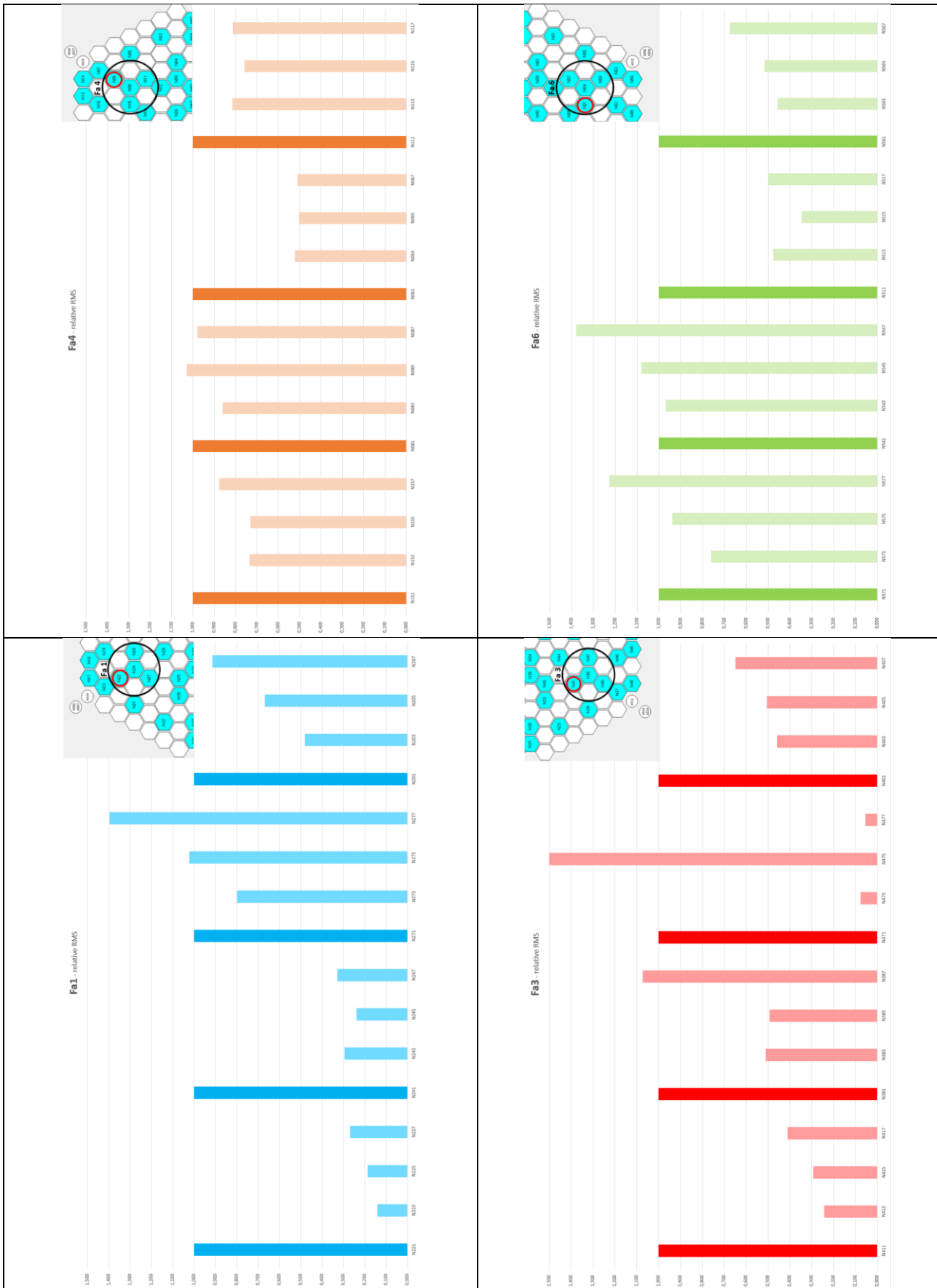
Figure 56: RMS values of 3,5,7 axial levels 3, 5 and 7 in relation to the lowermost level (axial level 1) for configuration sets Fa1, 3, 4 and 6 in the 0 – 50 Hz band from the calculated APSDs.

4.4.2.1.2 APSDs in the same axial position

Figure 57 presents the APSDs for all the in-core detectors in the same axial position, at level 5 (16 detectors).
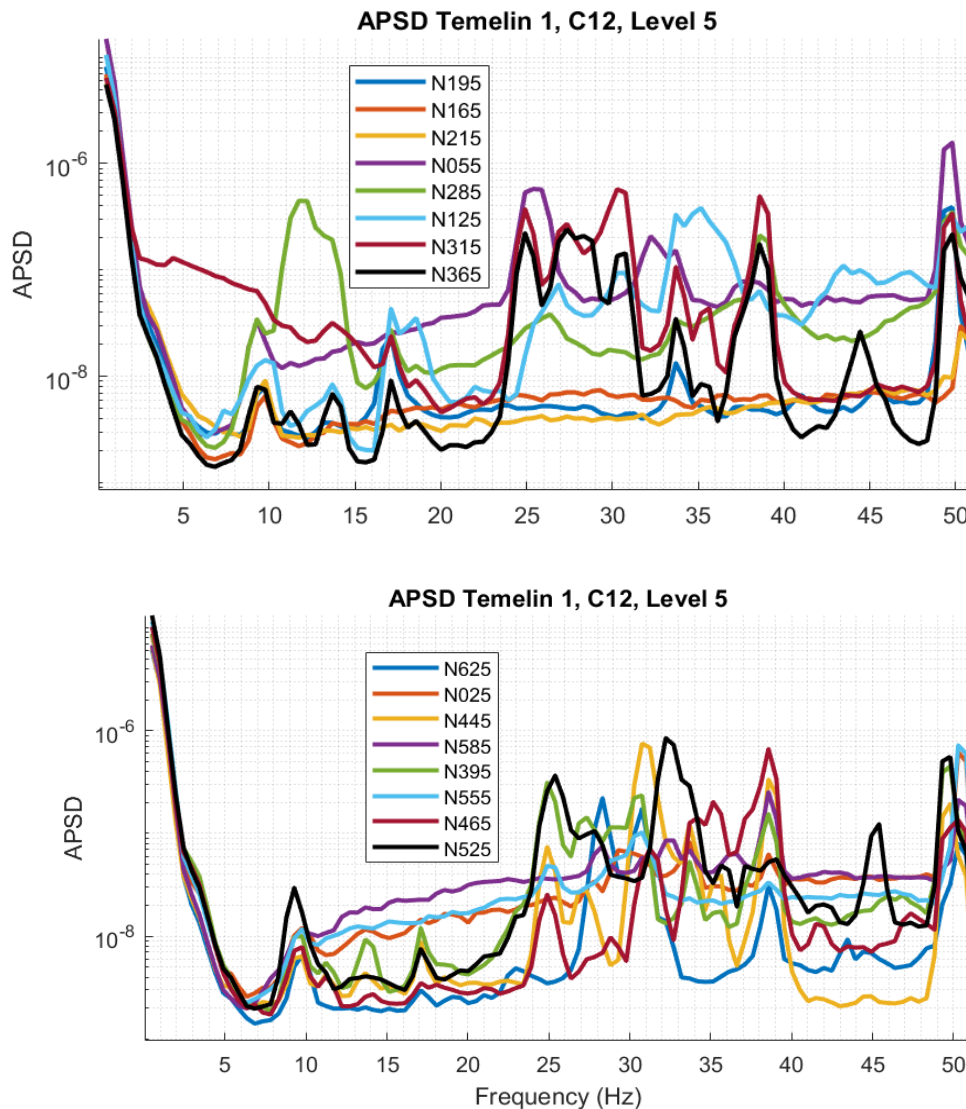
Figure 57: APSDs of the 16 detectors at level 5. To make the figure more readable, the 16 APSDs are divided into two graphs.

Some general observations on the APSDs are summarized below:
- The profiles of the APSDs are very similar to each other below 7 Hz.
- Above 7 Hz, the number of resonances presented in each APSD is different and depends highly on the location.
- However, for the APSDs of the detectors in the same string, we can observe regular patterns in the axial analysis – see Figure 52 to Figure 55.
- Regarding the content of the signal, most of the energy signal is located at low frequencies below 2 Hz, but the content generally increases above 7 Hz due to (a) the resonances and (b) the background noise that increases in amplitude in many cases – see Figure 52 to Figure 57.
- Regarding the location of the signal energy, we can state that out of the 63 monitored SPNDs, in almost 90% of the cases, the relative RMS value is the highest at the lowest level (i.e. level 1), as shown in Figure 56 for the 0 – 50 Hz band from the calculated APSDs. This conclusion is also confirmed by the JTFS spectrograms in Figure 61 – Figure 63, in accordance with the results given in the deliverable D3.3 (Stulik et al., 2019).

- We can observe a series of common resonance peaks in the axial analyses. Nevertheless, in the radial analysis, we can see that the resonances have a high dependency on the locations, except with the resonance at 9.5 Hz that is present in all the APSDs.

4.4.2.2 Coherences and Phases

These sections present and describe the coherence and phase relationships considered representative. Firstly, the coherence and phase between detectors in the same string are considered. Thereafter, detectors in different radial positions for both in-core and ex-core detectors are analyzed. All coherences and phases are represented up to 50 Hz.

4.4.2.2.1 Coherence and phase relationships in the same string

The coherence and phase relationships are presented between pairs of sensors in the same in-core radial position. Figure 58 presents the coherences and phases in only one radial position (same string), taking as reference the detectors at level 1. The strings considered are: N22, N41, N15, N57. Note that Lv 1 and Lv 7 are the lowermost and the uppermost levels, respectively, in the analysis.
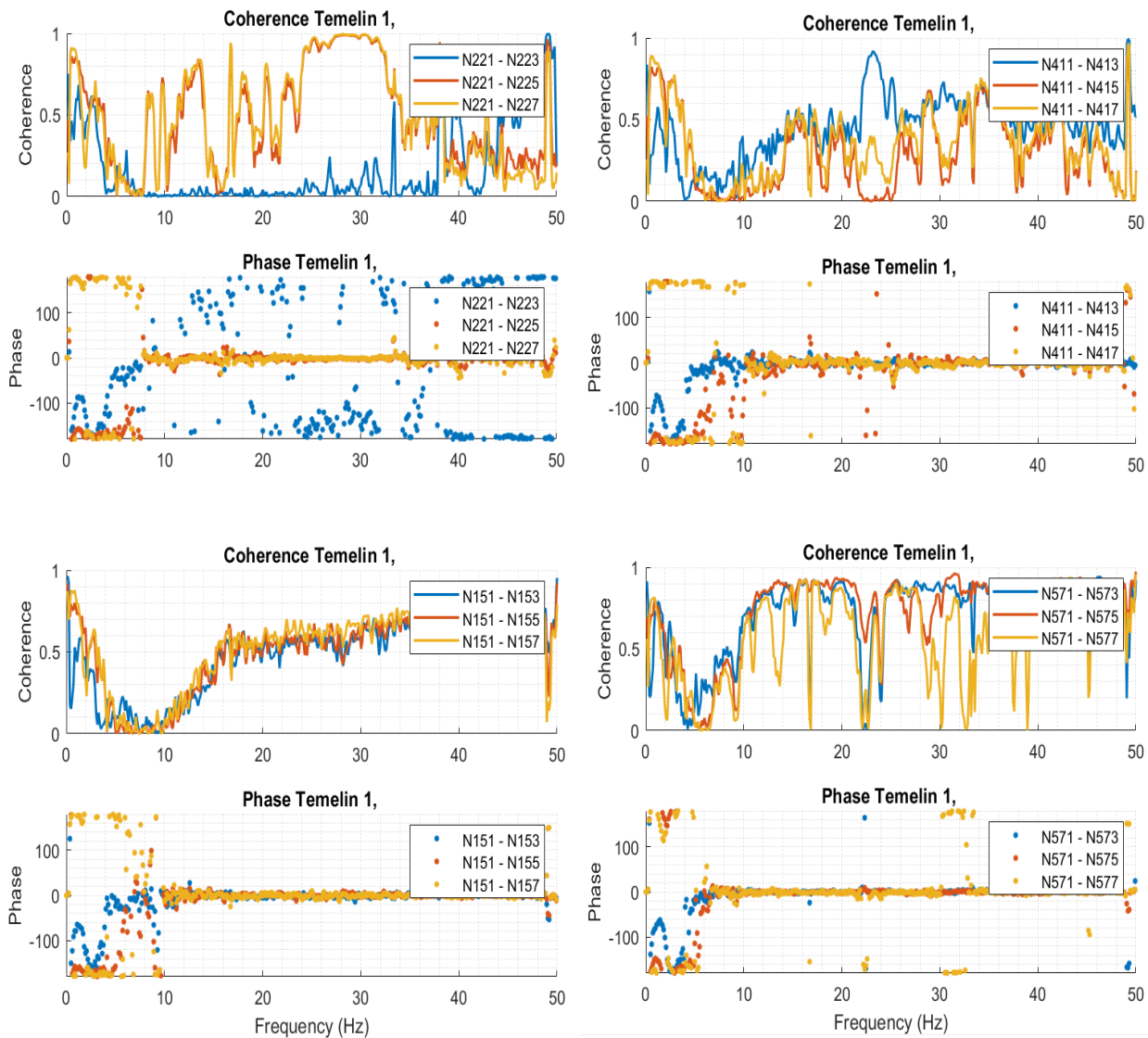
Figure 58: Coherences and phases in the strings N22, N41, N15, N57 (the last index in the legend represents the axial level).

4.4.2.2.2 Coherence and phase relationships at the same level

In this subsection, we present the coherence and phase relationships between different in-core radial positions.

In Figure 59, three sets of detectors are considered, each set highlighted in a specific colour: blue, red, or green, and the reference sensors taken in the upper left side for each set. The coherence and phase relationships calculated between the reference detectors and those located on the opposite side within the same set (i.e. having the same colour) are represented in Figure 60.
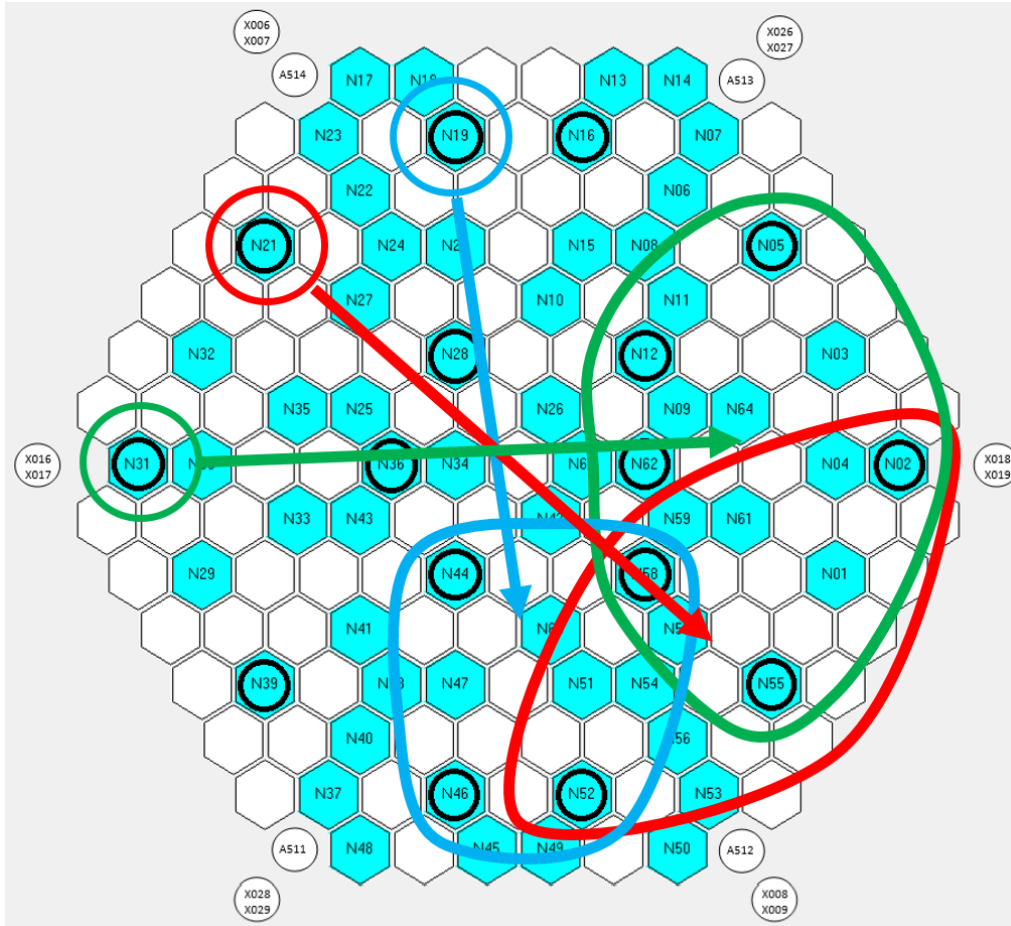
Figure 59: The three sets of detectors used for the analysis of coherence and phase between opposite detectors.
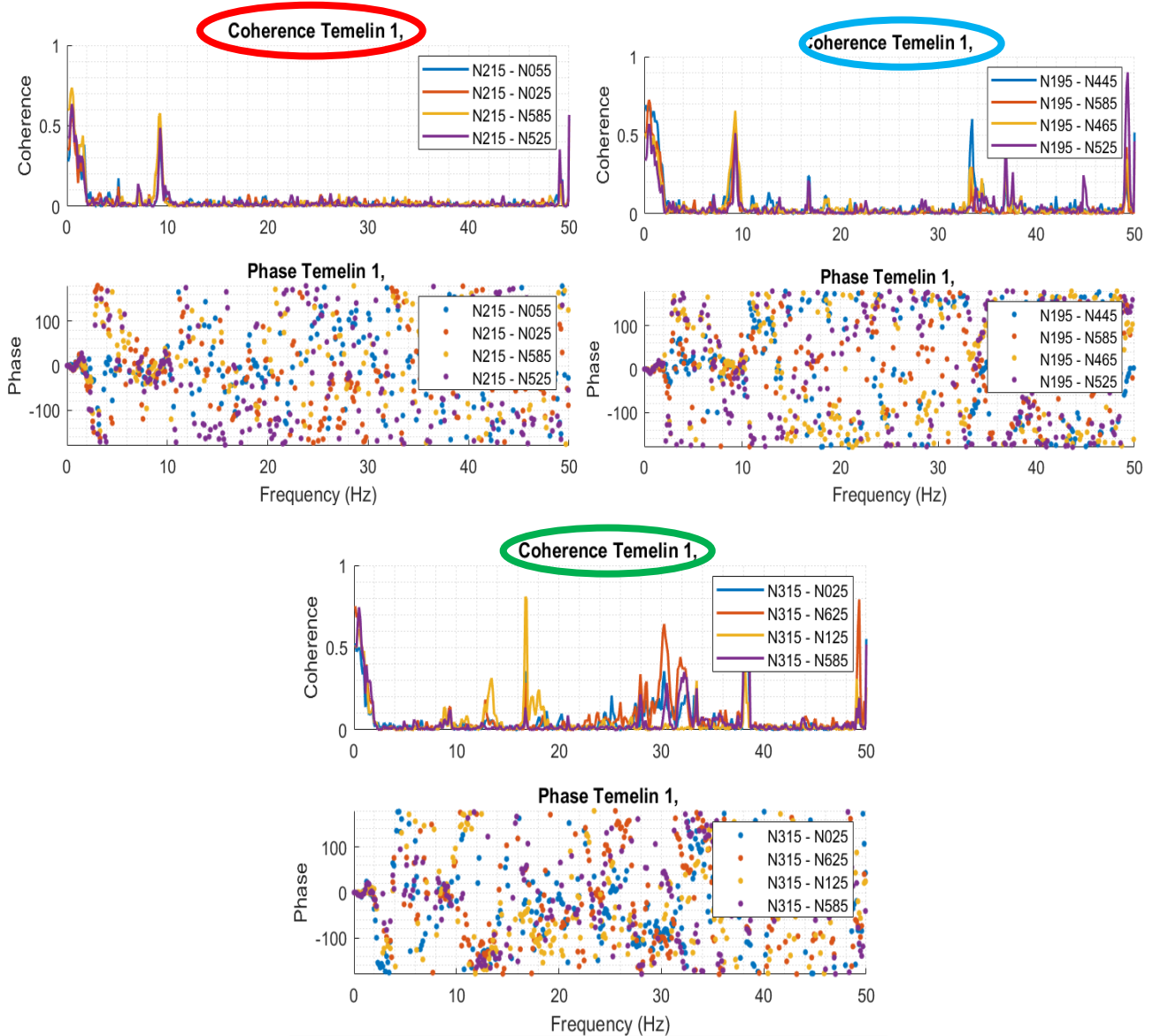
Figure 60: Coherences and phases between detectors in opposite regions for the three sets considered.

Some general observations on the coherences are summarized below, based on Figure 58, Figure 59 and Figure 60:

- In all the axial analyses given in Figure 58, at low frequencies, the linear phase observed in the KWU reactor is not visible. In the present case, an out-of-phase relation up to 9 Hz exists. Above 9 Hz, the detectors are in phase, like in the KWU case.
- In the case of the radial analysis given by Figure 60, both sides of the reactor are in phase for the resonances at 1 Hz (thermal-hydraulic) and 9 Hz. For the remaining frequency range, the phase is random.
- For the green set of detectors phase, a phase relationship at 13 Hz and a high coherence at 13 Hz, 18 Hz and around 30 Hz are visible – see Figure 60 lower part.

4.4.3 JFTS analysis

This section discusses possible aspects for subsequent processing of time data in the successive C09 – C12 cycles. The JTFS spectrograms have XYZ coordinates in [Hz] for frequency, in [s] for time, and for PSD amplitude in [1/Hz^2] given in dB. The PSD sequences in the 0 - 150 Hz range are

processed with sliding Hanning window in time intervals of 10 sec with resulting frequency resolution of 100 mHz. It should be noted that X-Z JTFS spectrograms are plotted in their maximum amplitude values, so that we can see the frequency dispersion of the peaks through the whole time of record. A more detailed description can be found in the internal WP4 Progress report (Stulik et al., 2020).

IRI sequences IrD

This part describes the nature of the time data measured during the fuel assembly CF06 migration through the core. The range of JTFS view includes selected SPND signals primarily in the vicinity of the migrating fuel assembly CF06 during the cycles C09 –C12 (Figure 61) before the IRI occurrence at EOC C12 (Figure 62 and Figure 63), i.e. strings N31, N15, N38 and N41.

2D spectrograms of the selected relevant fuel assemblies from the CF06 assembly vicinity are presented in Figure 61 to show the spectral dynamics of the core behavior in the lowermost axial level (i.e. level 1) during cycles C09 – C12. In most cases, this level shows the largest number of neutron field transients with respect to the imbalance of thermal and hydrodynamic conditions at the entrance to the core. This space can thus be a source of perturbations which are further moving along the height of the axial neutron field profile of the reactor.

It is possible to observe the transient phenomena during the 12 minutes measurement intervals in these JTFS spectrograms. In this way, it is possible to obtain substantial knowledge before processing the time data and also before the subsequent training of DNN aimed at finding the possible symptoms of the IRI phenomena.

Middle core InD

Middle core time series datasets are specified by fuel assembly configuration sets Fa1, Fa3, Fa4 and Fa6, the location of which are given in lower part of Figure 48. The JTFS 2D spectrograms on all levels of the N41 string in Figure 63 supplement the APSDs computed in cycle C12 and shown in Figure 52. It can be seen that the lowermost level has the highest RMS value over the whole frequency range – see Figure 56. We can see on Figure 64 the same situation as in the previous C11 cycle, with a similar relation as to the RMS values of the string levels but with different spectral PSD signatures (magnitudes, frequencies) during the time record.

Core periphery PeD

The core periphery behavior can be investigated via the time series datasets of the fuel assembly configuration sets AccXnnInn1-4, of which the location and the description of the signal behaviour are given with great detail in the Deliverable D3.3 (Stulik et al., 2019).
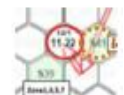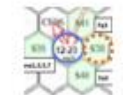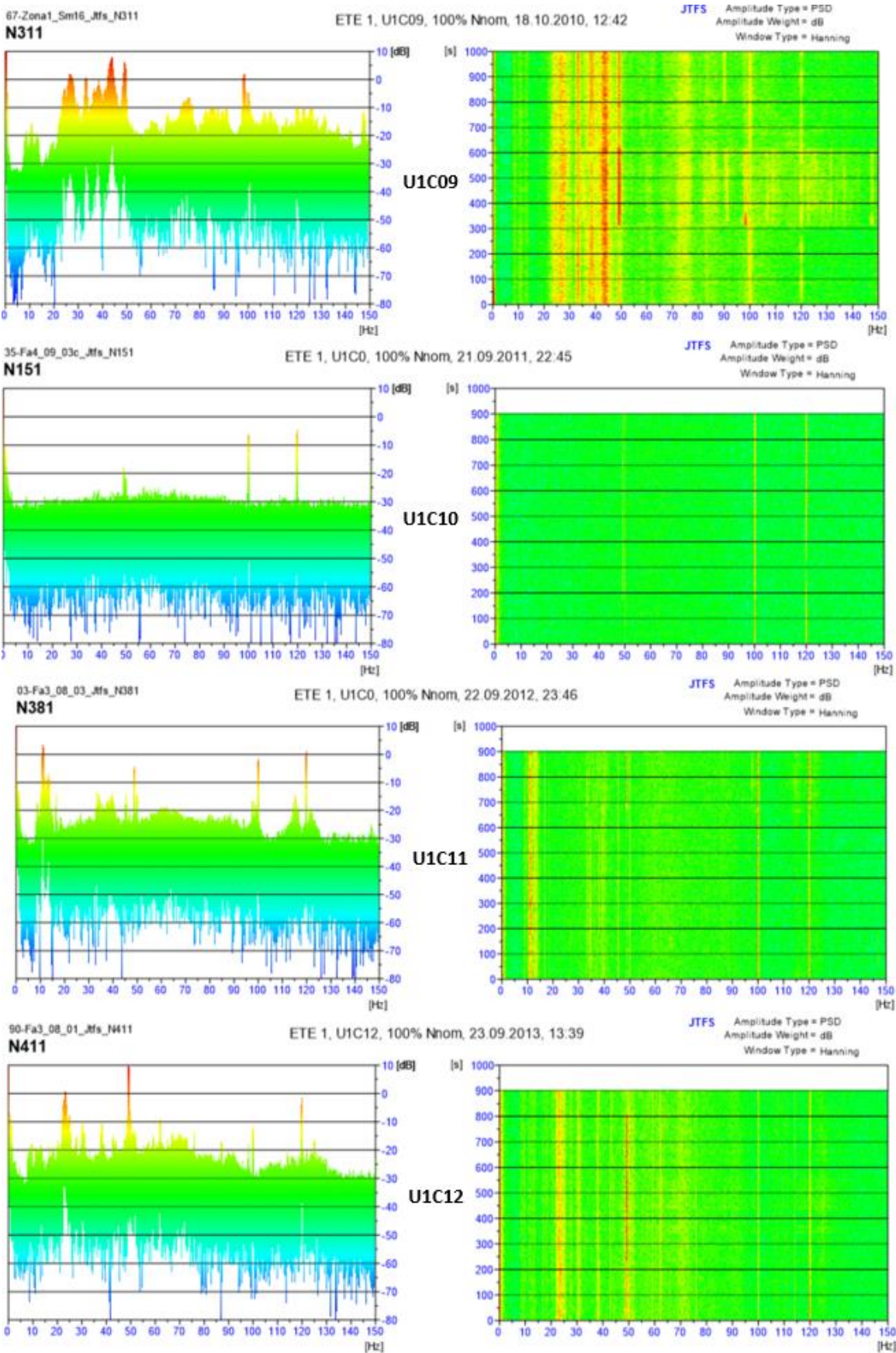
Figure 61: 2D spectrograms of the selected relevant fuel assemblies from the CF06 vicinity in the cycles C09 – C12.
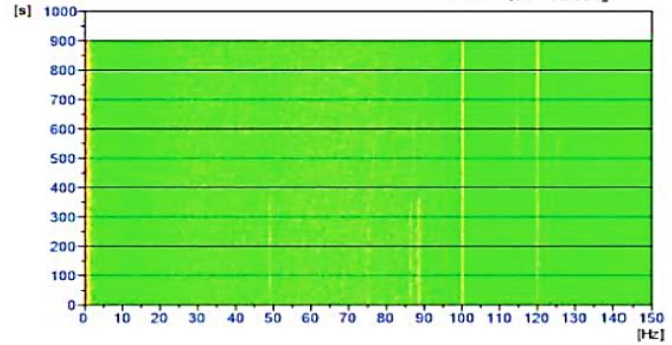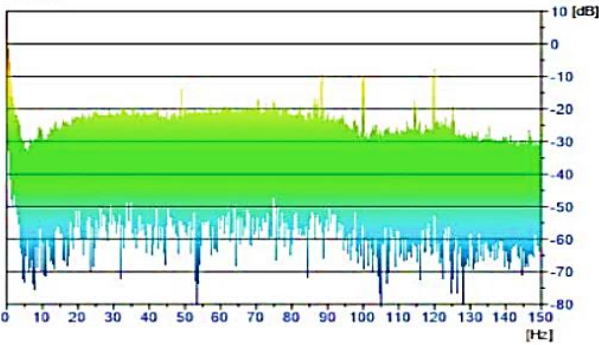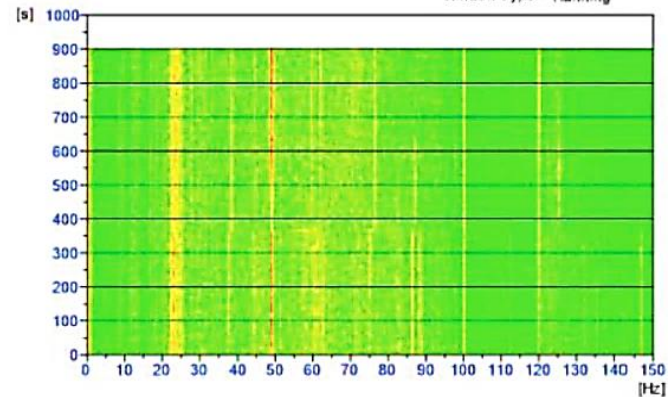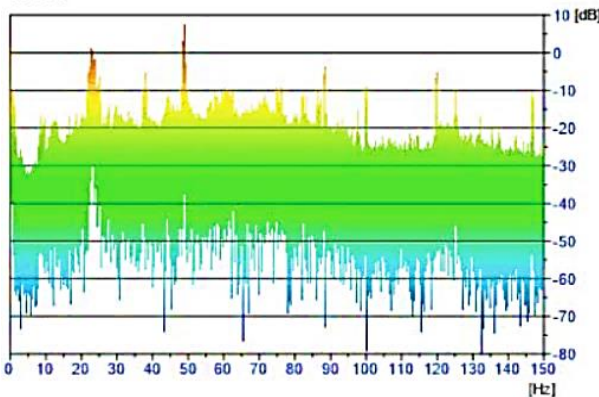
Figure 62: 2D spectrograms of N41 string in the C11 cycle.
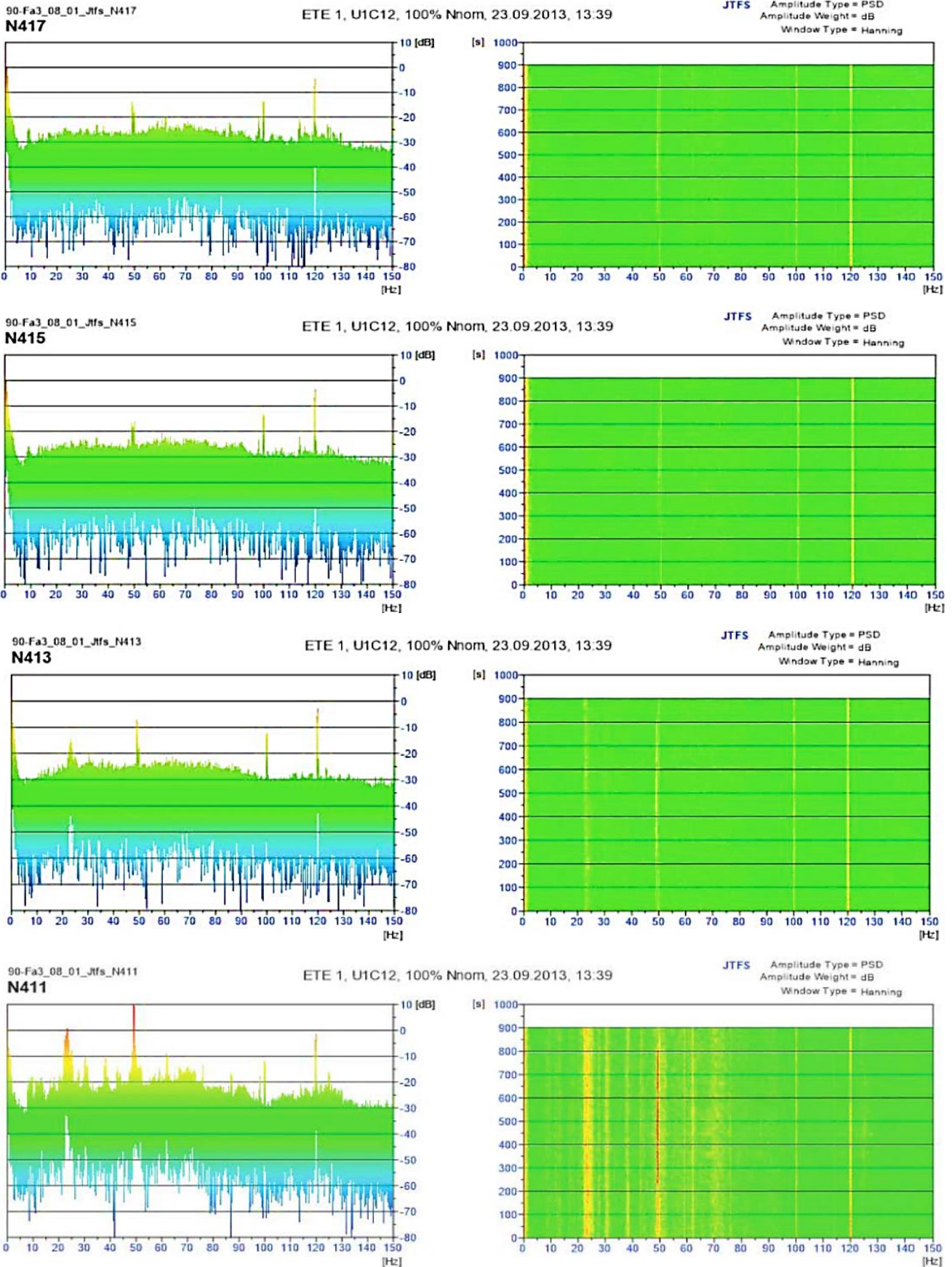
Figure 63: 2D spectrograms of N41 string in the C12 cycle.

4.4.4 Singular Spectrum Analysis

As mentioned in Section 4.4.1, the data used for the SSA investigation comes from the cycle C09. The data are in their initial form, i.e. they are not normalised and are in an unconditional form. Nevertheless, they contain all substantial time and frequency domain elements suitable for detrending purposes.

4.4.4.1 Cycle C09 and the SSA methodology

The data come from the excel files 69-Zona3.xlsx, 71-Zona5.xlsx, 75-Zona1_X_N.xlsx and 77-Zona7_X_N.xlsx and were placed in the zip file U1C09.zip made available to the CORTEX partners.

It is important to point out that the sampling frequency is 1000 Hz and the duration 15 min.

In Figure 64, we notice a trend in the in-core rhodium Self Powered Neutron Detector sensors (SPND) before achieving a steady state.

Also, Figure 64 shows that the sensors N623 and N393 present a specific behaviour in comparison to the other SPND sensors.

4.4.4.2 Detrending with the SSA methodology

In order to analyse the neutron noise, it is necessary firstly to detrend the signal acquired online. In Figure 65, we can see the presence of a trend for the sensor N315. Thus, we choose to apply the SSA methodology.

Figure 66 gives the evolution of the eigenvalues. The ideal grouping of eigenvectors is in pairs, where each pair has a similar eigenvalue, but differing phase which usually corresponds to sin-cosine-like pairs. Hence, from the shape of the leading singular values, we affect the first four factors, that is to say not paired values, to the trend.

In Figure 67, we see the reconstruction using the first four factors for the trend (S1). We can visualize the result in Figure 68 and at last, by difference between the raw data and the trend, the neutron noise estimation in Figure 69.

4.4.4.3 Raw data preprocessing

The overview of the whole Power Spectral Density Neutron Noise demonstrates:
- That the power spectrum still shows a 1/f spectral distribution at low frequencies below around 2 Hz.
- The presence of the 50 Hz frequency with its multiple (e.g. 100, 150, 200, 250, 300, 350, 400 and 450 with a high energy)
- A high energy at frequency 120 Hz.

In Figure 70, we can see that the frequencies 50 Hz and harmonics associated appear on all the signals except on the ex-core signals and the in-core sensor N623. At this point, it is necessary to notice that at 50 Hz the third harmonics of main circulation pump appears with its 1000 revolutions/min. Except the 120 Hz frequency, the range of the spectra to be studied lies between 0 and 50 Hz.

Doing a Singular Spectrum Analysis on such an input signal will highlight on the first factors these features. Indeed, the eigenvalue profile is related to the power spectrum ordered from the largest value to the smallest one. Such features are nevertheless not interesting in the study of the frequency structure. The SSA was thus carried out on a filtered signal instead. We applied a high pass filter

with a cut frequency equal to 2 Hz and several stop band to remove the 50 Hz and the harmonics – see Figure 71.

The record duration, around a quarter of an hour, with a sampling frequency equal to 1 kHz give good conditions for detecting the very low frequencies with FFT. The range under 2 Hz thus allows detecting the effect of the delayed neutrons – see Figure 72.

In fact, we see that, except for the frequency at 120 Hz, the range of interest for the time being is between 2 Hz and 50 Hz.

4.4.4.4   Frequency observation up to 50 Hz

We can see in Figure 71 (as well as in the overview given in Figure 70) that in fact the frequency range of interest is below 50 Hz. Thus, it is possible to decimate the signal by a factor 10 without losing information (except the frequency at 120 Hz) for further analysis.

Figure 73 shows the Power Spectral Density on several frequency ranges after the decimation:
*   Global: all the frequencies, from 0 to 50 Hz.
*   Part-1: the very low frequencies, certainly the delayed neutron frequency range.
*   Part-2: the range of interest according to us.
*   Zoom-part-2: a zoom on the part-2.

In Figure 73, we can observe the presence of a frequential spreading (cf. part-2 and zoom-part-2). In fact, there is certainly a shift of the frequency values in time. It is thus important to keep in mind this non stationarity for the physical analysis.

4.4.4.5   SSA analysis on the detrended signal

At this stage, we have detrended our signal and reduce the range of the spectral range to improve our analysis. We will do again the SSA approach to describe the spectral content. Actually, we will do two SSA, as explained in the two following sections.

The first SSA on the pre-processed signal

As expected, the leading eigenvalues – see Figure 74 – shows now only eigenvectors organised in pairs, there is no trend any longer, only oscillations. We decomposed the signal in 300 components but only 60 have been represented. Figure 75 shows the correlation matrix which propose to keep about twenty eigenvalues to reflect the maximum frequency response. In order to describe the spectral content, we first realise a classification of the components in 10 classes marked by a colour in Figure 76. This classification is similar to the so-called correlation clustering of variables used in multivariate statistics. We use the Ward criterion for the agglomerative algorithm.

Then, the power spectrum of every class was estimated employing Welch's method and we compared the spectra by superposition in Figure 77 with the same colours of Figure 76. The SSA improves the resolution of the spectrum as we can see in Figure 78 where we have superposed only four classes to facilitate the visualisation. We did a zoom of the spreading – see Figure 73 zoom-part-2.

But, although we calculated the SSA on 300 factors, we have no description of the low frequency domain. The intensity of the power spectrum for the low frequencies is too low and is considered as noise. So, we decided to pre-process again the raw data in order to enhance the low frequencies part of the spectrum and doing another SSA to describe the resulting power spectrum.

The second SSA on the signal with enhanced low frequencies

In order to give larger weights to the low frequencies, we applied a low pass filter on the signal. We defined an order 4 Butterworth filter with a cut off frequency of 20 Hz. We show in Figure 79 the filtering result. We fixed again the number of factors to calculate to 300. We can again keep around twenty components – see Figure 80 and Figure 81 – and do a classification on 10 classes – see Figure 82. But now we can access the spectrum description of the low frequency part. The SSA is able to extract two principal low frequencies – see Figure 83 – which could even be three frequencies, as we can see in Figure 84. We noticed that it was important to ask for many factors in the calculation because, if we calculate only one hundred factors, the SSA extracts only one low frequency as we can see in Figure 85.

Figure 86 and Figure 87 give some details on the separability of the classes. We only represented the classes 1, 4, 7, 10 to facilitate the observation. The position of the classes can be observed in Figure 82 with the same colour code.

4.4.4.6 Summary of the exploratory analysis with the SSA

Before classifying the sensors by neural network, it is important to analyse the power spectrum on a sensor alone for a better understanding. We noticed that:

- It was necessary to detrend the SPND sensor signal with SSA.
- SSA is able to improve the frequency resolution but there are many frequencies certainly due to the non-stationarity of the neutron noise.
- It is necessary to pre-process the data to study the low frequencies by SSA.

We would like now to extract some pertinent parameters from this analysis in order to prepare the step of images creation and sensors cross analysis. Besides, we applied the SSA on the decimated signal on all sensors in order to assess the trend of every sensor. We now have to detrend every sensor and repeat the analysis described above.

UJV data cycle U1C09
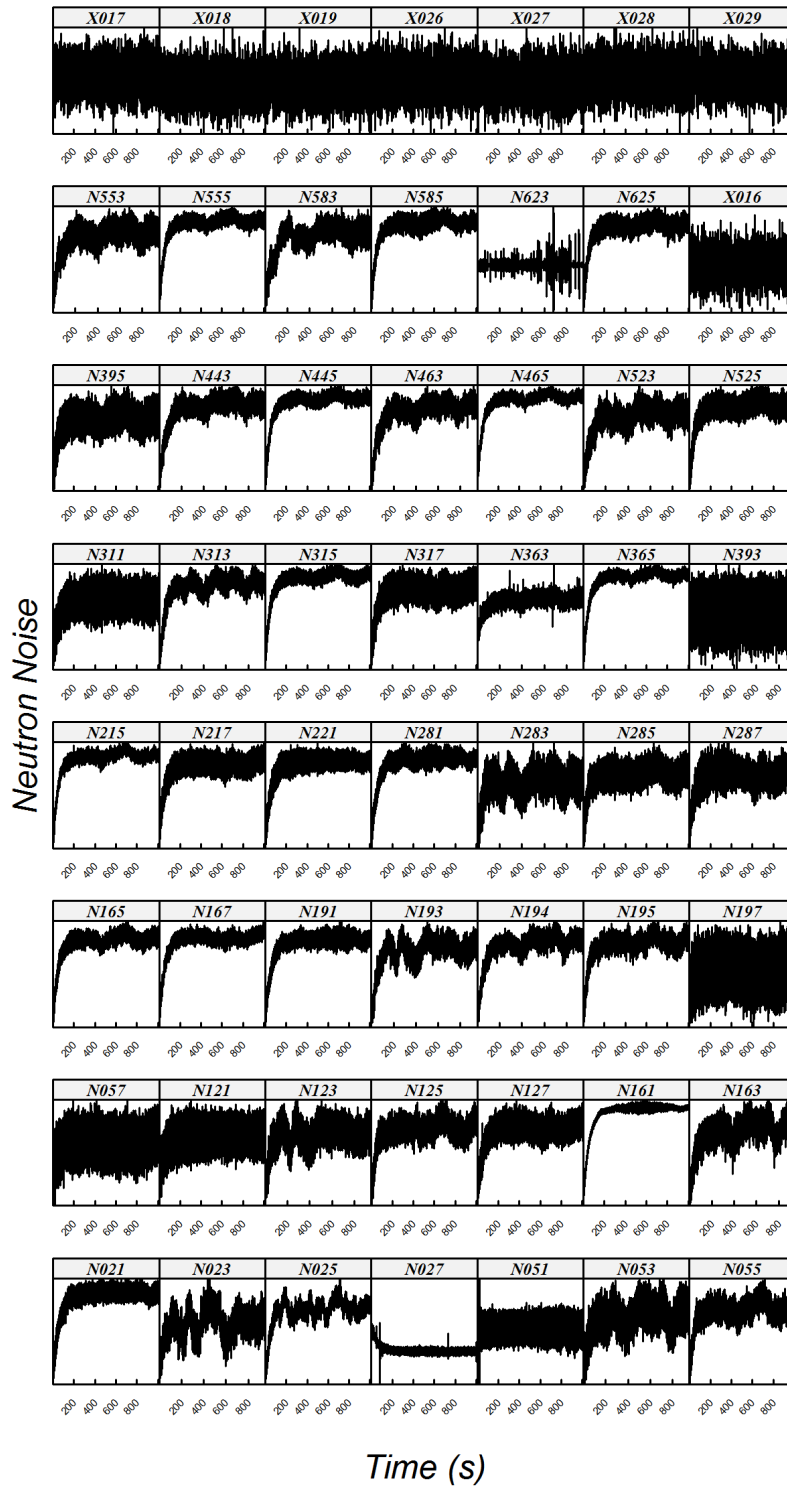
Figure 64: Overview of the cycle U1-C09 in time domain.

Trend of the N315 sensor
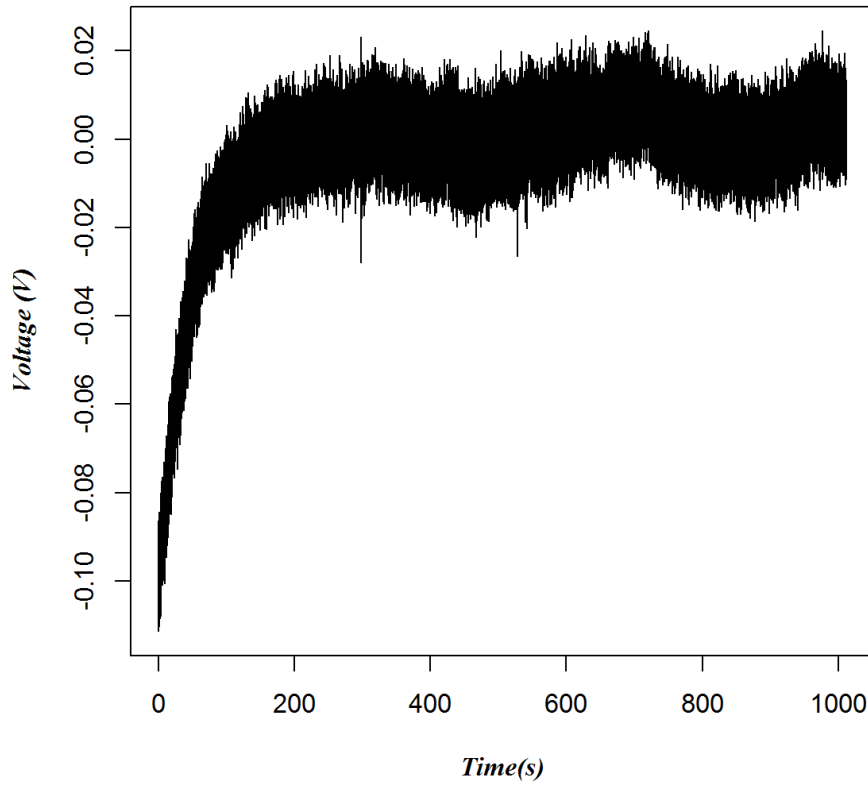
Figure 65: Trend of the N315 in-core-sensor (Self Power Neutron Detector).

Leading singular values
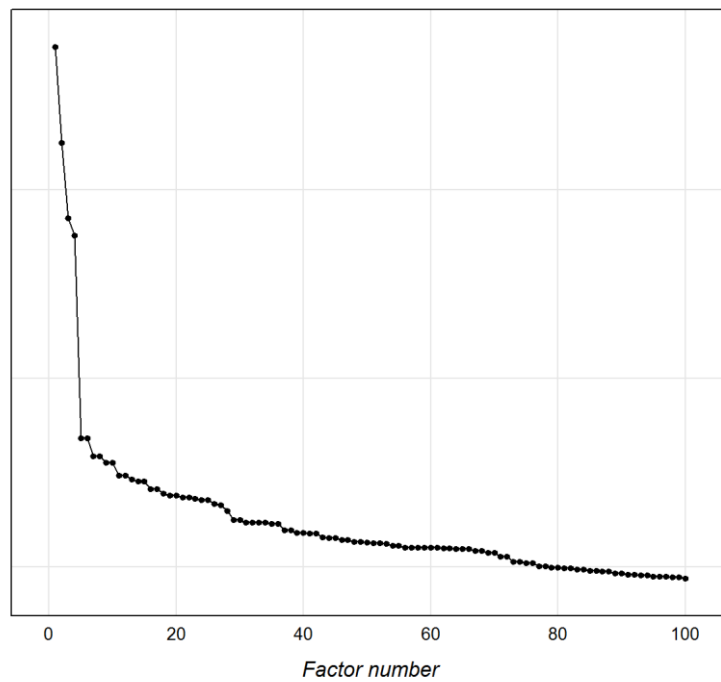
Figure 66: SSA eigenvalues.
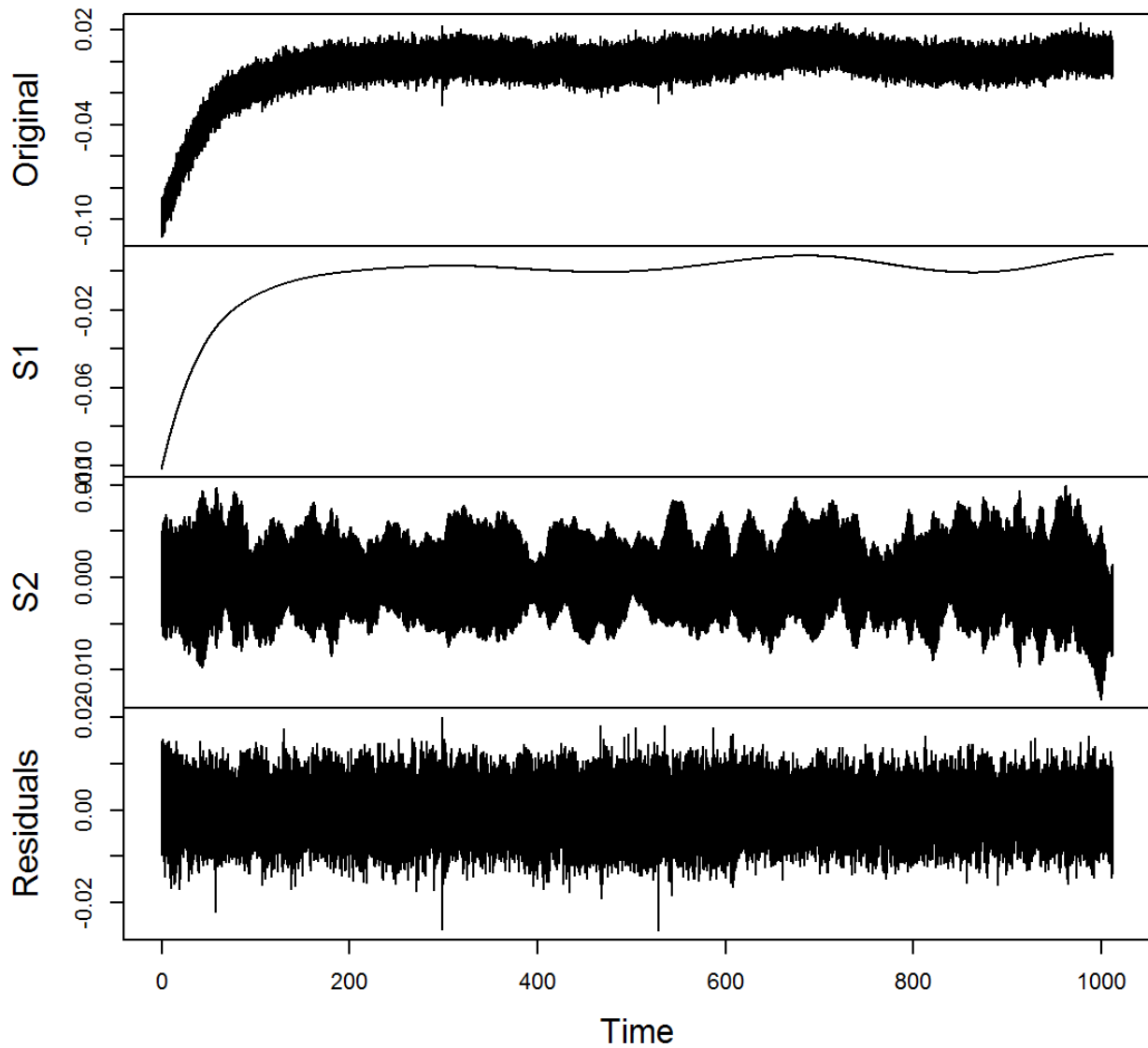
Figure 67: Assessment of the trend by the SSA analysis.

SSA detrending
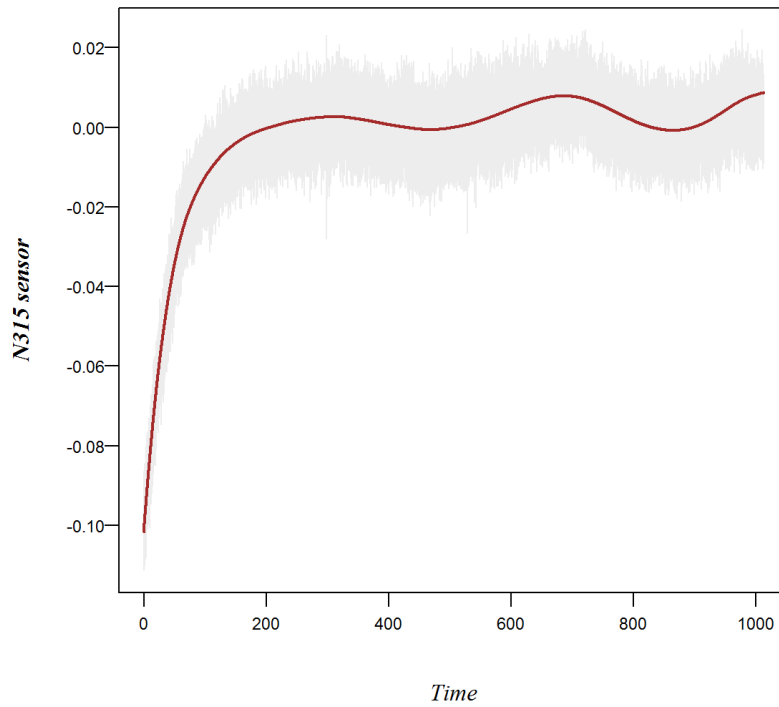
Figure 68: SSA detrending.

Neutron Noise assessment by SSA
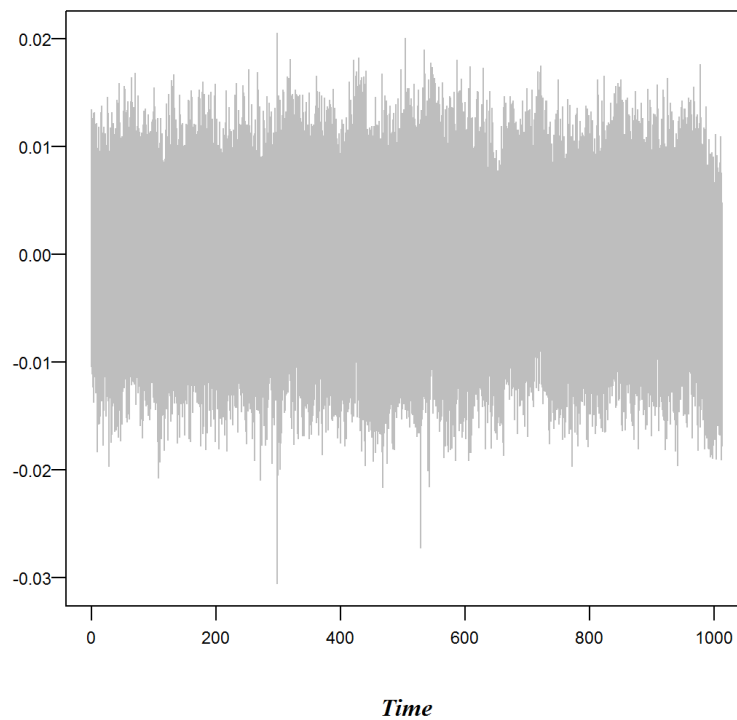
Figure 69: SSA neutron noise assessment.

UJV data cycle U1C09
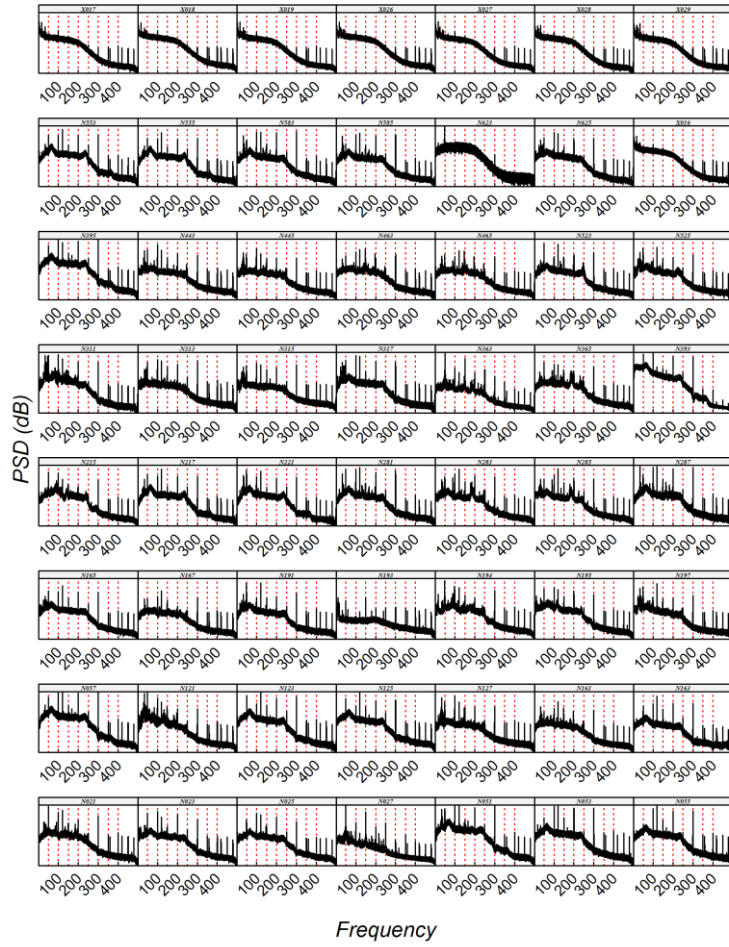
Figure 70: Overview of the cycle U1-C09 in the spectral domain.
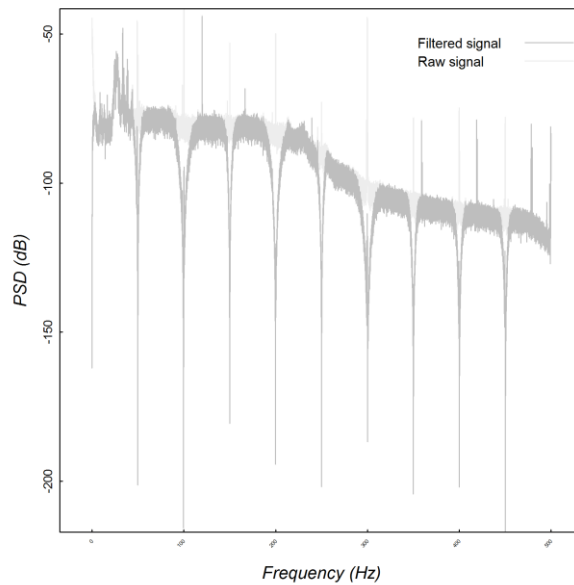
Figure 71: SSA applied on the filtered signal.

UJV data cycle U1C09
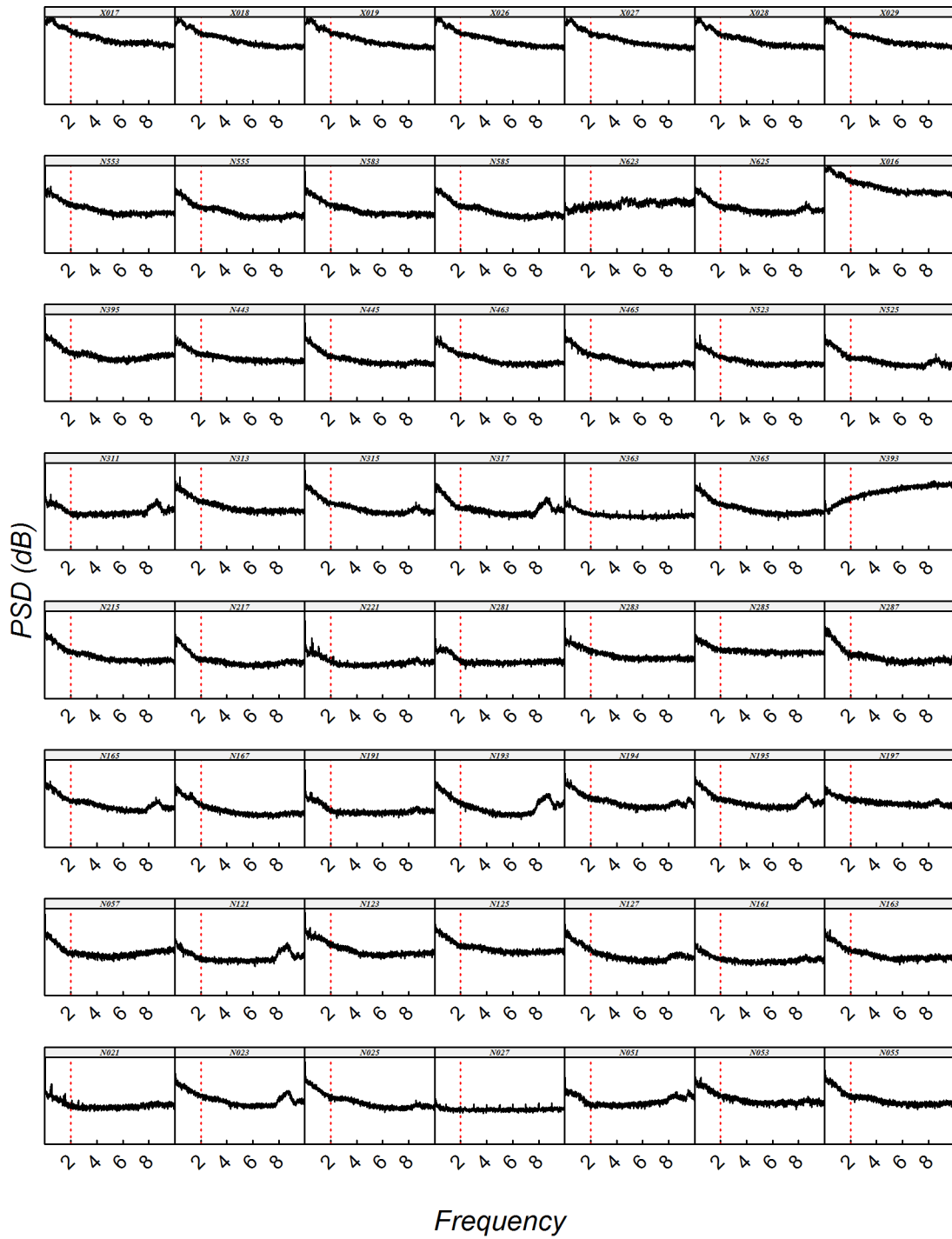
Figure 72: Cycle U1-C09 in the low frequency domain.

PSd Overview on decimated signal Δ f = 0.0988 Hz
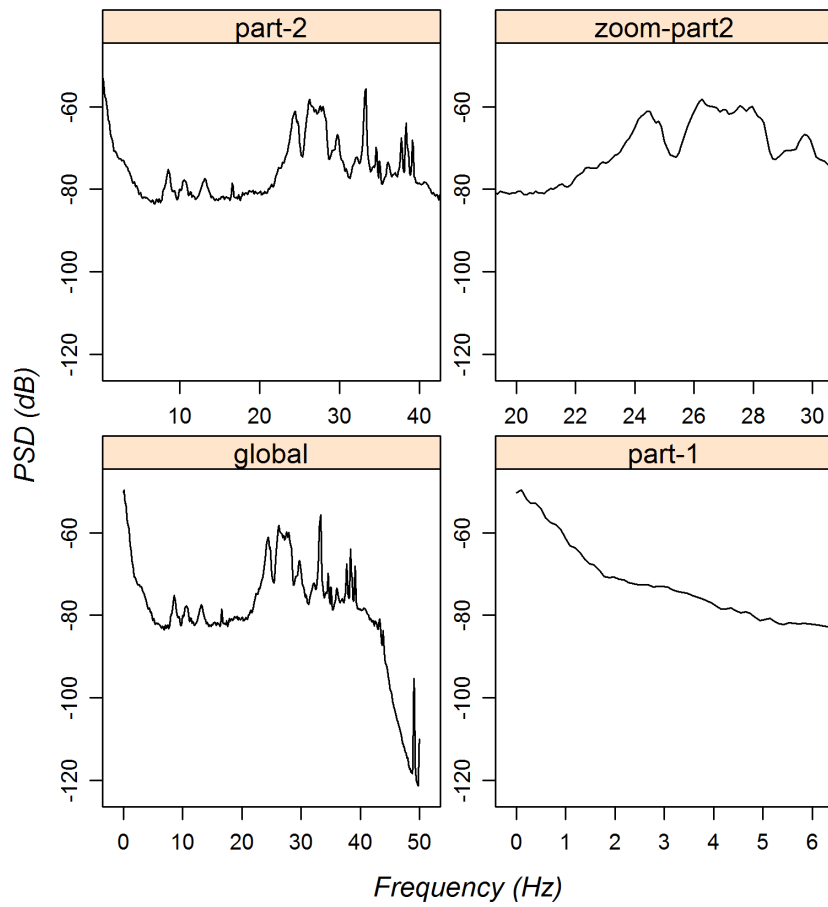
Figure 73: PSD overview on decimated signal (factor 10)

Leading singular values
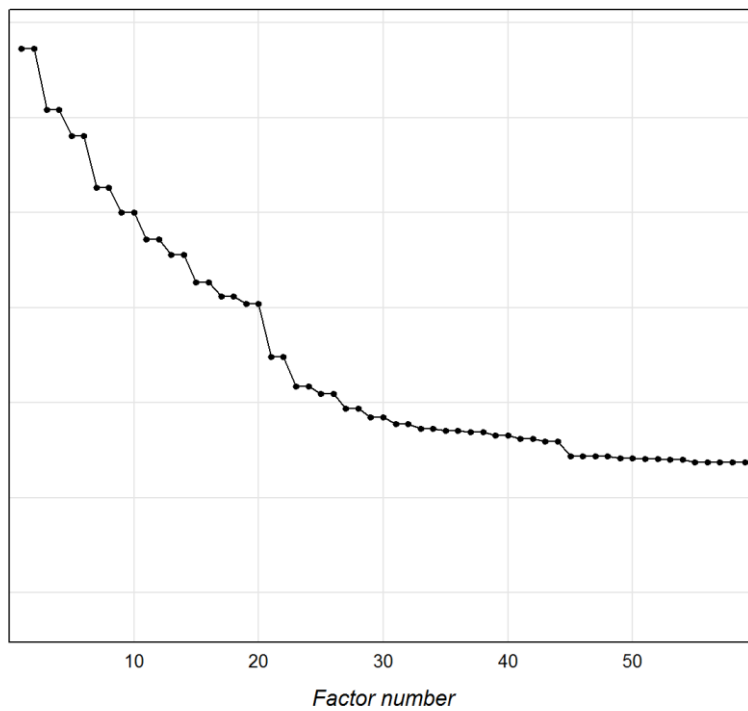
Figure 74: Eigenvalues after detrending.

Figure 75: Correlation matrix on the detrended data.
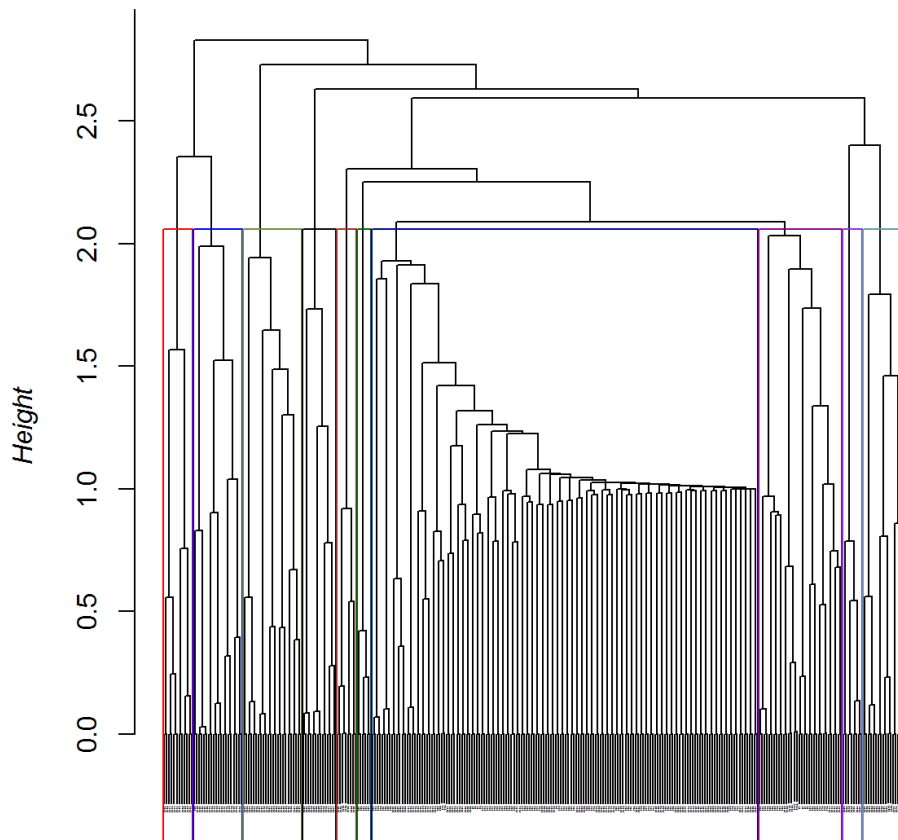
Figure 76: Factors classification on the detrended data.
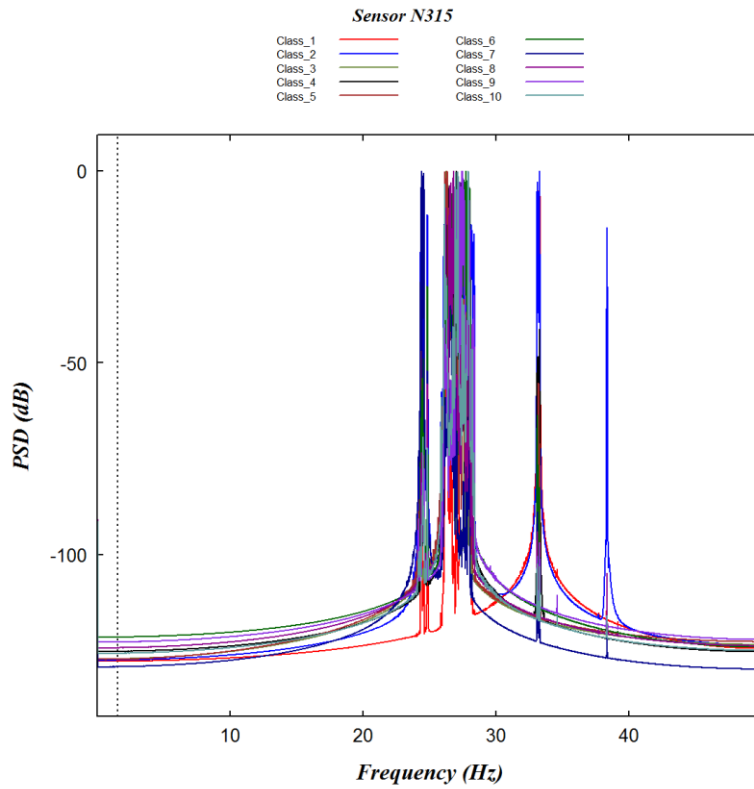
Figure 77: Spectral decomposition obtained by SSA on the detrended data.
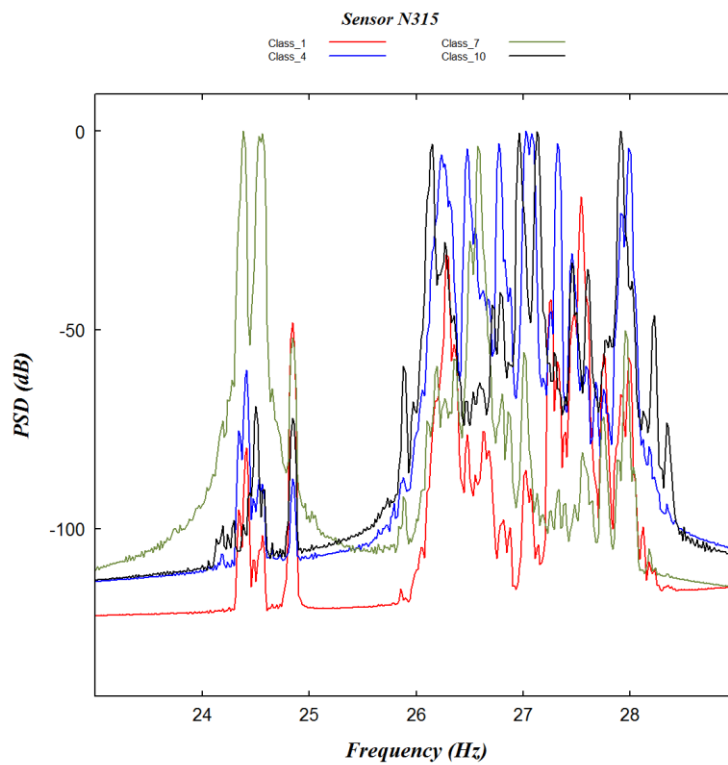
Figure 78: Spectral decomposition obtained by SSA on the detrended data, zoom on the frequency domain to highlight the SSA resolution.
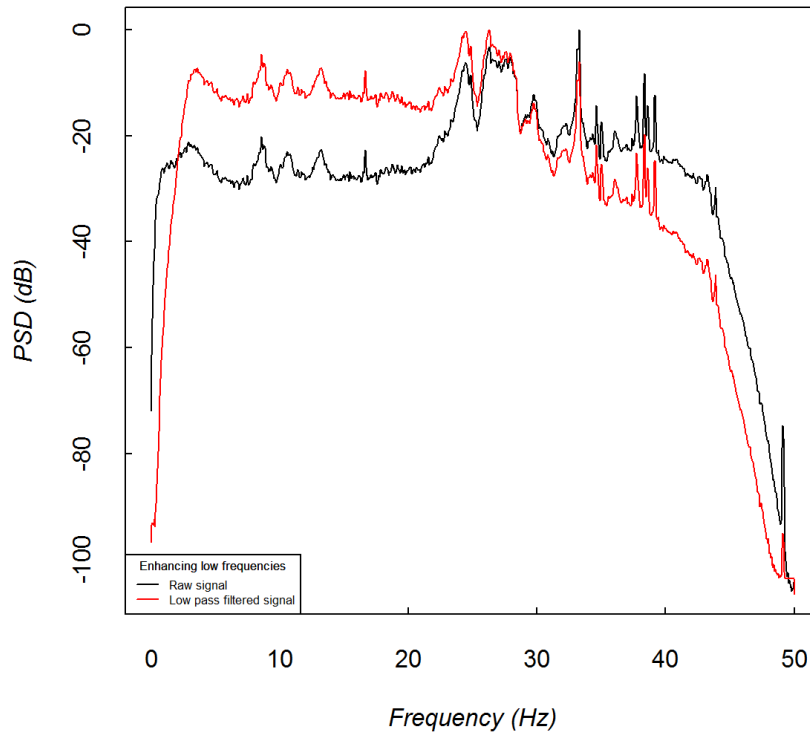
Figure 79: Enhancing the low frequencies by a low pass filter.
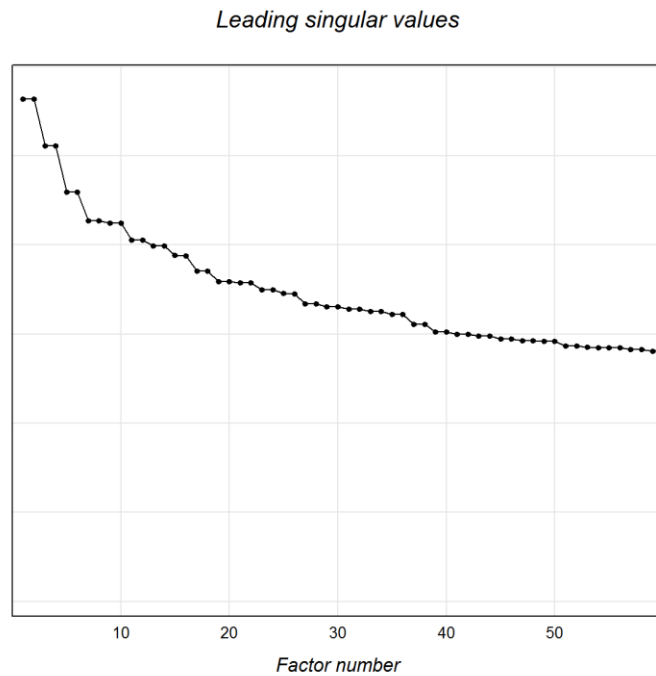
Figure 80: Eigenvalue after detrending with enhancement of the low frequencies.

Sensor correlation matrix
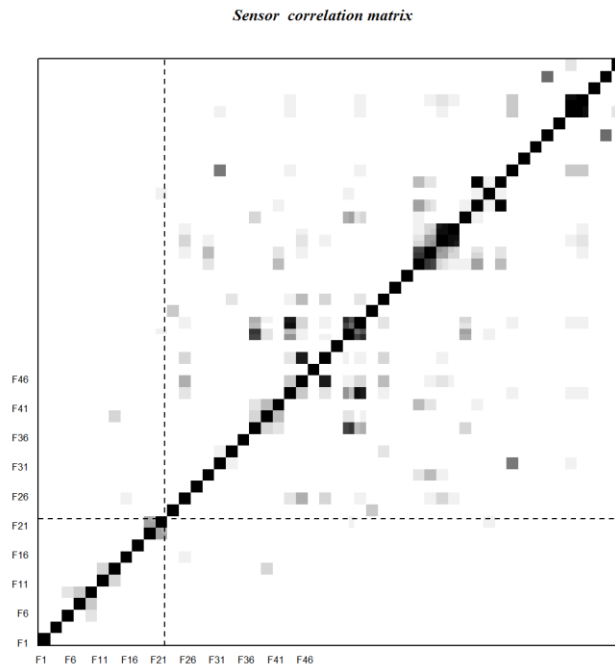
Figure 81: Correlation matrix with enhancement of low frequencies.

Factors classification low frequencies enhanced
Ward criterium
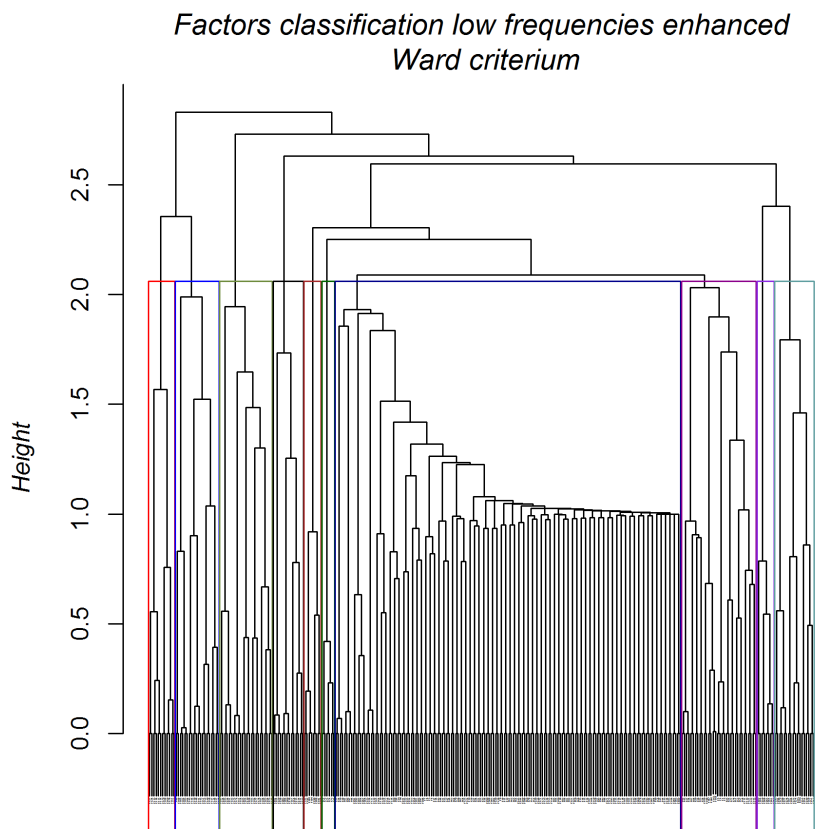
Figure 82: Factors classification with enhancement of the low frequencies.
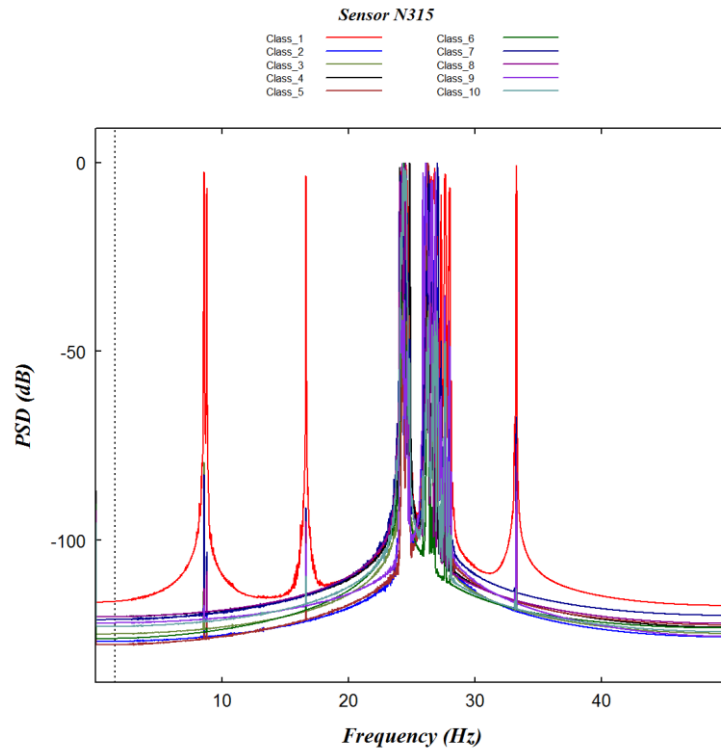
Figure 83: Spectral decomposition with enhancement of the low frequencies.
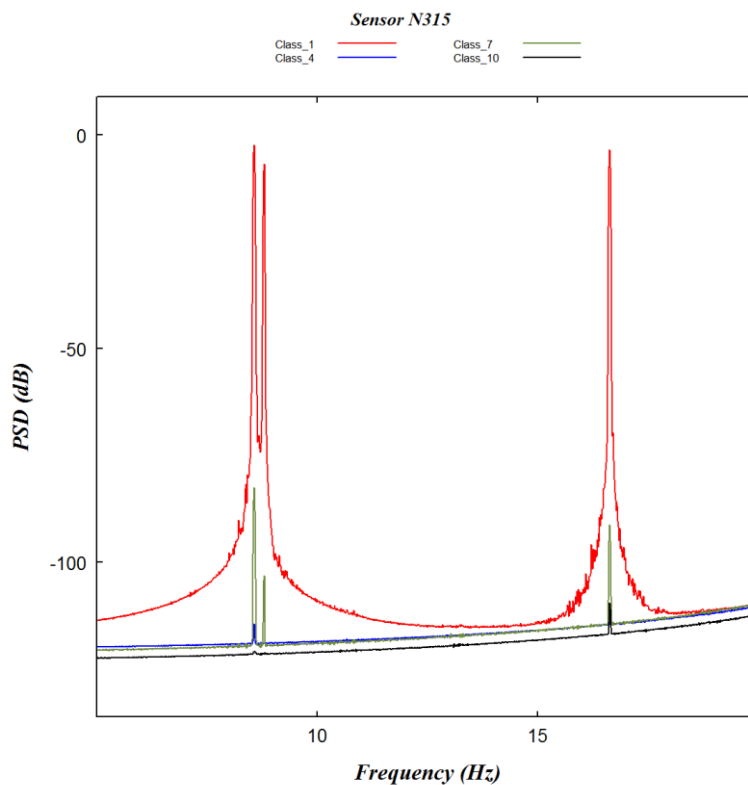
Figure 84: Spectral decomposition with enhancement of the low frequencies – zoom to highlight the improvement resolution by the SSA.
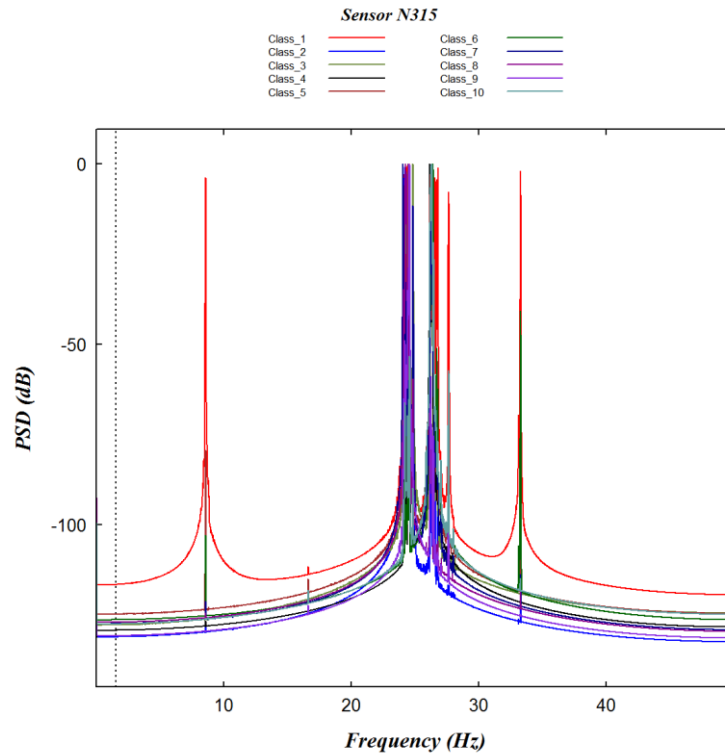
Figure 85: Calculating only 100 factors for the SSA extracts only one low frequency.
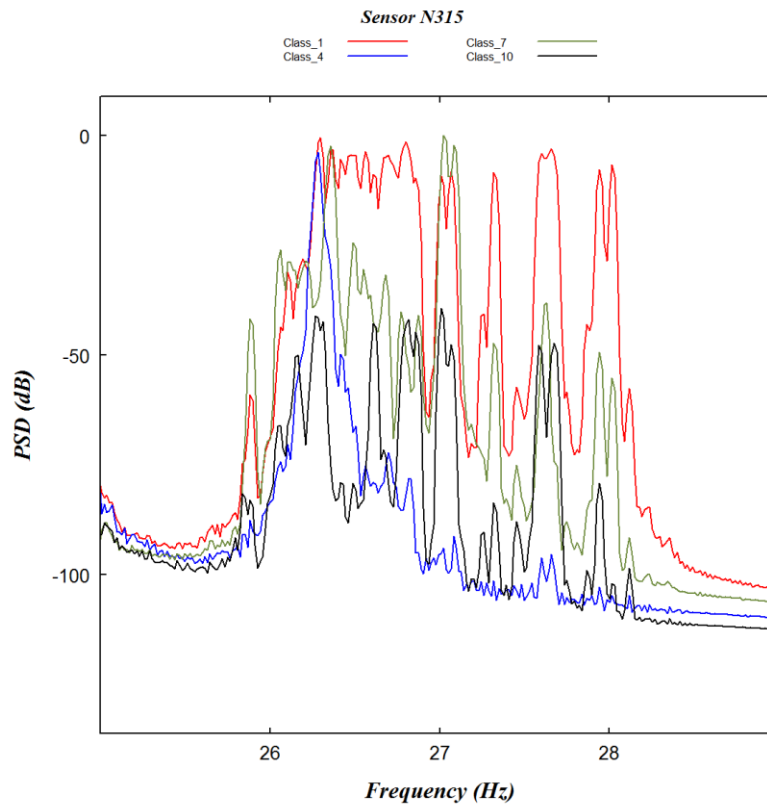
Figure 86: Special decomposition with enhancement of the low frequencies – zoom.
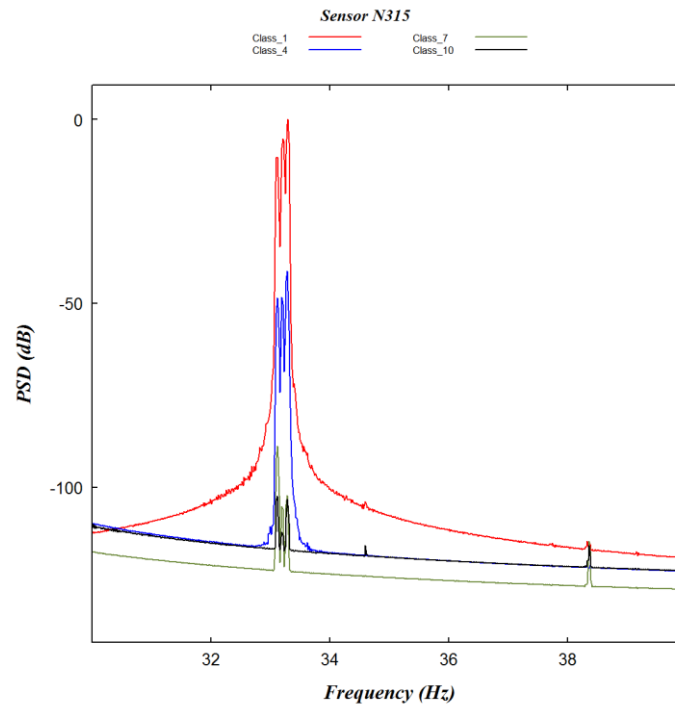
Figure 87: Spectral decomposition with enhancement of the low frequencies – zoom.

4.4.4.7 SSA analysis on every sensor from the cycle C09 UJV data

We did the SSA analysis for every axial sensor at a given radial position. We only describe hereafter the generated graphs made available to the CORTEX partners via the internal repository. From this analysis, we will extract the trend in order to continue the investigation, as described in the previous section on the N315 sensor. There are graphs pertaining to the decomposition and the reconstruction analysis.

4.4.4.7.1 Decomposition analysis

We show the results generated by the decomposition analysis for every radial position, e.g. the four axial sensors associated. We propose the following graphs:

1. The time evolution with the falling in of the eigenvalues.
2. The spectrum assessed by the periodogram calculation.
3. The first high contribution SSA eigenfactors.
4. The first paired vectors.
5. The correlation matrix.
6. The dendrogram of the hierarchical factors classification highlighting the selected classes.
7. The spectrum assessment for every class with the location (black dashed line) of the local maximum frequencies.

4.4.4.7.2 Reconstruction analysis

We propose two graphs:

1. A reconstruction graph with two groups of factors chosen from their decreasing contribution and the slowly varying shape.
2. A reconstruction graph with the groups obtained by the classification in order to estimate the type of variation introduced by every group.

Figure 88 displays an example for the radial position N31.
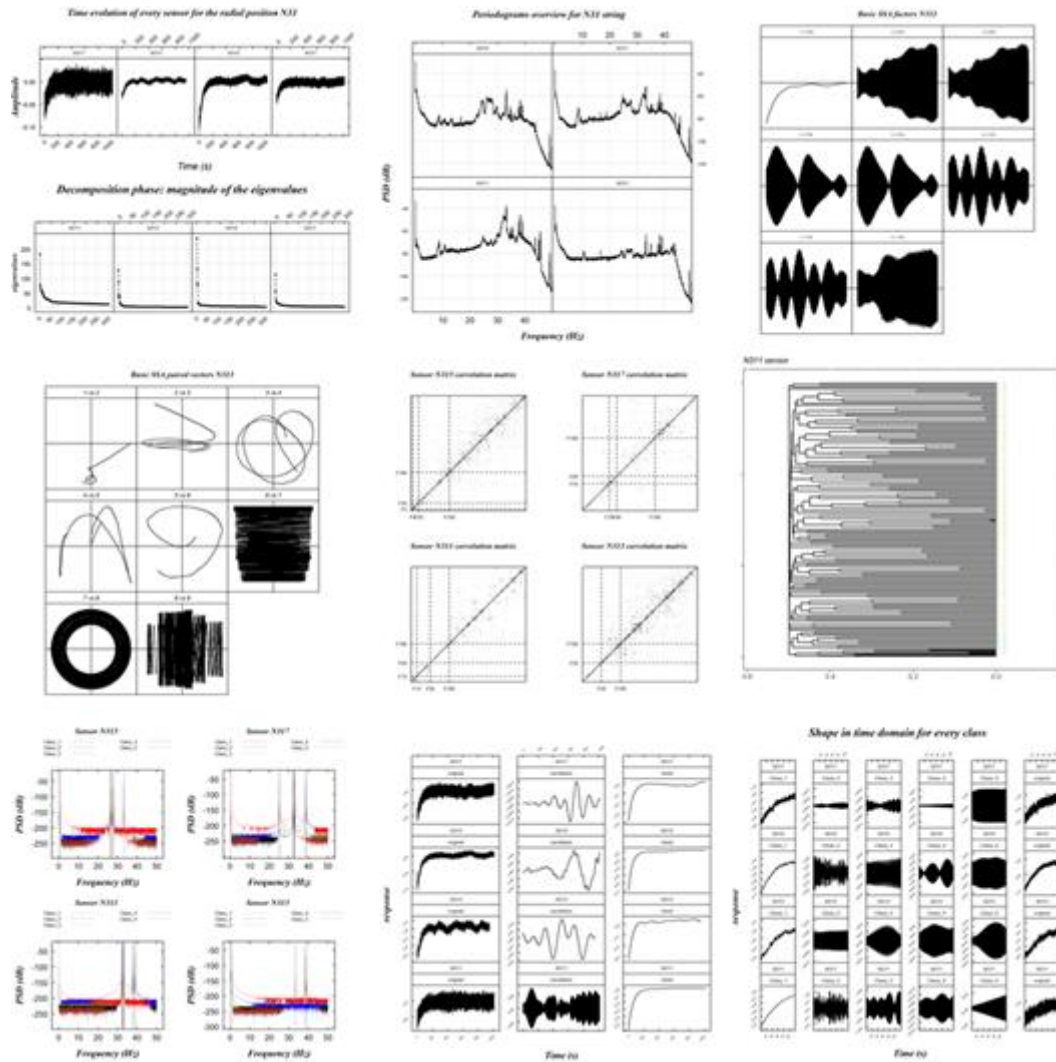
Figure 88: Analysis of radial position N31.

4.4.4.7.3 Overview of the frequencies calculation

On every spectrum obtained by the combination of every factors grouped by the classification, we can do the calculation of the principal frequencies searching for the local maximum. We decided to eliminate the frequencies whose amplitude is lower than -100 dB. These frequencies are marked on the graphs with a vertical black dotted line. The local-maximum values are calculated in a span of 201 values, e.g., according to the sample frequency, a resolution of about 1 Hz. We can notice that many frequencies are highlighted with a very close order of magnitude. There are different interpretations for that. The frequency may not be constant during the acquisition duration leading to some shift. Another explanation can be that we looked for a too high resolution. It would be better to smooth the periodogram with a larger span which will decrease the number of the local minima. The frequency values will have a more physical sense. Thus, if there are too many values very close to each other, it will take the average for further interpretation. Table 6 below gives an example of local frequencies for the radial position N31.

Table 6: Local frequencies for the N31 radial position

Radial position	Axial sensor	Class	Frequency (Hz)	Amplitude (dB)
N31	N311	Class_1	33.1219753	-97.16674
		Class_2	32.2360494	-48.95410
		Class_2	32.6251852	-50.02958
		Class_2	32.8069136	-50.80886
		Class_2	33.2444444	-39.21205
		Class_2	38.3200000	-87.38939
		Class_3	32.4533333	-94.65402
		Class_3	38.3308642	-50.24730
		Class_4	39.1575309	-56.92726
		Class_5	37.7165432	-63.51254
	N313	Class_1	0.2177083	-58.18020
		Class_1	0.3875000	-59.72159
		Class_2	0.3927083	-58.31108
		Class_3	33.2958333	-67.19375
		Class_4	38.3229167	-67.98242
		Class_5	39.1677083	-73.49147
	N315	Class_1	0.2054321	-54.66819
		Class_1	0.4088889	-56.01788
		Class_2	33.2483951	-57.18374
		Class_3	26.5441975	-73.30871
		Class_3	26.7950617	-73.11428
		Class_3	27.9911111	-79.92930
		Class_4	27.6395062	-70.20252
		Class_5	26.3160494	-73.62914
	N317	Class_1	0.2222222	-58.19729
		Class_1	32.1461728	-61.57921
		Class_1	32.2765432	-60.83816
		Class_1	32.6212346	-63.66363
		Class_1	32.8237037	-64.52763
		Class_1	33.2454321	-52.82293
		Class_2	38.3456790	-62.04431
		Class_3	24.8118519	-62.96398
		Class_4	39.1832099	-72.23649
		Class_5	25.4706173	-73.26446

4.4.4.7.4 Conclusion

We showed that the SSA methodology allow us to explore the time domain in order to extract the trend and the oscillation part of the signals. After revealing the different spectral components of the signal, we are able to assess the value of the frequencies with a better resolution than that appearing in the periodograms. The parameters chosen for the SSA and spectral analysis give us sometimes many frequencies in a very small range. We have to interpret these results following some physical

reasoning. In order to adjust the degree of precision, we can launch again the analysis asking for further refinement. The analysis has been carried out in such a way to generate a reproducible document automating the data processing. Thus, we can investigate different periodograms smooths, SSA decomposition (number of eigenvectors) and reconstruction (results of factor classifications). The next step of this work will be to improve the raw data, taking into account the sensors characteristics, and to perform a physical analysis crossing the signals features with the sensor locations and the operating physical quantities. Presently, the work in progress consists in detrending every sensor thanks to the results obtained by the SSA analysis on the raw data, keeping the first factors of every SSA. We will do again SSA calculation on the detrended data for further physical investigation and extract some pertinent parameters in order to prepare the phase of images creation and sensors cross analysis.

5 Machine learning-based anomaly classification and localization

In this section, machine learning techniques for anomaly classification and localization are going to be presented, based both on simulated data and actual plant measurements for the four reactor types examined in this deliverable. The typical analysis procedure for each reactor involves feature extraction, followed by comparisons with the simulated data. Subsequently, unsupervised learning methodologies are applied on the processed signals (namely, clustering) and finally, the machine learning-based anomaly classification and localization techniques are derived.

5.1 Feature Extraction

Feature extraction of feature engineering is the task of identifying those characteristics in data that are most helpful in describing their statistical properties. Since the quality of the obtained features greatly influences the performance of machine learning algorithms, this task is an important step prior to the application of the actual classification and localization procedures. In principle, various signal processing techniques may be used to transform the raw data into meaningful representations that help the training of ML algorithms.

In the following paragraphs, the extracted features from the plant measurements are going to be described in more detail. If $S(t)$ is the signal in the time domain (e.g. neutron flux captured by the detectors) and W is a time window (a hyper-parameter), then we consider the following basic features over W:

Mean Value of signal	$\mu_i = \frac{1}{W} \sum_{t=i}^{W+i} S(t)$	(19)
Standard deviation of signal	$\sigma_i = \sqrt{\frac{1}{W} \sum_{t=i}^{W+i}(S(t) - \mu_i)^2}$	(20)
Minimum of signal	$min_{i<t<W+i} S(t)$	(21)
Maximum of signal	$max_{i<t<W+i} S(t)$	(22)
Energy of signal	$E_i = \sum_{t=i}^{W+i} |S(t)|^2$	(23)

5.1.1 The frequency domain

The Fourier Transform is one of the most dominant transformation used in signal processing. It takes the time-domain signal and decomposes it to its frequency components. In this work, the Fourier Transform is going to be used to construct the following features:
- Energy of the whole spectrum of frequencies that were found in the signal.
- Finding the *top-k* (usually 3 or 5) frequencies with the highest energy. These frequencies are called the dominant frequencies and will help with matching and comparing them with the simulated signals.
- Extracting the spectrogram of a signal. The spectrogram is a heat map that represents the spectrum of the frequencies as it changes over time. The horizontal axis represents the time and the vertical one the frequency. The different amplitudes of each frequency are displayed as different intensity colors, out of a selected color map. Spectrograms are extremely useful because information of both the frequency domain, but, also, the time domain of a signal are compressed in a single image. This image can be processed by Machine Learning techniques, such as Neural Networks, and produce state-of-the-art results, which are going to be analyzed in a later subsection.
- Computing the APSD of a signal proves to be an additional useful feature, which depicts how the power of a signal is distributed across all frequencies that are present. It can detect

transient effects that last only a small amount of time by comparing APSDs from adjacent time windows.

- Another feature like APSD is the CPSD. The difference between them is that the CPSD is the correlation between two spectral densities. In other words, it shows the distribution of power of the cross-correlation function of two signals. In our setting, the two different signals are originating from two different sensors, measured during the same period. It is extremely useful to find various relations between different sensors across the whole spectrum, but also over time.

In continuous signals, a very important feature is the derivative. Its significance lies in the fact that it indicates the rate of change of the signal and it can identify sudden changes in its behavior. Since we are dealing with discrete signals, we cannot compute the derivative directly, but instead, we can compute the difference over consecutive time steps ($d(t) = S(t+1) - S(t)$). Obviously, the (discrete) difference may also be treated like a signal that has the same length to $S(t)$ minus one and the energy of the discrete difference may also be calculated.

Finally, another mathematical transformation linked with the Fourier Transform that can prove to be essential, is the Cepstrum. There are three variants that are mostly used, the Power, the Complex and the Real Cepstrum. The Real Cepstrum is computed as:

$$C_p = |\mathcal{F}^{-1}\{log(|\mathcal{F}\{S(t)\}|^2)\}|^2 \tag{24}$$

where $\mathcal{F}$ is the Fourier Transform and $\mathcal{F}^{-1}$ is its inverse. Generally, Cepstrum is used in speech analysis and pitch recognition, but, also, in machine vibration analysis. It can detect echoes in signals or other anomalies.

5.1.2 Machine learning-based feature extraction

Apart from using the formulas discussed above, we may also directly employ machine learning models to find useful representation of data and consequently, to extract new features. In the past, this was primarily achieved with techniques like the Principal Component Analysis of the Latent Dirichlet Allocation, but recently, more advanced techniques are used, like the Autoencoders, as illustrated in Figure 89.
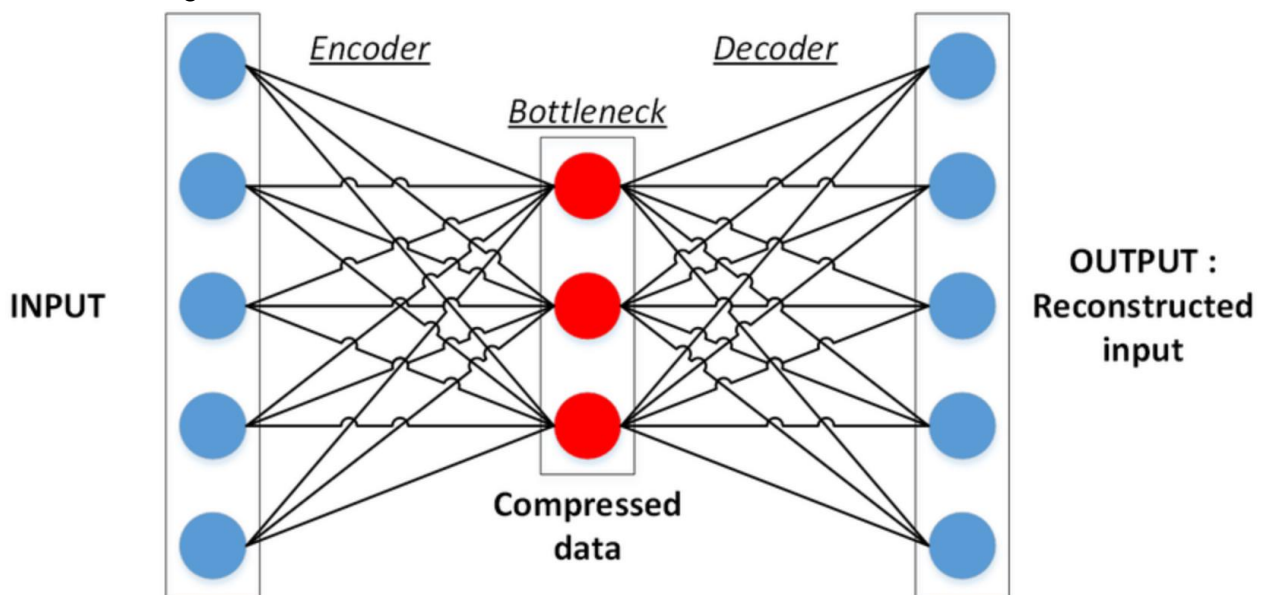
Figure 89: Basic Autoencoder architecture.

Autoencoders are a type of neural network that can reduce the dimensionality of the input space without losing significant information or knowledge from the data. The Autoencoder architecture consists of two parts, the encoder and the decoder. The task of the encoder is to transform the input into a space with less dimensions through multiple neural network layers. In other words, the output of the encoder is a compressed version of the input that preserves the most salient features. The decoder takes as input this encoding and tries to reconstruct the initial input of the network. So, the autoencoder is trained as a supervised model, where the output must match the input, while reducing data dimensions internally.
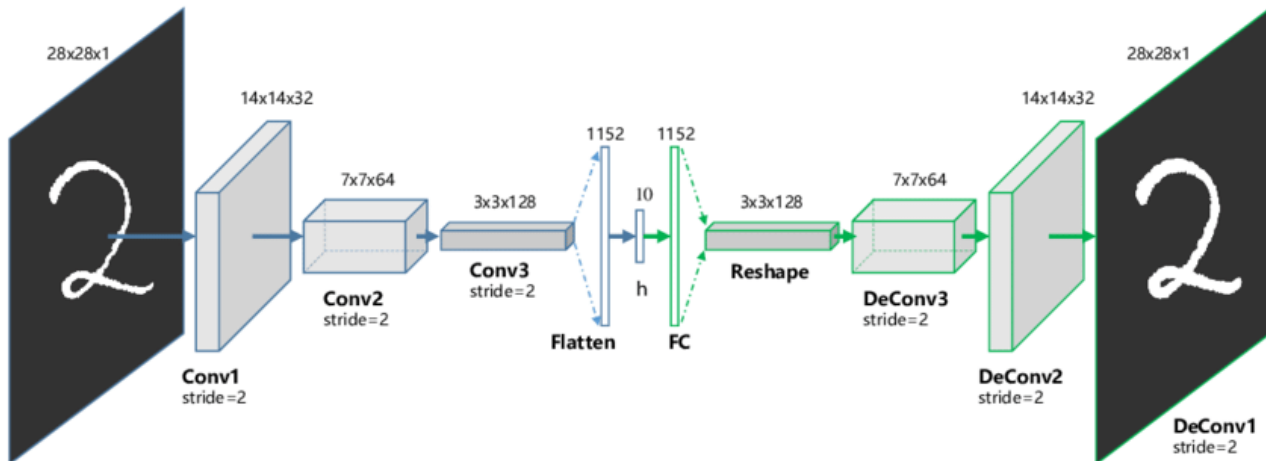
Figure 90: Example of Convolutional Autoencoder Architecture.

Various autoencoder types have been proposed in the literature. For two-dimensional data (e.g. spectrograms of signals), the Convolutional Autoencoder is among the optimal choices. This specific type utilizes Convolutional layers to construct the compressed encoding, while the decoder uses Deconvolutional layers or Upsampling layers to reconstruct the two-dimensional data as good as possible. An example of Convolutional Autoencoder Architecture is displayed in Figure 90. Another useful type of Autoencoder is the Recurrent Autoencoder. As the name implies, this Autoencoder uses Recurrent layers, such as LSTM (Long Short-Term Memory) units, in both the encoder and the decoder. This architecture is commonly employed when the dataset consists of signals, sequences, and any time series type of data. A typical Recurrent Autoencoder Architecture is displayed in Figure 91.

5.2 Comparisons between plant measurements and simulated data

This subsection discusses the comparisons between plant measurements and the provided simulated data. The latter predominately came from two different simulation setups. The first is SIMULATE-3K, which produces signals in the time domain, and the second is CORE SIM+, which produces signals in the frequency domain. The frequency domain data simulate both the Swiss pre-Konvoi 3-loop reactor, as well as the German pre-Konvoi 4-loop reactor. On the other hand, the time domain simulated data correspond to the Swiss 3-loop reactor. The comparison will be made between features extracted from both real and simulated signals.

The purpose of this comparison is twofold. Firstly, to tackle large deviations between the real and the simulated signals. Secondly, to search whether specific simulated perturbations are occurring within the real plant measurements.
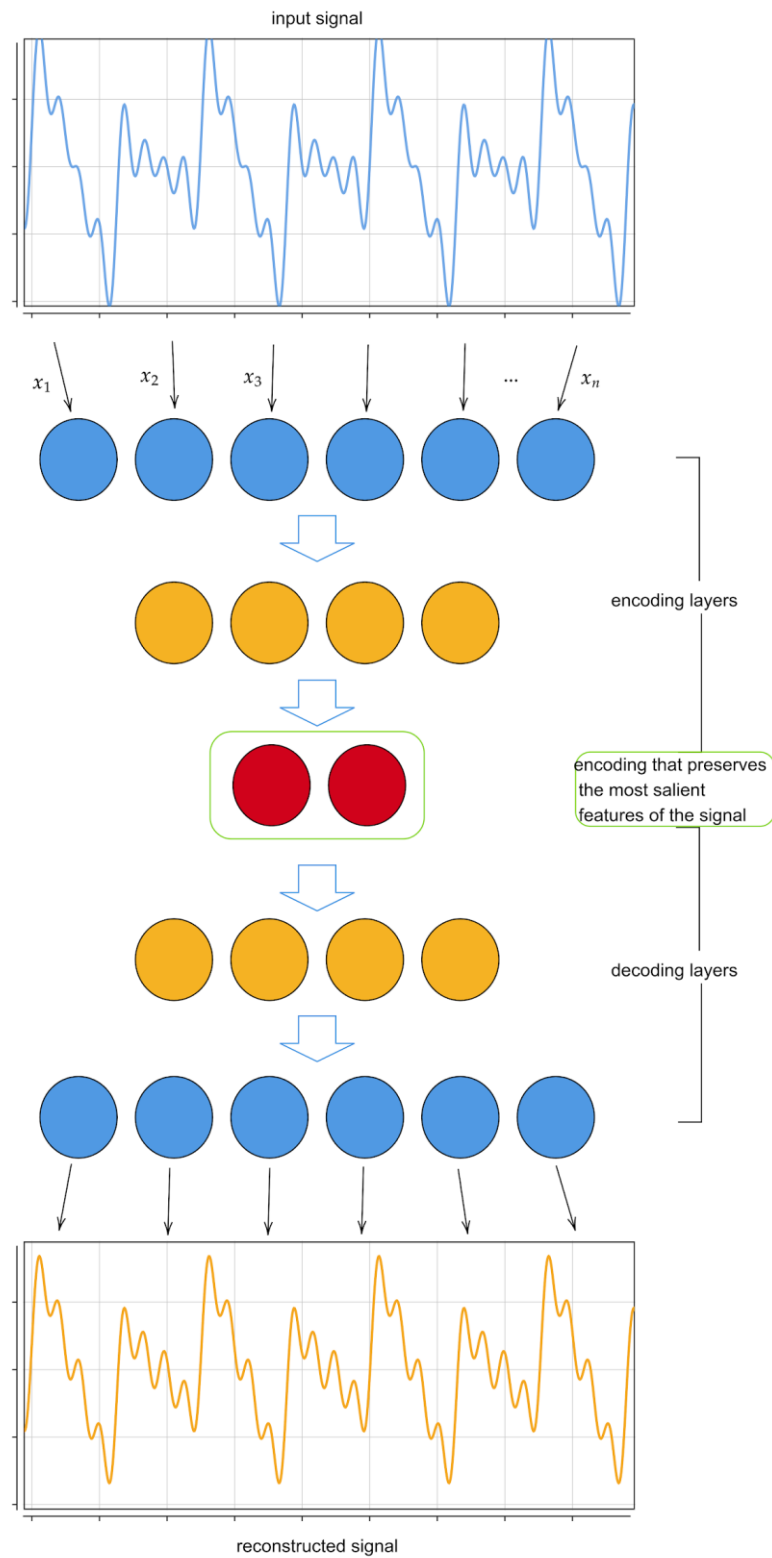
Figure 91: Recurrent Autoencoder with signals as its input.

5.3 Unsupervised learning

Unsupervised learning methodologies aim to extract knowledge from or to recognize patterns in data that are not accompanied by labels. This is extremely helpful in this setting, since actual plant measurements are unlabeled, i.e. we are unaware if any perturbations (and which) are taking place.

The conducted analysis will have two objectives: (i) *clustering* and (ii) *anomaly detection*. Clustering tries to find similar samples out of a dataset and eventually divide the dataset into the right amount of groups (clusters). This can help us identify different reactor core states, especially those evolving through time. On the other hand, the goal of anomaly detection is to specify which part of the dataset seems more out of place compared to the rest. This becomes important to distinguish any outliers hidden in the data (i.e. any perturbations).

In order to perform the aforementioned tasks, the data must be transformed into a smaller shape. It is a known fact that as the feature space grows, the more difficult it becomes for a clustering (or anomaly detection) algorithm to perform well. So, there is a need to reduce the dimensionality of the data. For this task, we employ the Autoencoders presented in Subsection 5.1.2. Then, the reduced data are processed with the following unsupervised algorithms:

- **k-Means** tries to group the dataset samples into *k* clusters based on a metric (most commonly used is the Euclidean distance). At first, it initializes *k* cluster centers and at each iteration, it assigns every data sample to the cluster that minimizes that metric. It converges when no further changes in cluster centers or cluster assignments are observed.
- **Mean-Shift clustering** is based around creating centroids, typically using a Gaussian kernel, and updating them by the mean of the data points. Kernels influence which data point belongs to which centroid. Different type of kernels may perform better at different situations.
- **Spectral clustering** is best suited for multivariate distributions. It takes advantage of a similarity matrix of the data points in order to compute the Laplacian matrix. Then, it calculates the *k* first eigenvectors (trying to cluster the data in *k* groups) and shapes them into matrices. These matrices are then provided as input to a *k*-Means like algorithm to construct the final clusters of the dataset.
- **DBSCAN** is a density-based clustering algorithm that groups together nearby data points with high density and singles out any outliers in low-density regions.
- **One-class SVM** (Support Vector Machine) is an anomaly detection algorithm that tries to fit the whole dataset in the smallest possible hypersphere. After training, every data sample that lies outside that space is regarded as an outlier, while the rest are considered normal instances.
- **Isolation Forest** is an anomaly detection algorithm that partitions the data points in a tree, by splitting them based on the value of a random feature. After the construction of the tree, out of all the external nodes (leaves), the ones with the shortest path length are considered the outliers.

5.4 German pre-Konvoi 4-loop reactor

The German pre-Konvoi 4-loop reactor measurements consist of 3 different cycles, 30, 31 and 32. In the reactor, there exist 64 detectors, divided in four categories: (i) in-core, (ii) ex-core, (iii) temperature and (iv) pressure. In total, 450.560 data points have been sampled (sampling rate is 250 Hz). The signals contained a DC component that has been removed. Additionally, a linear trend has also been detected and removed. Figure 92 displays an example signal before and after DC component and linear trend removal.

Example of signal of L-B11-3
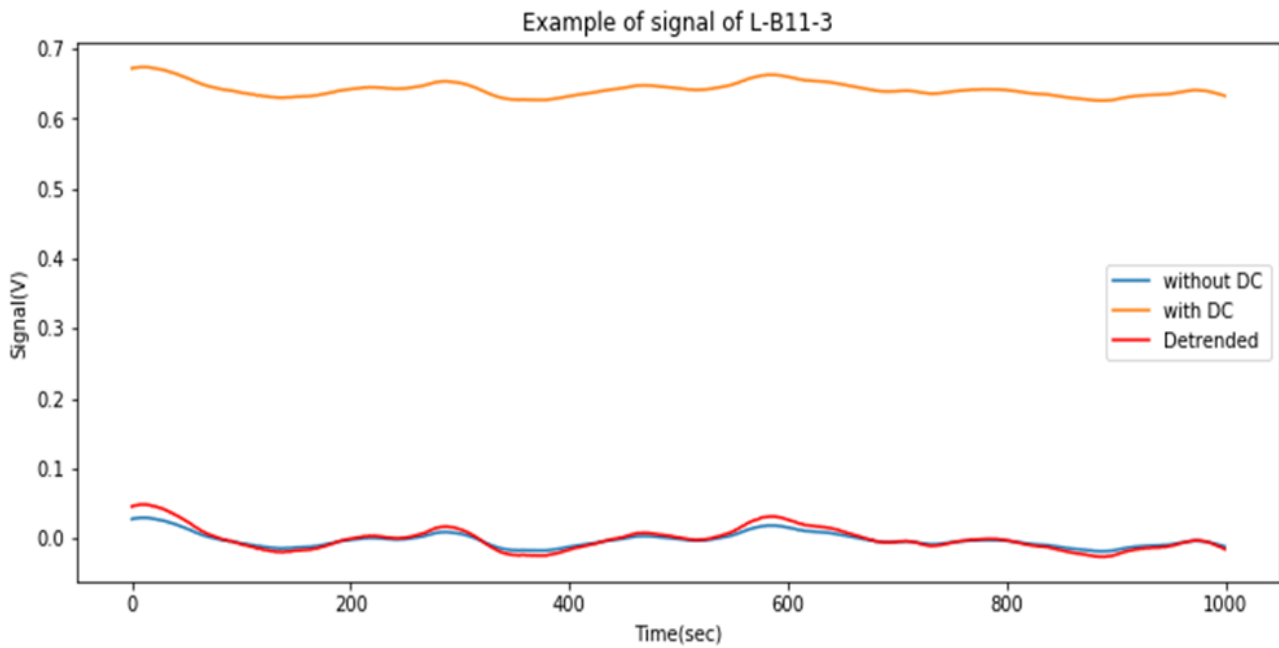
Figure 92: Example of in-core signal for the German 4-loop reactor.

5.4.1 Feature Extraction

5.4.1.1 Cycle 30

Figure 93 displays the Mean, Variance, Energy, Energy of Differences, Minimum value, Maximum Value and Cepstrum of a window in time of in-core sensor J06-3. For the Energy and Energy of Differences, the unit of measurement is V^2. For all the features, except Cepstrum, the x-axis is time windows. One time window is 10 seconds or 2500 time steps. The unit of Cepstrum is Volt and its x-axis is seconds.
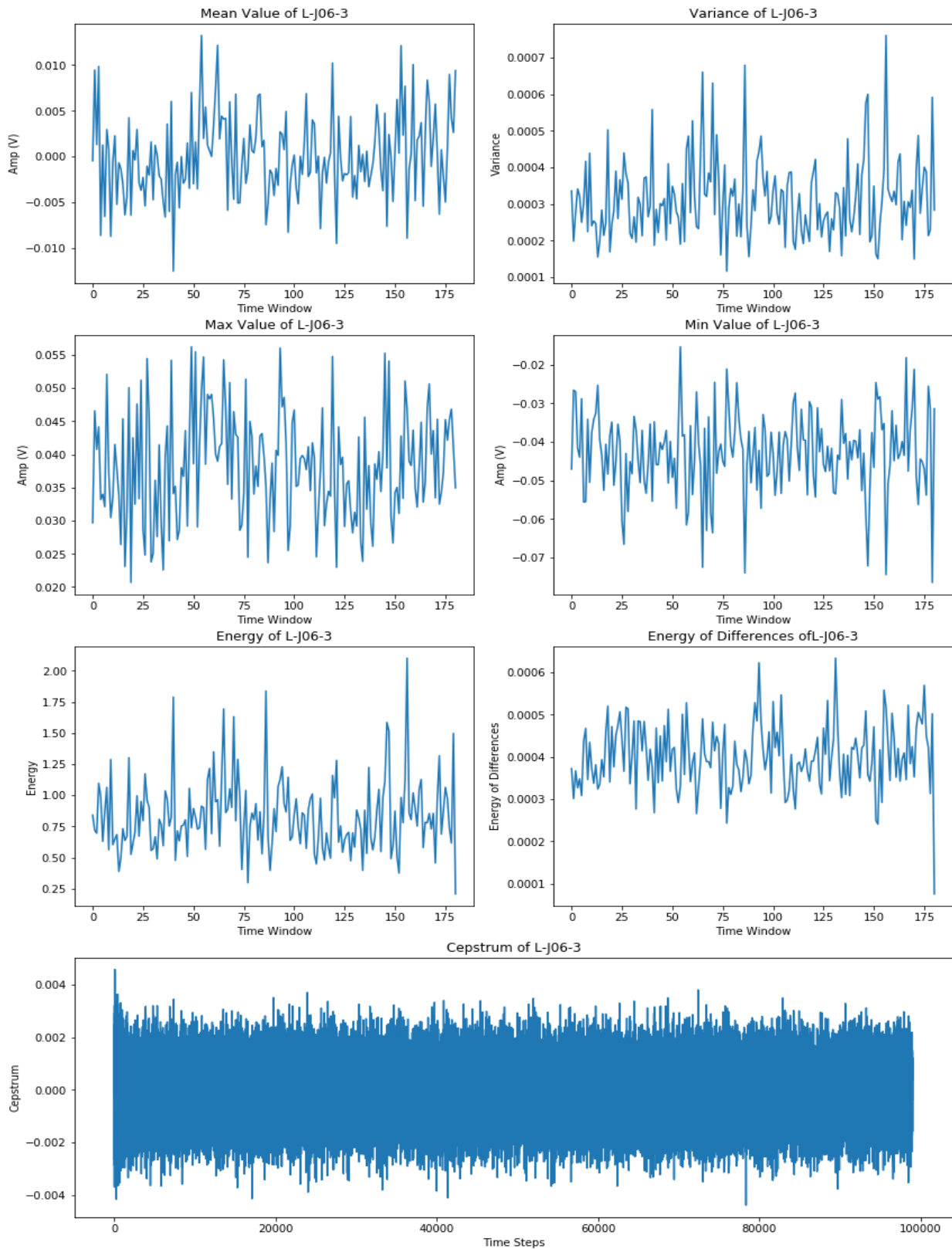
Figure 93: In-core sensor J06-3.

Figure 94 displays the most dominant frequencies of the same in-core sensor (J06-3).
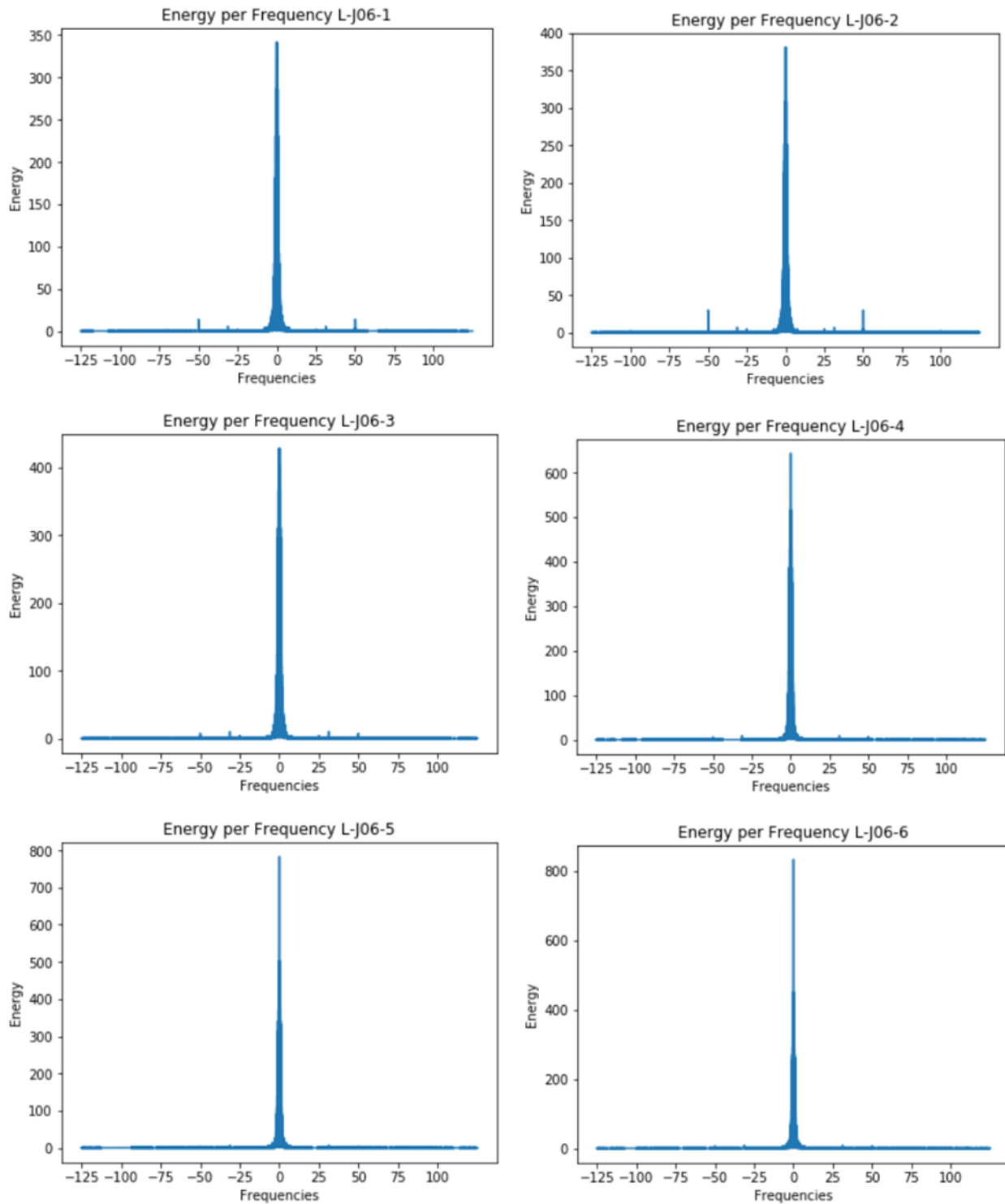
Figure 94: Most dominant frequencies of the J06 family of sensors.

Some observations are summarized below:

- The most dominant frequencies are located below 3 Hz with the small exception of the 50 Hz frequency.
- There are no extreme spikes from the energies or variance.

Figure 95 displays the Mean, Variance, Energy, Energy of Differences, Minimum value, Maximum Value and Cepstrum of a window in time of the ex-core sensor X-R135-O.
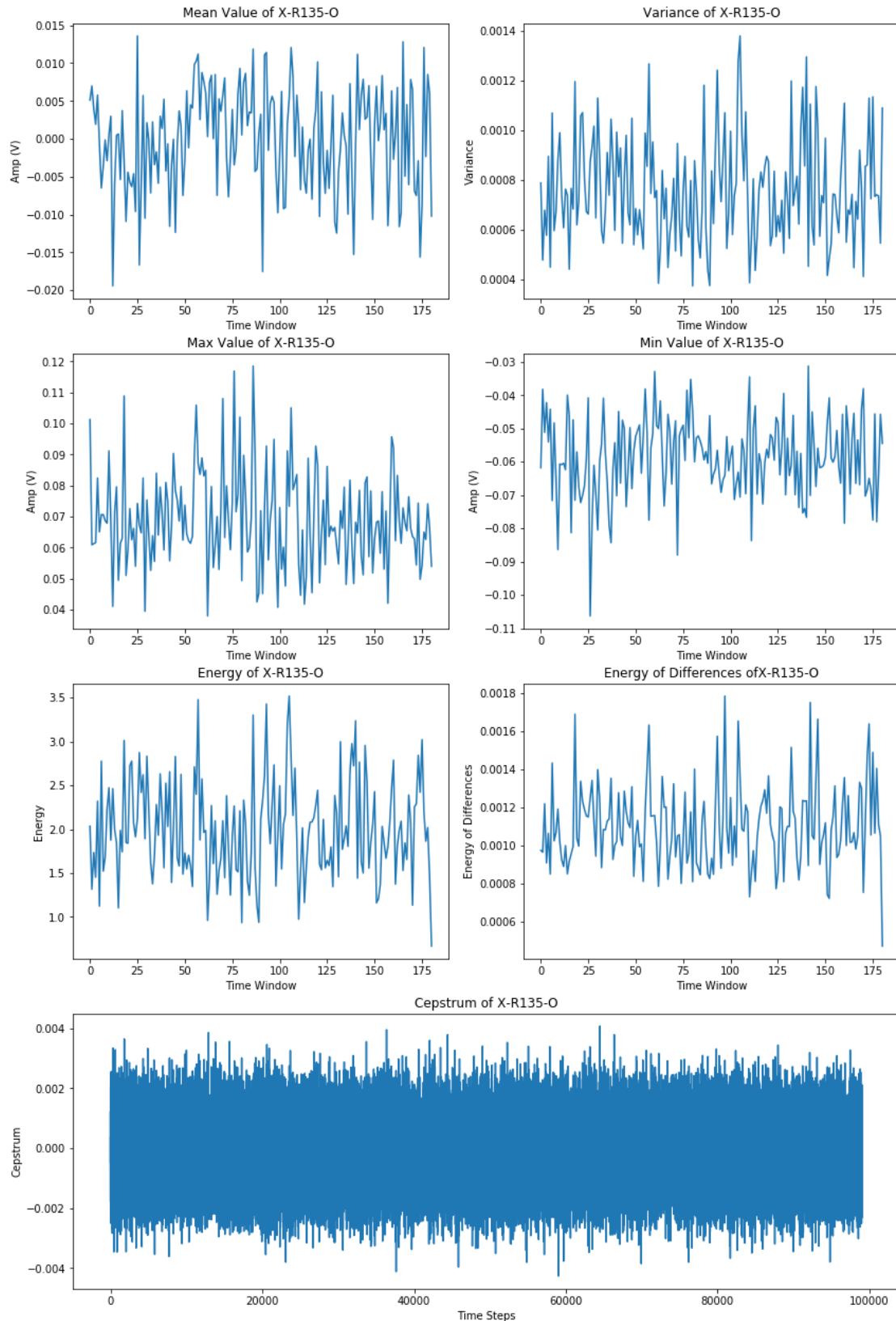
Figure 95: Ex-core sensor X-R135-O.

Figure 96 displays the most dominant frequencies of the ex-core sensors X-R045, X-R315, X-R225 and X-R315.
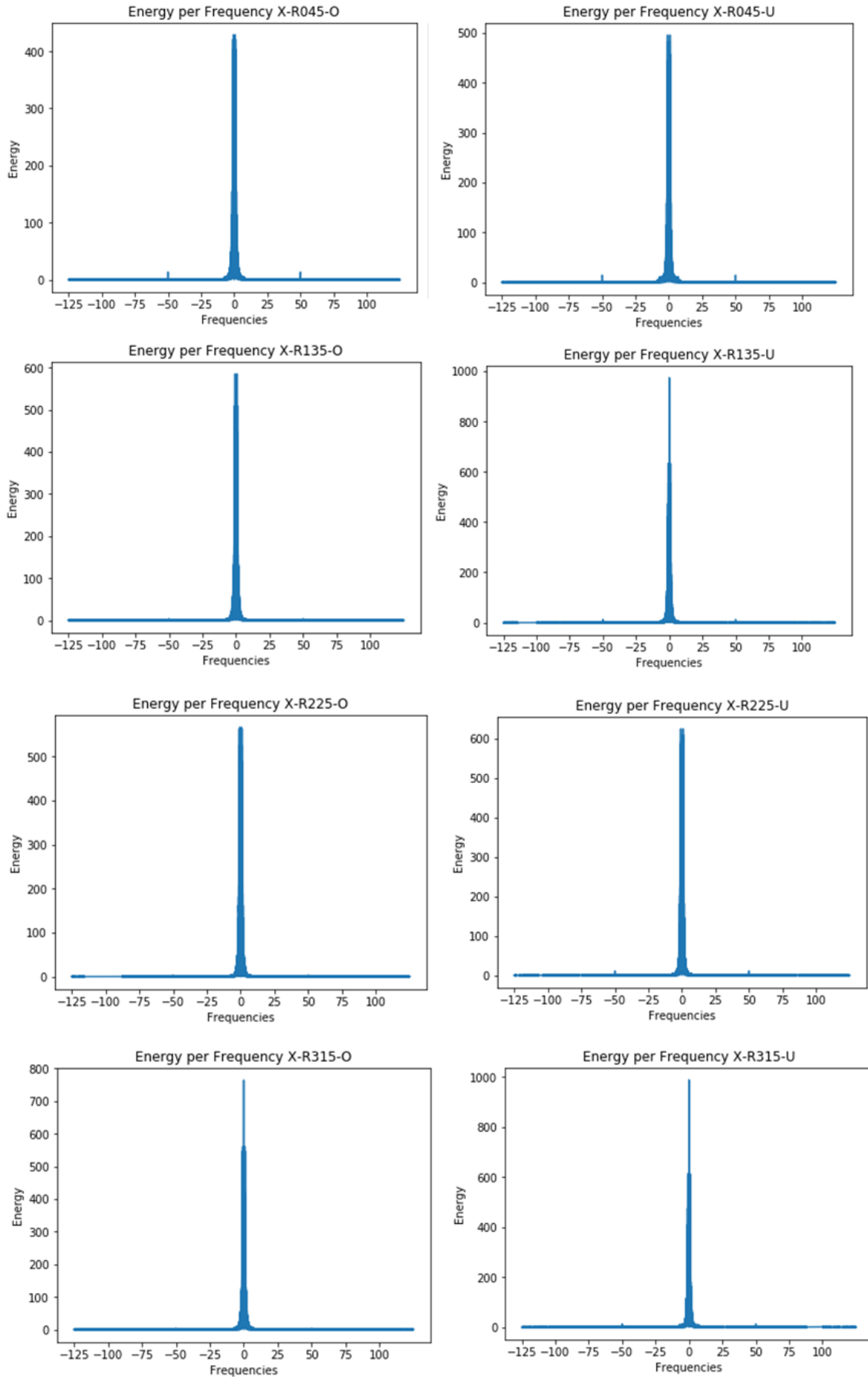
Figure 96: Most dominant frequencies of the ex-core sensors X-R045, X-R315, X-R225 and X-R315.

Some observations are given below:

● A similar behavior to the in-core ones is observed, with the dominant frequencies being < 3 Hz.

Figure 97 displays the Mean, Variance, Energy, Energy of Differences, Minimum value, Maximum Value and Cepstrum of a window in time of the temperature sensor T-N12-A.
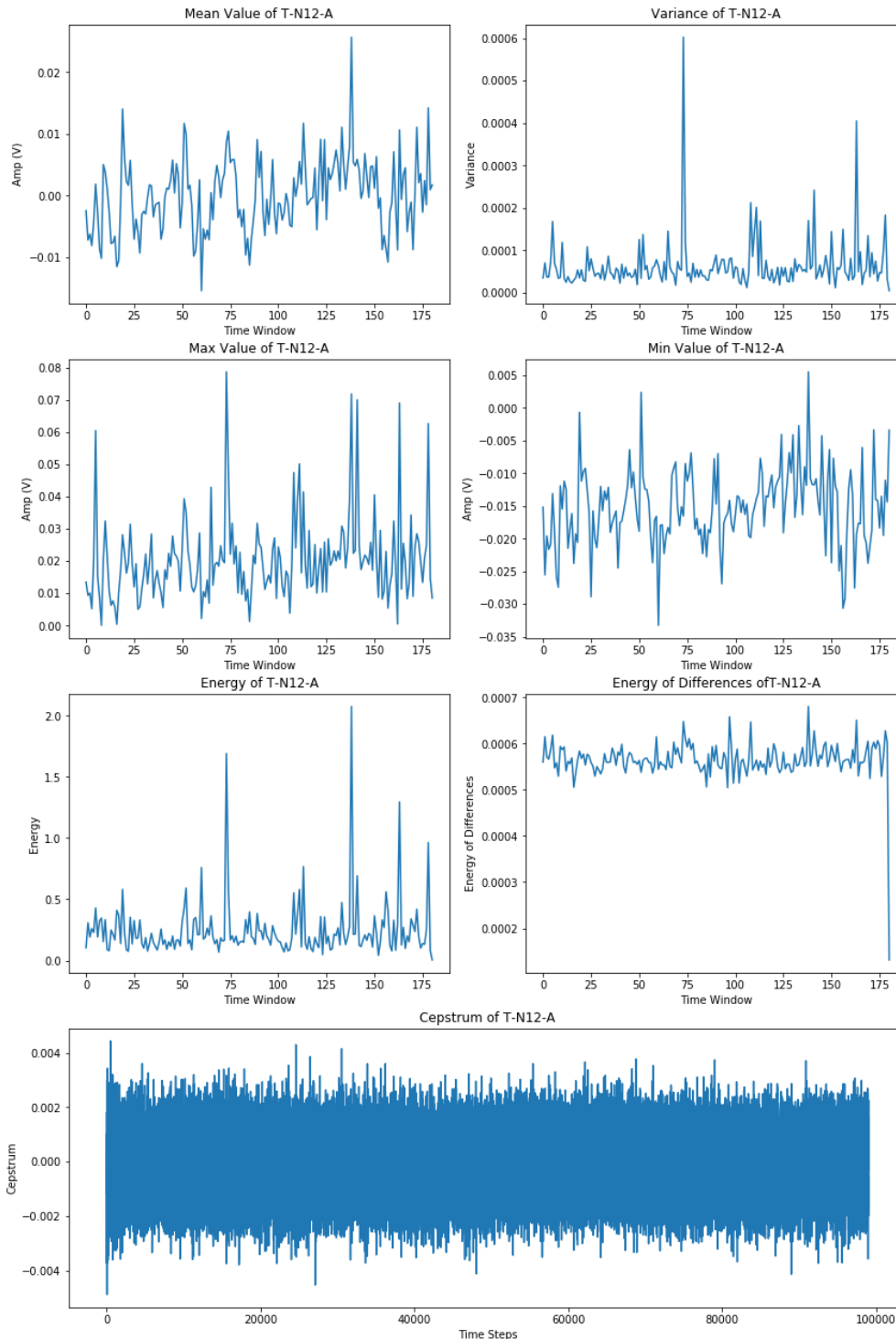
Figure 97: Temperature sensor T-N12-A.

Figure 98 displays the most dominant frequencies of the temperature sensors T-N12-A, T-C04-A, T-G10-A, T-G14-A, T-J02-A, T-J06-A, T-N12-A and T-O05-A.
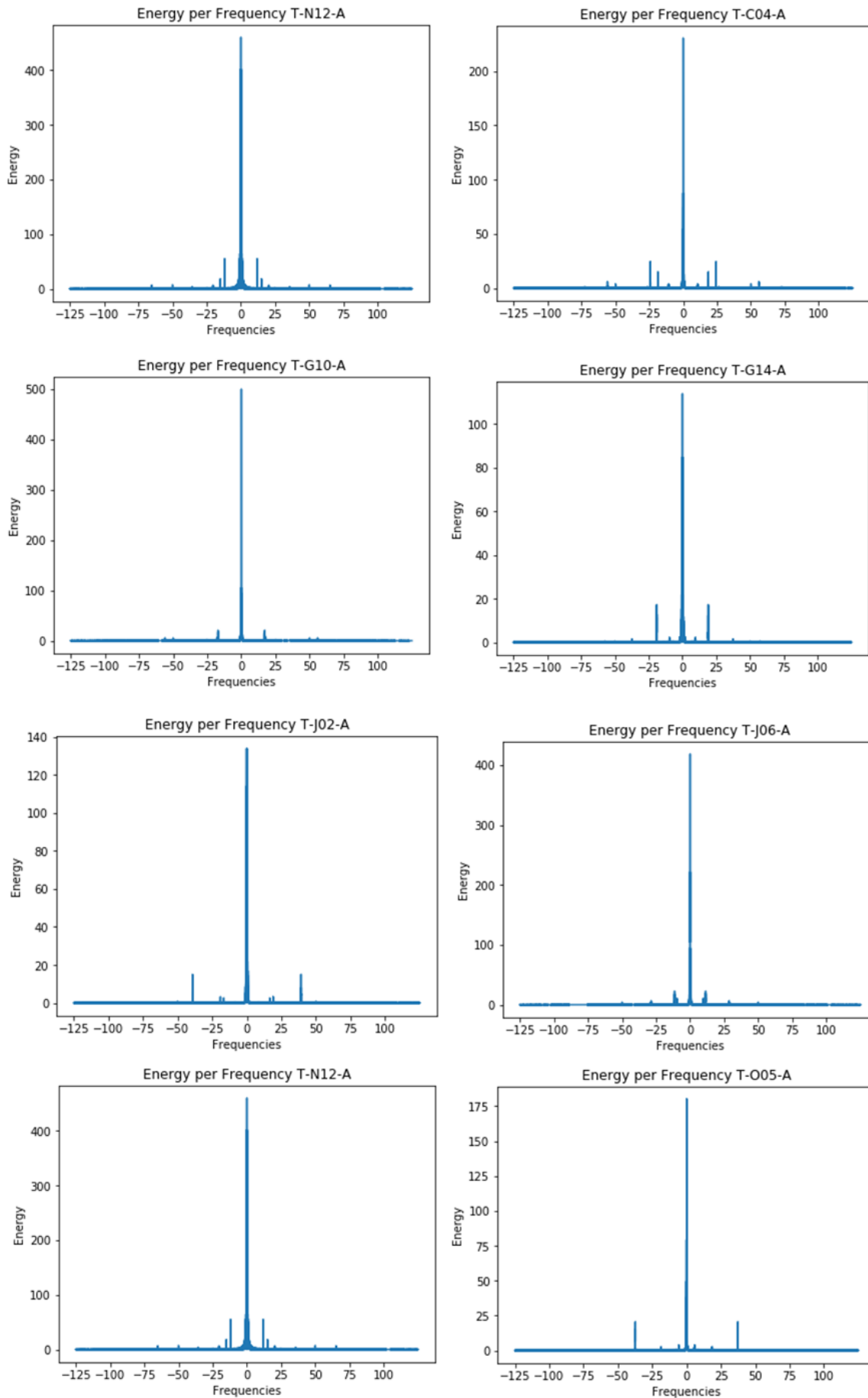
Figure 98: Most dominant frequencies of temperature sensors T-N12-A, T-C04-A, T-G10-A, T-G14-A, T-J02-A, T-J06-A, T-N12-A and T-O05-A.

Some observations are summarized hereafter:

- We can see that beyond the <3 Hz frequencies being dominating, the 22 Hz and 30 Hz components are also present.

Figure 99 displays the Mean, Variance, Energy, Energy of Differences, Minimum value, Maximum Value and Cepstrum of a window in time of the pressure sensors P-R025-E and P-R155-E.
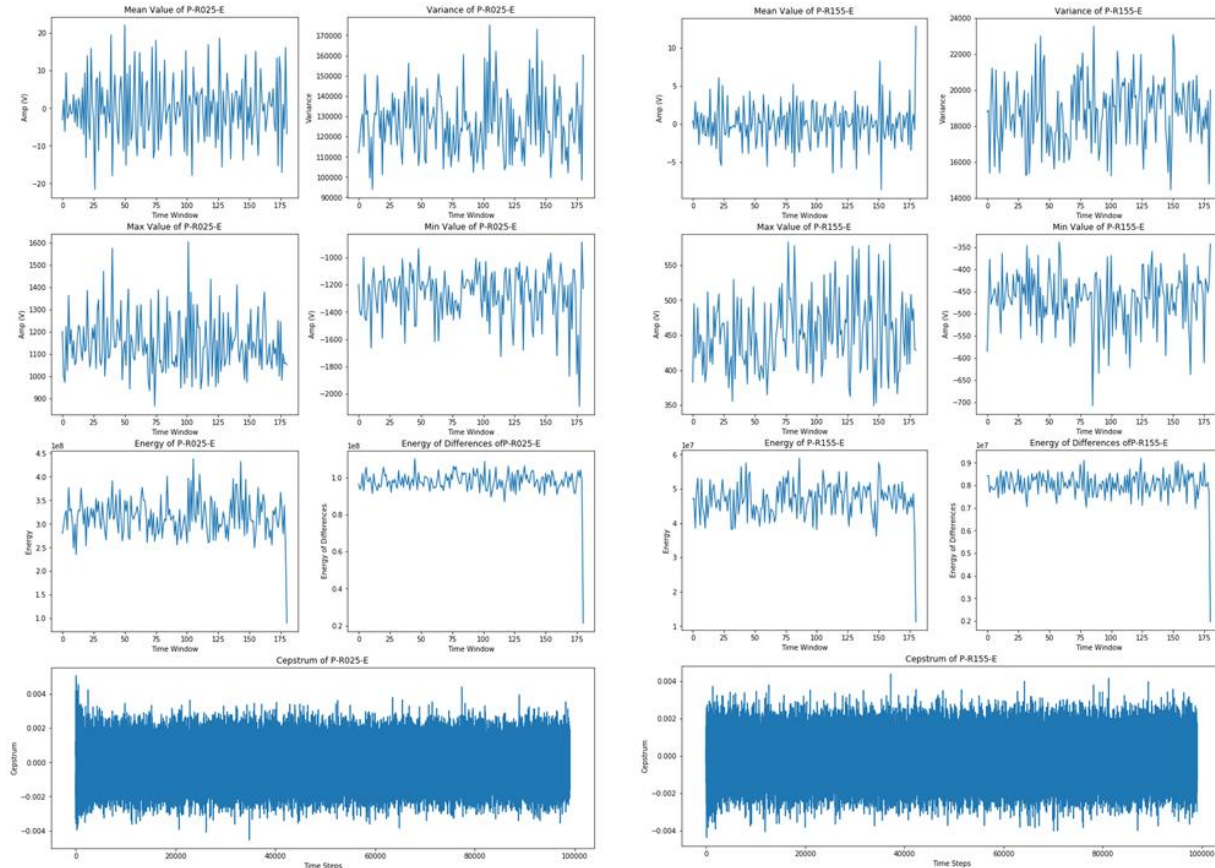
Figure 99: Pressure sensors P-R025-E and P-R155-E.

Figure 100 displays the most dominant frequencies of the pressure sensors P-R025-E and P-R155-E.
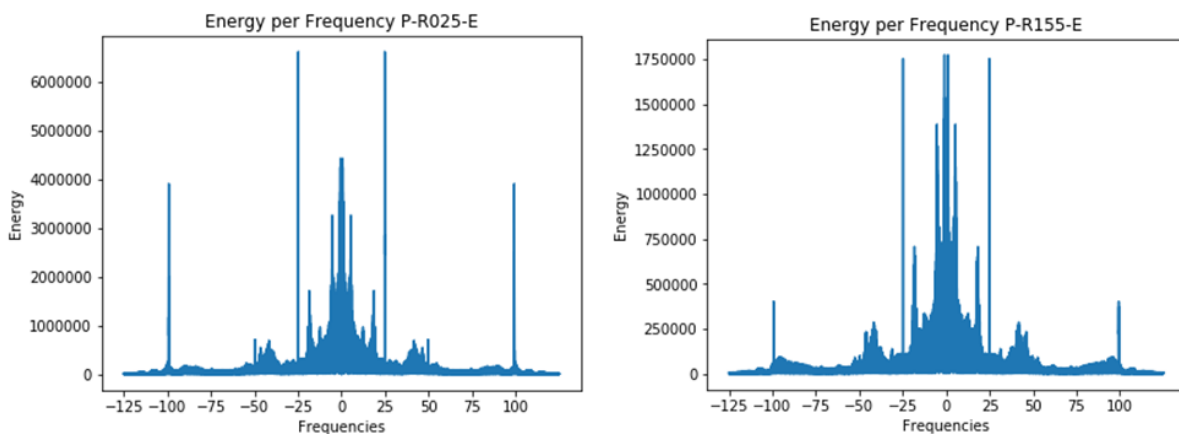
Figure 100: Most dominant frequencies of pressure sensors P-R025-E and P-R155-E

Some observations are given below:

- It is obvious that a much richer variety of frequencies are present in the pressure sensors. The most important peaks seem to be approximately around <5 Hz, 20 Hz, 25 Hz, 40 Hz and 100 Hz.

5.4.1.2 Cycles 31 & 32

In cycles 31 and 32, a similar behavior was detected regarding the change of frequencies over time. An interesting observation is the behavior of in-core sensors L-G10-2 and L-G10-6, which exhibit a high energy signal difference among the 3 cycles – see Figure 101 and Figure 102.
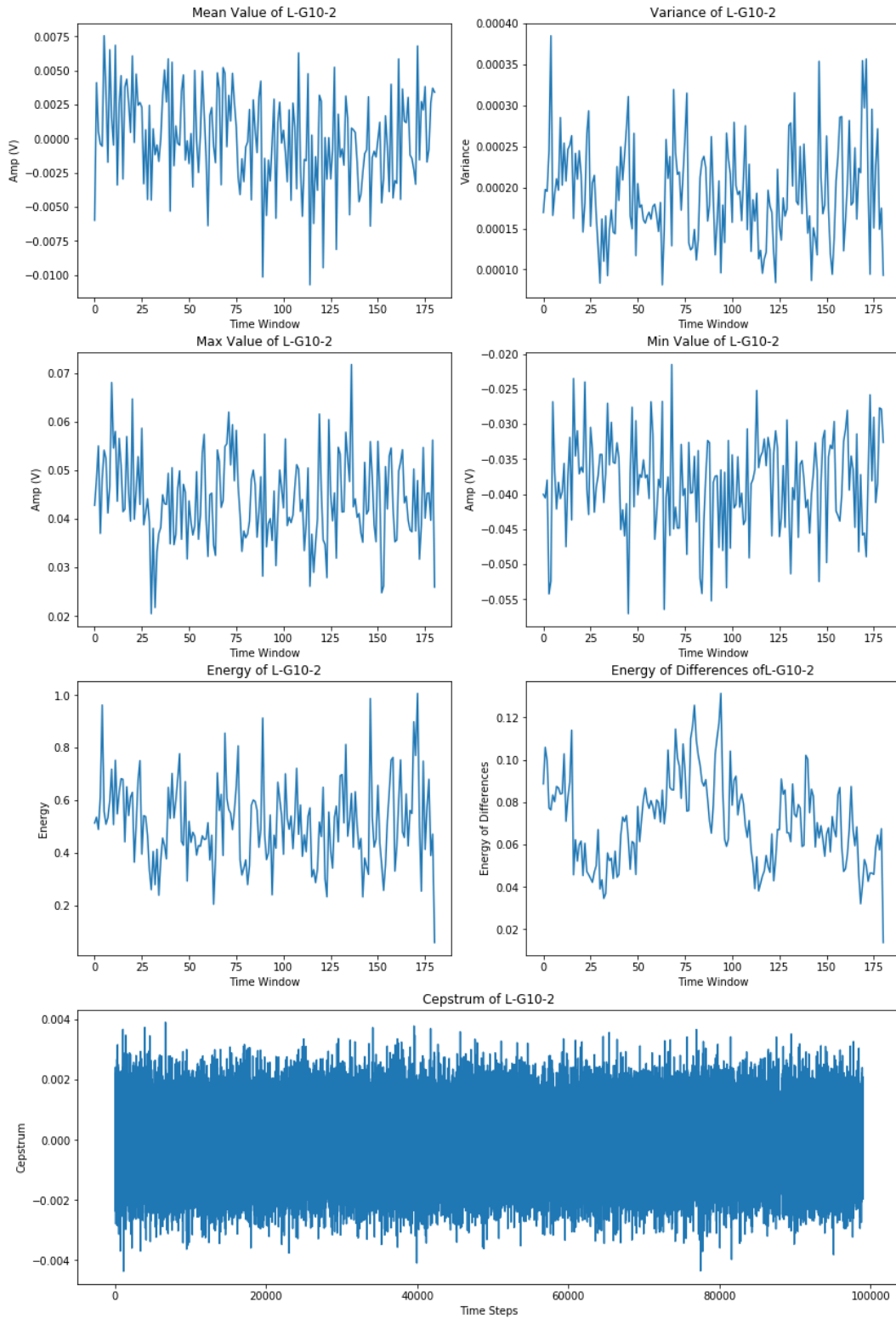
Figure 101: Energy difference characteristics of the in-core sensor L-G10-02 among the 3 cycles.
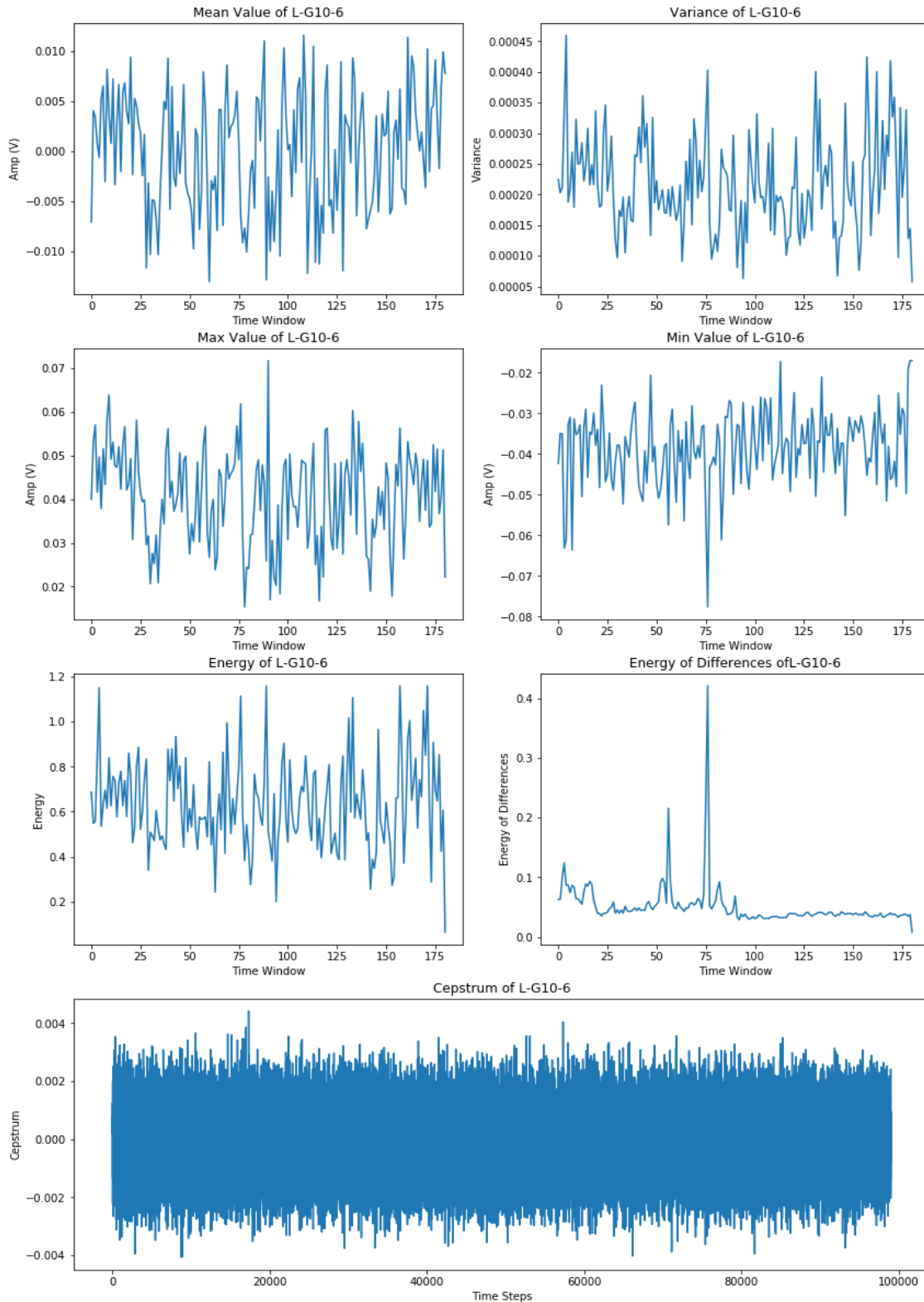
Figure 102: Energy difference characteristics of the in-core sensor L-G10-06 among the 3 cycles.

5.4.2 Comparison with simulated data

In this subsection, a spatial comparison will be made between the simulated data on the frequency domain and the actual plant measurements. The spatial comparison will determine areas where given perturbations are more likely to exist. This is achieved through the computation of the cosine similarity between the CPSDs of the actual measurements and the simulated data, for the different

location where a perturbation might occur. Then, a heatmap will be created with the similarity scores from each position in the grid where a perturbation has been simulated. Thus, we will be able to compare the likelihood of a perturbation happening in all areas of the reactor, but, also, we can compare the similarities between different perturbations.

From the feature and frequency analysis, we concluded that one of the most dominant frequencies of all signals in the 4-loop reactor is the 1Hz frequency. Thus, we have selected the 1Hz frequency for the simulated perturbations. The CPSDs were calculated between all fully working sensors (in cycle 30, 3 sensors were removed because of defects); 53 in total. Because the simulated data consist of only a single frequency, we selected only the CPSD value of that specific frequency from the plant measurements. So, a matrix of size 53x53 has been constructed for both real and simulated data for each perturbation. It should also be noted that the hyperparameters of ellipticity (k) and the direction of the vibration (θ) for fuel assembly and core barrel vibrations were kept constant at 0 both (the definition of those hyperparameters can be found in the CORTEX deliverable D3.1).

The examined perturbations include: (i) Absorber of Variable Strength (AVS), (ii) Travelling Perturbation (TP), (iii) Control Rod Vibration (CRV) and (iv) (Cantilevered, Supported, Cantilevered and Supported) Fuel Assembly Vibration (FAV).

5.4.2.1 Absorber of Variable Strength

Since neutron detectors are mostly sensitive to the energy group 2, the AVS experiments have been predominately focused on that group. Because there are many levels to plot, we selected the ones with the maximum similarity – see Figure 103. Both in energy group 1 and 2, maximum similarity occurred at coordinates (16,15,18), where the first coordinate corresponds to the horizontal axis, the second to the vertical axis and finally the third to the z-axis.
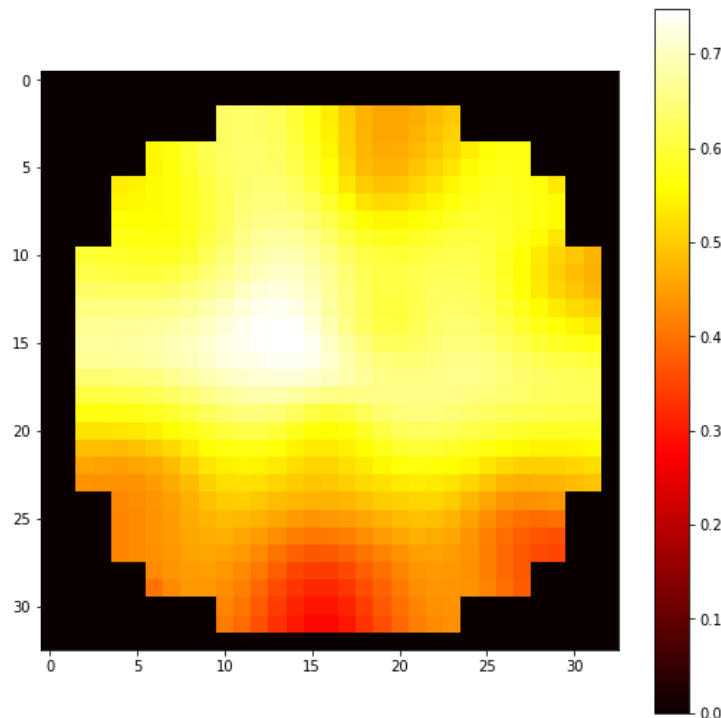
Figure 103: Heatmap of similarities of group 2 (z=18).

5.4.2.2 Travelling Perturbation

The TP experiments – see Figure 104 – showed a maximum similarity of 0.63 at (15,13). In this case, the coordinate system is two-dimensional (horizontal and vertical axis, respectively).
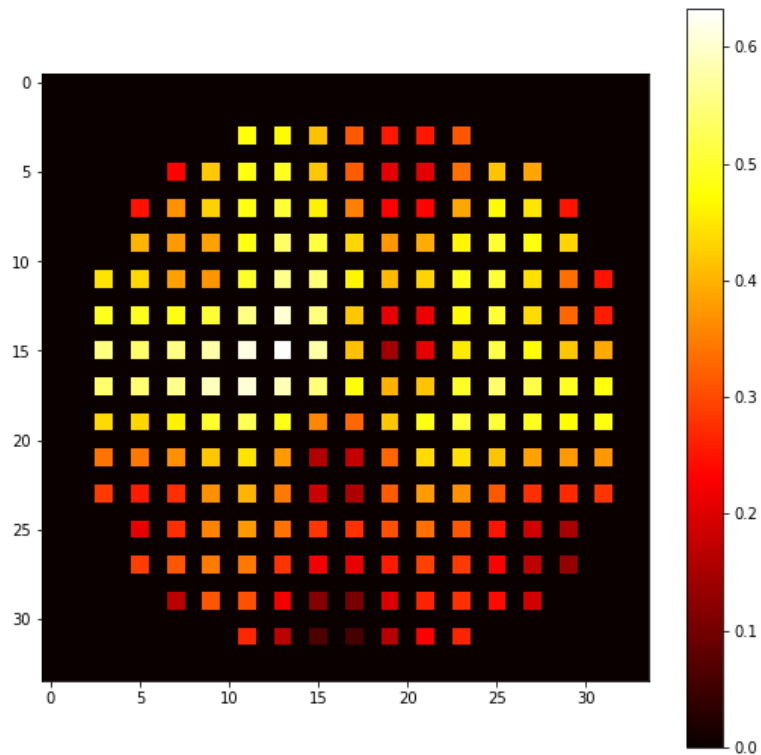
Figure 104: Heatmap of similarities of TP.

5.4.2.3 Control Rod Vibration

CRV experiments were conducted at two different levels on the z-axis, where z = {18, 31}. The maximum similarity for the z=18 level is located at (15,5) with value equal to 0.571 – see Figure 105. On the other hand, the maximum similarity of z=31 level is located at (17,3) with value equal to 0.448 – see Figure 106.
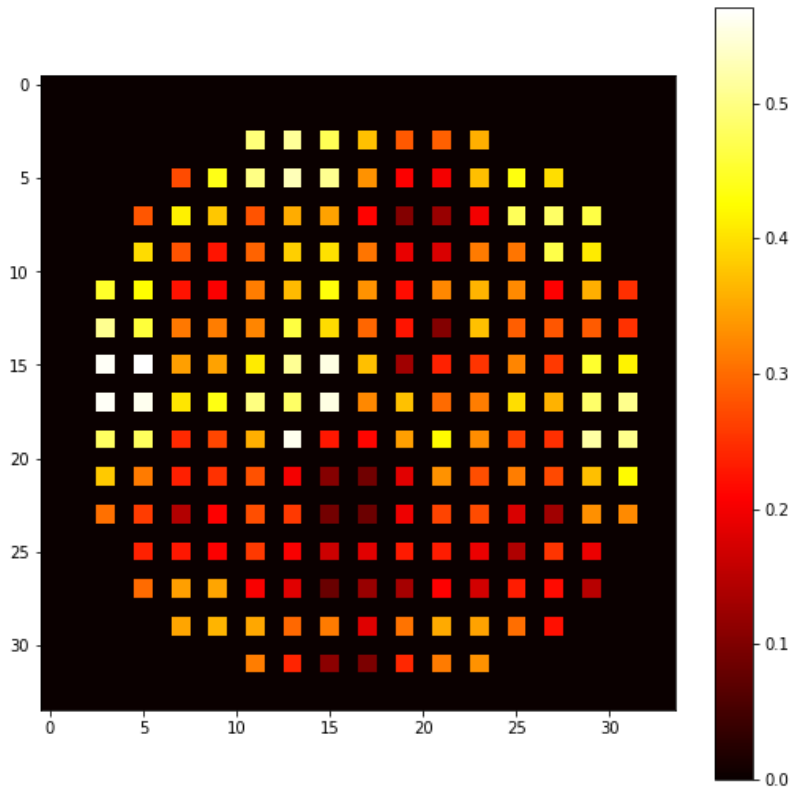
Figure 105: Heatmap of similarities of CRV at z=18.
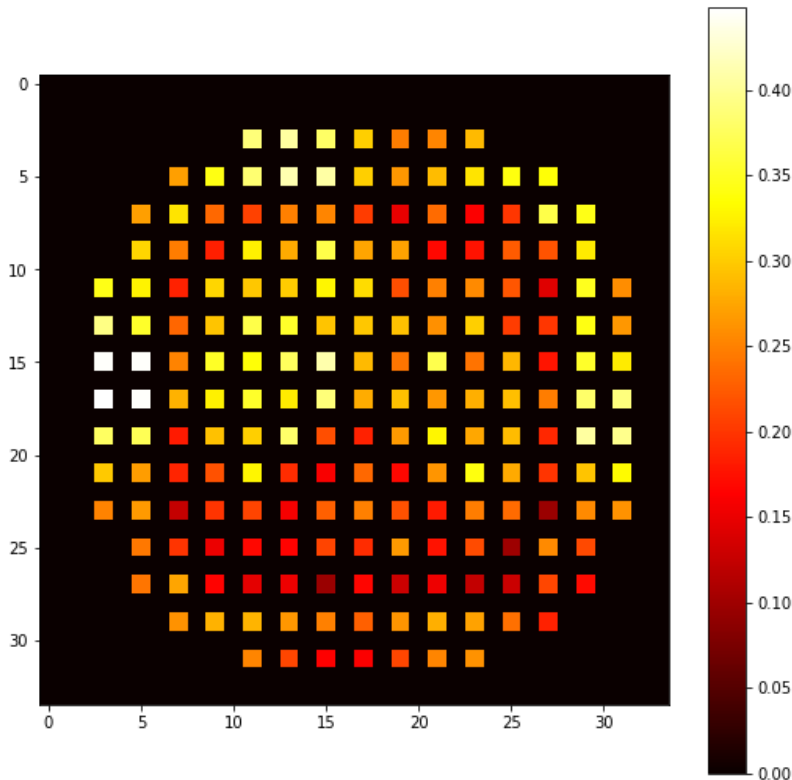
Figure 106: Heatmap of similarities of CRV at z=31.

5.4.2.4 Fuel Assembly Vibration

FAV experiments included Cantilevered mode, Supported mode and Cantilevered and Supported mode. In the first mode, maximum similarity was found at (11,9) with value equal to 0.751 – see

Figure 107. In the second mode, Maximum similarity was found at (15,15) with value equal to 0.752 – see Figure 108. Finally, in the third mode, maximum similarity was found at (15,13) with value equal to 0.766 – see Figure 109.
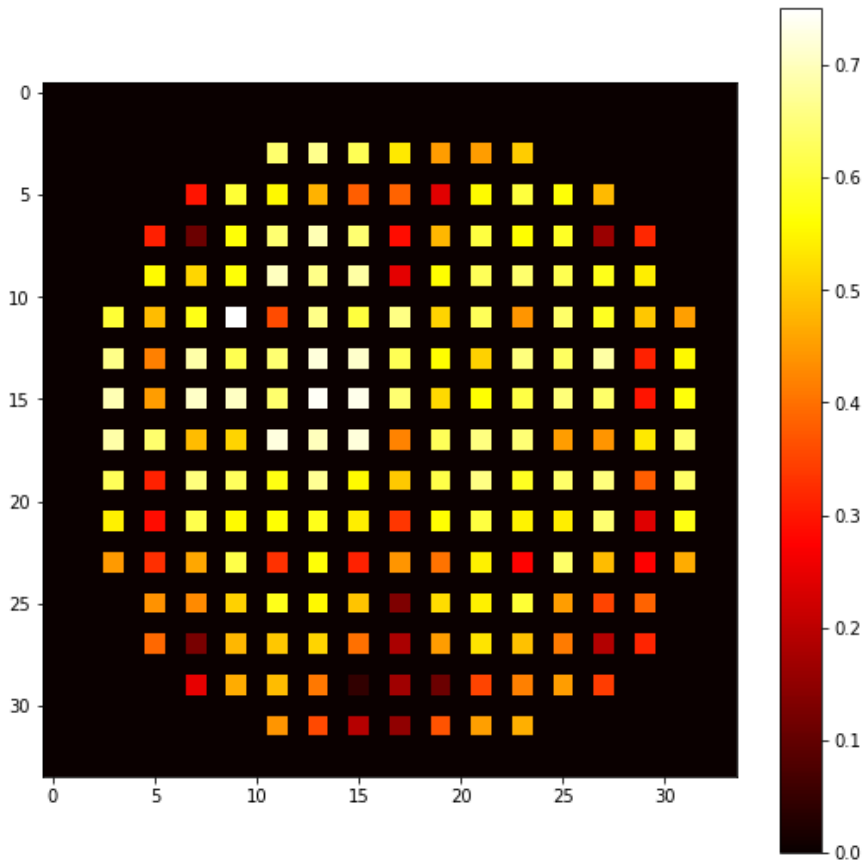
Figure 107: Heatmap of similarities of Cantilevered FAV.
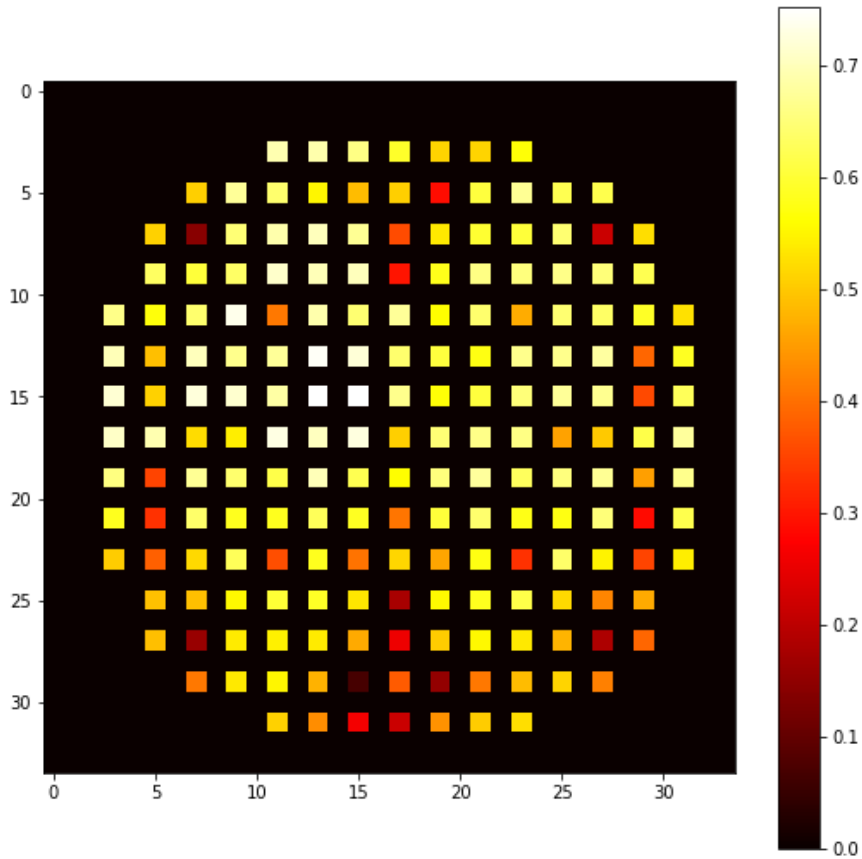
Figure 108: Heatmap of similarities of Supported FAV.
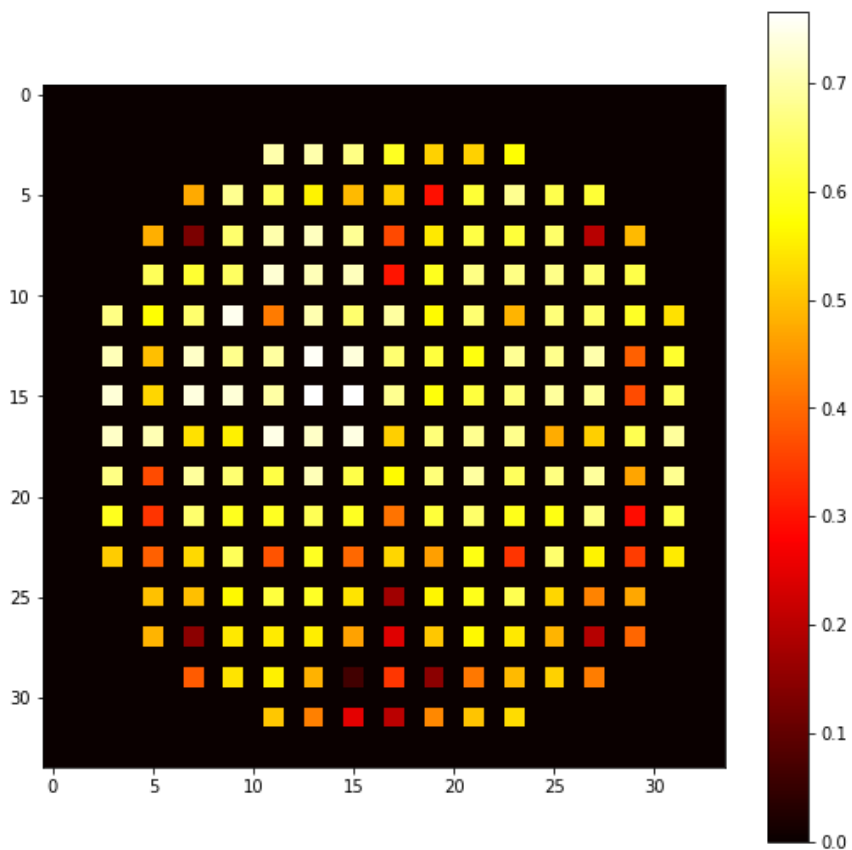
Figure 109: Heatmap of similarities of Cantilevered and Supported FAV.

5.4.3 Clustering

The clustering of the signals of the German pre-Konvoi 4-loop reactor has been performed, using the Autoencoder architecture of Figure 110, along with various clustering algorithms.
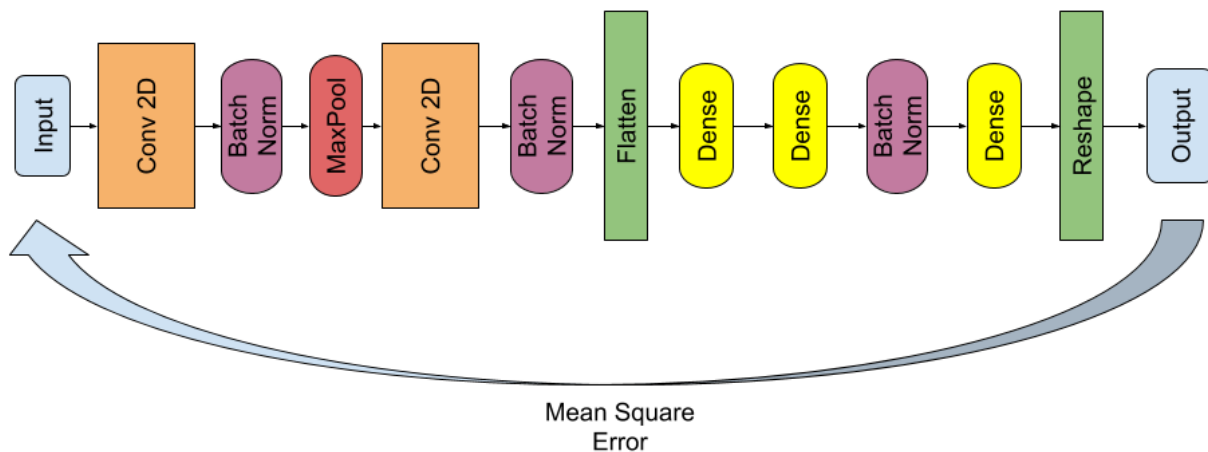
Figure 110: Autoencoder architecture used in the clustering of the German pre-Konvoi 4-loop signals.

The signals have been split into 10 s windows. Then, the spectrograms of each signal have been extracted and have been subsequently provided to the Autoencoder, which compressed them to a small vector of constant size (in our case, the vector has been set to 100). The reduced size helps the unsupervised algorithms to better group and distinguish each sample. After that, the clustering algorithms take the encoded form of each signal and separate them into clusters. The number of clusters that the signals will be divided into is a significant hyperparameter. We decided to set the number equal to 2, in order to force the algorithm to separate normal reactor states from outliers. In a similar manner to the clustering approach discussed above, the anomaly detection algorithms divided the data into normal and anomalous states.

Different algorithms tend to find different clusters, as every algorithm can find a different pattern of the data, providing better insight on the structure of the problem and the datasets. Any results that agree with each other have extra credibility, meaning that a robust pattern might have been identified, one that groups signals in an optimal manner. Because signals have been divided into two clusters, one of them is termed to be the majority cluster and the other the minority one, representing a slight abnormality. However, it is not necessary for abnormalities to occur and when in fact they do not, it is going to be noted. Below we are going to present the proportion of time

windows that got classified in the minority cluster and show how it can be connected with the results found from the feature extraction and analysis step discussed before.

Using the *k*-Means algorithm, we can see in Figure 111 that the sensors that appear to have the most out of the ordinary behavior are L-G10-2, L-G10-6, L-N12-2, L-J06-5, which quite agree with the observation made in the feature extraction section. Especially, sensor L-G10-2 seems to be extremely different from the rest, belonging to the minority cluster in its entirety. This means that almost every time window of L-G10-2 does not belong to the majority of the rest of the time windows.
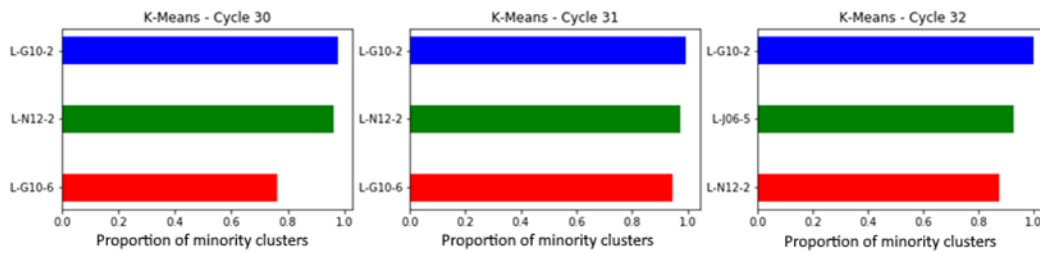
Figure 111: k-Means clustering of in-core signals.

Mean-Shift clustering still assigns L-G10-2 to the minority class, with the other 3 detectors mentioned above having a reduced proportion, as can be seen in Figure 112. These are similar results to *k*-Means clustering, despite the difference in proportions.
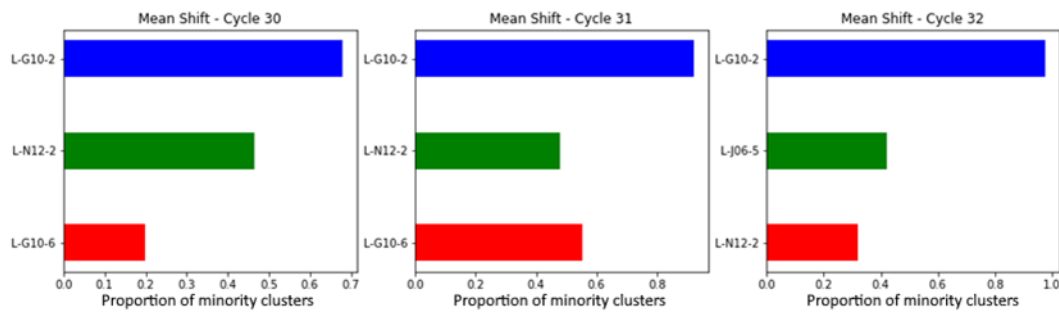
Figure 112: Mean-shift clustering of in-core signals.

DBSCAN did not identify any patterns that could distinguish somehow the signals or any time windows that could be considered anomalous. One-Class SVM, on the other hand, exhibits a similar behavior to the first two clustering algorithms, as shown in Figure 113, identifying 3 more sensors with similar behavior (L-O05-2, L-N12-4 and L-O05-4). Even though their proportions are quite smaller, it still is an indication of the algorithms' ability to locate abnormal behavior at various time windows.
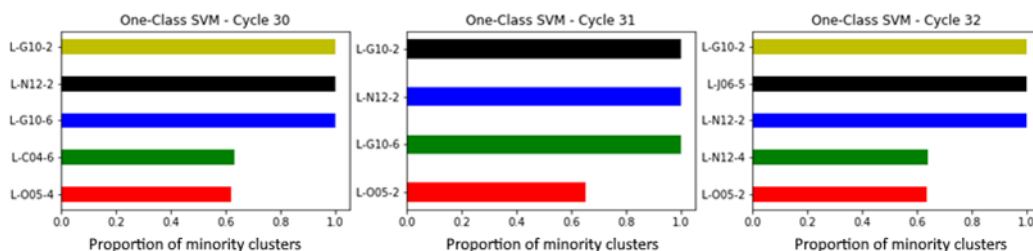
Figure 113: One-class SVM of in-core signals.

The Isolation Forest algorithm displayed similar results (Figure 114). Sensor L-G10-2 is the sensor that stands out again with L-N12-2, L-G10-6 and L-J06-5 coming next.
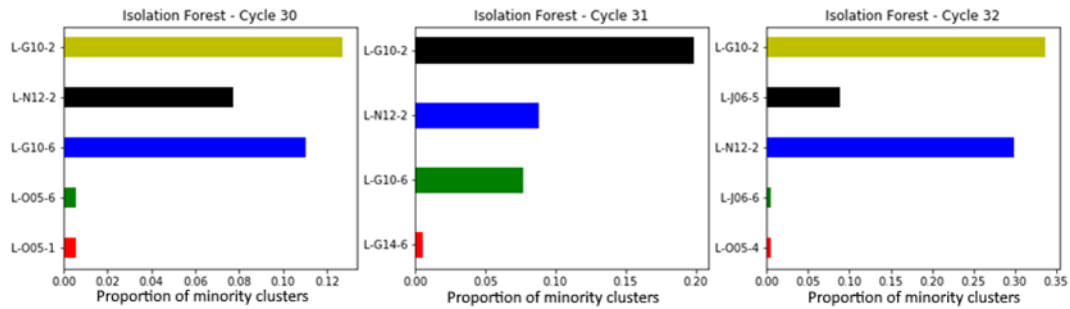
Figure 114: Isolation forest of in-core signals.

In conclusion, the unsupervised clustering and anomaly detection algorithms exhibited similar results. The sensors that have been identified as not normal were L-G10-2, L-N12-2, L-G10-6 and L-J06-5 – see Figure 115. Further analysis may reveal the causes of this differentiation.
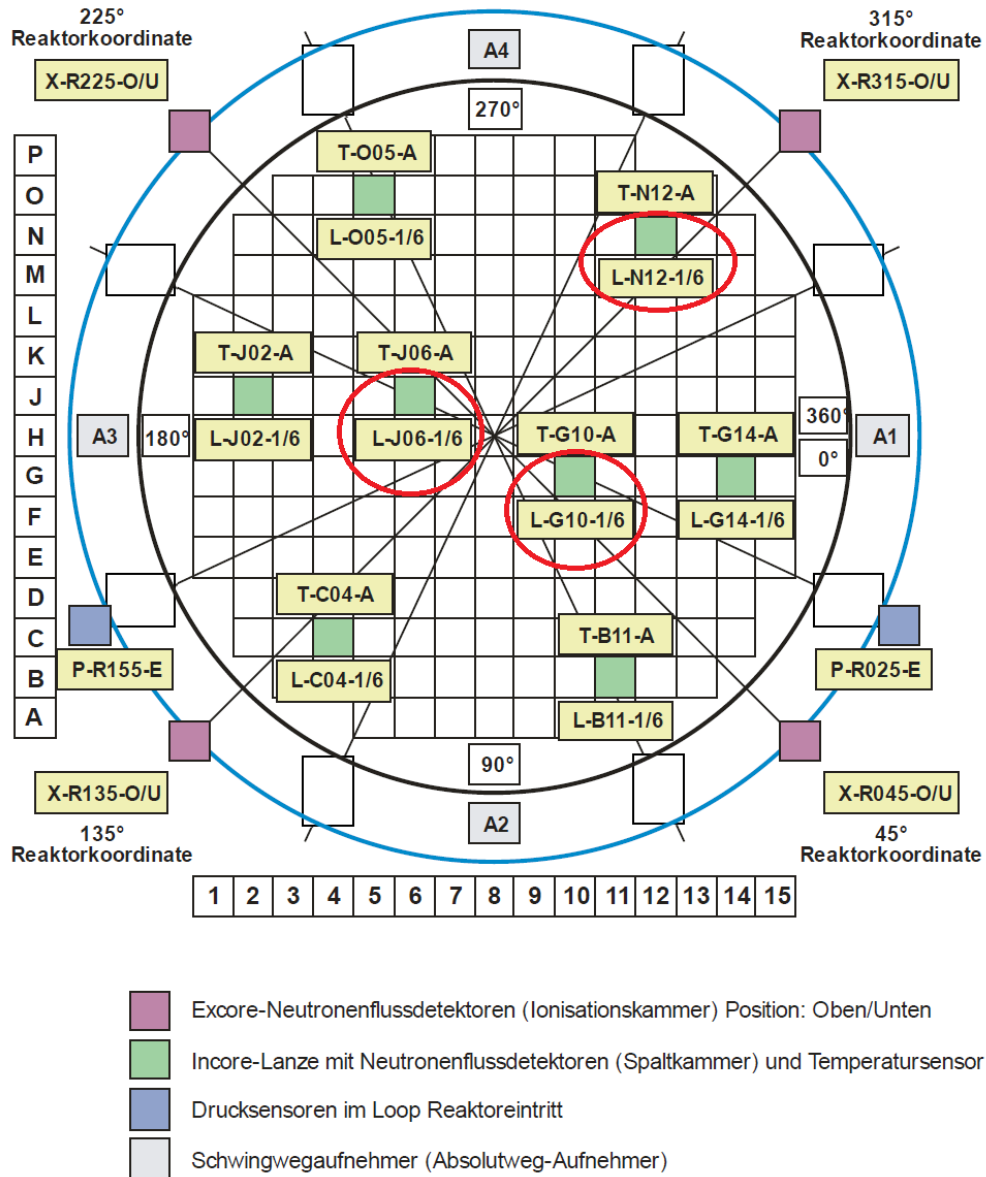
Figure 115: Location of signals exhibiting an abnormal behaviour (in red cycles).

5.4.4 Voxel-wise, semantic segmentation for simulated data classification and localisation of multiple, simultaneously occurring perturbations.

Handling multiple, simultaneously occurring perturbations is vital to successful classification of real plant measurements given that it is entirely probable, and in fact more than likely, that multiple perturbations will occur at the same time. Therefore, we propose a 3D convolutional, voxel-wise, semantic segmentation network extended from the deliverable D3.5 (Montalvo et al., 2020), trained and tested on CORE SIM+ (Mylonakis et al., 2020) reactor specific simulations.

This section outlines the data pre-processing, model architecture, and results trained and tested on the CORE SIM+ simulations of the German pre-Konvoi 4-loop. However, the data pre-processing and model are identical for both CORE SIM+ datasets (German and Swiss pre-Konvoi) with exception to input and output mesh dimensionality. Therefore, when discussing the Swiss pre-Konvoi 4-loop in Section 5.5.6, we refer to this section for implementation details and model architecture.

CORE SIM+ simulation data pre-processing

The dataset utilized in this section is the CORE SIM+ frequency domain dataset, for German pre-Konvoi 4-loop. However, this section also applies to Swiss pre-Konvoi 3-loop simulations, as both these reactor specific simulations are processed and handled identically, with exception to their dimensionality. For convenience, we will describe the process referring to the German reactor mesh of dimensions *34x34x34.* However, to describe the Swiss reactor mesh, simply undertake the same process with mesh dimensions *32x32x42.* Additional details will be given in Section 5.5.6 regarding the Swiss reactor.

The core stage of data pre-processing is the additive combination of single perturbations scenarios provided by the CORE SIM+ simulations. The combination process is like that described in the deliverable D3.5 (Montalvo et al., 2020), in which a selected number of perturbation scenario examples are combined within the same frequency, ensuring that no perturbations combined originate from the same source location. Also, as with all datasets, we maintain that perturbations originating from the same source location cannot be found across train, validation and test sets, avoiding the network testing on data it was trained on.

Before combination, the APSDs/CPSDs for the 36 in-core and 8 ex-core detectors are computed for each data sample (a single perturbation scenario for a given source location and frequency). At this stage, vibration parameters kappa and theta are provided in the APSD/CPSD calculation, where K = {0.25, 0.5, 0.75, 1.0} and θ = {¼π, ½π, ¾π, π} respectively. K and θ parameterize the vibration spectra of simulated vibrating perturbations, where $K \in [0,1]$ is the ellipticity or anisotropy of the vibrations, and $\theta \in [0, \pi]$ is the preferred direction of the vibration. Furthermore, for isotropic vibrations $K = 0$, for vibrations along a straight-line having angle θ, $K = 1$ (Demazière and Dokhane, 2019). The retrieval of vibration parameters, K and θ, are to be treated as a classification tasks, which for a vibration perturbation, we aim to classify which vibration parameter values relates to that noise response. The process of vibration parameter retrieval is discussed in the following section**.**

The combination of the data samples itself is performed via the addition of APSD/CPSD values. Although this may introduce complications due to cross-correlation of noise, it has been determined that given the time frame and scope of this project, combining noise before the APSD/CPSD calculation is a relatively challenging implementation undertaking. Nevertheless, the combined perturbation's APSDs/CPSDs are utilized as the input to the network. More specifically, the input into the network consists of the APSDs of every possible voxel position (34x34x34 voxels); the APSDs of the 48 detectors embedded into a volume (where all voxels but those of the detectors at their corresponding locations are zeros); the coherence of selected detectors with all other detectors embedded in the same manner as with the APSD. These volumes are concatenated channel-wise to produce a *(n+1)x34x34x34* volume, where *n* is the number of detectors chosen for the coherence of a detector with all other detectors. The 'n+1' originates from the fact that we also use the APSD of the detectors.

As with all previous methods in the frequency domain, the complex signals are decomposed into amplitude and phase components for use with ML frameworks. This results in a *2(n+1)x34x34x34* input volume. For the value of *n*, we conclude that 8 specifically chosen detectors for the coherence calculation is a good trade-off between number of channels and computation load, the detectors are: C4 axial 1, C4 axial 6, N12 axial 1, N12 axial 6, J2 axial 1, J2 axial 6, J6 axial 1, and J6 axial 6. We had concluded that using the coherence of all detectors to all other detectors introduces too many channels as an input to the network when utilizing our current approach. This results in a computational load that is too large to handle, therefore we only utilize the coherence between all detectors to 8 specific detectors as input. The use of all detectors is an ongoing investigation.

Finally, to help reduce computational load of the large core volumes and multiple channels, we reduce the core mesh by half, averaging across a *2x2x2* sub-section of the volume resulting in a

2(n+1)x17x17x17 volume. The intuition behind this choice is firstly, computational load. Secondly, given that CORE SIM+ models each assembly as *2x2* sub-assemblies, it is reasonable to assume for the case of classification and localization that a perturbation happening in a sub-assembly can be considered as occurring in the entire assembly.

3D fully-convolutional, semantic segmentation network for classification and localization of multiple, simultaneously occurring perturbations

A semantic segmentation network, extended from the deliverable D3.5 has been developed, inspired from (Kaul et al., 2020) to perform semantic segmentation on weakly supervised data (noisy, limited or imprecise sources are used in supervised ML tasks). Semantic segmentation is a methodology for the "linking" of each pixel in an input sample to a semantic (class) label, which has been mainly used in object detection and image-anomaly problems. In perturbation classification and localization, we aim to link each voxel in the input sample to a classification of the source voxel (i,j,k) at which that perturbation originates.
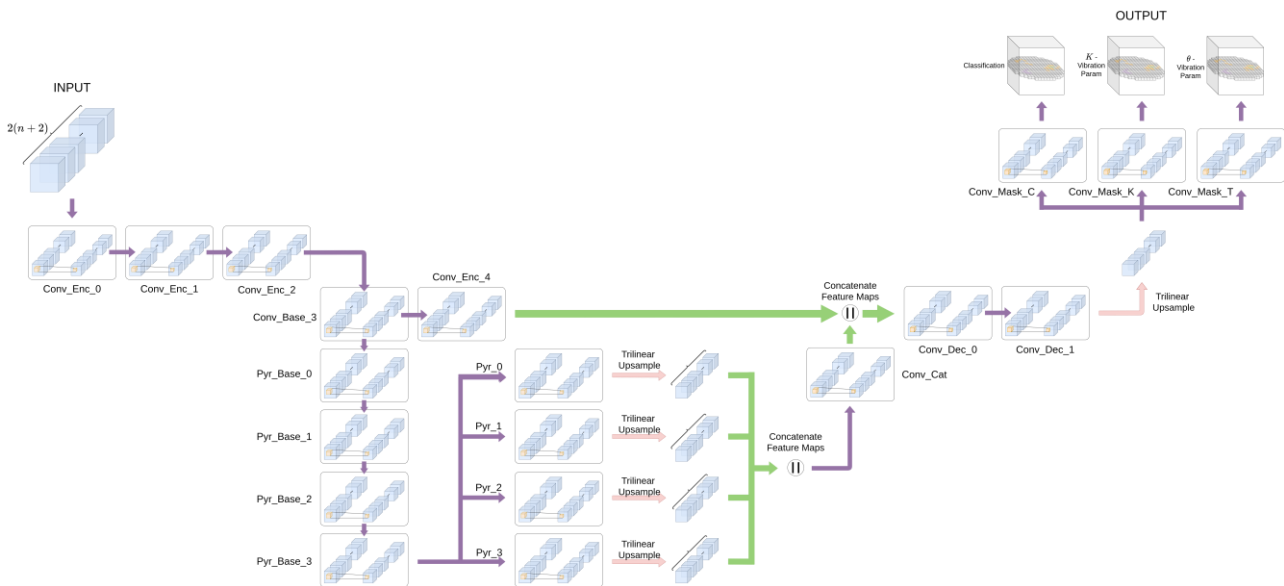
Figure 116: Fully-convolutional, modified RSS-Net architecture for pixel-wise semantic segmentation.

An encoder-decoder network is employed to extract high-dimensional feature representations of the input, with these latent vectors being decoded to the volumetric size of the input volume predictions – see Figure 116. The green arrows represent the concatenation of feature maps; the red arrows represent trilinear up sampling; the purple arrows represent direction/flow of the network. For network architecture details, refer to Table 7.

Table 7: Parameter values per layer for the fully-convolutional, semantic segmentation model depicted in Figure 116.

Layer	In Shape	Out Shape	In Feature	Out Feature	Kernel Size	Stride	Padding	Dilation
Conv_Enc_0	*17x17x17*	*17x17x17*	2(n+1)	32	7	1	3	1
Conv_Enc_1	*17x17x17*	*15x15x15*	32	32	5	1	3	2
Conv_Enc_2	*15x15x15*	*15x15x15*	32	64	5	1	2	1
Conv_Enc_3	*15x15x15*	*8x8x8*	64	64	3	2	2	2
Conv_Enc_4	*8x8x8*	*8x8x8*	64	48	1	1	0	1
Pyr_Base_0	*8x8x8*	*8x8x8*	64	128	3	1	1	1
Pyr_Base_1	*8x8x8*	*8x8x8*	128	128	3	1	2	2
Pyr_Base_2	*8x8x8*	*8x8x8*	128	128	3	1	1	1
Pyr_Base_3	*8x8x8*	*8x8x8*	128	128	3	1	2	2
Pyr_0	*8x8x8*	*8x8x8*	128	128	1	1	0	1
Pyr_1	*8x8x8*	*8x8x8*	128	128	3	1	1	1
Pyr_2	*8x8x8*	*8x8x8*	128	128	3	1	2	2
Pyr_3	*8x8x8*	*8x8x8*	128	128	3	1	3	3
Conv_Cat	*8x8x8*	*8x8x8*	128 * 4	128	1	1	0	1
Conv_Dec_0	*8x8x8*	*8x8x8*	128 + 48	64	3	1	1	1
Conv_Dec_1	*8x8x8*	*8x8x8*	64	32	3	1	1	1
Conv_Mask_C	*17x17x17*	*17x17x17*	32	10	3	1	1	1
Conv_Mask_K	*17x17x17*	*17x17x17*	32	5	3	1	1	1
Conv_Mask_T	*17x17x17*	*17x17x17*	32	5	3	1	1	1

The model proposed and depicted in Figure 116 is a variation of (Kaul et al., 2020) in which a fully convolutional network is employed, utilizing an encoder-decoder structure. As with the deliverable D3.5, the output of the network is a prediction mask of perturbation classes of size *17x17x17*, where each voxel represents perturbation origin and classification of that perturbation. Like with the deliverable D3.5, this network replaces pooling operations with strided convolutions to reduce information lost to down sampling. Also dilated convolutions (Wei et al., 2018) are introduced to capture more information with a larger receptive field, consequently assisting with the sparse nature of a limited number of detectors. Furthermore, we utilize CoordConv (Liu et al, 2018) to help maintain spatial information of the features. This is achieved by informing convolution kernels where they are in relation to the input activation, by introducing layer-wise cartesian coordinates of voxel positions. A notable design feature is the spatial pyramid pooling block (four bottom blocks of the network). It is implemented to learn rich semantic features at various scales, using four convolutions of differing kernel size, stride, and dilation to capture different information across scales.

In addition to our modified RSS-Net, we output three prediction masks, a classification mask, and two vibration parameter masks (K and θ). Given three output segmentation tasks, the network is trained to minimize a weighted sum of three focal losses, one for each task. Focal loss (Lin et al., 2017) is given in Equation 25 where γ represents a tunable focusing parameter to adjust the rate that easy-examples are down-weighted. The final loss is given by Equation 26.

$$FL(y, \hat{y}) = -\frac{\lambda_1}{P} \sum_{p=1}^{P} \left[y_p (\alpha_p (1 - \hat{y}_p)^\gamma \log(\hat{y}_p)) + (1 - y_p)((1 - \alpha_p) \hat{y}_p^{\gamma} \log(1 - \hat{y}_p)) \right] \qquad (25)$$

$$L(X;\mathbf{W}, \lambda_1, \lambda_2, \lambda_3) = \lambda_1 \cdot FL(y_1, \hat{y}_1) + \lambda_2 \cdot FL(y_2, \hat{y}_2) + \lambda_3 \cdot FL(y_3, \hat{y}_3) \tag{26}$$

P is the number of perturbation classification types. Subscripts 1, 2, and 3 represent tasks: perturbation classification, K vibration parameter retrieval, and θ vibration parameter retrieval respectively.

Additionally, a logarithmic class weighting scheme from (Kaul et al., 2020) has been employed to combat class imbalance between foreground classes (perturbations) and background classes (no perturbation). The loss function is weighted, α, depending on the true class using logarithmic weighting. The 'background' or nothing class is given a weight of 0.25 as this was empirically found to be the most appropriate weight for the classification task.

Experimental results on CORE SIM+ simulated data

Experimental results have been obtained for different numbers of combined perturbations. We aim to see how our model performs given different quantities of simultaneously occurring perturbations. As previously described, single perturbations are additively combined with the number of randomly chosen combinations lying within the range [1, x], where x denotes the maximum number of combinations for that experiment. In this case we choose x to be 15, 30, and 45.

The training procedure utilized the Stochastic Gradient Descent (SGD) optimization procedure for back propagation, with a starting learning rate of 0.01, decaying by a factor of 0.1 when the validation loss plateaus for 10 epochs within a threshold of 0.025. Additionally, a batch size of 64 was used and a gamma of 2 implemented as the modulating factor of the Focal Loss previously defined. The results of experiments are outlined in Table 8 for classification, Table 9 for retrieval of vibration parameter K, and Table 10 for retrieval of vibration parameter θ.

Table 8: German pre-Konvoi 4-loop simulated, per perturbation classification voxel accuracies for voxel-wise semantic segmentation of the unseen test set.

Per Class Voxel Prediction Accuracies *											
No. Comb	No. Det	Accuracy (%)									
		BG	AVS	CANT	SF	SS	CSF	CSS	CR	TP	BV
15	56	99.08	90.47	92.98	86.49	93.02	97.62	97.22	83.06	94.74	100.00
30	56	99.64	85.97	81.48	90.48	97.37	90.24	95.12	90.21	93.25	100.00
45	56	99.35	82.28	88.00	87.50	89.23	90.00	92.42	88.99	93.20	100.00

* Note: AVS = Absorber of Variable Strength, CANT = Fuel Assembly Vibration Cantilevered, SF = Fuel Assembly Vibration Supported First, SS = Fuel Assembly Vibration Supported Second, CSF = Fuel Assembly Vibration Cantilevered Supported First, CSS = Fuel Assembly Vibration Cantilevered Supported Second, CR = Control Rod Vibration, TP = Travelling Perturbation, BV = Core Barrel Vibration, BG = Background / No Class

Table 9: German pre-Konvoi 4-loop simulated, per perturbation vibration parameter, kappa, classification accuracies for the unseen test set.

Per Class Voxel Prediction Accuracies for Kappa Vibration Parameter					
No. Comb	No. Det	Accuracy (%)			
		BG	K=0.25	K=0.5	K=0.75	K=1.0
15	56	58.39	39.11	10.14	26.13	38.85
30	56	25.58	45.95	14.34	28.52	39.57
45	56	34.22	33.01	11.56	42.76	20.63

Table 10: German pre-Konvoi 4-loop simulated, per perturbation vibration parameter, theta, classification accuracies for the unseen test set.

Per Class Voxel Prediction Accuracies for Theta Vibration Parameter						
No. Comb	No. Det	Accuracy (%)				
		BG	$\theta=\frac{1}{4}\pi$	$\theta=\frac{1}{2}\pi$	$\theta=\frac{3}{4}\pi$	$\theta=\pi$
15	56	67.19	43.94	19.13	25.28	47.68
30	56	32.87	33.44	20.39	30.42	33.89
45	56	55.61	28.81	19.35	32.79	22.25

Accuracy per class is the performance metric of choice, defining the number of correctly classified voxels belonging to that class across the volume, averaged across the test set. In addition to per class accuracy metric, normalized confusion matrices are provided in Figure 117 for the best performing model. Note that these models have been ran only once and the best results presented above. Other methodologies have results presented as the mean of multiple runs. Nevertheless, given the computation time to process this data, this was found impractical in the present time frame.

As can be seen in Table 8 the results of classification and localization of multiple, simultaneously occurring perturbations performs well across all numbers of combinations. As we cannot see truly the performance from per class accuracies, it is further confirmed by the normalized confusion matrices shown below. It is noticed that it is often the case that the drop of performance comes from miss classifying a perturbation as not being present, i.e. not detecting a perturbation, false negatives. This is somewhat more promising from our perspective given that the network can determine between classes with high accuracy showing that our model learns good semantic understanding of the input volume. The issue of false negatives mainly arises in the absorber of variable strength classification. We make the assumption – as we will elaborate on later – that the more varied nature of absorber of variable strength origin introduces vastly larger variance into localizing this class complicating such localization. Work will continue to improve the detection of perturbations in the case of high numbers of simultaneous perturbations.
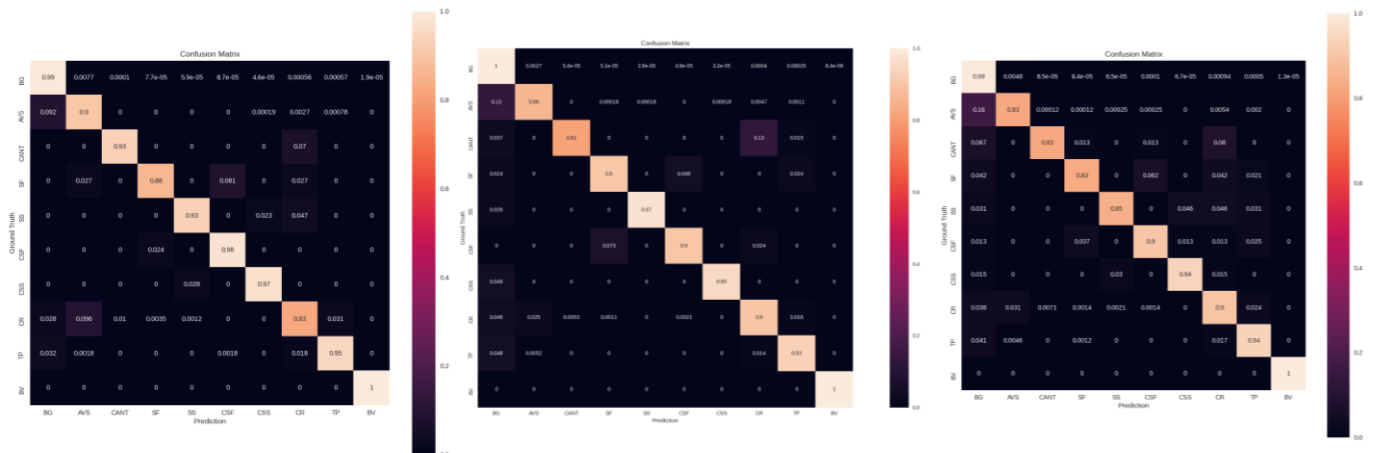
Figure 117: Normalized confusion matrix for each run of differing max combinations for per class per voxel classification accuracy for German pre-Konvoi simulations. This ground truth against predicted voxels per classification. Left: max number of combinations = 15. Middle: max number of combinations = 30. Right: max number of combinations = 45.
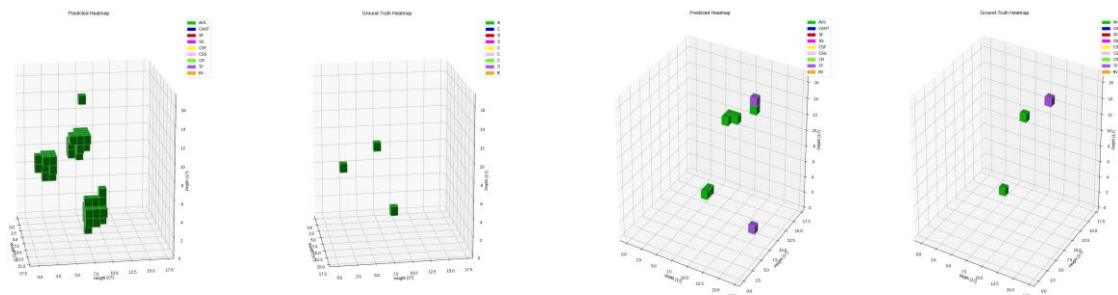
Figure 118: Visualizations of predictions and ground truth perturbation classifications and localizations in the core volume for x = 15. The prediction and ground truth of 3 absorber of variable strength perturbations (left two plots); the prediction and ground truth of 2 absorber of variable strength perturbations and 1 travelling perturbation (tight two plots).

It is also to be noted that increasing the number of simultaneous perturbations impacts the performance of more sporadic perturbations such as absorber of variable strength. We conjecture that due to the more uniform structure of fuel assembly vibrations, control rod, and barrel vibrations that there are far fewer variations of which this perturbation can originate, somewhat simplifying the problem for these classifications. This is further supported by the reduction in absorber of variable strength accuracy as number of combined perturbations increases. Additionally, this hypothesis can be visually supported by Figure 119 where predictions of absorber of variable strength tend to be less precise, with predictions occupying the space around the ground truth (the true source location of the simulated perturbation) source location. On the other hand, the travelling perturbation is predicted at the top and bottom of the core volume at the same azimuthal coordinates, giving a more precise prediction.

As for retrieval of vibration parameters, more work is necessary to improve the accuracy of the parameter retrieval. It is a non-trivial task given the number of additional noise sources coming from various other perturbations that obscure the noise induced by vibrations. Additionally, with the current system, the retrieval of these parameters relies heavily on the performance of the classification and localization. In future, we aim to reduce this dependency and investigate more appropriate pre-processing steps to ensure that information is maintained and most appropriately utilized in the feature extraction process. We believe there is much room for improvement given more time for tuning, and further testing regarding these values. We will continue our efforts to ensure that classification, localization and parameter retrieval of multiple, simultaneous perturbations is of the best quality we can produce.

5.4.5 *Self-supervised domain adaptation for real plant data training and inference*

It is important to ensure that robust and effective networks are developed to allow for accurate adaptation and inference of real plant data from models trained with simulation data. Therefore, we utilize models trained and tested on vast quantities of simulated data from Section 5.4.4 to transfer knowledge to make predictions given real plant data. More specifically, we utilize a method of domain adaptation through self-supervision to learn to reduce the naturally occurring domain shift between simulated and real plant measurements.

As with the previous Section 5.4.4, we define the data pre-processing and ML implementation with the German pre-Konvoi 4-loop. However, the methods described here are identical to the Swiss reactor with exception to core dimensionality. Details discussing the difference to the Swiss pre-Konvoi are given in Section 5.5.7.

Plant measurement pre-processing

Self-supervised domain adaptation (DA) utilizes both simulated and real plant data to train the network. DA aims to train a network to perform the necessary tasks whilst also minimizing the difference between source (simulated) and target (real) domains interpreted by the network. Therefore, we utilize the same pre-processing for the simulated German pre-Konvoi 4-loop described in Section 5.4.4.

As for the real plant data, we first take processed measurements from UPM – the process of which is described in Section 4 and the deliverable D3.5 (Montalvo et al., 2020) – and aim to arrange them in a manner that is identical to that of the simulated data. The reasoning is that we want for data inputs from both domains to be identical in arrangement. To achieve this, we embed all detector APSDs into a *17x17x17* volume at their corresponding locations within the core. We additionally provide further inputs using coherence of selected detectors to all other detectors, as done with the simulated data. The value for *n* remains the same, 8, as does the detectors chosen – the detectors are: C4 axial 2, C4 axial 6, N12 axial 1, N12 axial 6, J2 axial 1, J2 axial 6, J6 axial 1, and J6 axial 6.

Moreover, it is also documented that for measurements from the 4-loop pre-Konvoi, certain detectors are in fact pressure detectors and not simulated. Consequently, we remove these detectors (G14-2, C04-1, and G10-3) from the input of both real and simulated data. Furthermore, we do not include temperature sensors throughout our work, only considering the in-core and ex-core neutron detectors. Given that we have available only one set of real measurements with limited number of samples with the intention to perform inference on the frequencies that the simulations provide, we split the real plant measurements into a train and test set. Note we do not need validation as we have no metric of performance as the data is unlabeled, therefore a validation set is redundant. The train set of real data is constructed of the samples from frequencies that lie in between the frequencies simulated, e.g. 11.5 Hz. The test set is therefore constructed of the frequencies that are simulated, e.g. 11 Hz, 12 Hz. The test set samples are the predictions presented in the following section.

Unsupervised domain adaptation through self-supervision for multiple, simultaneously occurring perturbation classification and localization

To provide a short summary, domain adaptation considers the setting in which the task between each distribution setting source and target remain the same, yet the distributions themselves differ. The difference between the source and target distributions is commonly referred to the covariate shift, or domain shift, where DA aims to learn a discriminative classifier or other predictor in the presence of a shift. We aim to learn a discriminative classifier for classifying perturbations in the presence of a domain shift from simulated to real data, the classifier is trained to align the two domains in some shared feature space represented by the discriminative model. Self-supervised learning on the other hand, is a methodology for learning good representations from unlabeled data by auxiliary tasks, which are generated from the data itself rather than by human interaction/labelling. Predicting by how much an input has been rotated is one example of such auxiliary task. The goal of this is to learn good generalized features of the input that can be considered useful for downstream semantic tasks.

The methodology we employ is unsupervised domain adaptation through self-supervision, proposed by (Sun et al., 2020). The idea is to achieve alignment between the source and target domains through training a model on the same task for both target and source domains simultaneously. As we do not have labelled in the target domain, we use self-supervised auxiliary tasks to provide a unified task across domains. Each task is designed to induce alignment through capturing information that is structurally relevant across both domains. This encourages the network to align both domains through the understanding of spatial augmentation.

Depicted in Figure 119 is the network architecture and training procedure for both input domains and output tasks. The feature extractor network is that proposed in Section 5.4.4 pre-trained on only simulated data. Both the source and target domain data are used simultaneously to train the network. Both are fed through the network identically to the simulated case. However, the output of the feature extractor network is the layer before the classification layers. This is due to the addition of the auxiliary tasks that do not provide any downstream classification. Both source and target domain data are fed to the auxiliary tasks: rotation prediction, flip prediction, and patch prediction. Each of the auxiliary tasks provide an individual loss in addition to the loss produced by source domain classification tasks. The combination of these losses via weighted sum produce the final loss to minimize during training. The auxiliary loss is given by Equation 27 and the weighted sum given by Equation 28.

$$L_T(y_T, \hat{y}_T) = \frac{1}{C} \sum_{C=1}^{C} \Big[y_T^c \cdot \log(\hat{y}_T^c) + (1 - \hat{y}_T^c) \cdot \log(\hat{y}_T^c) \Big] \tag{27}$$

$$\begin{aligned} L(X_S, X_T; \mathbf{W}, \lambda_1, \lambda_2, \lambda_3) = (\lambda_1 \cdot FL(y_1, \hat{y}_1) + \lambda_2 \cdot FL(y_2, \hat{y}_2) + \lambda_3 \cdot FL(y_3, \hat{y}_3)) \\ + L_{T1}(y_{T1}, \hat{y}_{T1}) + L_{T2}(y_{T2}, \hat{y}_{T2}) + L_{T3}(y_{T3}, \hat{y}_{T3}) \end{aligned} \tag{28}$$

T is a given auxiliary task; *C* is the number of classes for the auxiliary task *T*. $\lambda_1, \lambda_2, \lambda_3$ and *FL* are defined in Equation 25.

The pretext tasks are simple SoftMax, linear classification layers, each aiming to correctly classify which augmentation has been applied to both source and target input data volumes. The rotation task aims to classify whether the input has been rotated by 0, 90, 180, or 270 degrees clockwise. Flip Task aims to classify if the input has not been flipped, horizontally flipped, or vertically flipped. Lastly the patch task breaks the volume into four sub volumes, one of which is fed to the network. The network is tasked to predict which of the four sub-volumes was fed into the network.

At inference time, the target domain data of the desired frequencies are input to the feature extractor, a resulting set of predictions are made for perturbation classification, and vibration parameters K and θ. Prediction masks made for each frequency are presented in the following sub-section along with comparisons with the signal analysis methodologies presented throughout this report. The network had been trained identically to the simulated case for 1 - 45 randomly combined simultaneous occurring perturbations.
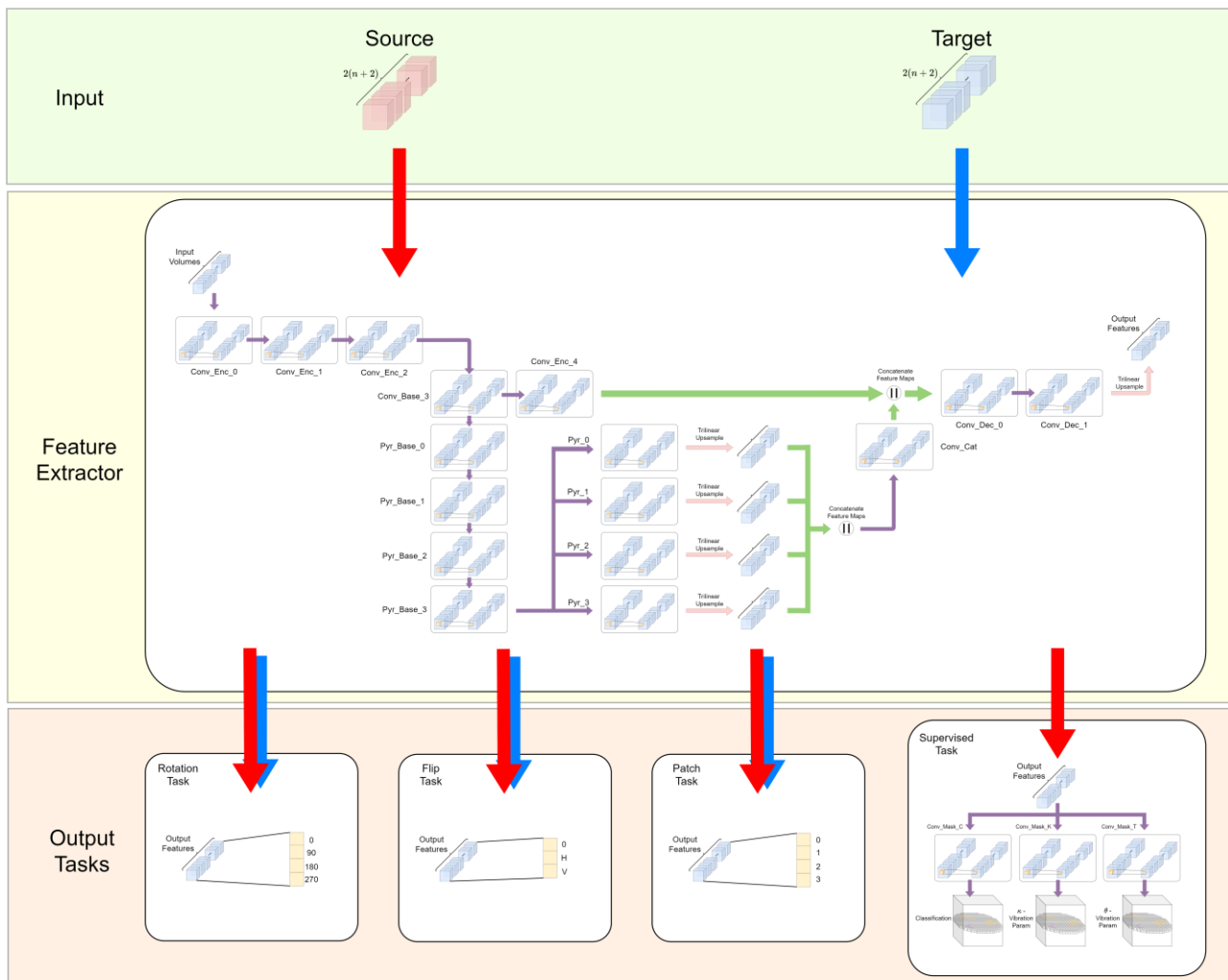
Figure 119: Self-supervised domain adaptation network depicting the previously defined segmentation network (feature extractor). The three auxiliary tasks and three supervised down-stream (supervised) tasks are shown. The red arrows represent flow of source (simulated) data and the blue arrows represent flow of target (real) data.

Anomaly prediction and analysis of plant measurements

The results of inference on real plant measurements for the German pre-Konvoi 4-loop for middle of cycle 30 are discussed here. The model was trained on simulated data and domain adaption methodology applied to reduce covariance shift, the details of which are previously discussed. Additionally, we only consider the prediction of anomaly type/classification and source location of the anomaly, we do not predict the vibration parameters or amplitudes in this case. Moreover, we also do not predict the control rod vibrations insertion level, instead we trained the model to predict a control rod vibration, assuming that it occurs in that assembly throughout the whole assembly height. We display such anomalies with axial views (top down) of the assemblies for clearer interpretation, all figures are defined with a voxel-wise Cartesian coordinate system (i, j, k).

This sub-section places emphasis on comparison to analytical signal processing techniques made in the deliverable D3.5. Of course, the predictions made are not validated, nor can be considered accurate at this stage. Further processing and analytical comparisons need to be made to ensure the correct adaptation to reduce domain shift has taken place and that the model is in fact capable of performing inference on real plant measurements. On the other hand, the initial predictions are positive and align with some aspects of the signal processing findings.

First, we notice that in the lower frequencies there is a consistent prediction of travelling perturbations originating from the lower level cartesian coordinates, (*2, 2*), (*12, 2*), (*2, 12*), and (*12, 12*) travelling vertically upwards in the core, from k=0 to k=16. This anomaly is present in the frequency ranges 0.1 Hz – 2 Hz, aligning with the analysis provided in the deliverable D3.5 section 2.4.3.1 and Section 4.1 of this deliverable in which it is hypothesized that transport phenomenon is present. This can be seen visually in Figure 120 where 0.5 Hz, 0.7 Hz, 1 Hz, and 2 Hz prediction maps are shown. For additional detail, the model itself has been trained with travelling perturbations originating from all possible (i,j) cartesian coordinates within the core at the lowest vertical level of the core (k=0), in other words, any axial position in the core, not just the inlet locations, avoiding possible bias towards the inlet locations. This is due to the model being trained for a large variation of origin locations meaning a random prediction, or a prediction from misunderstood input would not result in such uniform origins. This adds further weight to the prediction that travelling perturbations are present within the same regions across many frequencies.

Throughout the lower frequencies, there is a consistent block of control rod-vibrations running diagonally when viewing on a horizontal plane (*i, j* cartesian plane), this can be seen in the second and third columns of Figure 121. Throughout the measurement period of MOC 30, the control rods are located by the black crosses in the following figures. Throughout the measurement period control rods remain stationary, inserted 3 axial levels into the core from top to bottom for the real plant measurements.. The control rod predictions are somewhat consistent with the locations of the control rods, showing signs of variance in the predictions. Moreover, every prediction made – if not at a control rod location – is located at neighboring positions at furthest. Finally, again at the lower frequencies, we observe a fuel assembly vibration prediction in the area (*13, 13, -*) which is indicated by the magenta and yellow voxels. We are skeptical of this reading given how close it lies to the predicted travelling perturbation. Additionally, as fuel assembly vibration response does not occur at these low frequencies we conjecture that this is merely a mis-classification of travelling perturbation.
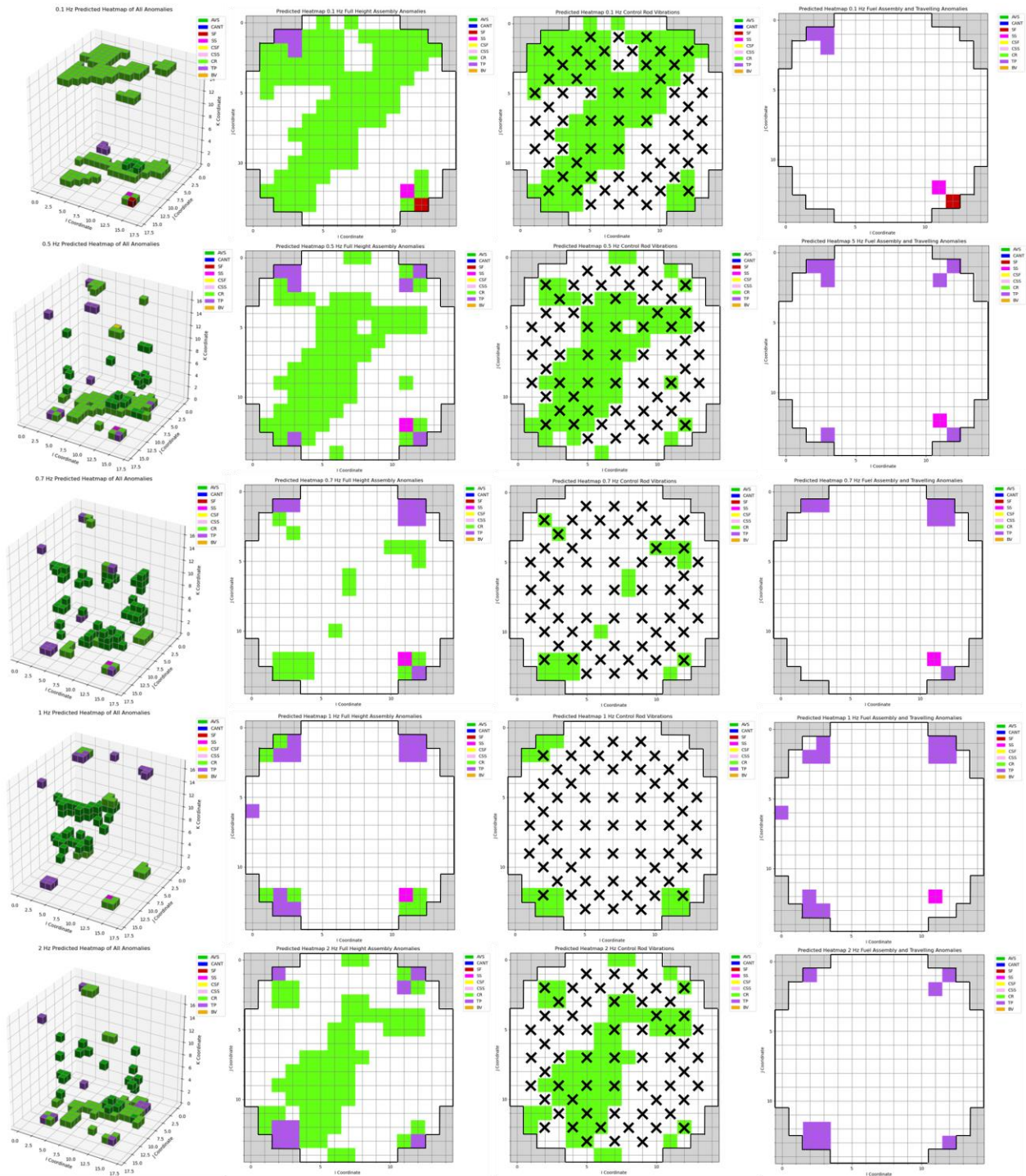
Figure 120: Prediction masks for the German pre-Konvoi 4-loop MOC 30. Frequencies 0.1 Hz, 0.5 Hz, 0.7 Hz, 1 Hz, 2 Hz, ordered row wise from top to bottom. Axial (top down) views of all assembly, control rod, and travelling perturbations are shown (column 2), along with figures separating control rod (column 3) from fuel assembly and travelling perturbations (column 4). Grey pixels represent outside of the pressure vessel and the black crosses represent the position of the control rods.

Into the higher frequencies, we observe continued travelling perturbations in region seen in the lower frequencies. Additionally, the predictions are more sporadic across frequencies, becoming less consistent than with the lower frequencies. Notably, in the range 5 Hz-7 Hz, our model predicts a central cluster of vibrating fuel assemblies of a cantilevered second supported mode, running diagonally. This again aligns with the out-of-phase relationships defined in the deliverable D3.5 section 2.4.3.2 describing such phenomena.
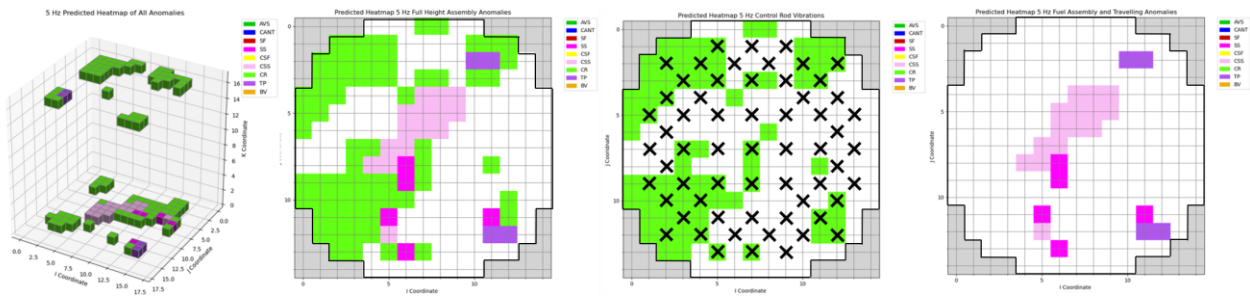
Figure 121: Prediction masks for the German pre-Konvoi 4-loop MOC 30. Frequency 5 Hz showing central fuel assembly of cantilevered supported second mode (light pink voxels). Axial (top down) views of all assembly, control rod, and travelling perturbations are shown (column 2), along with figures separating control rod (column 3) from fuel assembly and travelling perturbations (column 4). Grey pixels represent outside of the pressure vessel and the black crosses represent the positions of the control rods.

Finally, the higher frequencies do not show much variation across frequencies 15 Hz – 25 Hz. All within this range show the same vertically travelling perturbations originating near all four inlets, and a variety of absorber of variable strength perturbations throughout the central core. This pattern is common across all higher frequencies, an example of which is given below.
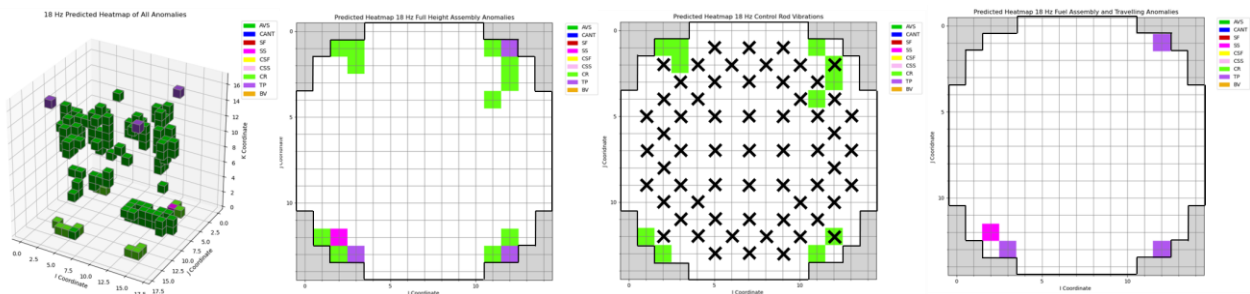
Figure 122: Prediction masks for the German pre-Konvoi 4-loop MOC 30. Frequency 18 Hz showing very few anomalous readings, with travelling perturbations shown in purple. Axial (top down) views of all assembly, control rod, and travelling perturbations are shown (column 2), along with figures separating control rod (column 3) from fuel assembly and travelling perturbations (column 4). Grey pixels represent outside of the pressure vessel and the black crosses represent the position of the control rods.

The results presented of the real plant data analysis, although initial, look promising. Similar phenomena identified in signal analysis approaches correspond to our predictions. However, we still have many unanswered questions and doubts of our model predictions. Firstly, the vast amounts of control rod vibration predictions cast doubt onto how well our model has learnt features belonging to control rod vibrations, although the predictions made do in-fact align and lie within a margin of one assembly from a present control rod in nearly all cases (exception to 5 Hz). Secondly, the lack of validation for our output will in-turn induce doubt. However, it is important that we consider these predictions a fundamental block on which we continue to work and build upon our proposed methods. It is positive to see that predictions are being made with alignment to characteristics seen in signal analysis. Moreover, it is vital to gain some validation of these predictions to ensure that our model produces are accurate.

5.5 *Swiss pre-Konvoi 3-loop reactor*

The Swiss pre-Konvoi 3-loop reactor measurements correspond to different burnups and boron concentrations and describe different cycle phases, namely MOC39, EOC39, BOC40, MOC40 and EOC40. This dataset of 5 time periods has been further analyzed and processed for the extraction of useful features and the identification of patterns related to different perturbation types and their localization. The provided data were neutron noise measurements, that had a duration of approximately 50 minutes and a sampling rate of 250 Hz. These measurements contained both AC and DC components, which have been normalized. Figure 123 and Figure 124 show an example of these signals before and after normalization. Additionally, simulated data have been provided both in the frequency and in the time domain.
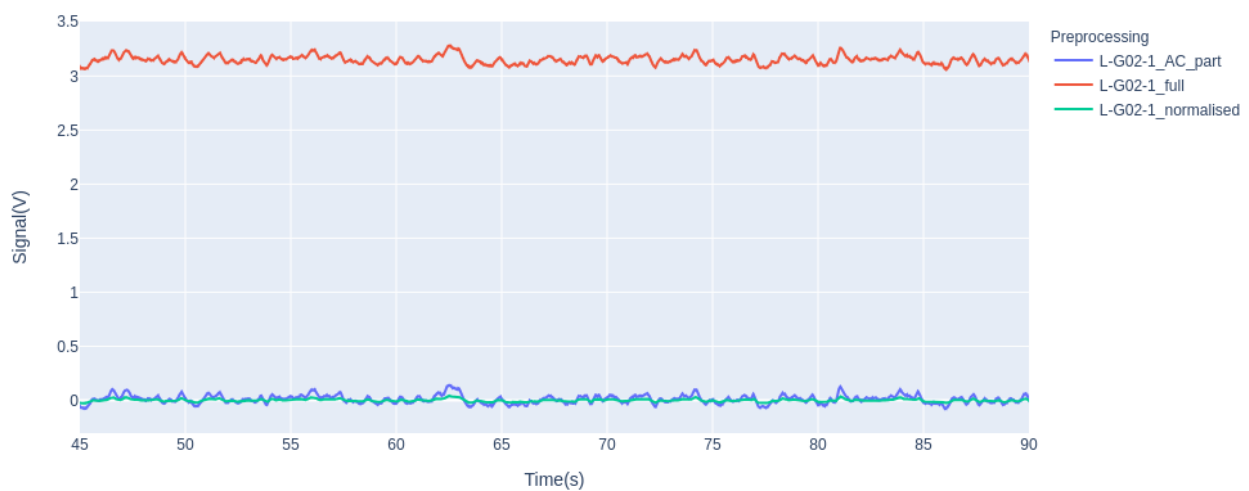
Figure 123: Example of internal signal of the Swiss 3-loop reactor (cycle 39).
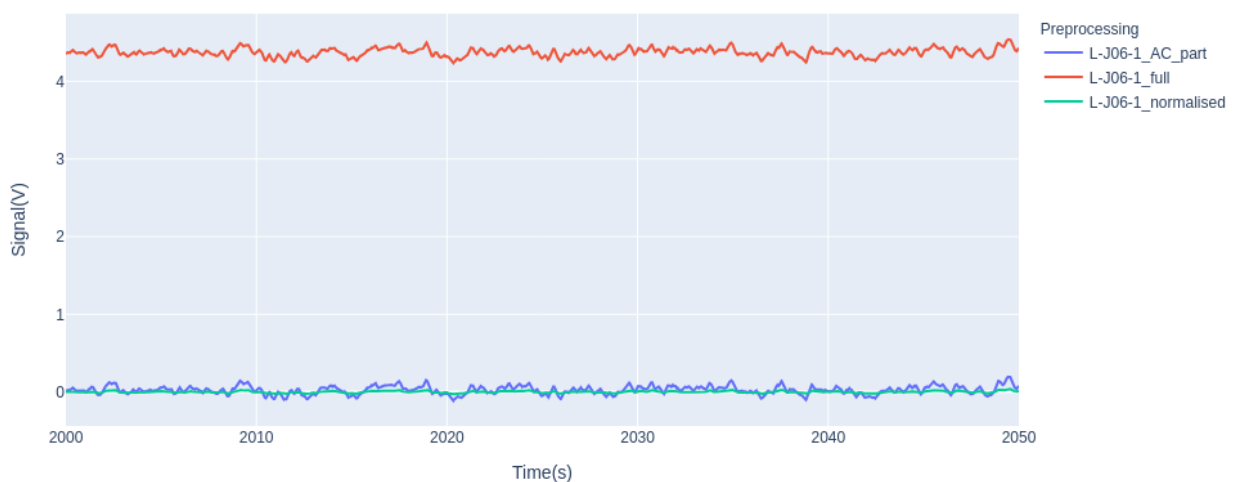
Figure 124: Example of internal signal of the Swiss 3-loop reactor (cycle 40).

Since some of the detectors were defective, the subsequent analyses have been performed on a subset of the in-core, ex-core detectors and thermocouples that were functional in all measurements. As a result, out of the 50 available detectors, we have considered only 45 signals.

5.5.1 Feature Extraction

5.5.1.1 Cycle 39

Figure 125 displays the Mean, Variance, Energy, Energy of Differences, Minimum value, Maximum Value and Cepstrum of a window in time of in-core sensor L-C08-3. For the Energy and Energy of Differences, the unit of measurement is V^2. For all the features, except Cepstrum, the x-axis is time windows. One time window is 10 seconds or 2500 time steps. The unit of Cepstrum is Volt and its x-axis is seconds.
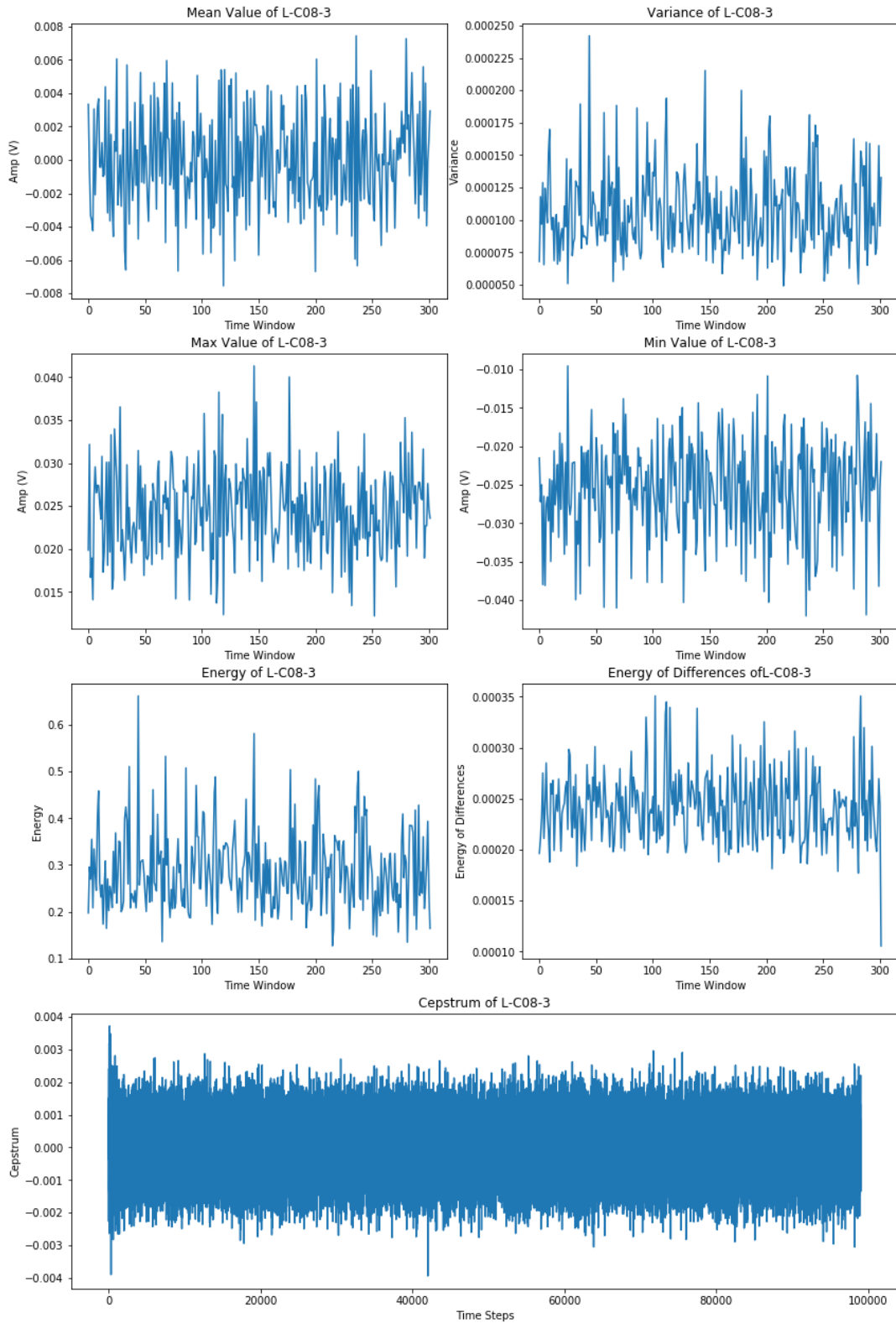
Figure 125: In-core sensor L-C08-3.

This is how most of the features from the in-core sensors look like, but there are some exceptions in the N08 family of sensors – see Figure 126.
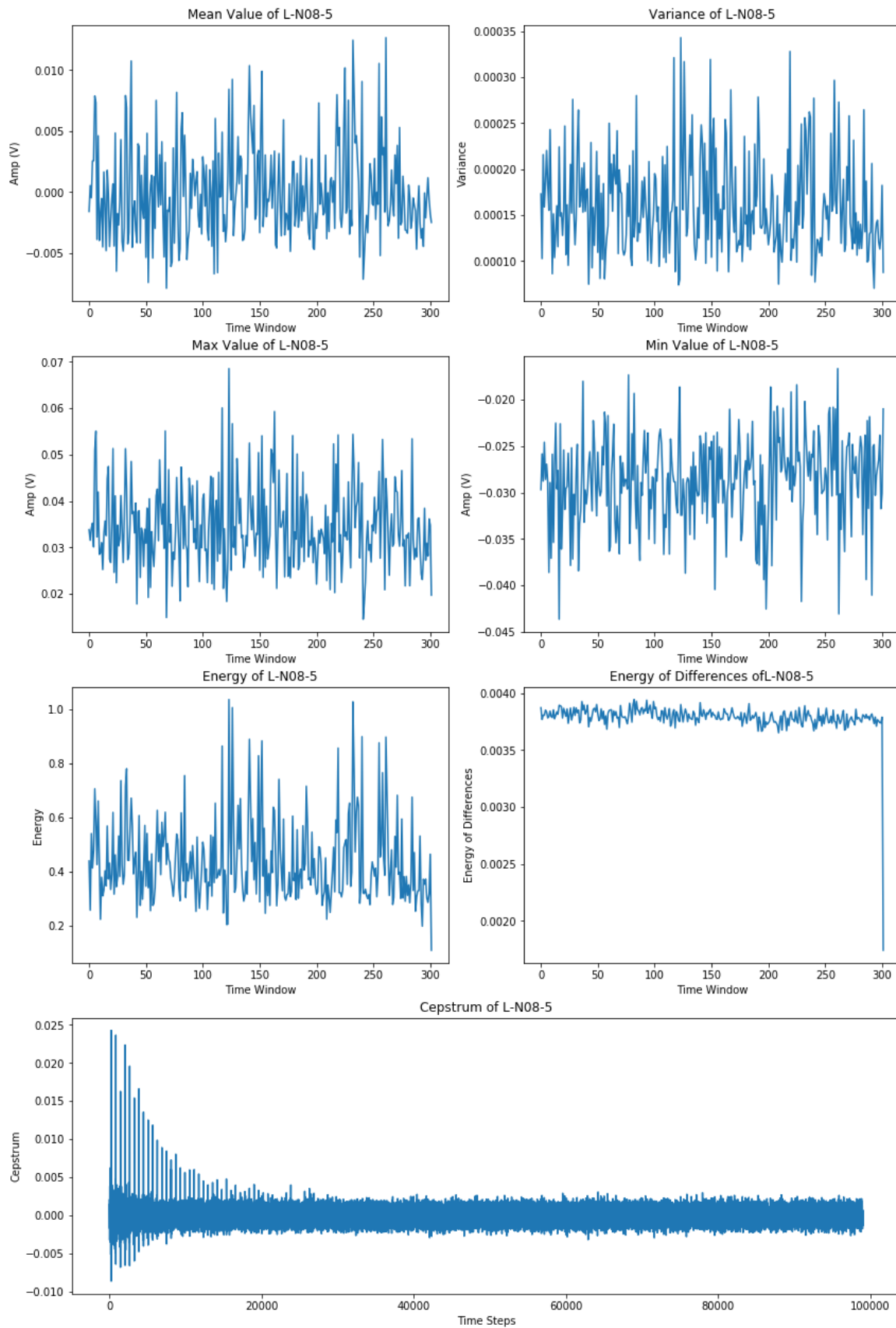
Figure 126: In-core sensor L-N08-5.

Some observations are summarized below:
 ● The energy of differences seems constant over time, but it drops to almost zero in the end.

- The cepstrum has a completely new behavior than the rest of the signals. Instead of oscillating between (-0.002, 0.002), its variance has increased to 0.005 and at the beginning of the signal it displays some extreme peaks at 0.025, which tend to decrease over time.

The above observations about the differences between those sensors can be also seen in the most dominant frequencies in Figure 127 below.
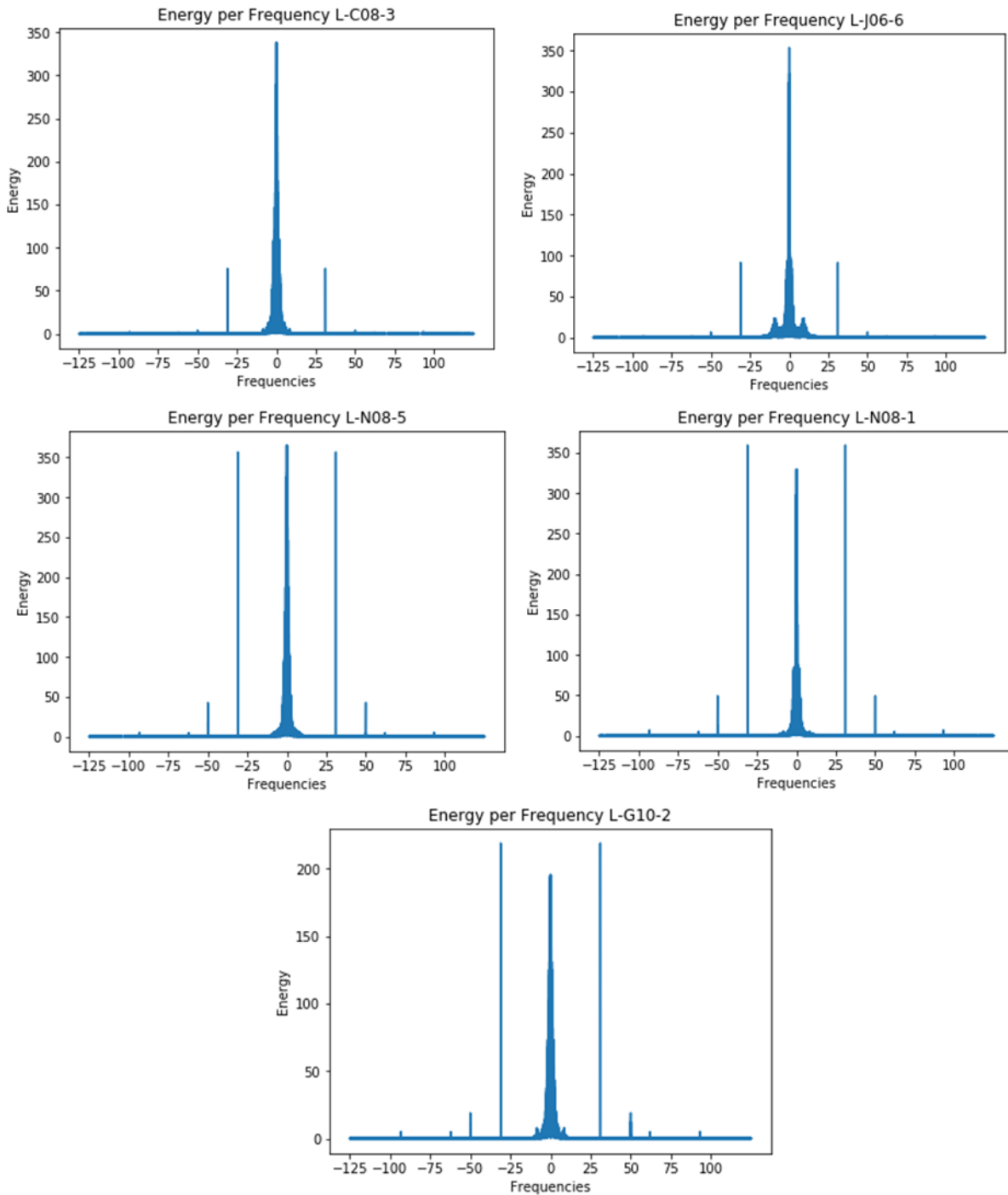
Figure 127: Most dominant frequencies of in-core sensors L-C08-3, L-J06-6, L-N08-5, L-N08-1 and L-G10-2.

Some observations are given hereafter:

- The main differences of the dominant frequencies lie in the magnitude of the frequencies around 30 Hz, where sensors N08 and G10 have much higher energy than the rest of the sensors.
- It is also important to note that, in every sensor, the spectrum <10 Hz seems to gather the majority of the energy. Nevertheless, in N08 and G10 sensors, the energy of that spectrum is reduced.

Ex-core and temperature sensors exhibit a similar behavior. In the former, the dominant frequencies lie below 10 Hz – see Figure 128. This is the case with the latter as well, with the exception of the 50 Hz frequency – see Figure 128.
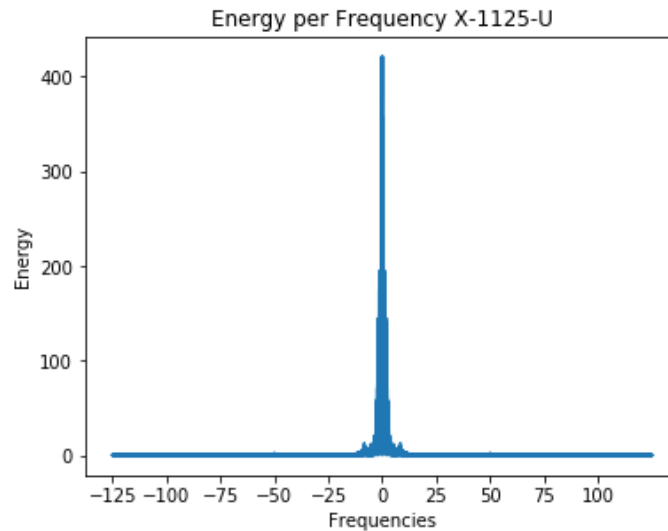
Figure 128: Energy spectrum of the X-1125-U ex-core sensor.
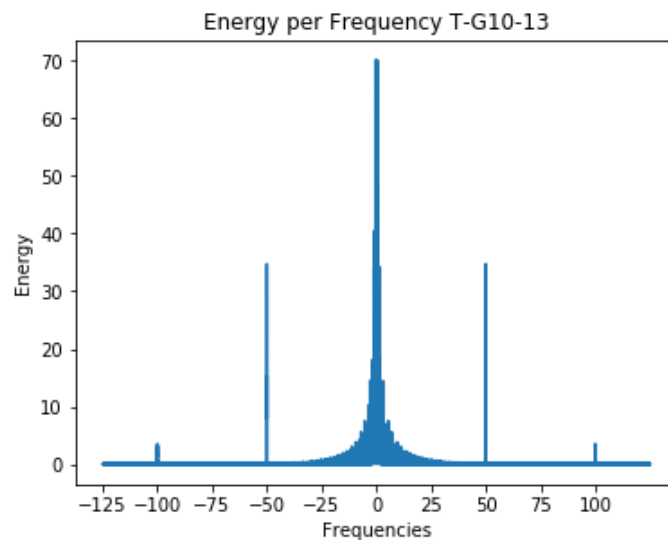
Figure 129: Energy spectrum of the T-G10-33 temperature sensor.

5.5.1.2 Cycle 40

In cycle 40, the most interesting observations can be summarized in the following points:
- Just like the previous cycle, three families of sensors seem to stand out: N08, G10, J14.
- In BOC40 and EOC40, the J14 sensors – see Figure 133 – exhibit a high energy compared to others.

- The N08 – see Figure 130 – sensors have high peaks in their cepstrum and in EOC40 they exhibited one of the highest peaks in energy out of all the measurements (around the 200th second).
- The N08 sensors also show the lowest energy in frequencies below 5 Hz – see Figure 132 – compared to the rest, while their dominant frequency is around 30 Hz. Frequencies around 50 Hz seem to always exist in a medium magnitude of energy – see Figure 131.
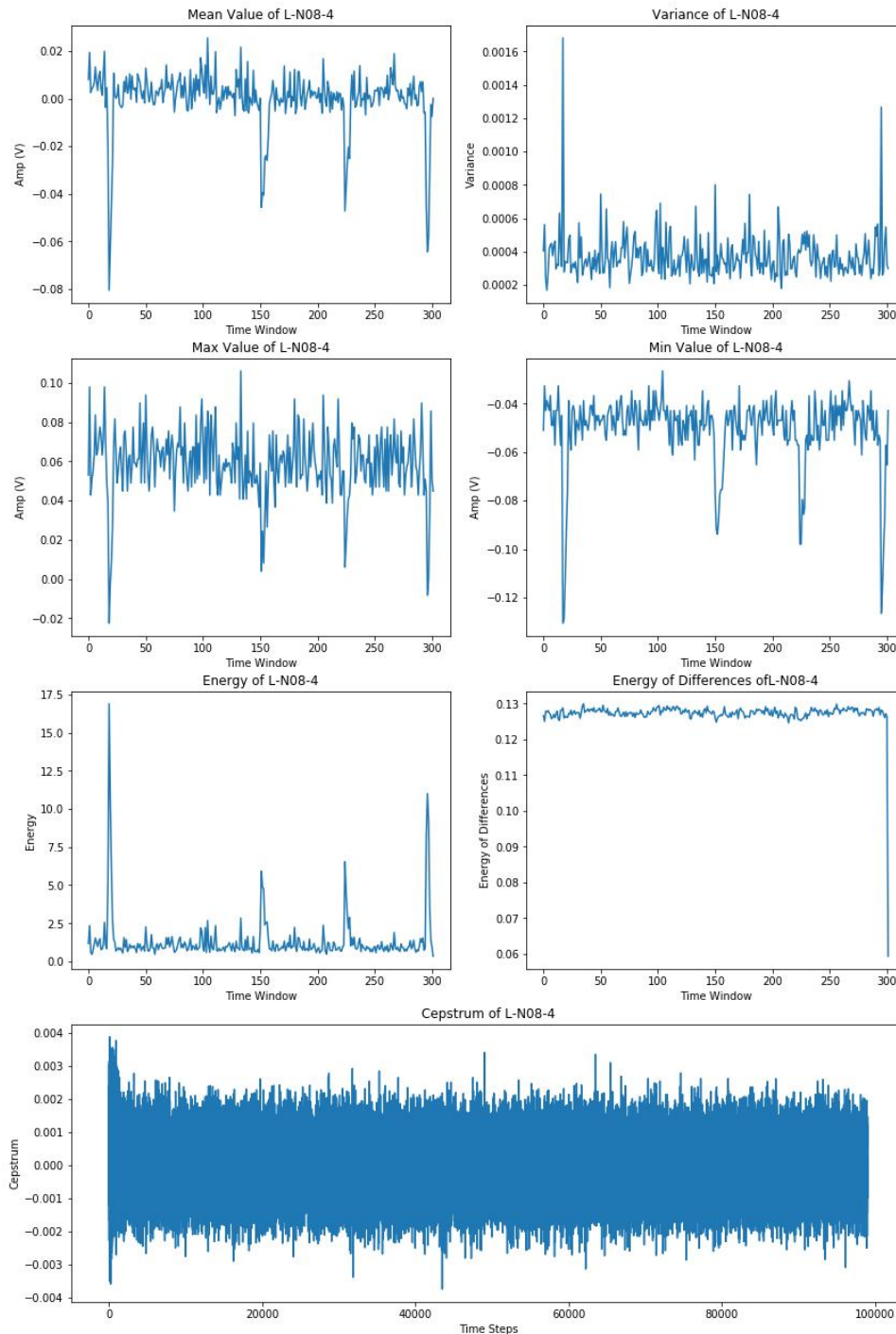
Figure 130: In-core sensor L-NO8-4.
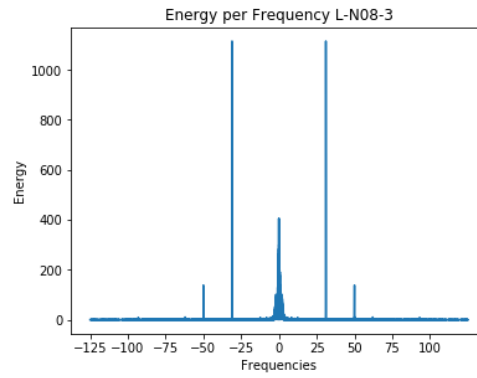
Figure 131: Energy spectrum of the L-N08-3 sensor.
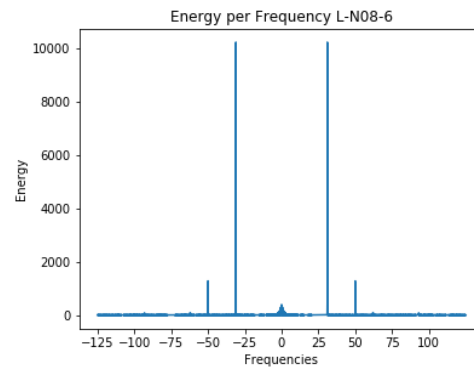
Figure 132: Energy spectrum of the L-N08-6 sensor.
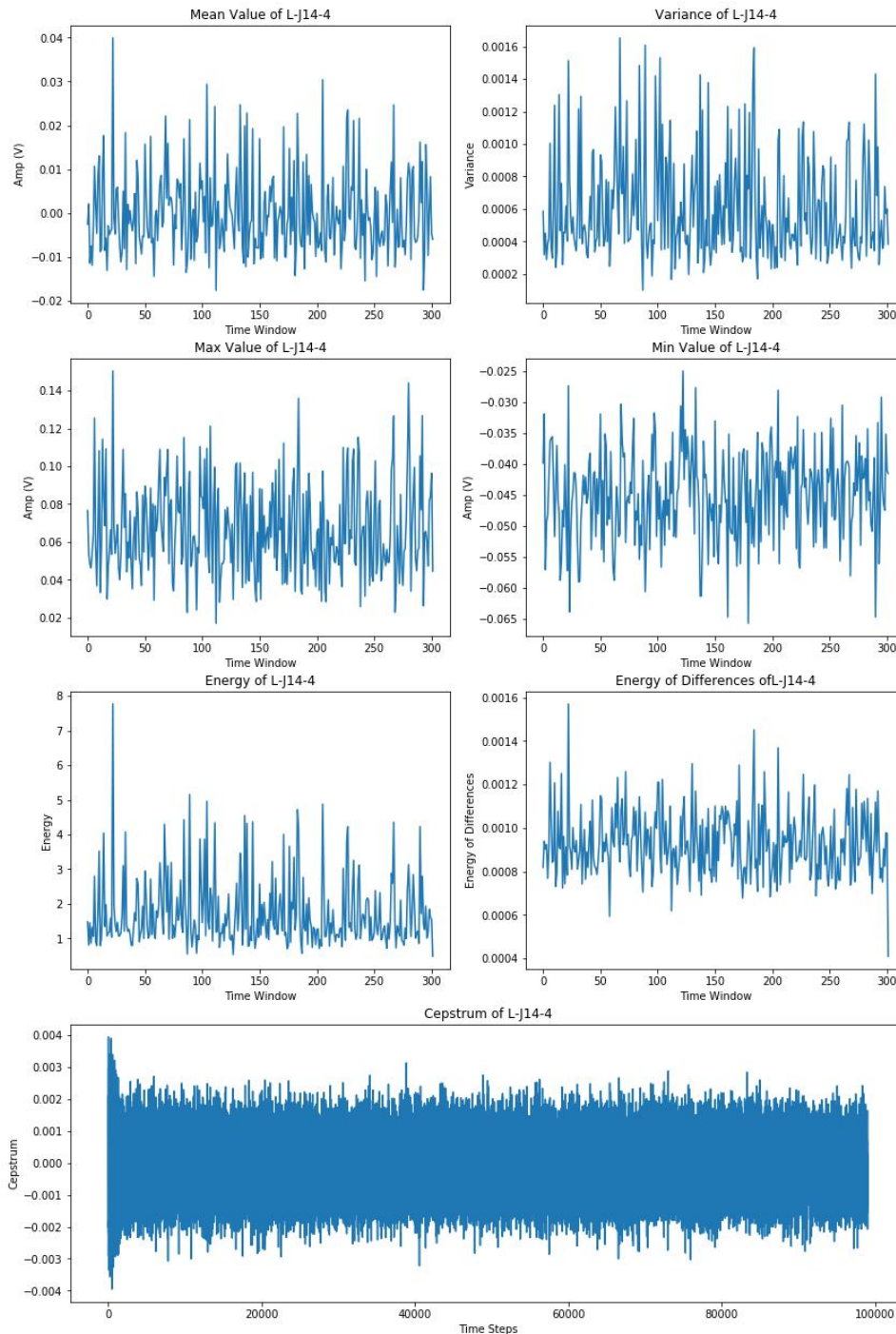
Figure 133: In-core sensor L-J14-4.

5.5.2   Comparison with simulated signals

The purpose of the comparison between plant measurements and the simulated signals in the time domain is the recognition of patterns between them, for the preemptive identification of possible sources of perturbation on reactor cores. The objective is to draw insight about the reactor core function across cycles and across different phases of the same cycle.

Two different approaches have been tested: *spectrograms* and *PSD features*. For the first approach, different 25-second windows have been sampled out of the 50-minute long real measurements and have subsequently been compared with the simulated perturbations at different locations.

For the latter approach, a different methodology has been followed. It involved the direct computation of the APSDs and CPSDs for both plant measurements and simulated data. This analysis produces vectors of power spectral densities that can be compared with distance metrics like cosine similarity or Euclidean distance. If plant measurements align well to a simulated perturbation, we can consider that as a strong indicator of the existence of that perturbation in the reactor core. This, as well as the computation of the magnitude-squared coherence and cross-power spectral density between the simulated data and real measurements, can be used both as features for a Machine Learning model or as standalone predictors of the ongoing perturbation.

The APSDs of specific detectors of plant measurements were compared with data from simulations – see Table 11. The header of the table holds the name of the plant measurement, whereas each subsequent row calculates the cosine similarity between each simulated perturbation occurring at specific phase of the cycle 40, with the plant measurements. The first column describes the label of the various simulated scenarios in the time domain. From this comparison, two key observations can be made: firstly, that the simulated data, especially at BOC40, are more aligned with their respective plant measurements, indicating that the simulation of the core conditions of the reactor core at that specific cycle was successful. Secondly, it is shown that the C4 dataset of PSI, constituting of the vibration of a 5x5 central cluster and thermal and hydraulic perturbations is more similar to the real measurements, indicating the possible presence of those specific perturbations on the reactor core during cycle 40.

Another metric that has been studied for the comparison between simulated and real measurements is the magnitude-squared coherence, which is a number between 0 and 1 for each frequency found on both signals. In order to compute similarity, a heuristic has been used that summed the results that were above a specific threshold (0.001 in our case), in order to more accurately count the frequencies that have some correlation between the real measurements and the simulated data – see Table 12.

Table 11: Cosine similarity between real and simulated on L-G10-1 detector.

	BOC40	MOC40	EOC40
MOC40_C3	0.004905	0.00816	0.011941
MOC40_C4	0.062265	0.048613	0.044893
EOC40_C5	0.017604	0.036273	0.046624
BOC40_C5	0.011682	0.024079	0.032079
EOC40_C2	0.014655	0.030935	0.040351
EOC40_C4	0.026229	0.022848	0.023822
BOC40_C2	0.023391	0.044589	0.056346
BOC40_C4	0.150573	0.122492	0.112968
BOC40_C3	0.006519	0.009391	0.0131
EOC40_C3	0.005951	0.01355	0.019356
MOC40_C5	0.012338	0.021074	0.026876
MOC40_C2	0.010378	0.021446	0.028429

Table 12: Coherence comparison between real and simulated data.

	BOC40	MOC40	EOC40
MOC40_C3	0.009557	0.019712	0.007323
MOC40_C4	0.001016	0.019722	0.001063
EOC40_C5	0.00103	0.021602	0
BOC40_C5	0	0.008476	0
EOC40_C2	0.021099	0.032139	0.018274
EOC40_C4	0	0.10728	0
BOC40_C2	0.049638	0.048282	0.040419
BOC40_C4	0	0.009815	0
BOC40_C3	0	0.022292	0
EOC40_C3	0	0.012489	0
MOC40_C5	0.009927	0.022367	0.006242
MOC40_C2	0	0.01355	0

5.5.3 Clustering

Clustering is performed in a similar manner to the German 4-loop reactor case (Section 5.4.3), with the analysis being based on the same clustering and anomaly detection algorithms. The metric used is again the proportion of minority (or anomaly) class in a signal of a sensor in order to categorize it as an out of the ordinary case.

K-Means separated the signals in 2 clusters. While the separation was not as one sided as the other algorithms, meaning that the number of samples per cluster is not entirely in favor of the "normal" cluster, nonetheless, it was able to distinguish outlier behavior. In Figure 134 below, we can see that sensors L-G10-6, L-N08-1, L-G10-1 and L-N08-5 show signs of abnormality in MOC 39 and EOC 39. During BOC40, more sensors exhibited "irregular" behavior. These were located in the family of N08 sensors and especially sensor L-N08-4 kept the same patterns during MOC 40 and EOC 40.

Mean-Shift clustering did not manage to find any significant outlier patterns in the signals and, thus, single out any sensors. DBSCAN distinguished only one sensor that was behaving out of the ordinary and that was sensor L-N08-3. The severity of the anomaly reached a peak in BOC 40, which matches the results of *k*-Means.

On the other hand, One-Class SVM did recognize multiple outliers in all parts of cycles 39 and 40. The most significant observation is that the family of N08 sensors still have high proportion of minority cluster time windows and, as a result, are labelled as abnormal, just like in *k*-means. Figure 135 below exhibits that, in BOC40, there is an increased number of sensors behaving out of the ordinary.

Isolation Forest put less sensors in the minority category. However, sensors L-N08-1, L-N08-4, L-N08-6 and L-G10-1 are still present, like in the previous cases – see Figure 136.
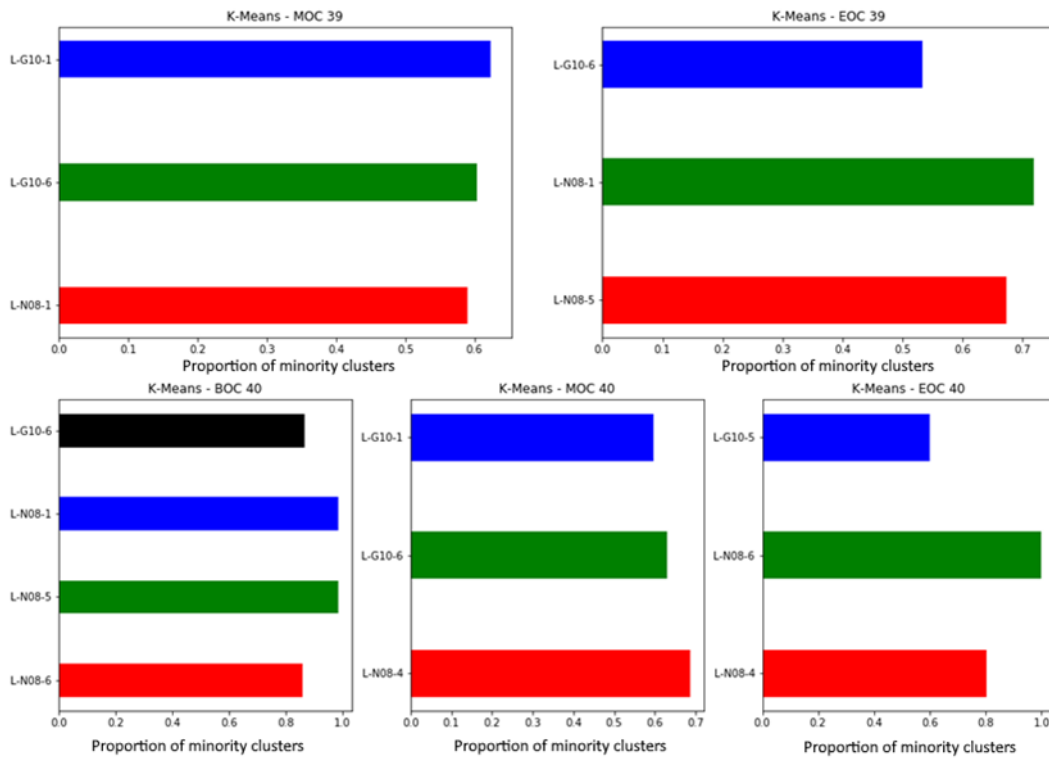
Figure 134: k-Means clustering.
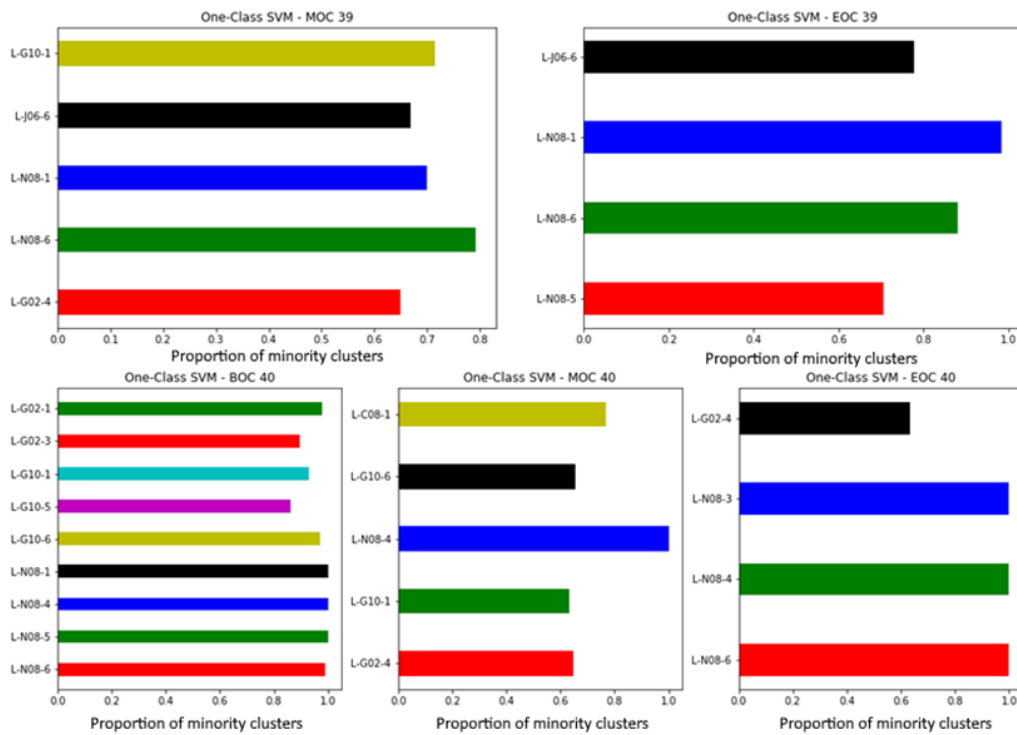
Figure 135: One-class SVM.
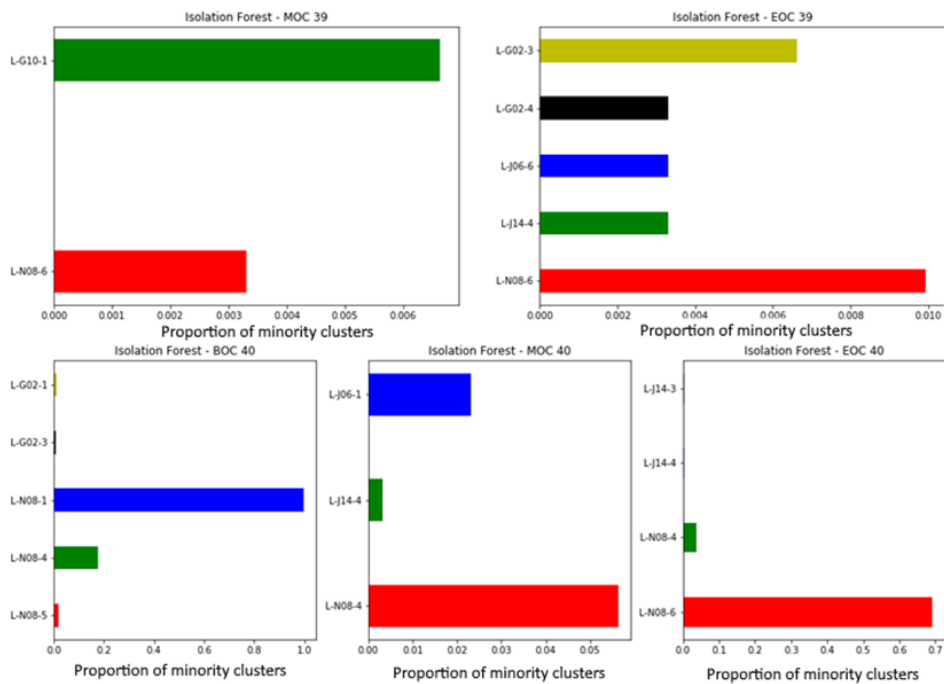
Figure 136: Isolation Forest.

Overall, the sensors that have been constantly considered to be abnormal were L-G10-1, L-G02-1, L-G10-6 and most of the N08 sensors. Figure 137 below pinpoints the position of these sensors in the reactor core.
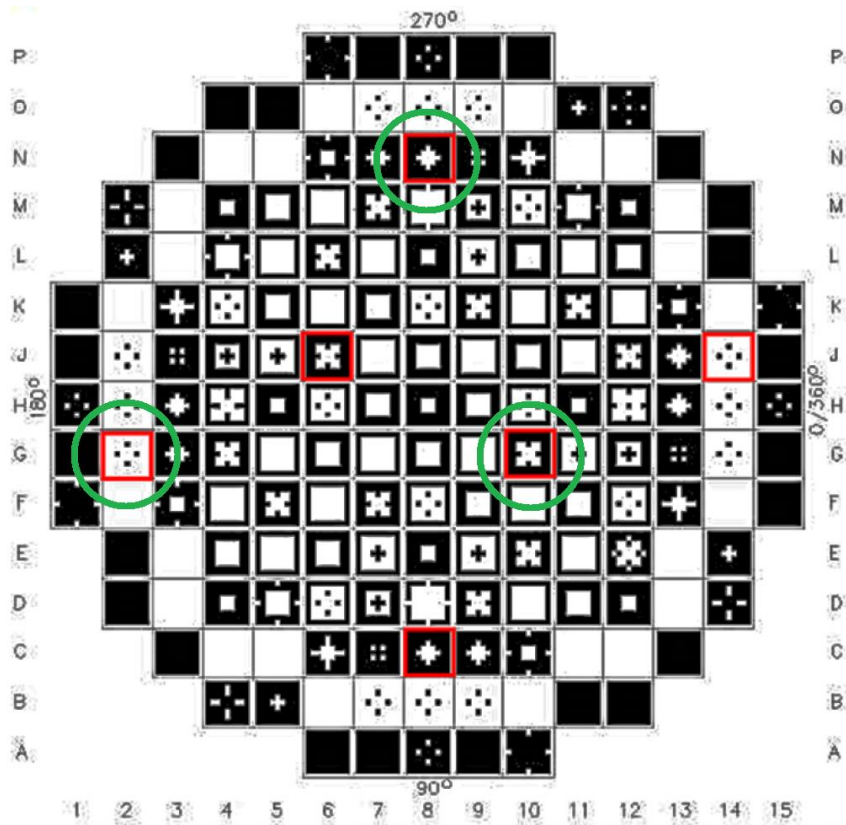
Figure 137: Location of N08 sensors in the reactor core (green cycles).

5.5.4 Localization

Extending earlier work (Tagaris, 2019), (Ioannou, 2020), we have used the time-domain simulations for the vibration of one FA in cantilevered mode for the localization task, specific to the conditions of BOC40 (PSI dataset 2020-02-Dataset8-C1a - Table 2). The simulated datasets contained measurements from 36 in-core detectors (6 different radial positions at 6 different axis levels) and 8 out-core detectors (4 different radial positions at 2 different axis levels). A Deep Learning architecture has been created, based on the spectrograms of the signals.

An important design choice has been the selection of the subset of detectors that should be considered for the localization task. This choice is crucial as more detector signals pinpoint more accurately the source of the perturbation, but it is sometimes impractical to consider all of them as some may be defective or may not be present in actual measurements. In order for our model to generalize better to previously unseen configurations, an additional input has been given, specifying the (x, y) coordinates of the detectors on the core.

Four different subsets of detectors have been chosen as input to the Deep Learning models. These include: (i) a signal from one in-core detector, (ii) a signal from 3 in-core detectors, (iii) signals from 3 in-core detectors plus the 8 ex-core detectors and finally (iv) signals from all available detectors.

Spectrogram creation is a task that involves several hyper-parameters. Due to the small duration of the signals representing each perturbation (100 seconds), different random windows of 25 seconds have been chosen. Additionally, a Hamming window of 50% overlap and a size of 128 data points has been used. The last 25 signal seconds were also kept out, for evaluation purposes. Figure 138 displays example spectrograms, used to train the models. As the entire power spectrum of the signal lies on small frequencies, only the frequencies below 10 Hz have been used for the plots.
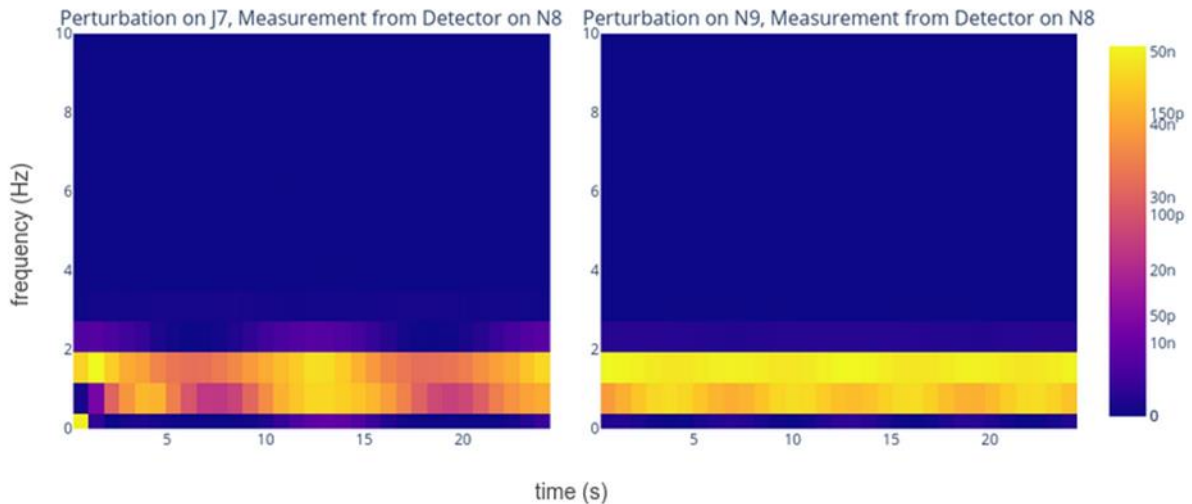
Figure 138: Example spectrograms. The colorbar outlines the power of a frequency at a specific time in logarithmic scale. Yellower colors represent more power of a frequency. This aligns with the fact that the neutron noise signals have the majority of their power spectrum in low frequency ranges.

Four different Convolutional Neural Networks architectures have been trained on the different input subsets. The proposed architecture is summarized in Figure 139.
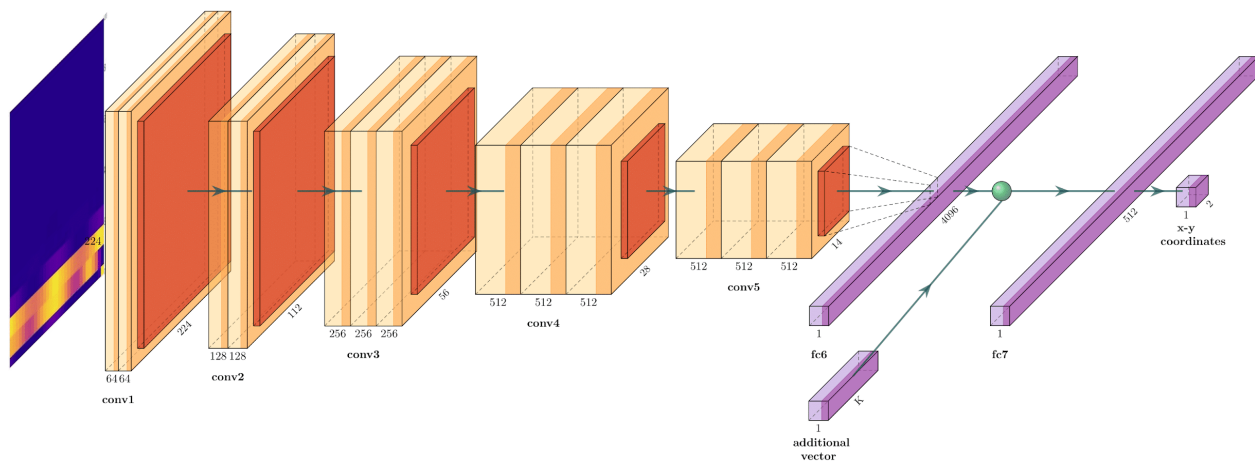
Figure 139: Convolutional Neural Network Architecture. The input is a 1-channel image, whose width equals to the time window used and whose height corresponds to the frequencies. The power of a specific frequency at a specific time is expressed in logarithmic scale.

The results of the training and the test phase of each CNN architecture is depicted in Figure 140. In all cases, the training loss steadily decreases over time. This implies that the CNNs can successfully recognize the location of a perturbation on the training data. However, the aim of these models is to generalize well to unseen data. From that perspective, it is shown that the CNN trained with signal from only one detector as input fails to generalize well. This result is expected, as information from only one position in the grid cannot accurately capture all phenomena. It is also shown that input from signals from all detectors yields the best discriminative ability for this specific task. Another important result of this analysis is that a CNN architecture manages to generalize well, even though its input consists of only a subset of in-core detectors. This latter observation signifies the applicability of the proposed method to missing input.
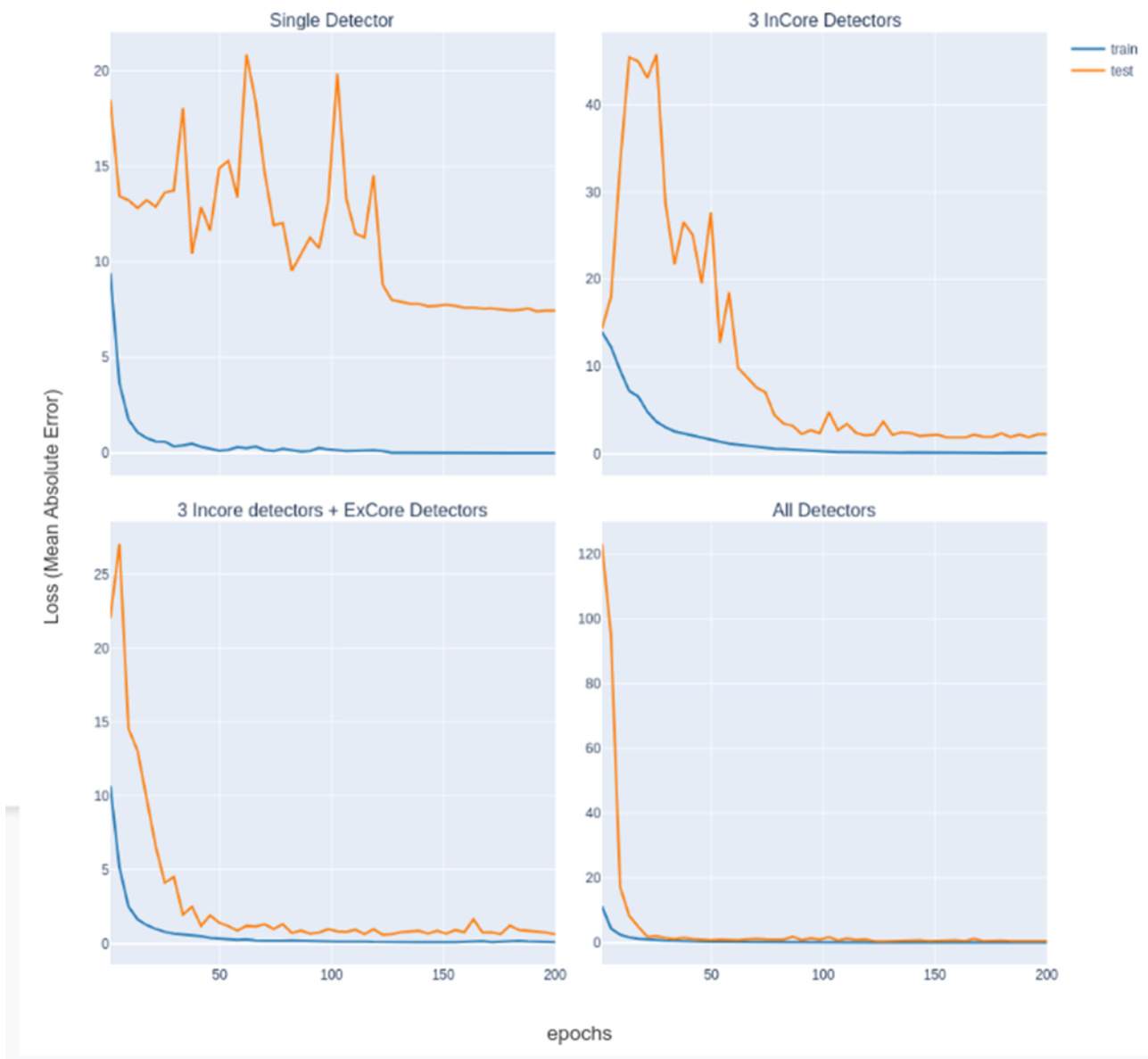
Figure 140: Training and evaluation results for the four different subsets of detectors. Epochs represent the passes of the training dataset through the Neural Network. As a loss metric, the Mean Absolute Error was used, which measures the difference between actual x-y coordinates of perturbations and the predictions produced by the network.

Predictions from the best trained model on previously unseen data are shown in Figure 141 below. These results underline the robustness of the proposed method on simulated data and indicate that Machine Learning algorithms may be used for the accurate localization of a perturbation on a reactor core.
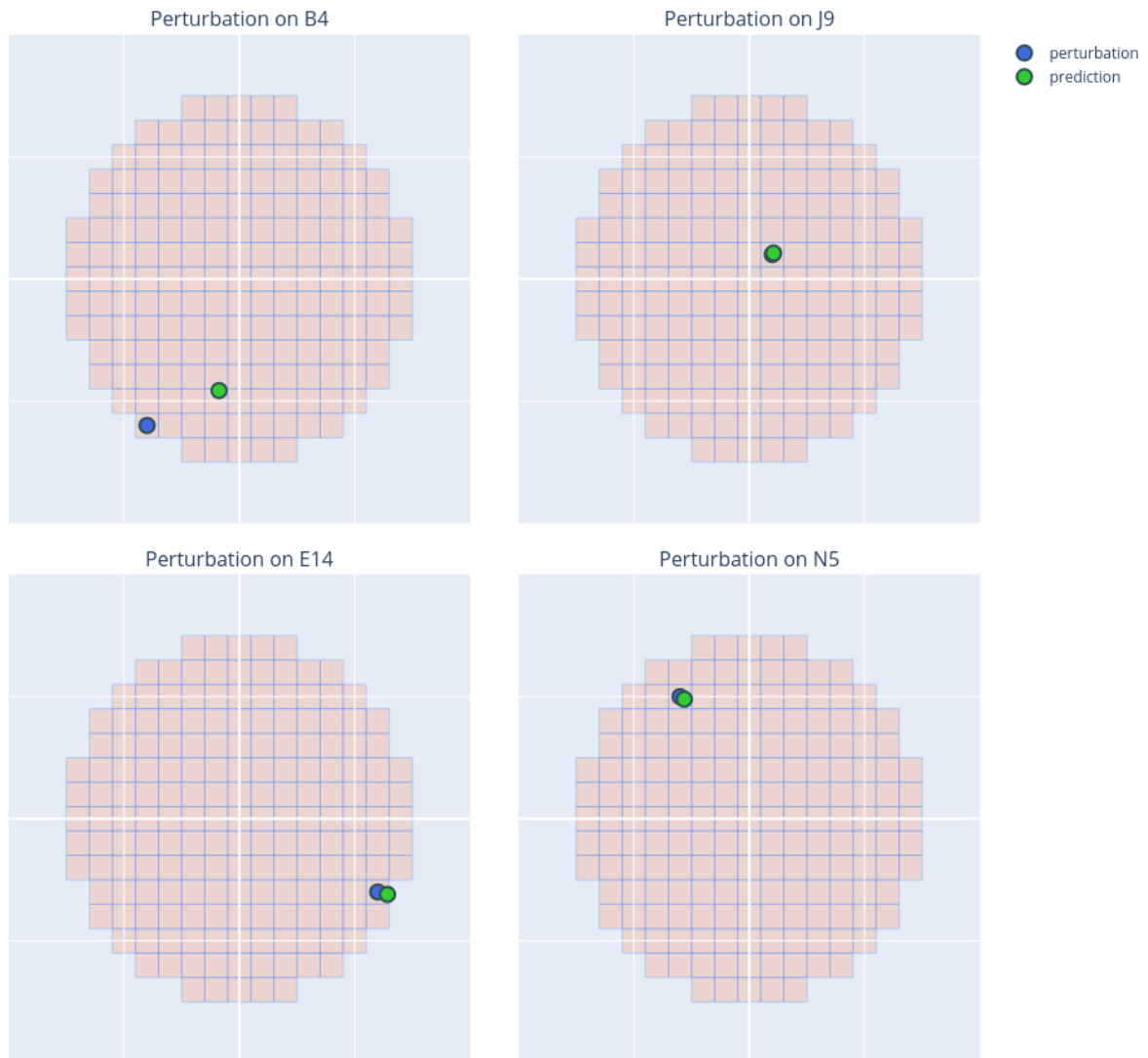
Figure 141: Localization model predictions. The 4 different subfigures show a top view of the reactor core, in which a perturbation is occurring. The positions of both the location of perturbation and its prediction are shown in blue and green circles, respectively. The x-axis is measured from 1-15 from left to right, and the y-axis from A to P from bottom to top according to Figure 137.

5.5.5 Time series Simulate-3K simulation perturbation classification and localization

The time domain simulations correspond to the Simulate-3K (Grandi, 2011) simulation data for the Swiss 3-Loop pre-Konvoi for cycle 40. The simulated dataset (Dataset8) is composed of perturbations originating from both static and non-static locations, therefore introducing both classification and localization tasks into the dataset. We present a convolutional, recurrent neural network to classify and localize perturbations within a given time frame, i.e. 100 time-steps (1 second), or 250-time steps (2.5 seconds). This network provides a robust and accurate basis pre-trained and tested on the simulated Swiss 3-Loop pre-Konvoi to perform inference on the real plant readings.

Simulate-3K simulation data pre-processing

To align with previous deliverables and developments, the time series data has been pre-processed similarly to previous developments in (Kollias et al. 2019 and Montalvo et al., 2020). Each data sample is augmented via a sliding window to first produce more data samples than delivered in DataSet8, and secondly to reduce the computational demand. The sliding window is either 100 time-steps (1 second) or 250 time-steps (2.5 seconds), with a 25 time-step and 50 time-step overlap respectively. Moreover, this window is applied across all 36 in-core detectors and 8 ex-core detectors producing 160 samples of size (*44 x 100*), and 60 samples of size (*44 x 100*) respectively for window length, per scenario. The expanded dataset is also split into training, testing and validation sets for the training procedure, ensuring that samples with perturbations originating from the same core location are not present across sets. Additionally, as with previous deliverables, additive white gaussian noise (AWGN) has been added at signal to noise ratio (SNR) 3 and 1 to help ensure robustness to noise is promoted throughout the network. Lastly, windowed signals are normalized to have zero mean and standard deviation of one, applied feature wise.

Furthermore, to more closely align simulated data to real plant data, and to perform inference on such data, defective detectors in the real data samples are also removed from the simulation data samples. This ensures that the network learns data inputs that are present in the real data, consequently, not to confuse the network at inference time by removing data features.

LSTM-CNN network for time series classification and localization of single perturbations

Localization of perturbation origin is a non-trivial task in the time-domain, this is due to the necessity of embedding spatial understanding into the learning procedure of time-series signals. To promote learning of spatial features, CNNs are employed and to understand the temporal nature of the data RNNs are utilized, more specifically Long Short-Term Memory (LSTM) cells. The network in Figure 142, depicts the procedure to first learn temporal features in the data by means of the LSTM, and then use CNNs to learn more structural features produced from the output of the learnt temporal features. This combination of temporal and structural feature learning allows for both classification and localization of perturbation origin. For a more detailed explanation of RNNs and LSTMs, refer to the deliverable D3.4 (Kollias et al, 2019).

The LSTM network is constructed of two layers each with 128 units, outputting feature vectors of 128 dimensions for every 100 or 250 time-steps. These 100 vectors of 128 dimensions are input into a four-layer one-dimensional CNN, where each CNN layer is followed by Batch Normalization and ReLU activation function. The resulting output of the CNN are *256x5* feature vectors. Global Average Pooling (GAP) is applied to the CNN output for dimensionality reduction to allow for linear classification and regression. The network output is a two-neuron linear regression layer of the cartesian coordinates in the horizontal plane of the perturbation origin (*i and j*), and a six-neuron, sigmoid activated layer for the multi-label, multi-class classification.
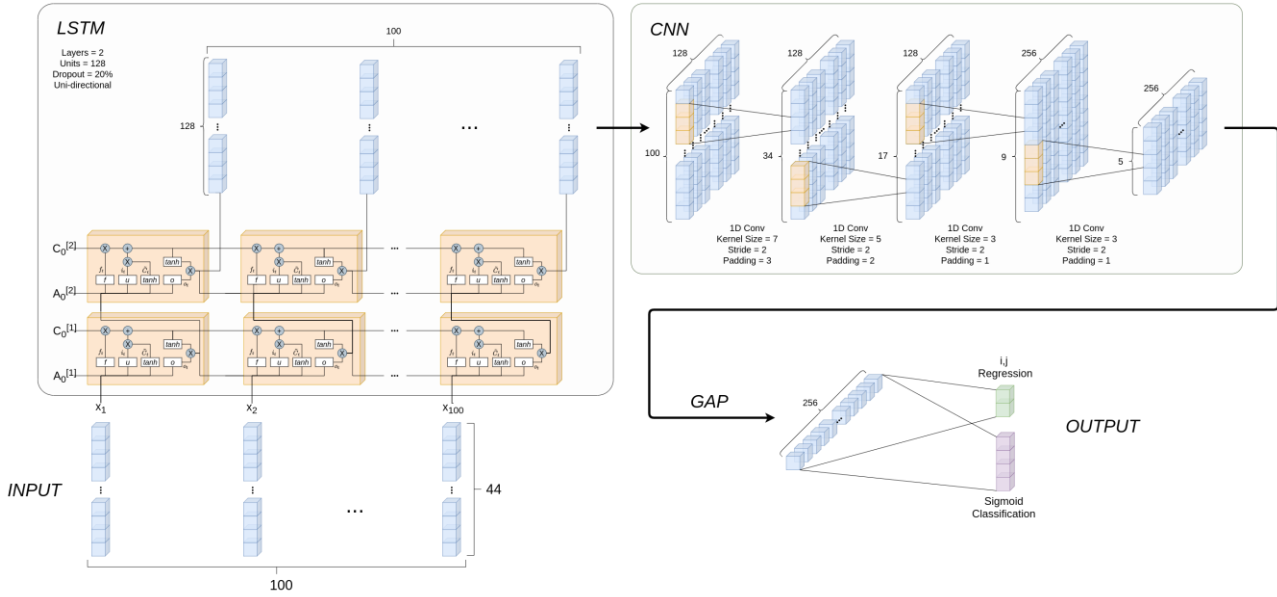
Figure 142: LSTM-CNN network for the feature extraction of structural and temporal features. The time series signal is fed to a two-layer LSTM network of 128 units and then passed to a four-layer CNN network. The output is reduced in dimensionality by a GAP layer before being fully connected to a six-neuron Sigmoid and 2-neuron output layers.

The network has been trained with Stochastic Gradient Descent (SGD) to minimize the multi-task loss in Equation 29 comprised of multi-class binary classification loss (the first term inside the outer sum of Equation 29), and L1 / MAE loss in Equation 33.

$$L(X; \mathbf{W}, \lambda_1, \lambda_2) = -\frac{1}{N} \sum_{i=1}^{N} \left[\frac{\lambda_1}{P} \sum_{p=1}^{P} \left[y_1^p \cdot \log(\hat{y}_1^p) + (1 - \hat{y}_1^p) \cdot \log(\hat{y}_1^p) \right] + \frac{\lambda_2}{C} \sum_{c=1}^{C} \left| y_2^c - \hat{y}_2^c \right| \right]_i \quad (29)$$

P refers to the number of perturbation types to classify and *C* refers to the number of cartesian coordinates to regress, in this case 2, (*i, j*). Mean absolute error refers to the difference between two continuous variables, in this case the cartesian coordinates of the perturbation origin (*i, j*). This is formally defined in Equation 33.

In addition to this, the learning rate is reduced during training by a factor of 0.1 when validation loss plateaus within a threshold of 0.025. This encourages the network to settle into more appropriate minima in the learning space, starting with a large learning rate to avoid poor local minima, and settling within a minimum once a good one has been found. Furthermore, dropout is employed in the LSTM, setting 20% random neurons to zero for each training batch. L1 regularization (weight decay) of 0.001 is introduced to penalize the cost function, both of these methods help reduce the potential of overfitting in the network, improving generalization to the test set.

Experimental results on Simulate-3K simulated data

The aforementioned network is trained and evaluated on two differently augmented sets, either 100 time-steps, or 250 time-steps, details of which are previously stated. The intention of which is to analyze the performance of localization given a longer signal and therefore consider if 100 time-steps (1 second) is satisfactory to enable the appropriate localization of perturbation origin.

Experimental results of the classification task are presented using accuracy and F1-score metrics. It should be noted that in the case of this dataset, there is an imbalance of number of samples per

class, meaning that accuracy cannot be considered as the most appropriate metric. Therefore, we state F1-score and confusion matrices to be more appropriate measures of classification performance. The definitions of the evaluation metrics are as followed:

$$\text{precision} = \frac{\text{TruePositive}}{\text{TruePositive} + \text{FalsePositive}} \tag{30}$$

$$\text{recall} = \frac{\text{TruePositive}}{\text{TruePositive} + \text{FalseNegative}} \tag{31}$$

$$\text{F1-Score} = 2 \times \frac{\text{precision} \times \text{recall}}{\text{precision} + \text{recall}} \tag{32}$$

$$\text{Mean Absolute Error (MAE)} = \frac{1}{n} \sum_{j=1}^{n} \left| y_j - \hat{y}_j \right| \tag{33}$$

$$\text{Mean Squared Error (MSE)} = \frac{1}{n} \sum_{j=1}^{n} \left\| y_j - \hat{y}_j \right\|^2 \tag{34}$$

Table 13: Results of classification of perturbations and localization of the coordinates of a vibrating fuel assembly (i, j), in the time-domain utilizing the proposed LSTM-CNN model. Mean and standard deviation of 3 runs are presented.

Classification and Localization of Single Perturbations in the Time Domain.					
Window Size	SNR Value	Classification Metrics		Regression Metrics	
		Acc Error (%)	F1-Score	MAE	MSE
100	No Noise	0.205±0.015	0.9947±0.0002	0.3604±0.018	0.7447±0.094
100	3	4.041±0.140	0.8689±0.0048	1.2836±0.002	3.8943±0.051
100	1	5.990±0.070	0.8219±0.0015	1.4064±0.004	4.3927±0.004
250	No Noise	0.390±0.045	0.9875±0.0019	0.4189±0.012	1.0881±0.037
250	3	2.825±0.055	0.9160±0.0003	1.2403±0.001	3.8570±0.005
250	1	5.825±1.805	0.8354±0.0106	1.3321±0.012	4.1282±0.049

Results of all experiments are given in Table 13**.** Firstly, it is noticed that increasing signal length which is fed into the network does not provide significant performance improvements. It is to be expected that the performance will improve given the longer signal, however, it comes as a surprise that a larger window size reduces the classification performance by, at best case, ≈0.19%. We conjecture that longer signals introduces more variation in signal response, introducing a greater challenge to classification. On the other hand, longer signals lengths improve localization performance, but only by a small margin, 0.04 MAE at best case, which does not warrant performance to computational cost of longer signals. We do not know how perturbations with low frequency (well below 1 Hz) will respond to such a change, due to such perturbations not being simulated. We therefore suggest this as a potential direction of future work to confirm if the aforementioned findings still hold under this new case.

The good performance across Dataset8 for the Swiss pre-Konvoi 3-loop provides a strong basis for performing inference on real plant data. This work has much room for further investigation and exploration, such as blended methodologies to most appropriately leverage simulated data for use in making predictions in real plant measurements. We intend to continue work on this subject, focusing on domain adaption and transfer learning to achieve the best possible performance when testing on real plant data.

5.5.6 *Voxel-wise, semantic segmentation for simulated data classification and localisation of multiple, simultaneously occurring perturbations*

As alluded in Section 5.4.4 whilst proposing our 3D convolutional, voxel-wise, semantic segmentation network for the German pre-Konvoi 4-loop, one model has been developed to undertake both the German and Swiss pre-Konvoi reactors. Hence, this section will define the changes in dimensionality of reactor mesh, detectors, and outputs to our developed approach. Furthermore, we will provide experimental results for the CORE SIM+ simulated Swiss pre-Konvoi 3-loop MOC 39 for a varying number of simultaneously occurring perturbations, additively combined.

CORE SIM+ simulation data pre-processing

As with the German pre-Konvoi, our single perturbations have been additively combined, split, and manipulated following the same processing pipeline. The change of reactor architecture in-turn arises as a change of reactor mesh dimensions. The Swiss pre-KONOVI has the dimensions *32x32x42*, producing *2(n+2)* volumes of size *16x16x21*, each concatenated channel-wise (*2(n+2)x16x16x21*).

The same number of maximum additive combinations to be experimented are: 15, 30 and 45. However, the Swiss reactor contains fewer detectors – 44 opposed to the Germans 56 – as well as different locations of the detectors. For all details involving the data pre-processing of the CORE SIM+ reactor specific simulations, refer to Section 5.4.4 for the German pre-Konvoi 4-loop, substituting the aforementioned Swiss pre-Konvoi parameters.

3D fully-convolutional, semantic segmentation network for classification and localization of multiple, simultaneously occurring perturbations

Similarly to data pre-processing, the model proposed in Section 5.4.4 is identical in structure for both German and Swiss reactors. We therefore state that only the volume input, output and activation dimensionality are different between the reactors. Additionally, the training procedure and details of which remain unchanged, for full model details substitute German reactor volumetric dimensionalities for Swiss in Section 5.4.4.

Experimental results on CORE SIM+ simulated data

Table 14 shows the experimental results for different numbers of combined perturbations, x = {15, 30, 45}, where number of combined single perturbations are in the range [1, x]. The training procedure remains the same as for the German reactor case, employing Stochastic Gradient Descent (SGD) optimization procedure for back propagation, with a starting learning rate of 0.01, decaying by a factor of 0.1 when the validation loss plateaus for 10 epochs within a threshold of 0.025. A batch size of 64 was used, gamma of 2 for Focal Loss focus parameter. Moreover, the results of experiments for retrieval of vibration parameter K, and θ can be found in Table 15 and Table 16 respectively.

Table 14: Swiss pre-Konvoi 3-loop simulated, per perturbation classification voxel accuracies for voxel-wise semantic segmentation of the unseen test set.

No. Comb	No. Det	Per Class Voxel Prediction Accuracies *									
		Accuracy (%)									
		BG	AVS	CANT	SF	SS	CSF	CSS	CR	TP	BV
15	56	99.43	87.64	89.47	82.14	82.93	89.66	86.11	93.05	91.16	100.00
30	56	99.68	84.45	83.72	92.86	86.54	86.49	81.63	87.85	90.48	100.00
45	56	99.11	80.95	79.41	82.50	90.79	85.71	90.14	89.86	91.81	100.00

* Note: AVS = Absorber of Variable Strength, CANT = Fuel Assembly Vibration Cantilevered, SF = Fuel Assembly Vibration Supported First, SS = Fuel Assembly Vibration Supported Second, CSF = Fuel Assembly Vibration Cantilevered Supported First, CSS = Fuel Assembly Vibration Cantilevered Supported Second, CR = Control Rod Vibration, TP = Travelling Perturbation, BV = Core Barrel Vibration, BG = Background / No Class

Table 15: Swiss pre-Konvoi 3-loop simulated, per perturbation vibration parameter, kappa, classification accuracies for the unseen test set.

No. Comb	No. Det	Per Class Voxel Prediction Accuracies for Kappa Vibration Parameter				
		Accuracy (%)				
		BG	$K=0.25$	$K=0.5$	$K=0.75$	$K=1.0$
15	56	96.51	65.33	22.18	68.86	42.48
30	56	95.17	69.93	20.07	60.51	68.35
45	56	94.50	54.05	26.30	64.49	53.87

Table 16: Swiss pre-Konvoi 3-loop simulated, per perturbation vibration parameter, theta, classification accuracies for the unseen test set.

No. Comb	No. Det	Per Class Voxel Prediction Accuracies for Theta Vibration Parameter				
		Accuracy (%)				
		BG	$\theta=\frac{1}{4}\pi$	$\theta=\frac{1}{2}\pi$	$\theta=\frac{3}{4}\pi$	$\theta=\pi$
15	56	91.28	73.26	55.11	57.85	41.26
30	56	88.57	69.70	17.71	64.34	28.71
45	56	87.46	56.82	72.92	65.64	52.81

Accuracy per class is the performance metric of choice, it is the number of correctly classified voxels belonging to that class. In addition to per class accuracy metric, normalized confusion matrices are provided in Figure 143 for the best performing model. Note that these models have been ran only once and the best results presented above. Other methodologies have results presented as the mean of multiple runs. Given the computation time to process this data, such methodologies were found impractical in the present time frame.

The experimental results presented in Table 14 show similar findings to that found for the German reactor in Section 5.4.4. We observe that our model correctly classifies between perturbation types with high accuracy, whilst false negatives make up the majority of lost performance. We believe further time spent on tuning and training will improve the performance of false negatives. On the other hand, the issue of false negatives is something that has continually impacted performance, with large number of perturbations masking weaker signals causing the miss classification. However, it is observed from the confusion matrices in Figure 143 that the per class performance is in fact good showing good semantic understanding.
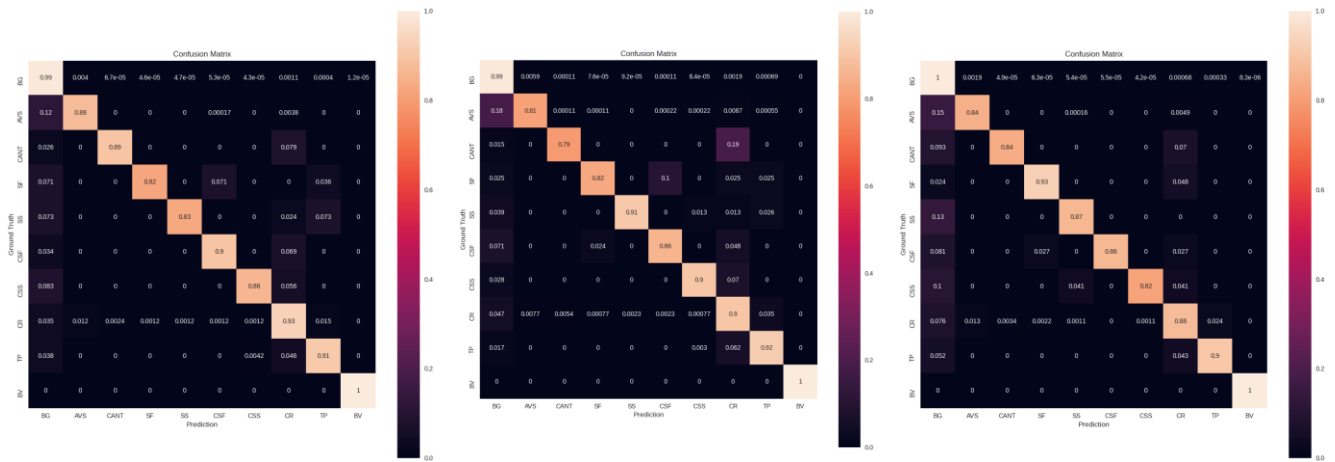
Figure 143: Normalized confusion matrix for each run of differing max combinations for per class per voxel classification accuracy for swiss pre-Konvoi simulations. This ground truth against predicted voxels per classification. Left: max number of combinations = 15. Middle: max number of combinations = 30. Right: max number of combinations = 45.
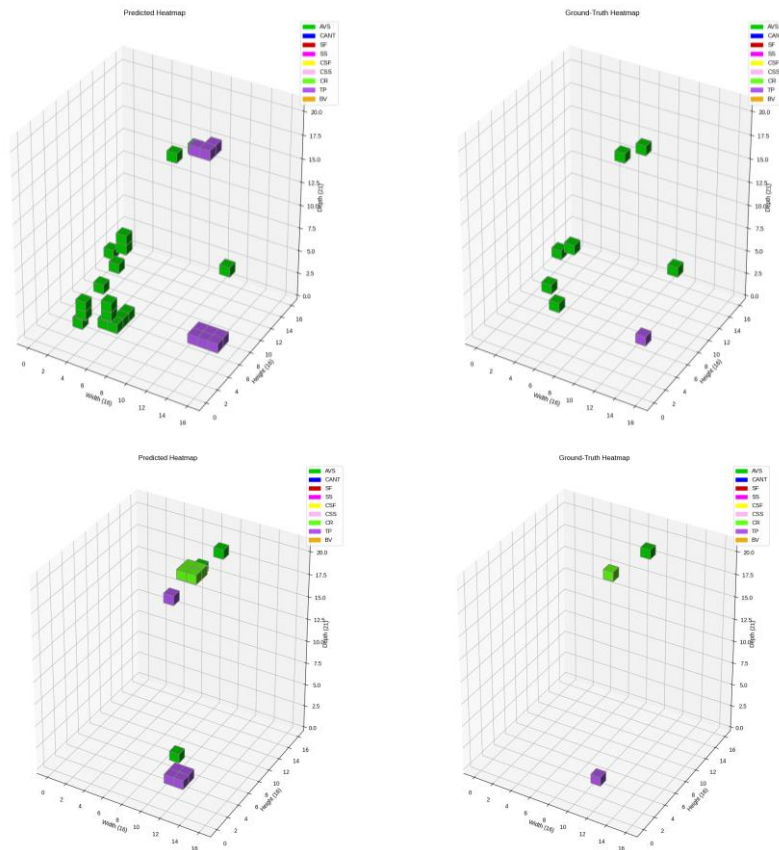
Figure 144: Visualizations of predictions and ground truth perturbation classifications and localizations in the core volume for x = 15 and x = 30. The prediction and ground truth of 7 absorber of variable strength perturbations and 1 travelling perturbation (top two plots). The prediction and ground truth of 1 absorber of variable strength perturbation, one control rod vibration and 1 travelling perturbation (bottom two plots).

As with the results of the German pre-KONOVI simulations, the Swiss pre-KONOVI exhibits the same degradation of sporadic perturbation performance as the number of simultaneous perturbations increases. It is observed that the same effect of absorber of variable strength perturbations performance decreases whilst perturbations originating from more uniformed origins

do not see as much of a decrease. As we conjecture in Section 5.4.4 we attribute this to the greater variation of origin of absorber of variable strength. Additionally, the slightly overall lower performance of the Swiss pre-Konvoi simulations can be attributed to the larger mesh dimensions, meaning more voxels are present and adding more difficulty to the localization procedure. Although, untested we can make the assumption that a reduced mesh size or relaxed localization requirements will reduce the variation in source localization, consequently simplifying the localization task. We plan to test coarser mesh dimensions in the future, however with some hesitation, as the goal is still set at accurately and confidently making predictions at the core mesh dimensions. Additionally, as we introduce a coarser mesh, we also introduce the potential of having multiple perturbations occurring in the same voxel, consequently outputting multiple prediction for the same voxel, not possible for this current architecture.

Finally, we observe the same behavior as in Section 5.4.4 for the retrieval of vibration parameters. However, we do observe that for many combined perturbations the performance does marginally increase over both the smaller values. Further investigations are needed to understand this behavior and we conclude that more work is necessary for the accurate prediction of vibration perturbation parameters. Furthermore, we acknowledge, as we did in Section 5.4.4, that we aim to re-evaluate our approach to vibration parameter prediction and potentially adjust to obtain better performance. Nevertheless, we will continue work on this aspect as well as all other of the classification procedure to improve our results and provide a more appropriate base for inference on real plant measurements.

5.5.7 *Self-supervised domain adaptation for real plant data training and inference*

The self-supervised domain adaptation model proposed in Section 5.4.5 to promote alignment across domains from simulated (source) to real plant measurements (target) remains largely unchanged across reactors. As with the prior sections for the Swiss pre-KONOVI 3-loop, we elaborate on changes in mesh dimensionality, detectors and outputs to the model that inherently vary across different reactor types. Moreover, we provide predictions made on the processed data of the Swiss pre-Konvoi 3-loop MOC 39, using our model trained in a semi-supervised manner.

Plant measurement pre-processing

The data pre-processing pipeline remains unchanged from both Section 5.4.4 and Section 5.4.5 for the simulated and real plant measurements respectively, with omission to core dimensionality and detectors available. Input into the model is a *2(n+2)x16x16x21* volumes embedded with 39 detectors. This is both the case for simulated and real data given that 5 of the 44 detectors available are defective, therefore we exclude them from the input. The defective detectors are: G02-6, C08-4, J06-2, N08-2, and N08-4. For details regarding the data pre-processing, please refer to section for simulated data and Section 5.4.5 for real plant measurements, substituting the German pre-Konvoi 4-loop dimensions, detectors and parameters for the Swiss pre-Konvoi 3-loop values.

Unsupervised domain adaptation through self-supervision for multiple, simultaneously occurring perturbation classification and localization

The self-supervised, domain adaptation model of the 3D convolutional semantic segmentation network proposed in Section 5.4.4 is implemented for use in both German and Swiss pre-Konvoi settings. We perform the same training procedure, with the pre-processed source and target data adjusted for Swiss reactor dimensions, etc. We perform the same auxiliary tasks aiming to align the two domains, then performing inference on the trained model with selected frequencies. The prediction masks for classification and vibration parameters K, and θ for plant measurements are visually and numerically shown in the following sub-section, along with comparisons made to signal processing analysis.

Anomaly prediction and analysis of plant measurements

The results of inference on real plant measurements for the Swiss pre-Konvoi 3-loop for middle of cycle 39 are discussed here. As with Section 5.4.5, the model was trained on simulated data and domain adaption methodology applied to reduce covariance shift. Here comparisons are made to the predictions made by our trained and adapted model from the signal analysis conclusions made previously in this deliverable and in the deliverable D3.5. It is also necessary to note that these results are a prediction of a network with no ground truth value in the adaptation procedure, therefore cannot be considered as entirely accurate without further analysis and validation. Finally, as with Section 5.4.5, we only consider the prediction of anomaly type/classification and source location of the anomaly, we do not predict the vibration parameters or amplitudes in this case. Moreover, we do not predict the control rod vibrations insertion level, instead we trained the model to predict a control rod vibration, assuming that it occurs in that assembly throughout the whole height of the core. Although extremely unrealistic in the present analysis, future analyses will consider actual control rod locations. Furthermore, as with Section 5.4.5, we display such anomalies with axial views (top down) of the assemblies for clearer interpretation, and all figures are defined with a voxel-wise Cartesian coordinate system (i, j, k), and grey pixels representing the area outside of the pressure vessel.

First, for the lower frequencies, below 7 Hz, we observe very distinct blocks of axial travelling perturbations shown by purple voxels in Figure 145. These distinct areas of travelling perturbations are less pronounced in later frequencies. This observation aligns with the signal analysis in Section 4.2 and the deliverable D3.5 section 2.3.3 of the presence of such phenomena, specifically transport phenomena within this frequency range. Additionally, we notice four distinct areas of travelling perturbations rather than the three inlets of the swiss reactor travelling vertically from bottom (k=0) to top (k=20) in the core volume. Although a simple observation, this provides some intuition that our model may be misclassifying an additional anomaly. On the other hand, the four areas of travelling perturbations could quite possibly be attributed to the four-fold symmetry of the core. Further analysis is required to make such conclusions, however, we conjecture that this is potentially a fuel assembly vibration, as it is consistently classified as such. Furthermore, as such vibrations do not occur at these frequency, we hypothesize that this vibration could be the result of a transport phenomenon. As such, the vibration of assemblies could be the result of oscillations of the coolant, which is observed here, resulting in the fuel assembly being excited at lower than natural frequencies.

In addition to the previous observation, we observe a cluster of fuel assembly vibrations present throughout the lower frequency range 2 Hz – 9 Hz which reside centered at radial coordinates (*5,7*). Furthermore, we notice as with the German pre-Konvoi that large quantities of control rod vibrations are present in the predictions, potentially being the result of underperforming feature extraction of control rod vibrations. Conversely, the control rod predictions are somewhat consistent with the locations of the control rods, similarly to that seen with the German pre-KONVOI. The control rod predictions seen in the following figures depict this, with the predictions aligning with the reactor control rod layout with some variance in its prediction of one control rod. We must note that for these reactor measurement predictions our model predicts a large quantity of control rods which inspires further investigation. As with Section 5.4.5, we attribute these to misclassification in the lower frequency ranges, and potential poor alignment from the domain adaptation techniques for this specific anomaly. More investigations will be undertaken to support our claims in the future.
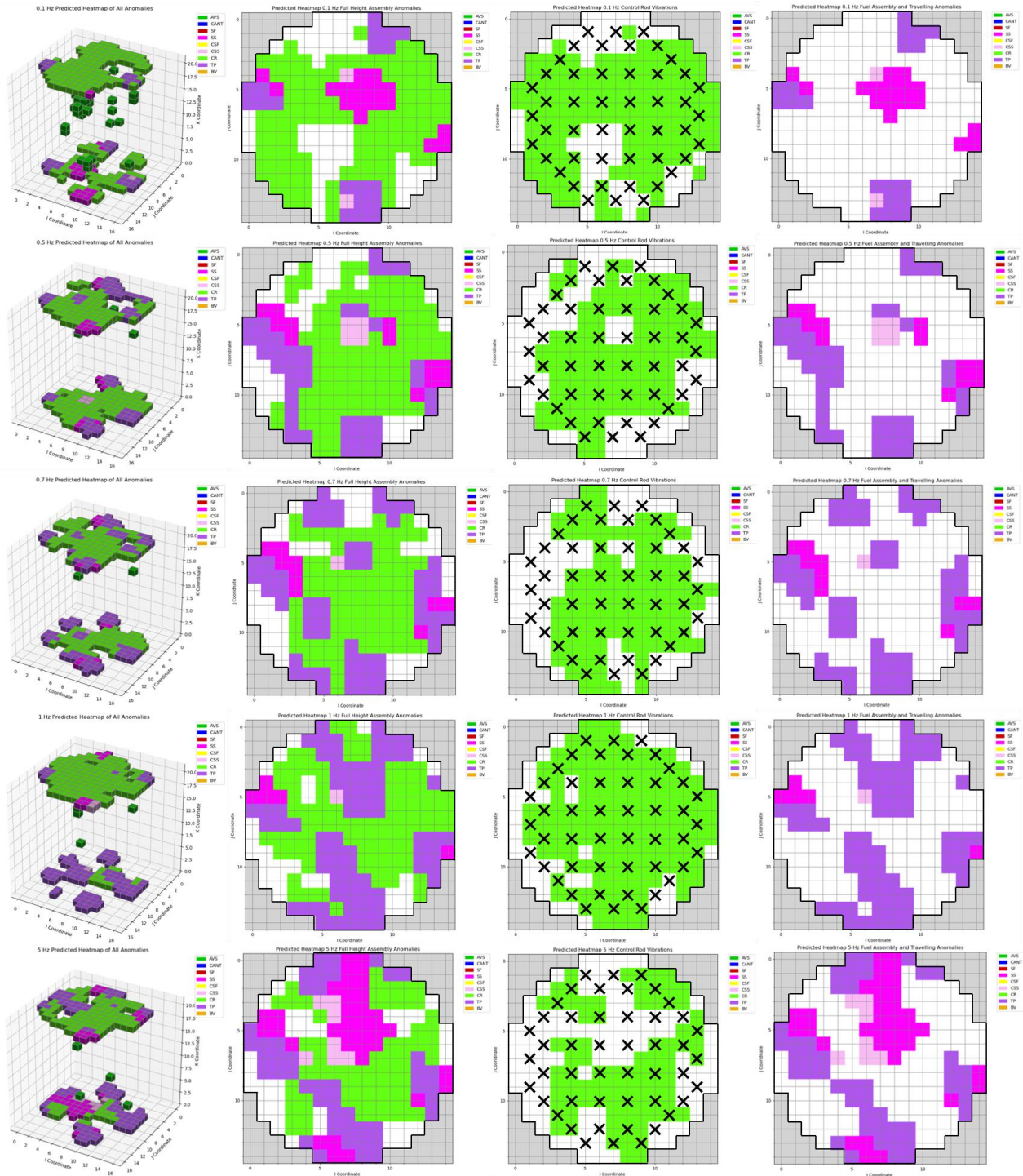
Figure 145: Prediction masks for the Swiss pre-Konvoi 3-loop MOC 39. Frequencies 0.1 Hz, 0.5 Hz, 0.7 Hz, 1 Hz, 5 Hz, ordered from top to bottom row wise. Axial (top down) views of all assembly, control rod, and travelling perturbations are shown (column 2), along with figures separating control rod (column 3) from fuel assembly and travelling perturbations (column 4). Grey pixels represent outside of the pressure vessel and the black crosses represent the position of the control rods.

At the middle of our prediction frequency range, we see clear and large cluster of fuel assembly vibrations of mode second simply supported at 7 Hz. This large block is shown in Figure 146 where previously largely present travelling perturbations are no longer observed. This large block of vibrations could be the cause of the axial level phase behavior reported in the deliverable D3.5 section 2.3.3.2. However, further validation and analysis must be undertaken before conclusions can be made.

Figure 146: Prediction masks for the Swiss pre-Konvoi 3-loop MOC 39. Frequency: 7 Hz. Purple voxels represent travelling perturbations and light green represent control rod vibrations, dark green absorber of variable strength and magenta fuel assembly vibration. Axial (top down) views of all assembly, control rod, and travelling perturbations are shown (column 2), along with figures separating control rod (column 3) from fuel assembly and travelling perturbations (column 4). Grey pixels represent outside of the pressure vessel and the black crosses represent the position of the control rods.

Finally, at the higher frequencies (10 – 25 Hz), we observe very little in regard to signification output, instead we see consistently scattered absorber of variable strength clusters in vertically structure columns. We do not have any intuition if these anomalies are supported by signal analysis. However, the lack of fuel assembly vibrations at these higher frequencies show our model has not made any misclassification of such no-existent anomalies within these ranges. The prediction mask of 12 Hz is shown below in Figure 147.
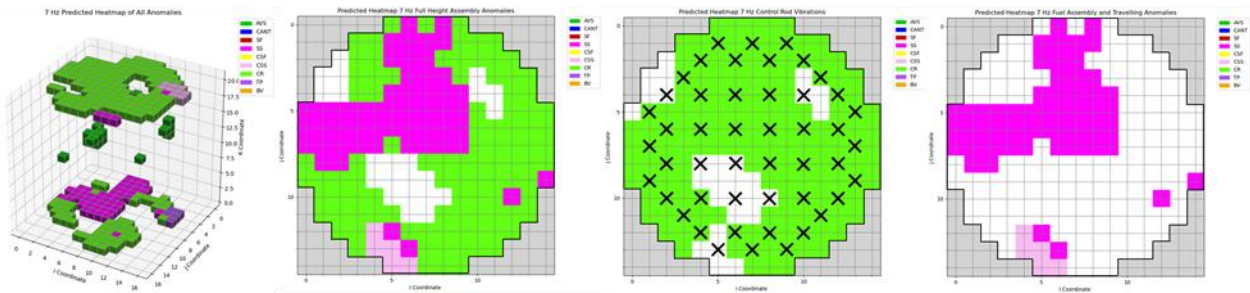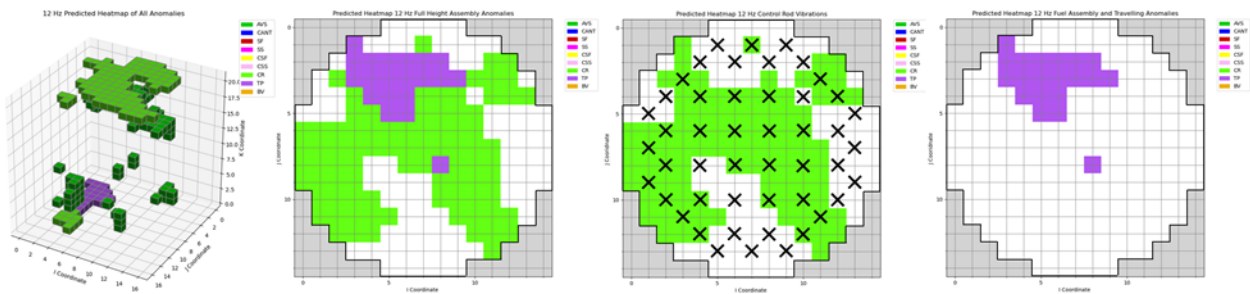

Figure 147: Prediction masks for the Swiss pre-Konvoi 3-loop MOC 39. Frequency: 12 Hz. Purple voxels represent travelling perturbations and light green represent control rod vibrations, dark green absorber of variable strength. Axial (top down) views of all assembly, control rod, and travelling perturbations are shown left to right shown (column 2), along with figures separating control rod (column 3) from fuel assembly and travelling perturbations (column 4). Grey pixels represent outside of the pressure vessel and the black crosses represent the position of the control rods.

We conclude that, similarly to the German pre-Konvoi predictions, phenomena identified in signal analysis approaches correspond to our predictions. Yet the prediction masks for the Swiss pre-Konvoi are far more chaotic and less clear in terms of anomaly cluster structure. We still observe vast numbers of control rod vibrations which we attribute to misclassification through poor domain alignment, and potentially a poorly learnt feature extractor for these classes. Although there are still doubts in terms of validation of our approach, this is a vital step in continuing research and implementation of machine learning. As with Section 5.4.5, it is essential to gain some validation of these predictions and continue work to fully understand and adjust our methodologies to combat potential misclassification and localization of anomalies.

5.6 Hungarian VVER-440 reactor

Data provided by MTA-EK include three measurements of fuel cycle 32 of Unit 2 of the Paks VVER 440/213 reactor during 3 different time periods (beginning, middle and end of cycle, respectively). For the purposes of analysis and machine learning adaptation, the provided data in the time domain have been firstly processed in a similar way to the pre-Konvoi 3-loop and 4-loop plant measurements. As the measurements were already normalized, the only subsequent processing was the detrending of the signals by subtracting their mean.

5.6.1 Feature Extraction

The Hungarian VVER-440 reactor has quite many differences from the 3-loop and 4-loop reactors that have been examined previously, regarding feature analysis and extraction. One of the most important changes that were observed were the dominant frequencies of the signals and the overall distribution of the spectrum. Pre-Konvoi 3-loop and 4-loop reactors usually had multiple low frequencies and one or two single higher ones. This is not the case for the Hungarian reactor. Figure 148 below displays the dominant frequencies of some example in-core sensors. For the Energy and Energy of Differences, the unit of measurement is V^2. For all the features, except Cepstrum, the x-axis is time windows. One time window is 10 seconds or 1000 time steps. The unit of Cepstrum is Volt and its x-axis is seconds.
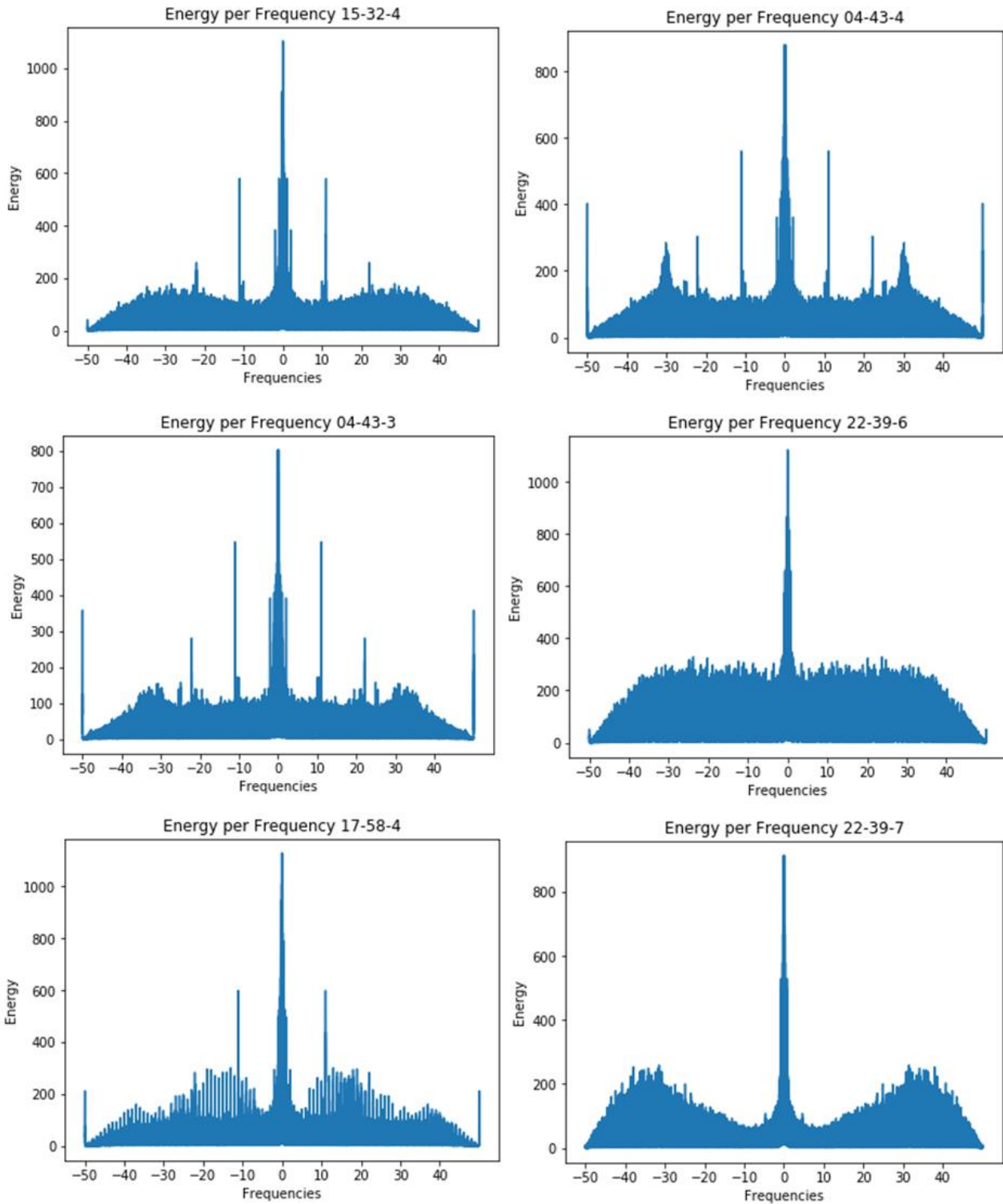
Figure 148: Dominant frequencies of 15-32-4, 04-43-4, 04-43-3, 22-36-6, 17-58-4 & 22-39-7 in-core sensors.

Some observations are presented below:
- The most dominant frequency still lies under 5 Hz.
- It is clear that a continuous spectrum of frequencies is present, in contrast with the previous reactors, where the most dominant frequencies were specific and discrete.

Figure 149 below displays some basic features extracted from in-core sensor 04-37-4.

Figure 149: In-core sensor 04-37-4.

Apart from the in-core sensors, there also exist three other types of sensors in the VVER-440 reactor: (i) on the leg (Figure 150), (ii) on the cable (Figure 151) and (iii) at the exit (Figure 152). Leg and exit sensors are thermocouples, while the sensors on the cable measure the signal (Volts).
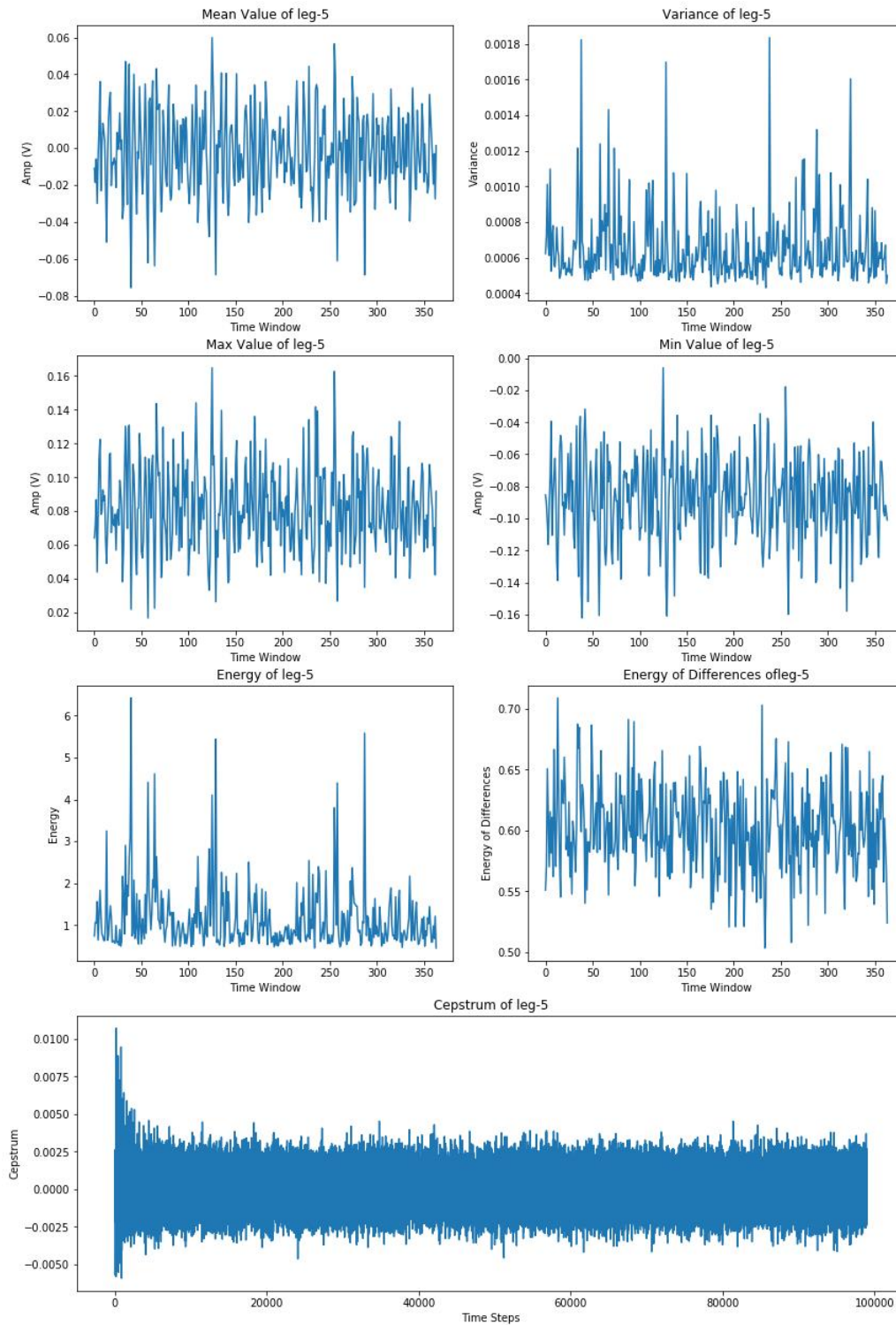
Figure 150: leg-5 sensor.
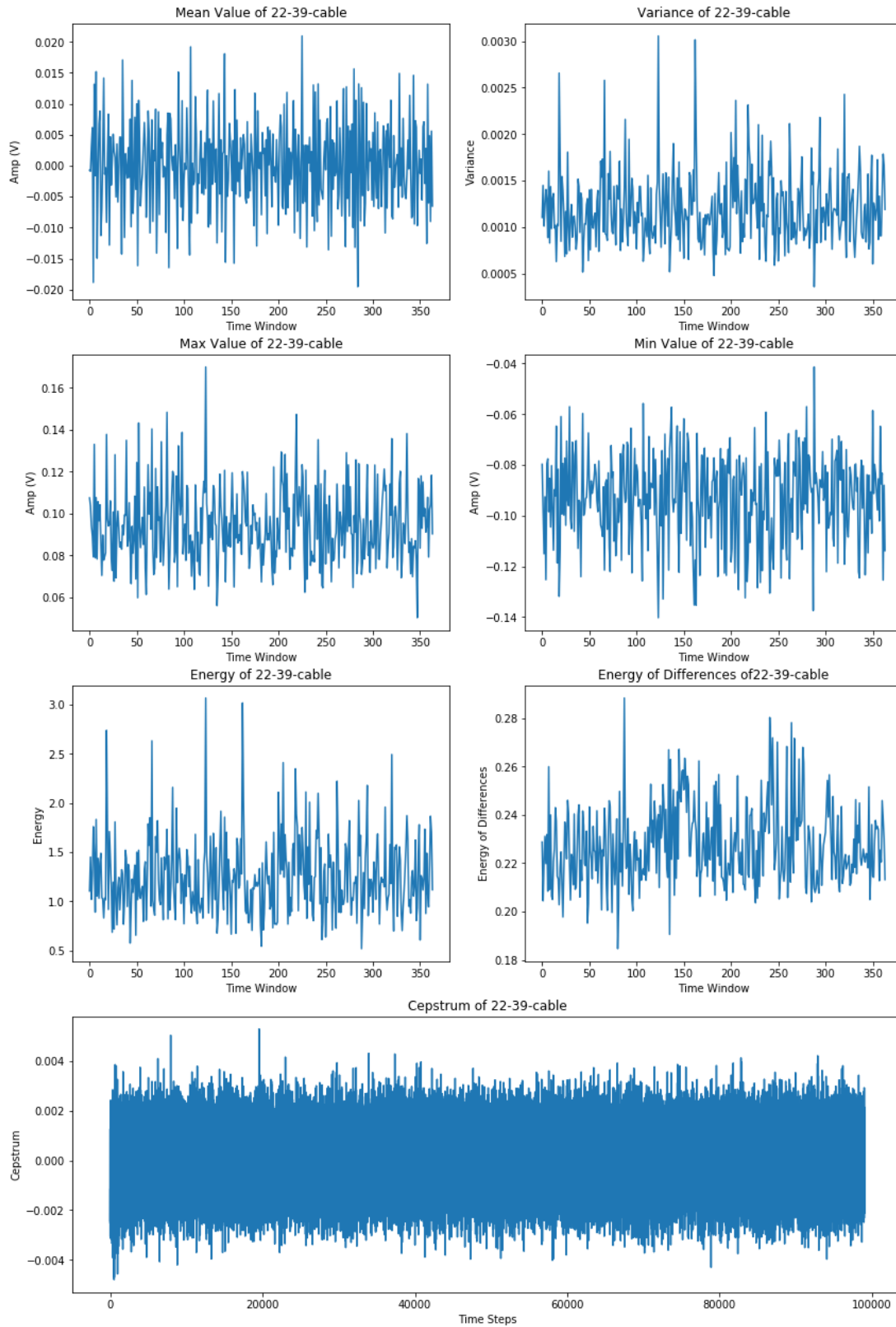
Figure 151: 22-39-cable sensor.
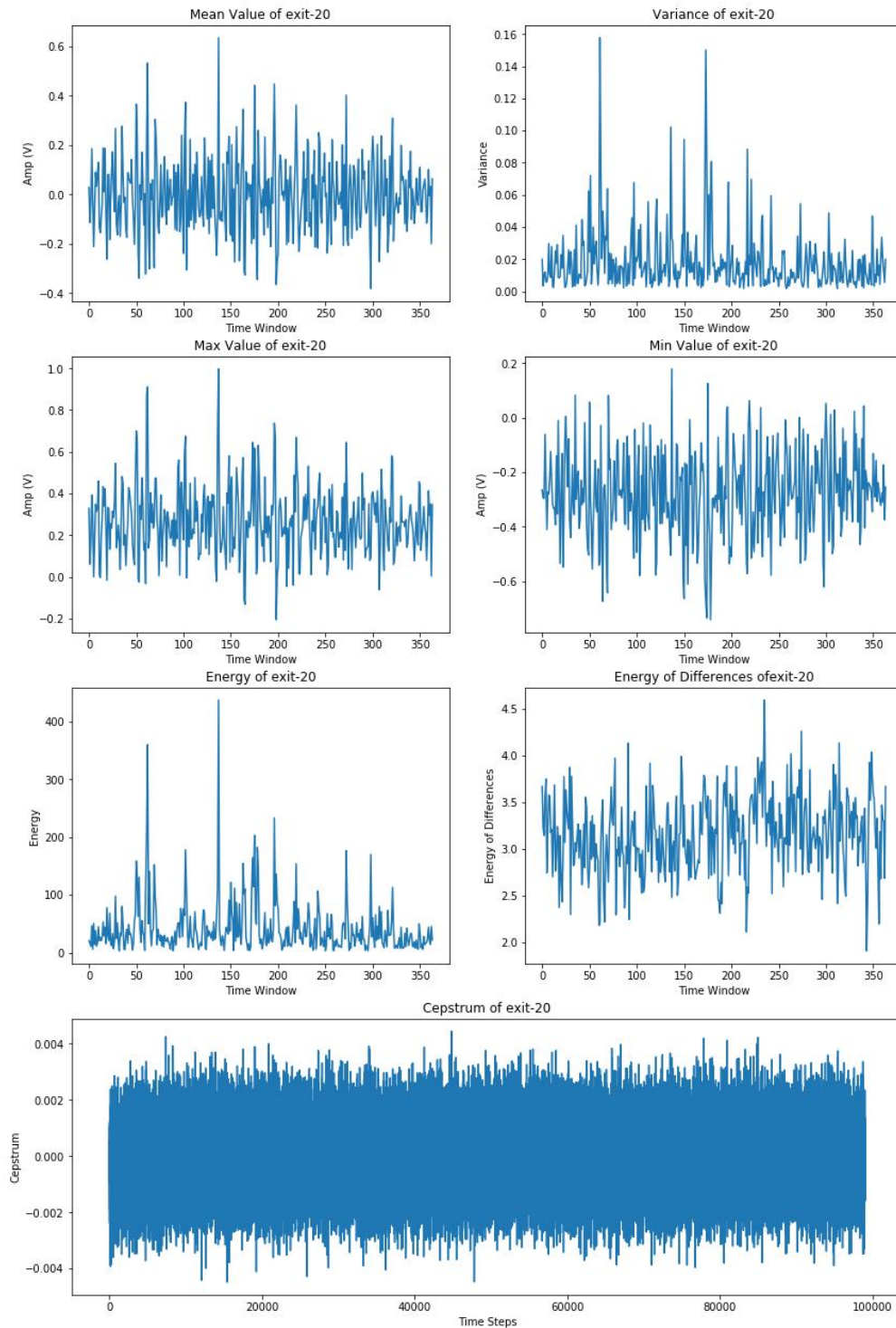
Figure 152: exit-20 sensor.

5.6.2 Clustering

The setup for the clustering of the signals of VVER-440 reactor is similar to the previous ones.

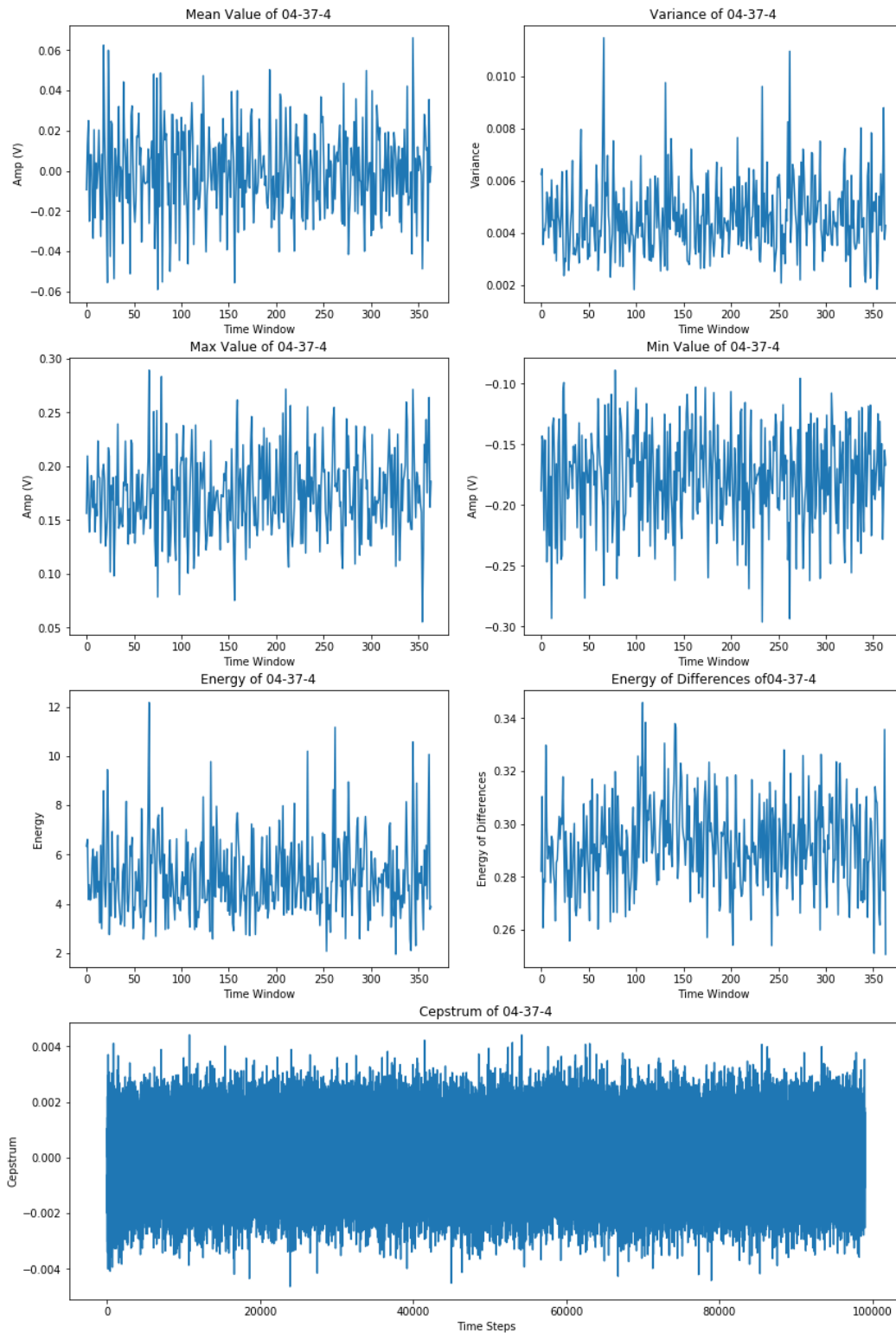*k*-Means did not separate the signals in minority and majority clusters, meaning that there is not a large difference in the number of samples between the two clusters. This probably shows that there are not quite distinguishable anomaly cases and more or less the data can be divided into two equal clusters. Figure 153 below displays the cluster with the fewer signals.
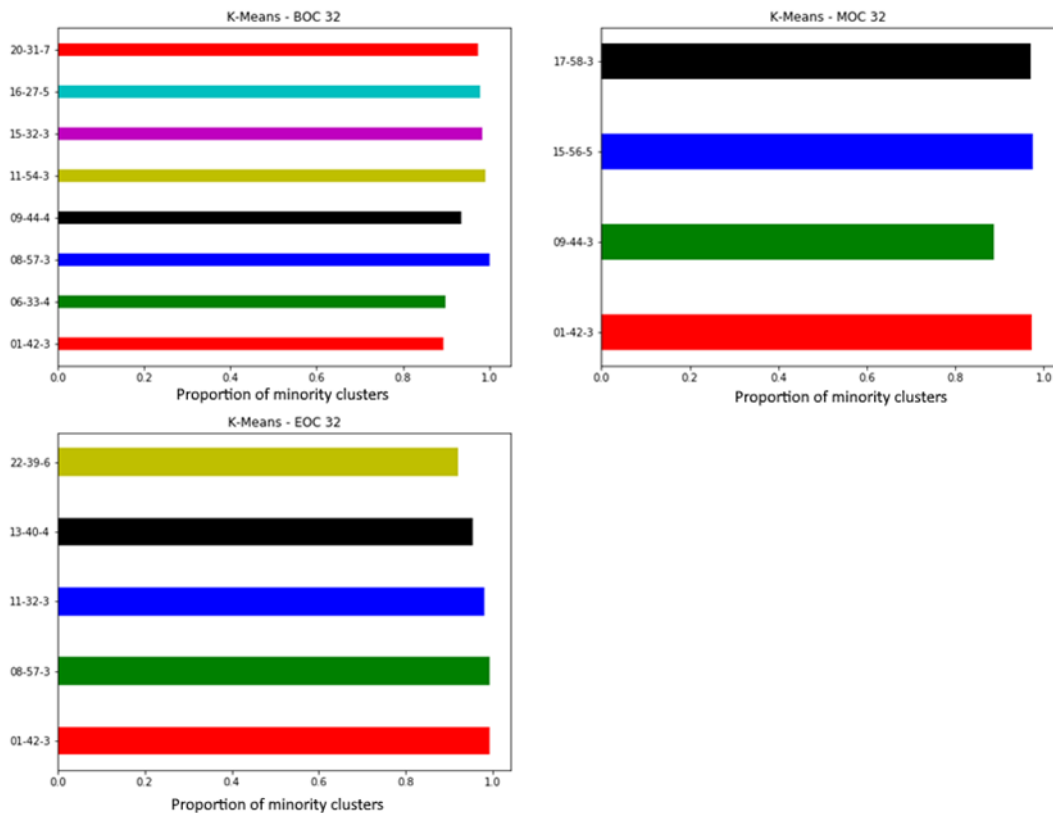
Figure 153: k-Means clustering on VVER-440 reactor signals.

Mean-Shift, DBSCAN and One-class SVM did not find any irregularities in the data and did not produce a minority cluster. Considering the results of the k-Means as well, it is rather safe to assume that there are not probably any sensor that recorded any anomalous behavior.

Isolation Forest produced the following results shown in Figure 154, that come in agreement with *k*-Means clustering. As we can observe during BOC and EOC more outliers are detected. The sensors that have exhibited the most out of the ordinary behavior are 8-57-3, 11-32-3, 22-39-6, 7-48-4 and 4-43-3.
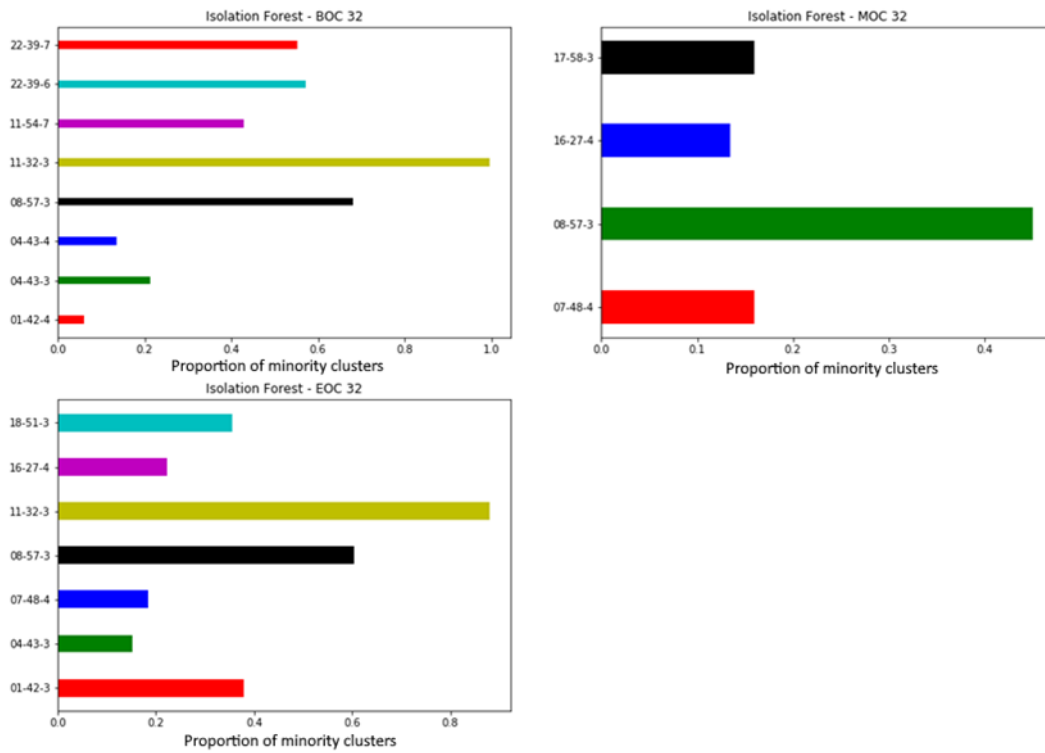
Figure 154: Isolation forest on VVER-440 reactor signals.

Figure 155 below shows the position of the aforementioned sensors on the grid.
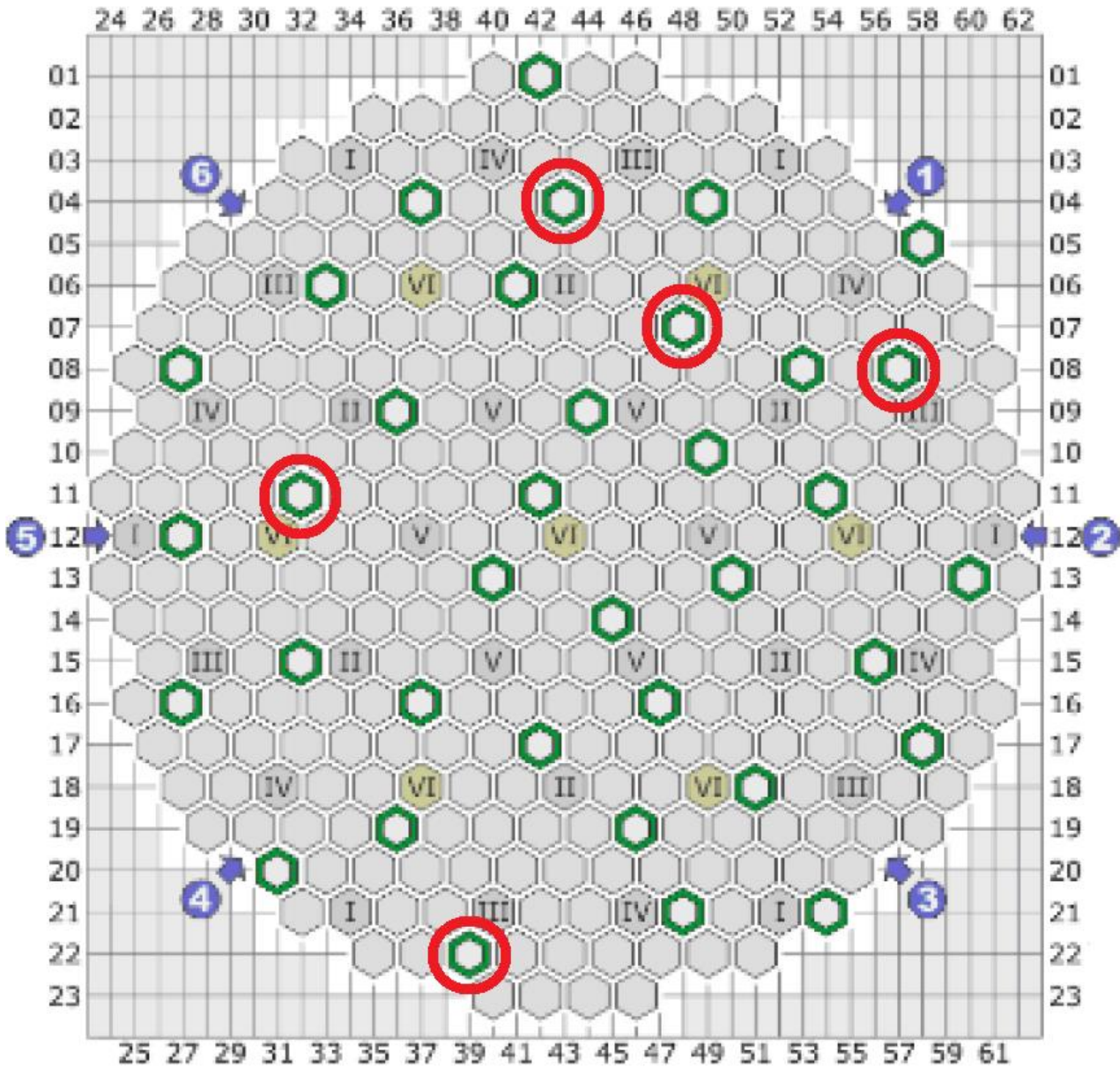
Figure 155: VVER-400 sensors exhibiting out of the ordinary behavior (in red circles).

5.6.3 *FEMFFUSION simulated single perturbation classification and localisation.*

The VVER 440 reactor has been modelled using the FEMFFUSION (Vidal-Ferràndiz et al., 2020a, 2020b) simulation tools, producing simulated neutron flux responses for 252 detectors for two different scenarios of induced perturbation at varying origins. These simulations, like those produced by CORE SIM+, are in the frequency domain. This poses the question of how our previously developed models in the deliverable D3.4 (Kollias, et al. 2019) perform in the same domain of data, i.e. frequency domain, for a different reactor architecture and configuration. Therefore, we test the model presented in (Demazière et al., 2020) with the simulations produced by FEMFFUSION for the hexagonal VVER440 reactor for perturbation types: Absorber of Variable Strength and Travelling Perturbation.

FEMFFUSION simulation data pre-processing

The primary concern of pre-processing VVER-440 reactor simulations is the hexagonal structure of the reactor, and henceforth the hexagonal spatiality in which we aim to localize perturbations.

Standard CNNs – neural networks that we utilize in our approach for frequency domain feature extraction – require data to be in a known grid-like topology, specifically a square lattice arrangement. Although work has been proposed to allow hexagonal lattice structures, these are not commonplace in ML, rather it is more typical to convert the hexagonal grid to square grid. Additionally, given that we aim to compare the results of the VVER-440 to the generic pre-Konvoi from the deliverable D3.4, it is necessary to utilize the same network. Therefore, we convert the hexagonal grid to a square grid via offsetting every other row to form a *25x25x48* volume of the VVER-440 core. This conversion is visually depicted in Figure 156.

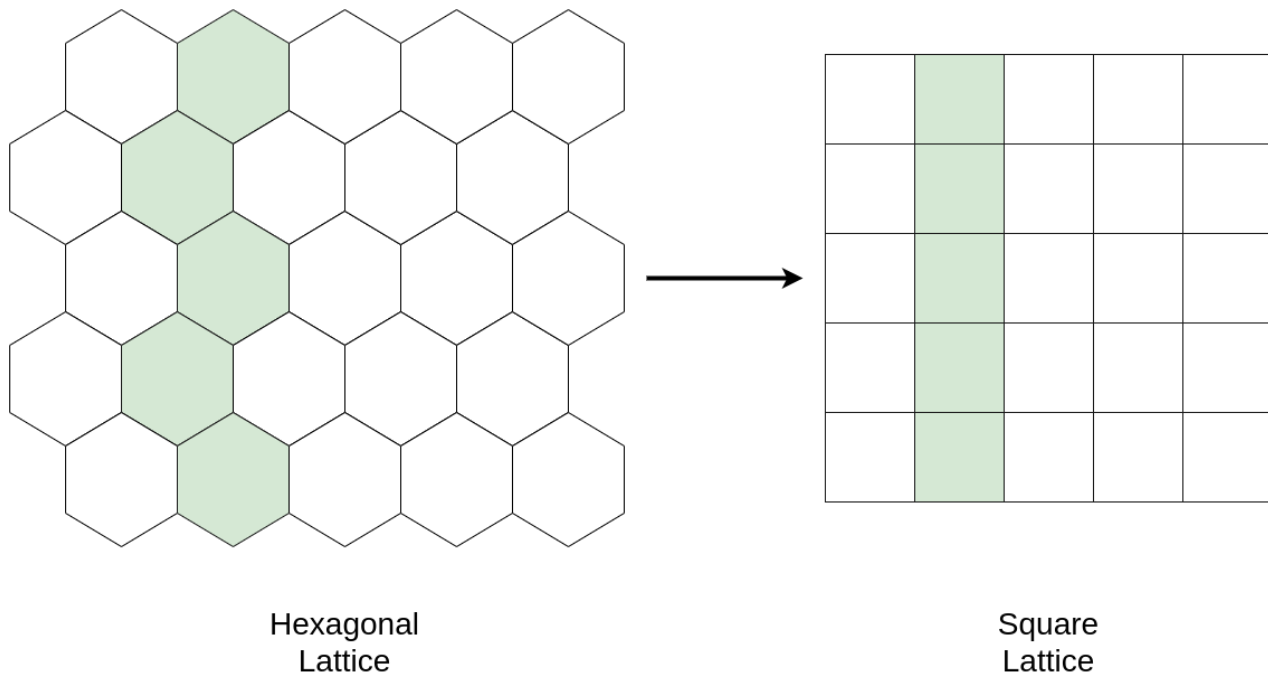Hexagonal
Lattice

Square
Lattice

Figure 156: Visual depiction of the shifted column approach to the conversion of a hexagonal lattice to square lattice for the implementation into proposed ML models.

Pre-processing of the VVER-440 simulated data samples has been handled in a similar manner to those proposed in the deliverable D3.4 (Kollias, et al. 2019). The dataset is first split into train, validation, and test sets (70%,15%,15% respectively), ensuring that for each set the perturbation origin per perturbation type does not appear across sets. Each individual data sample APSD is computed from the induced neutron flux detector readings, and the APSD of each detector is placed within a *25x25x48* volume of zeros in its corresponding location. Note its hexagonal location is transformed to the square lattice VVER440 core volume. This procedure embeds spatial understanding into the volume. The volume is decomposed into amplitude and phase components of APSD detector values, as complex values are not supported in ML frameworks. Thus, producing a *2x25x25x48* volume to be fed into the model. Finally, the volume is normalized to have zero mean and a standard deviation of one.

3D densely connected, fully-convolutional neural network for single perturbation classification and localization

As aforementioned, it is of interest to evaluate the performance of the developed models in different reactor settings, e.g. architecture, configuration. This case examines the performance given a change in reactor architecture. The ML model to be trained and evaluated is the model presented in (Demazière et al., 2020) and the deliverable D3.4 (Kollias, et al. 2019) for a close comparison with the CORE SIM+ simulated data for a generic PWR.

The network is fully described in the deliverable D3.4, however, given different reactor architectures and difference in perturbation scenarios, the network has been adapted. Firstly, the 3D CNN

DenseNet (Gao et al. 2017) input and GAP dimensionality have been modified to accommodate different input dimensions from *2x32x32x32* to *2x25x25x48.* Secondly, the output layer is changed from SoftMax categorical cross entropy and replaced with a single sigmoid neuron. The second change is more fundamental to the performance comparisons, where FEMFFUSION simulation provides two perturbation scenarios (binary classification), while CORE SIM+ provides five scenarios. This results in the classification output of the network being a single neuron for binary classification, and therefore trained to minimize the binary cross entropy loss.
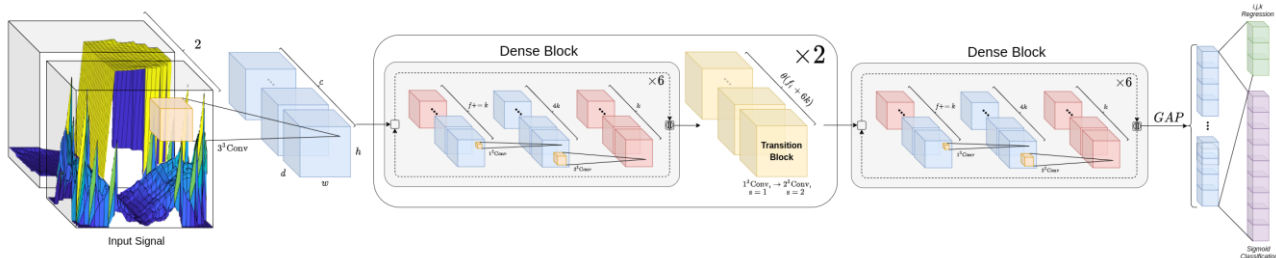

Figure 157: 3D fully-convolutional neural network for the classification and localization of single perturbations in the frequency domain, proposed in (Demazière et al., 2020).

As with (Demazière et al., 2020), the network was trained with the Adam optimizer to minimize the multi-task loss in Equation 29. Similarly to section 5.5.5, this loss is comprised of the L1 loss Equation 33 for regression of the *i,j,k* coordinates of perturbation origin, and a binary cross entropy loss Equation 29 where =1**.** For details regarding training procedures and model architectures, refer to D3.4 (Kollias, et al. 2019) and (Demazière et al., 2020).

Experimental results on FEMFFUSION simulated data

Experiments have been conducted to classify perturbation type and regress its source coordinates under different values of additive white gaussian noise: No Noise, SNR=3, SNR=1. The results of these experiments are given in Table 17 and confusion matrix of each experiment in Figure 158. Each model is trained three times per experiment, and the mean and standard deviation of the three runs presented below.

Table 17: Results of VVER-440 classification of perturbations and localization of the coordinates of classified perturbations, simulated in FEMFFUSION utilizing the 3D fully-convolutional model. Mean and standard deviation of 3 runs are presented.

Binary Classification and Localization of Single Perturbations in VVER440 Simulations				
SNR	Classification Metrics		Regression Metrics	
	Acc Error (%)	F1-Score	MAE	MSE
No Noise	0.28±0.022	0.996±0.002	0.796±0.006	1.690±0.017
3	0.75±0.086	0.992±0.009	1.760±0.013	7.979±0.078
1	1.79±0.154	0.976±0.012	1.854±0.021	9.021±0.083

Results show that for binary classification of classes absorber of variable strength (AVS) and travelling perturbation (TP) in the VVER440 simulations, performance is excellent. For all experiments, even with the addition of noise at SNR=1 the network was able to determine between the two at near perfect accuracy. As for localization performance, the network performs worse than the generic PWR demonstrated in the deliverable D3.4 by some considerable margin. Although at first this may appear to be negative, we find this is an expected drop in performance. Moreover, even though this is worse performance than in the deliverable D3.4, a MAE of approximately 0.8 is an

excellent result, localizing these perturbations to within one assembly on average over the test dataset.
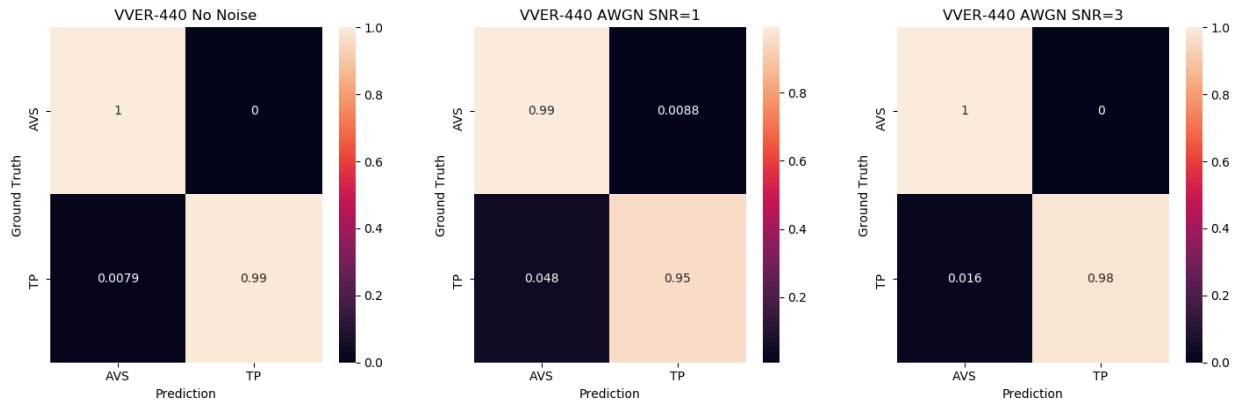

Figure 158: Confusion matrices of prediction of absorber of variable strength or travelling perturbation under different SNR of AWGN. No noise (left); SNR=3 (middle); SNR=1 (right).

Furthermore, we conjecture that the worse performance when making comparisons to the deliverable D3.4 is primarily due to the dataset size. This is in fact a large contributing factor to the aforementioned training procedure, where far fewer examples are presented in the VVER440 simulations in comparison to the generic PWR simulations provided by CORE SIM+. Simply put, the network has fewer examples to learn from and with less variation in signal response, resulting in less information. We conclude this is also the reasoning behind the drop of regression performance with the addition of AWGN, as limiting the variety in the training data results in fewer robust features learnt. Furthermore, the conversion procedure from a hexagonal lattice to a square lattice could be an additional cause for greater localization error, where spatial understanding may be misinterpreted by the network. This may require more specialized methods to ensure hexagonal spatial understanding is learnt or maintained in the future.

5.7 Czech VVER-1000 reactor

Data provided by UJV included measurements of 4 cycles from the Temelin Power Plant. These measurements have been taken between cycles 9-12. Unlike the reactors discussed previously, it is known that a problem occurred at the end of cycle 12. The problem of IRI (Incompatible Rod Insertion), as this operational failure is called, constitutes a good evaluation of the robustness of the proposed tools and techniques.

5.7.1 Feature Extraction

The measurements of this reactor pertain to three types of sensors: (i) in-core (Figure 159), (ii) ex-core (Figure 160) and (iii) accelerometers (Figure 161). For the Energy and Energy of Differences the unit of measurement is V^2. For all the features, except Cepstrum, the x-axis is time windows. One time window is 10 seconds or 10000 time steps. The unit of Cepstrum is Volt and its x-axis is seconds.
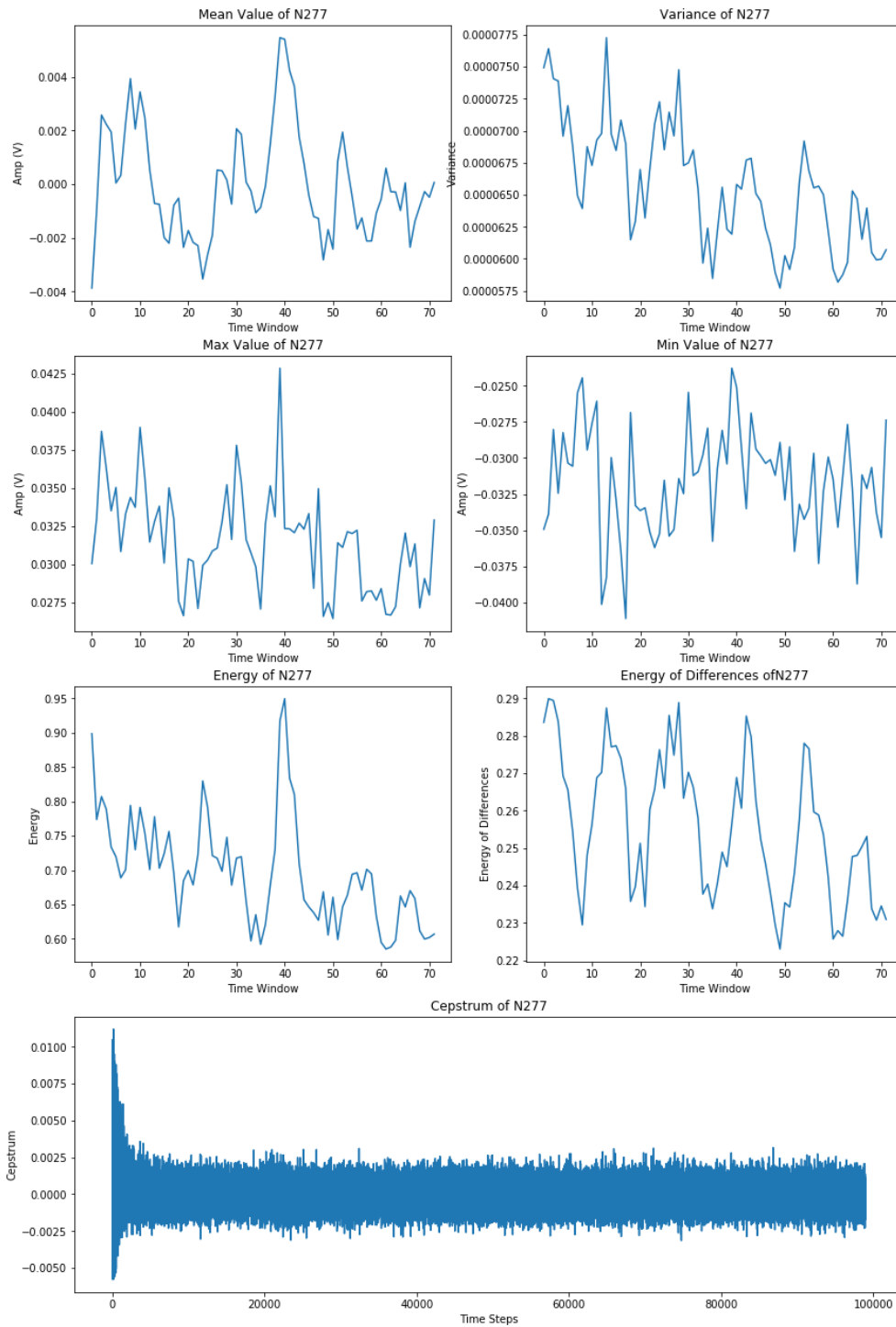
Figure 159: In-core sensor N277.
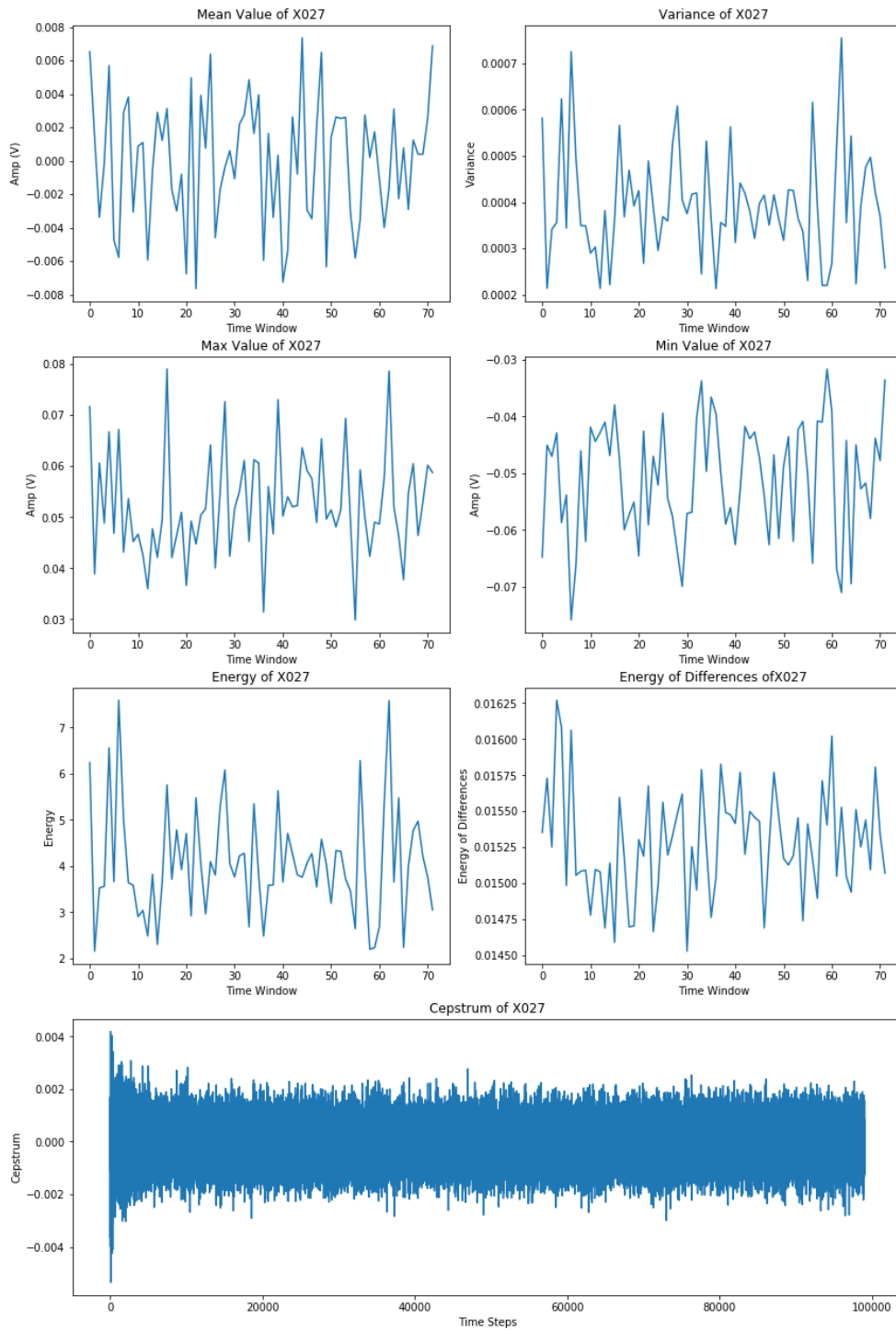
Figure 160: ex-core sensor X027.
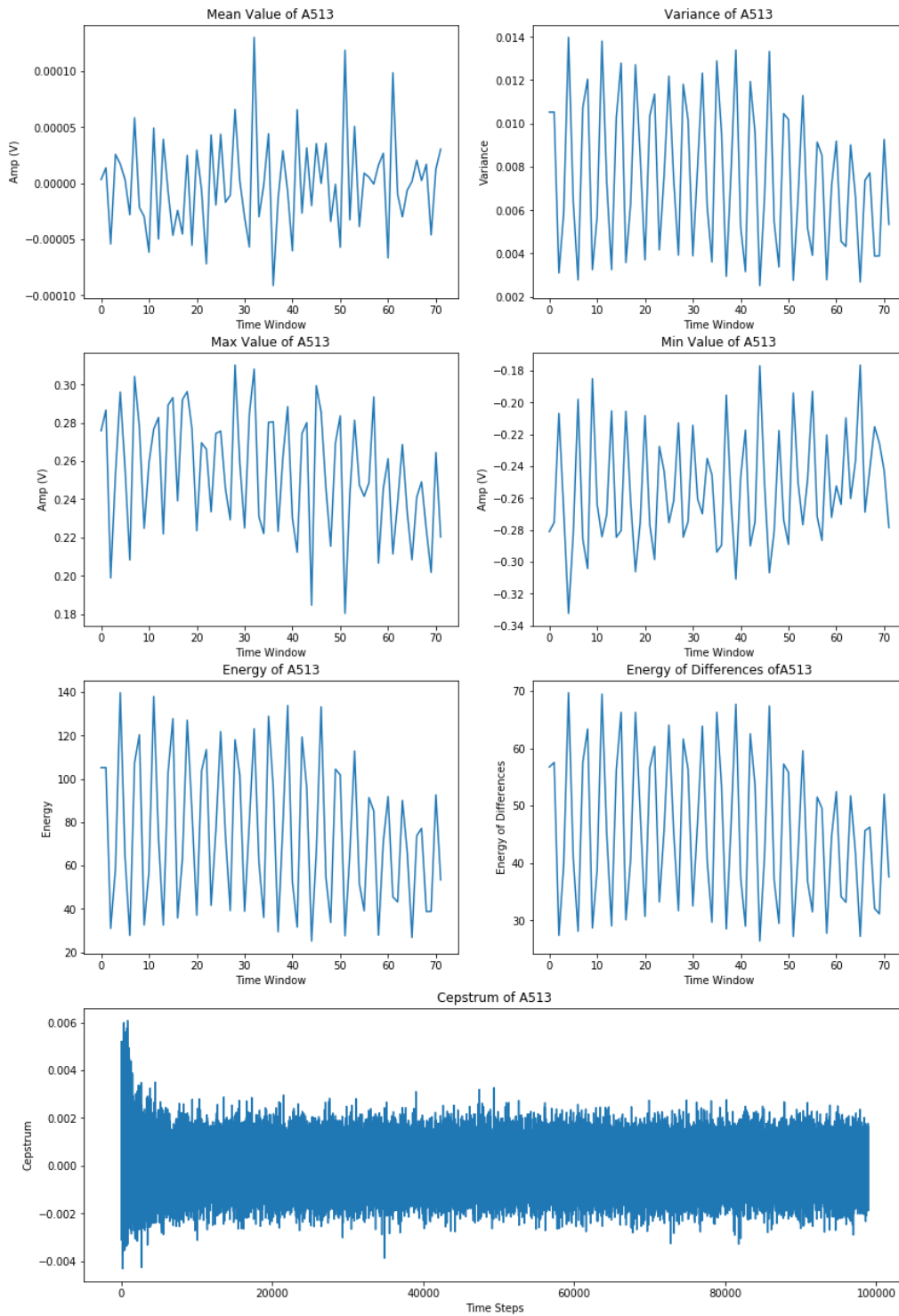
Figure 161: accelerometer sensor A513.

It is known that during cycle U1C12 an issue occurred. Therefore, it is interesting to compare the dominant frequencies from different sensors between the previous cycles and cycle 12. The left column of Figure 162 depicts the energy of the captured signals of three in-core sensors during cycle 10 and the right column of Figure 163 depicts the energy of the same sensors during cycle 12.

Figure 162: Energies of in-core sensors N157, N161 & N371 during cycle 10 (left column) and cycle 12 (right column).

Figure 163: Energies of in-core sensors N471 & N485 during cycle 10 (left column) and cycle 12 (right column).

Some observations are summarized below:

- It is clear that the energy per frequency has increased greatly during cycle 12.
- At some cases, especially sensor N485, more dominant frequencies seem to have emerged.
- Other sensors, like N157 and N471, have fewer dominant frequencies.
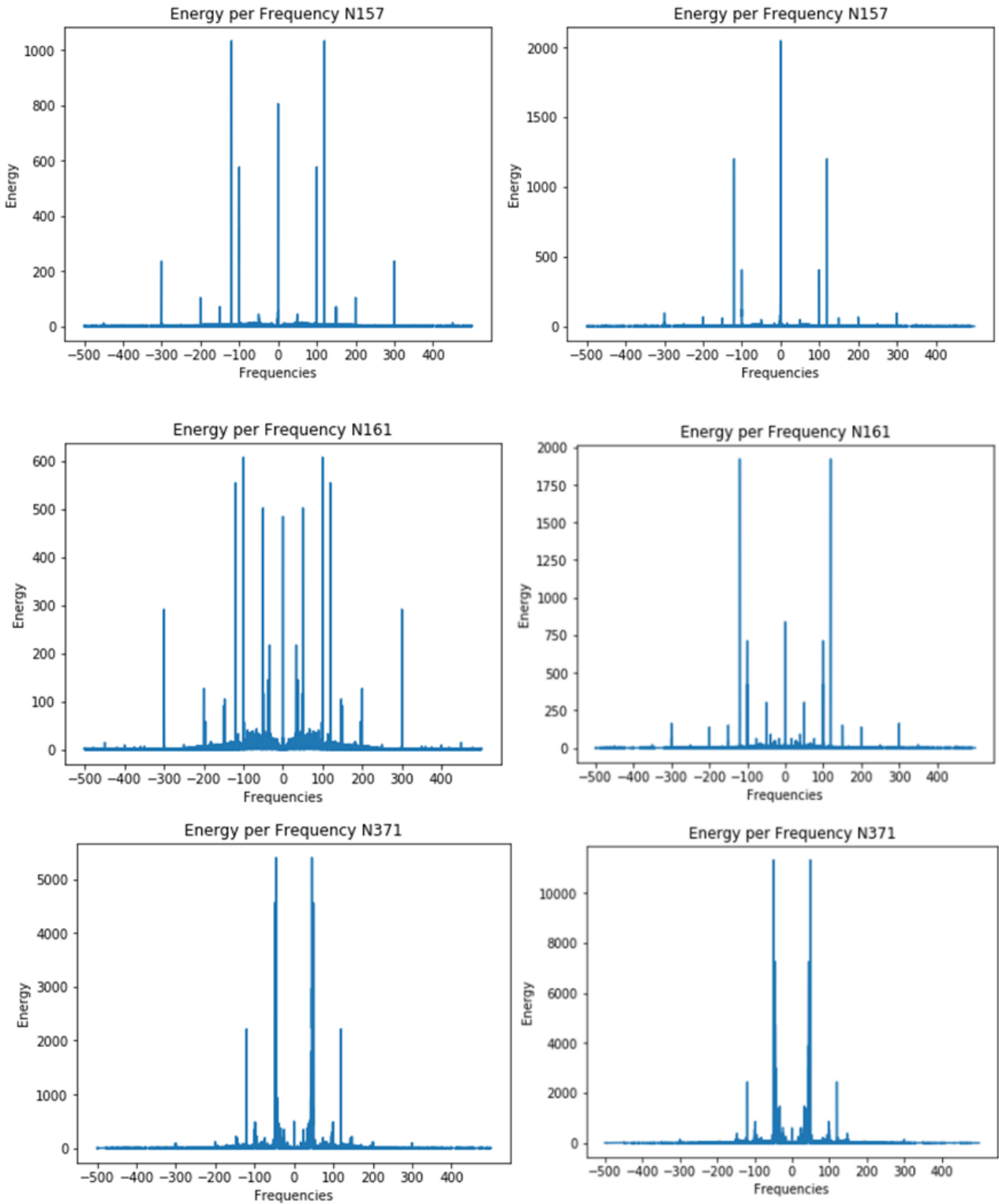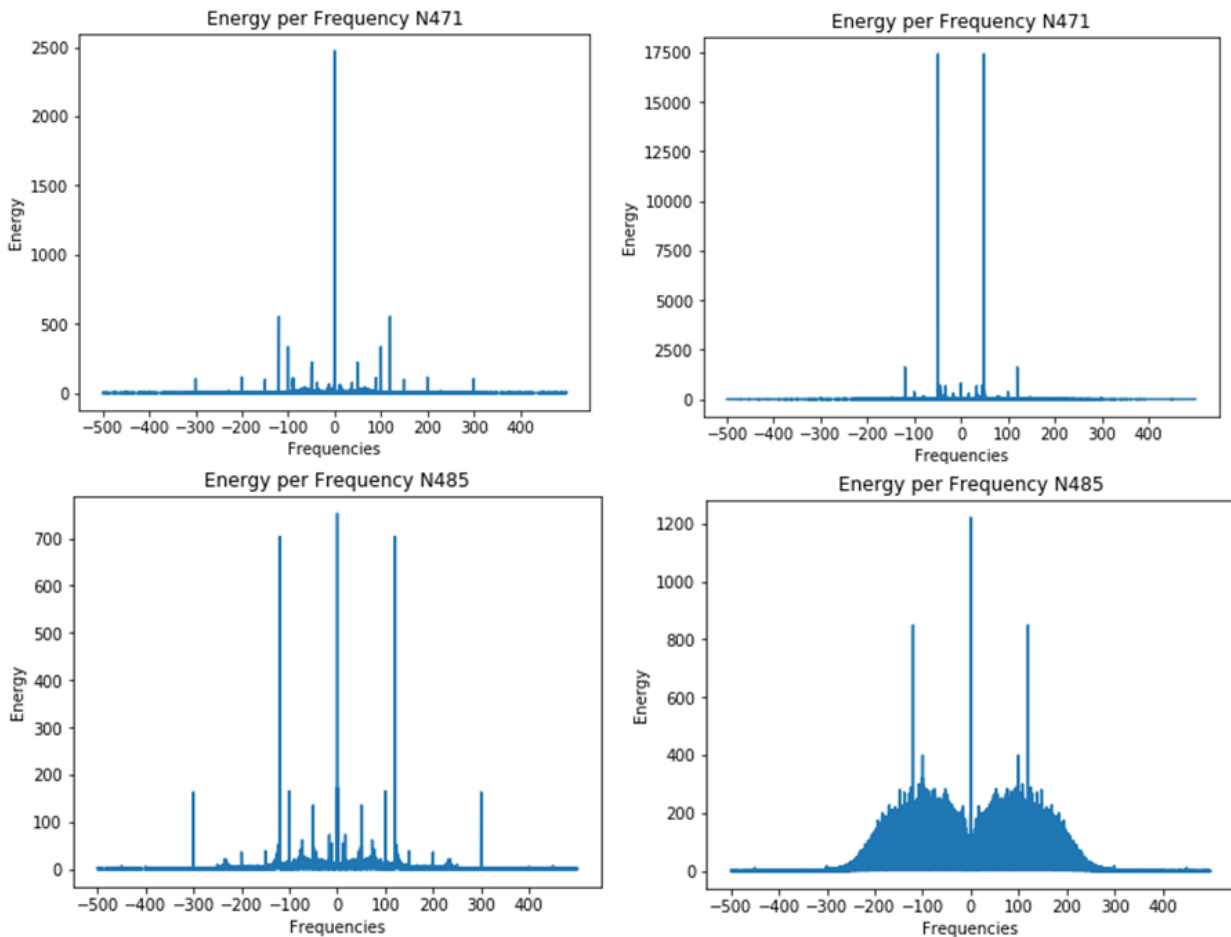
5.7.2 Clustering

Since simulated data for this type of reactor were only recently generated, we proceed with the clustering approaches discussed in Section 5.3.

k-Means shows an abundance of sensors that display signs of anomaly – see Figure 164. Specifically, in cycle U1C09, seven sensors have been singled out, with N027 and N367 being the ones with the higher proportions. It is also clear that the following cycles show a continuous increase of anomalous sensors. In cycle U1C12, there is the biggest peak of the number of sensors that exhibit an anomaly. Some sensors, like N623, N531, N191, were also found in the previous cycles, but others like N481, N521, N411 started exhibiting outlier signals in the last cycle.
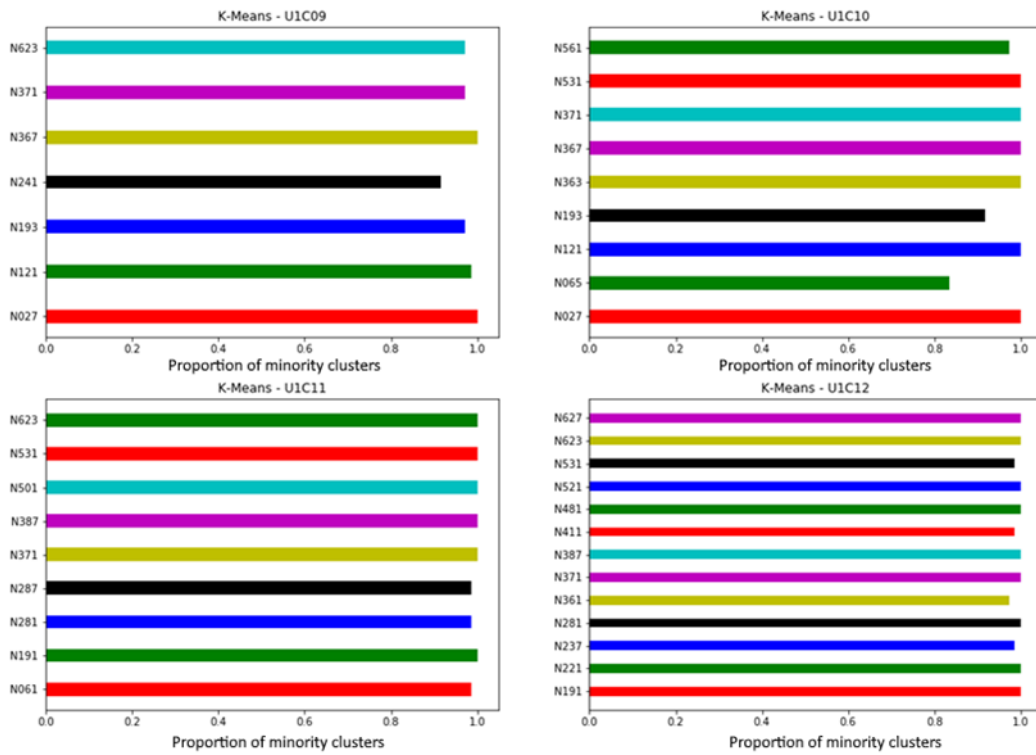
Figure 164: k-Means clustering on VVER-1000 reactor signals.

Mean Shift shows less sensors with outlier behavior overall, but still the majority is located in cycle U1C12 – see Figure 165. The main "minority cluster" sensors are N623, N371, N191, N531, N027. Their proportions seem to have decreased compared to the K-Means ones.
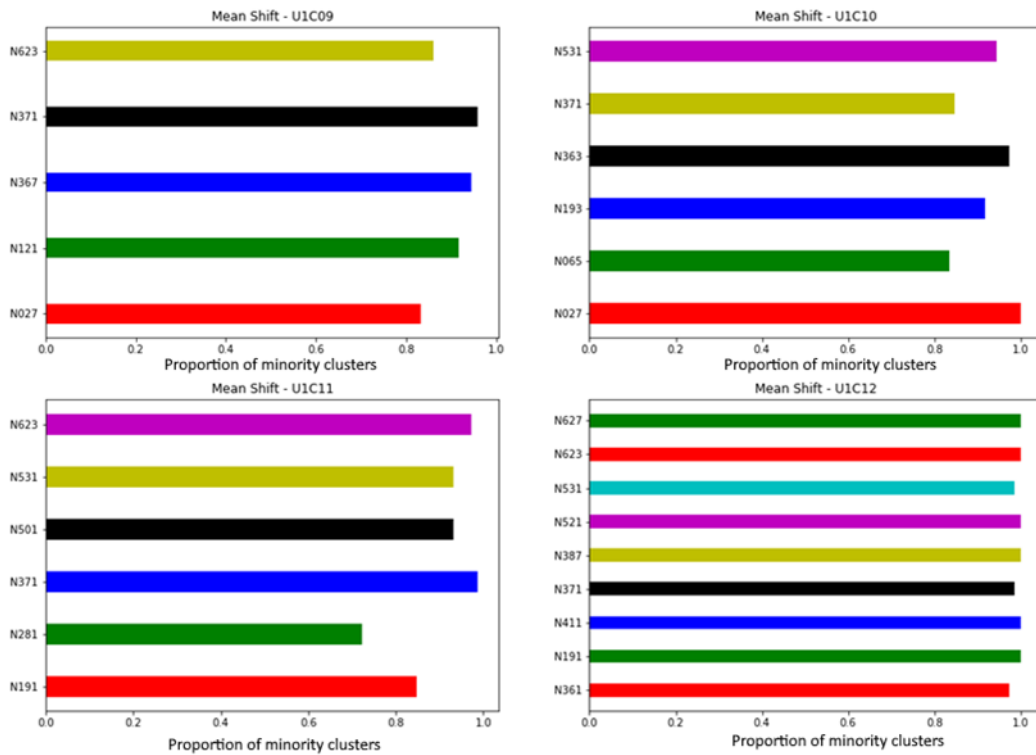
Figure 165: Mean-shift clustering on VVER-1000 reactor signals.

In the first two cycles, DBSCAN results are in compliance with the other clustering algorithms, regarding sensors N027, N371 and N623 – see Figure 166. It also supports the observation that cycle U1C12 has by far the most cases that exceed the other 3 cycles.
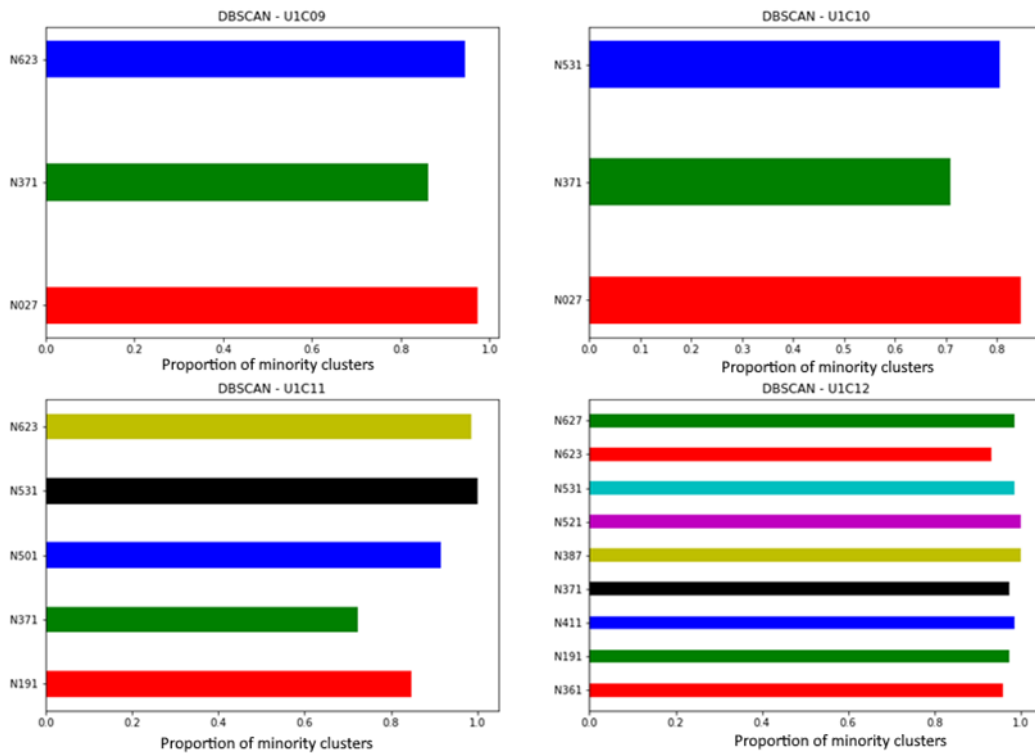
Figure 166: DBSCAN clustering on VVER-1000 reactor signals.

One-Class SVM displays a more polarizing view than the other clustering algorithms – see Figure 167. It reveals that the first three cycles only have a couple of sensors that exhibit an abnormal behavior, while in cycle U1C12 almost the same number of sensors have been labelled as anomalous cases as the rest of the algorithms. It also seems that the sensors found were the same as the ones in the previous cases.
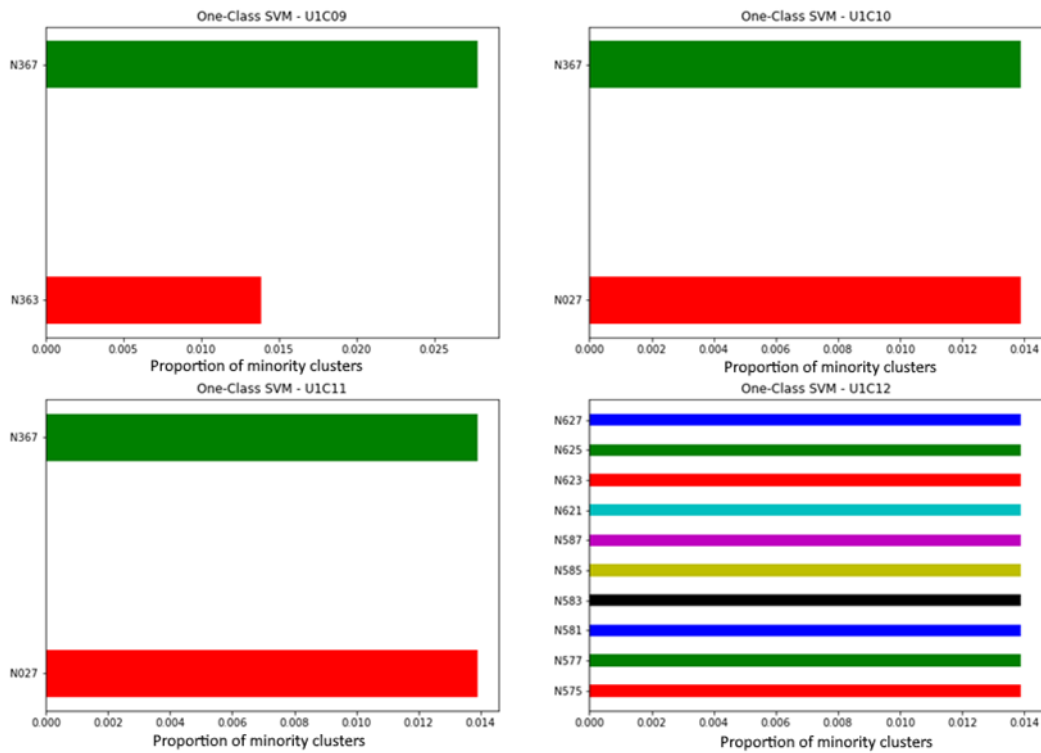
Figure 167: One-class SVM on VVER-1000 reactor signals.

The Isolation Forest exhibited a different result – see Figure 168. Although the number of sensors in the high minority cluster is larger in cycle U1C12, their respective proportions are not as high as depicted in the other clustering attempts. Nonetheless, the same groups of sensors again appear to exhibit outliers, like N623, N627, N371, N027.
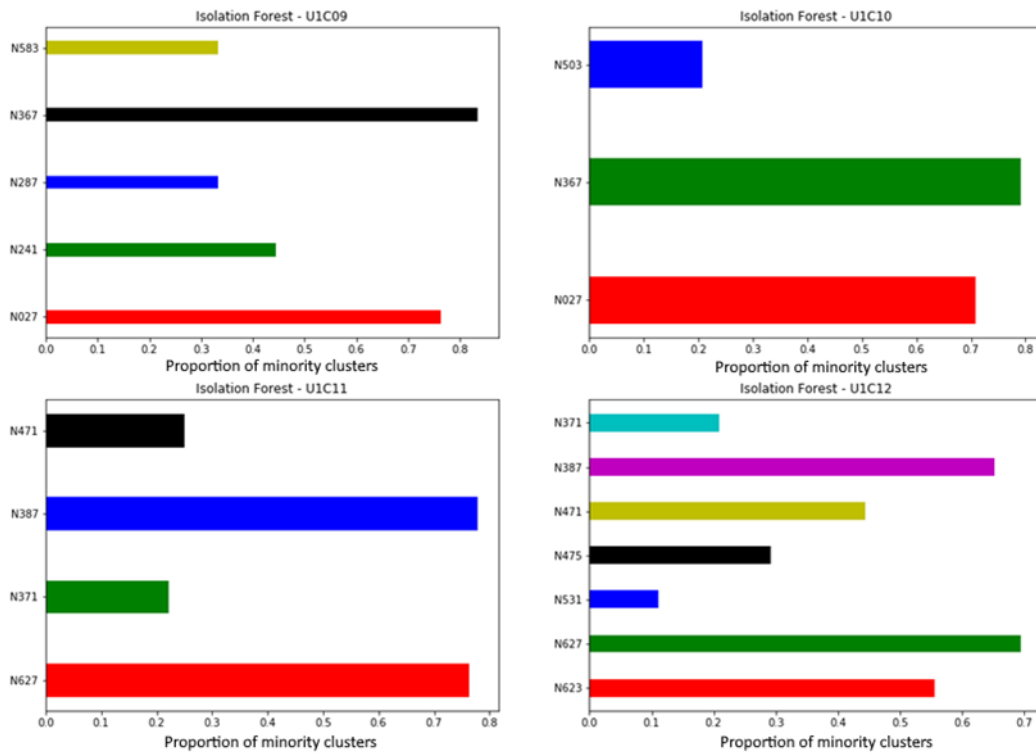
Figure 168: Isolation Forest on VVER-1000 reactor signals.

The overall analysis showed that, in all examined cycles, sensors N027, N367, N623, N627, N371, N531, N191 detect signals that exhibit out of ordinary behavior. Additionally, every algorithm suggested that there was an increase in anomaly cases during the last cycle, U1C12, which does agree with the fact that a known problem occurred during that cycle. Figure 169 below shows the position of the aforementioned sensors on the grid.
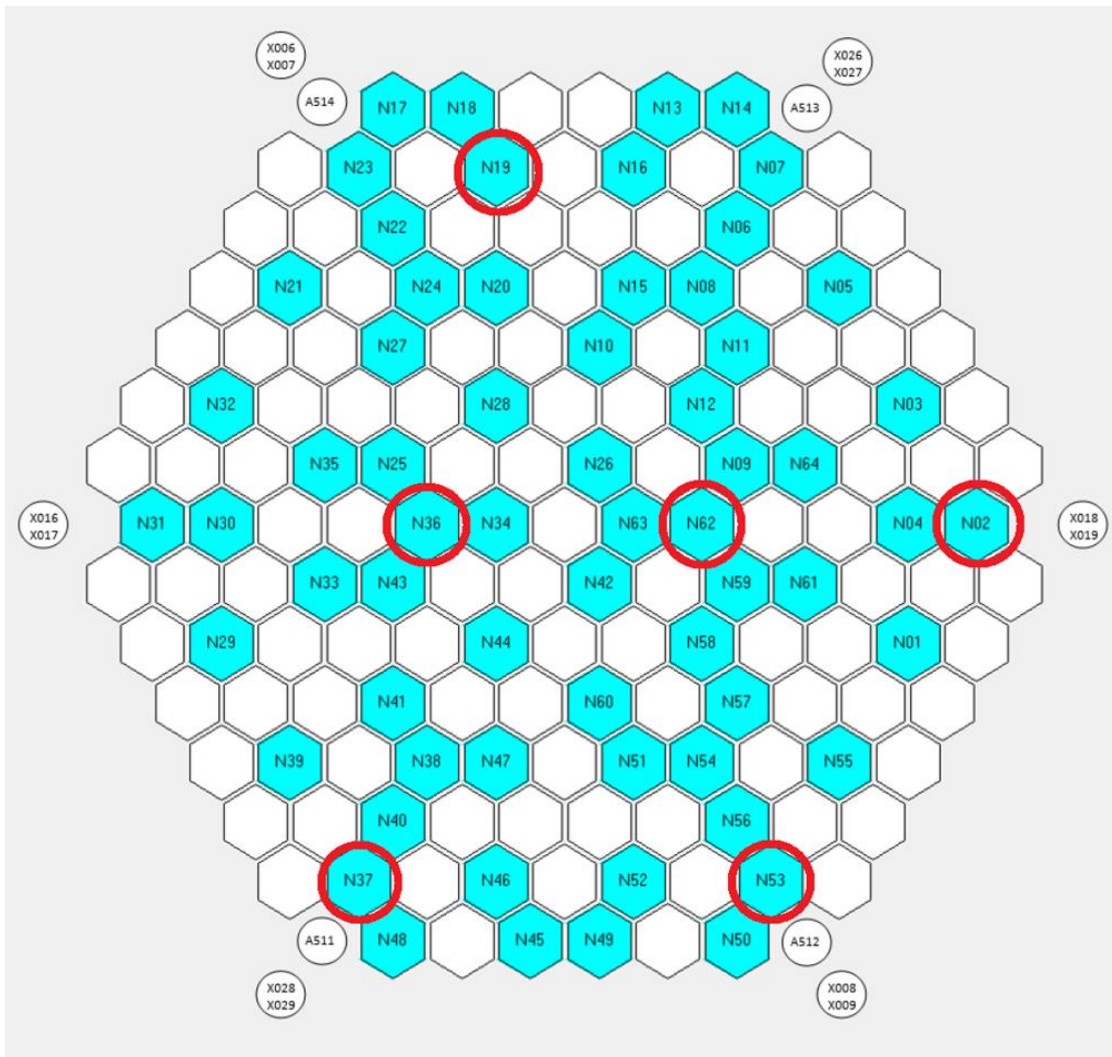
Figure 169: VVER-1000 sensors exhibiting out of the ordinary behavior (in red cycles).

6 Conclusions

This report provided a detailed analysis on the application of the tools developed, both within the framework of the CORTEX project and outside of it, for reactor noise analysis, advanced signal processing and machine learning methodologies on actual plant data, yielding interesting results. More specifically, the studied fluid-structure interaction simulations with the GRS mechanical model, under generic excitation scenarios revealed, among other things, that core-wide oscillations are unlikely to have a local source or that motions of fuel assemblies are transferred to the core barrel only weakly and only if there is a non-zero net reaction force.

Additionally, the coupled simulations of a reduced order mechanical model and the reactor core code DYN3D provided plausible results. It was demonstrated that under the assumption that the fluidic near-field coupling is very weak and that the driving force of the mechanical oscillations is mainly a stochastic force on the core barrel and RPV, an out-of-phase behavior of neutron noise signals in opposite core halves could be observed. This shows that the loading pattern of a core could be a factor in the noise characteristics due to different mechanical properties of the fuel assemblies.

The application of the signal processing techniques on both plant measurements and simulated data confirmed previous findings, like the linear phase between in-core detectors of the same string, the high response amplitude at low frequencies (below 1 Hz), a characteristic that seems to be related to the thermal-hydraulic oscillations produced in the core. In addition, the SSA methodology allowed us to explore the time domain in order to extract the trend and the oscillation part of the signals. After revealing the different spectral components of the signal, we were able to assess the value of the frequencies at an advanced resolution.

Finally, the application of machine learning-based techniques helped both in anomaly classification and the localization of the perturbations. Using a variety of unsupervised learning algorithms, detector signals have been grouped to two classes, the majority and the minority one, with the latter containing those signals whose characteristics appeared to be extraordinary. It was further demonstrated that certain signals have been classified by the majority of the examined techniques as not normal, an indication of their suitability for the given task. Lastly, the different deep learning architectures for perturbation localization achieved very good results on the simulated data and at the same time they reveal new insights, like strong indications of fuel assembly oscillations at frequencies different from their natural frequencies, on the actual plant measurements.

7 References

Bläsius, C. (2018). Private communication. Gesellschaft für Anlagen- und Reaktorsicherheit (GRS) gGmbH.

Demazière C. and Dokhane A. (2019), Description of scenarios for the simulated data. CORTEX deliverable D3.1.

Demazière, C., Mylonakis, A., Vinai, P., Durrant, A., De Sousa Ribeiro, F., Wingate, J. and Kollias, S. (2020). Neutron Noise-based Anomaly Classification and Localization using Machine Learning. *Proc. Int. Conf. Physics of Reactors (PHYSOR 2020: Transition to a Scalable Nuclear Future)*, Cambridge, UK, March 29th - April 2nd, 2020.

Dokhane A. and Mylonakis A. (2019), Description of simulated data. CORTEX deliverable D3.2.

Gao H., Liu Z., Van Der Maaten L., and Weinberger K. Q. (2017). Densely connected convolutional networks. IEEE Conference on Computer Vision and Pattern Recognition.

Girardin, G., Meier, R., Alander, A., and Jatuff, F. (2017). Neutron flux oscillations phenomena at Kernkraftwerk Gösgen (KKG). Berlin: Annual Meeting on NuclearTechnology, AMNT 2017.

Grandi G. (2011), SIMULATE-3K models and methodology. SSP Technical Report SSP-98/13, Rev. 7.

Herb, J., Bläsius, C., Perin, Y., Sievers, J., and Velkov, K. (2017). Analyses of Possible Explanations for the Neutron Flux Fluctuations in German PWR. Berlin: 48th Annual Meeting on Nuclear Technology.

Ioannou, G., Tagaris, T., Alexandridis, G., & Stafylopatis, A. (2020). Intelligent techniques for anomaly detection in nuclear reactors. In Proc. Int. Conf. Physics of Reactors− Transition to a scalable nuclear future (PHYSOR2020), London, UK

S. Kollias, et al. (2019). Development of machine learning techniques and evaluation of analysis results. Deliverable D3.4. CORTEX Project. GA nº 754316.

Kaul, P., De Martini, D., Gadd, M., & Newman, P. (2020). RSS-Net: Weakly-Supervised Multi-Class Semantic Segmentation with FMCW Radar. arXiv preprint arXiv:2004.03451.

Kuentzel M., Stulik P., Seidl M., Lipcsei S., Girardin G. and Schumaker B. (2018), Core data for steady state calculations. CORTEX deliverable D4.2.

Lin T., Goyal P., Girshick R., He K. and Dollár, P. (2017). Focal loss for dense object detection. Proceedings of the IEEE international conference on computer vision.

Lipcsei S., Kiss S., Pohlus J., Paquee U., Girardin G., Pohl C., Seidl M., Stulik P., Bem M., Machek J., Schumaker B. and Riggsbee E. (2018), Document describing all validation data. CORTEX deliverable D4.3.

Liu, R., Lehman, J., Molino, P., Such, F. P., Frank, E., Sergeev, A., and Yosinski, J. (2018). An intriguing failing of convolutional neural networks and the coordconv solution. In Advances in Neural Information Processing Systems (pp. 9605-9616).

Montalvo C., et al. (2020). Preliminary analysis of actual plant data and adaptation of techniques. Deliverable D3.5. CORTEX Project. GA nº 754316.

Mylonakis A.G., Vinai P. and Demazière C. (2020). Numerical solution of two-energy-group neutron noise. Annals of Nuclear Energy, 140, 107093.

Pohlus, J. and Paquée, U. (2018). Untersuchung veränderter Neutronenflussschwankungen und Brennstab-Beanspruchungen in DWR-Anlagen im Rahmen der Sicherheitsforschung. TÜV Rheinland ISTec GmbH, ISTec - A – 3695, in German.

Pohlus J., Paquee U. and Girardin G. (2018), Report about the measurement results of Gösgen. CORTEX deliverable D4.1.

Rohde, U., Kliem, S., Grundmann, U., Baier, S., Bilodid, Y., Duerigen, S., Fridman, E., Gommlich, A., Grahn, A., Holt, L., Kozmenkov, Y. and Mittag, S. (2016). The reactor dynamics code {DYN3D} – models, validation and applications. Prog. Nucl. Energy 89, 170–190. https://doi.org/10.1016/j.pnucene.2016.02.013

Runkel, J. (1987). Rauschanalyse in Druckwasserreaktoren. Dissertation, University of Hannover, in German.

Seidel, M., Kosowski, K., Schüler, U., and Belblidia, L. (2015). Review of the historic neutron noise behavior in German KWU built PWRs. Progress in Nuclear Energy, Vol. 85, pp. 668-675.

Tagaris, T., Ioannou, G., Sdraka, M., Alexandridis, G., & Stafylopatis, A. (2019). Putting Together Wavelet-based Scaleograms and Convolutional Neural Networks for Anomaly Detection in Nuclear Reactors. In *Proceedings of the 2019 3rd International Conference on Advances in Artificial Intelligence* (pp. 237-243).

Viebach, M., Lange, C., Bernt, N., Seidl, M., Hennig, D. and Hurtado, A. (2019). Simulation of low-frequency PWR neutron flux fluctuations. Prog. Nucl. Energy 117, 103039. https://doi.org/10.1016/j.pnucene.2019.103039

Viebach, M., Lange, C., Seidl, M., Bilodid, Y., Hurtado, A. (2020). Neutron Noise Patterns from Coupled Fuel-Assembly Vibrations, *Proc. Int. Conf. Physics of Reactors (PHYSOR 2020: Transition to a Scalable Nuclear Future)*, Cambridge, UK, March 29th - April 2nd, 2020.

Vidal-Ferràndiz A., Carreño A., Ginestar D., Demazière C. and Verdú G. (2020), A time and frequency domain analysis of the effect of vibrating fuel assemblies on the neutron noise. *Annals of Nuclear Energy*, **137**, 107076.

Vidal-Ferràndiz A., Ginestar D., Carreño A., Verdú G. and Demazière C. (2020), A finite element method for neutron noise calculations in hexagonal reactors. *Proc. Int. Conf. Physics of Reactors (PHYSOR 2020: Transition to a Scalable Nuclear Future)*, Cambridge, UK, March 29th - April 2nd, 2020.

Stulík P., Torres L., Montalvo C., García-Berrocal A., Salazar C., Alexandridis G., Tambouratzis T., Machek J., Pantera L., Bem M. (2019). Development of advanced signal processing techniques and evaluation results. Deliverable D3.3 CORTEX project, GA nº 7543162019.

Stulik P., Bem M., Tschiesche J., Machek J. (2020). WP4 Progress Report on subtask T4.2.3, CORTEX project, GA nº 7543162019.

Sun, Y., Tzeng, E., Darrell, T., & Efros, A. A. (2019). Unsupervised domain adaptation through self-supervision. arXiv preprint arXiv:1909.11825.

Pantera L. (2020). Use of the Singular Spectrum Analysis (SSA) methodology to assess the frequency contents of the neutron noise in UJV WWW-1000 reactor. WP4 Progress Report, CORTEX project, GA nº 7543162019.

Wei, Y., Xiao, H., Shi, H., Jie, Z., Feng, J., and Huang, T. S. (2018). Revisiting dilated convolution: A simple approach for weakly-and semi-supervised semantic segmentation. In Proceedings of the IEEE Conference on Computer Vision and Pattern Recognition (pp. 7268-7277).